Dissertation
submitted to the
Combined Faculties for the Natural Sciences and for Mathematics
of the Ruperto-Carola University of Heidelberg, Germany
for the degree of
Doctor of Natural Sciences

Put forward by

Jamie O'Sullivan, M.Sc.

born in Limerick, Ireland

oral examination: 02.12.2009

Molecular Cooling and Emissions in Large Scale Simulations of Protostellar Jets

Referees:

Prof. Dr. Max Camenzind
Dr. Robi Banerjee

Abstract

The origin of infrared molecular emission associated with Class 0 and Class I protostellar outflows (such as HH211 and HH46/47) is still not fully resolved. One successful model for describing such phenomena is the jet-driven outflow model. It proposes that the emission occurs as a high velocity collimated jet outflow shocks, excites and entrains the molecular ambient matter. Although this scenario does achieve significant success in describing the dynamics and morphology of the outflow, the exact nature of the type of shock causing the emission in such a case - J-type or C-type - is still unclear.

Physical conditions in the gas, such the ionisation fraction and magnetic field, are crucial parameters determining the type of shock that will form. However, the immediate region around the class 0 sources producing molecular outflows usually consists of dense, high-extinction gas within a molecular core, impeding observational data regarding these details. Therefore, numerical modelling can play an important role in explaining the observed outflows.

We have developed and tested a module, implemented within the PLUTO astrophysical code, to simulate the non-equilibrium molecular chemistry and cooling in a jet outflow which is interacting with its surrounding molecular core gas. Using large scale adaptive mesh magnetohydrodynamical simulations, we predict observationally significant amounts of infrared emissions from J-shock excited molecular gas. We find that the emission can be caused either by direct shocking ("prompt entrainment") or entrainment and ablation of the ambient gas. We find that the nature of this emission is strongly dependent on absolute and relative densities of the jet and ambient medium, and on the presence of moderate magnetic fields ($30 - 120\,\mu$G) in the core. Comparing our results with observations, we confirm that the magnitudes for the emission strength agree with those observed in several sources. Furthermore we demonstrate how the appearance of the emission in different sources depends on the parameters explored here.

Zusammenfassung

Der Ursprung der molekularen Infrarotemission im Zusammenhang mit protostellaren Jets der Klasse 0 und Klasse 1 (z.B. HH211 und HH46/47) ist nicht vollständig verstanden. Ein Modell, das diese Phänomene erfolgreich beschreibt ist das „jet-driven outflow“ Modell. Dieses erklärt die Abstrahlung durch einen kollimierten Jet, der mit hoher Geschwindigkeit auf die molekulare Materie in der Umgebung trifft und diese in Schocks anregt und mit sich reit. Obgleich dieses Szenarium sehr erfolgreich die Dynamik und Morphologie des Ausflusses beschreibt, ist weiterhin unklar, ob Schocks des Typ J oder C diese Emission verursachen.
Die physikalische Beschaffenheit des Gases, namentlich der Ionisierungsgrad und das Magnetfeld, sind wesentliche Parameter, die die genaue Art des Schock bestimmen. Da jedoch die direkte Umgebung von Klasse 0 Objekten aus dichtem Gas hoher Extinktionsrate innerhalb eines molekularen Kerns besteht, ist die direkte Beobachtung dieser Daten unmglich. Daher spielt die numerische Modellierung eine wichtige Rolle bei der Erforschung der beobachteten Ausflüsse.
Wir haben ein Modul für den astrophysikalischen Simulationscode PLUTO entwickelt und getestet, das die molekulare Nichtgleichgewichtschemie und Khlung in einem Jet während seiner Interaktion mit dem molekularen Gas des umgebenden protostellaren Kerns simuliert. Unter Verwendung von großskaligen magnetohydrodynamischen Simulationen auf adaptivem Gitter finden wir bedeutende Infrarotemissionen von molekularem Gas das in J-Schocks angeregt wurde. Unsere Ergebnisse zeigen, dass diese Abstrahlung sowohl durch direkte Schocks („prompt entrainment“) oder durch Abtragung und Abdampfung des Umgebungsgases verursacht werden kann. Die Eigenschaften der Emission sind stark von den absoluten und relativen Dichten der Jetmaterie und des Umgebungsgases und von dem Vorhandensein eines moderaten Magnetfeldes (in der Größenordnung $30 - 120\,\mu$G) um protostellaren Kern abhängig. Beim Vergleich mit Beobachtungen zeigt sich, das die berechnete Abstrahlungsintensität von der selben Größenordung wie die beobachtete ist. Wir zeigen wie die Emission verschiedener Quellen am Himmel von den hier untersuchten Parametern abhängt.

Contents

List of Figures

List of Tables

1 Introduction

The subject of this thesis is the origin of the molecular hydrogen emission from outflows associated with protostellar jets. In this chapter we begin with a description of these objects and summary of what is known about their origin. This is followed by more details of the specific aspects of these jets which are of interest to us and to which our research relates. Finally we outline the specific questions we intend to address and set out our procedure for going about it.

1.1 Protostellar Outflows and Herbig-Haro Objects

It was initially found puzzling that the G-type star T Tauri could excite an emission nebula in lines such as SII and OII. First discovered independently by Herbig and Haro (Herbig, 1950; Haro, 1952), this mysterious emission was later identified as being due to shocks associated with stellar winds from the star (Schwartz, 1975; Dopita, 1978). The spectra of these emissions showed line widths suggesting velocities of around 100km s^{-1}, leading to early speculation by Osterbrock (1958) that high-velocity matter ejected from the star was somehow responsible for the emission. This was later supported by further measurements, such as the proper motions of Herbig-Haro objects HH1 and HH2, which were observed to be moving in opposite directions away from the central stellar object (Herbig & Jones, 1981). Around the same time, highly collimated outflows or "jets" were being discovered emanating directly from the protostars (Mundt & Fried, 1983; Reipurth *et al.*, 1986) and by the mid-80s the exact nature of the connection had become clear; these "nebulae" indeed appeared to be termination shocks powered by jet outflows from nearby young stellar objects (Mundt, 1985; Lada, 1985).

Jets are among the most spectacular of astrophysical phenomena, and since their relatively recent discovery 454 (at time of writing) have been catalogued, see Reipurth (2000). Although the earlier discoveries were in the optical wavelengths, more and more sources are now being discovered in the infrared wavelengths (e.g. Davis *et al.* (2009)). A perfect example is the HH212 outflow (see figure 1.1), which originates

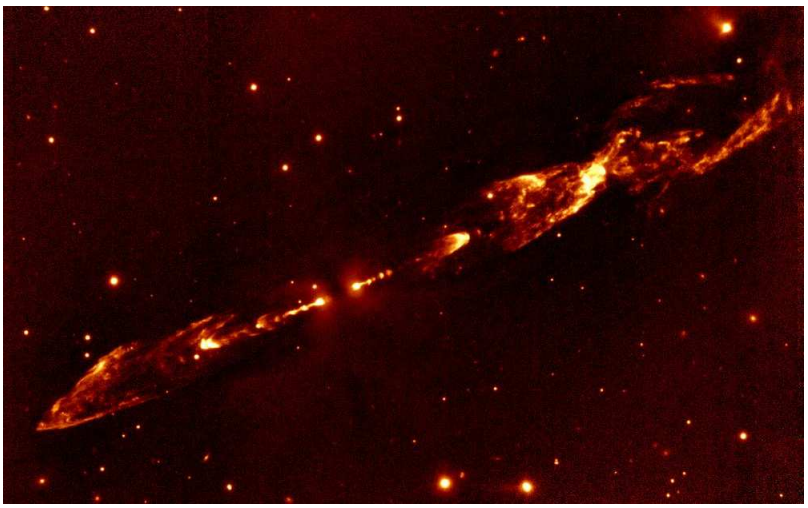

Figure 1.1: As symmetric as it gets: HH212, an infrared molecular jet (Zinnecker *et al.*, 1997) shown here appropriately in the H_2 ro-vibrational 2.12 μm infrared line

from a deeply embedded source itself obscured behind a dense accretion envelope.

A somewhat anomalous example of a molecular jet is the counterjet in the HH46/47 bipolar outflow (see figures 1.2 and 1.3), where the infrared observations show what appears as a cocoon-shaped emission.

In the intervening years since their relatively recent discovery, these objects have been the subject of intense observational, theoretical, and even experimental work as they provide a valuable window on the star formation process on scales we can observe, and their potential to affect their environment and subsequent star formation has also been considered (Mac Low & Klessen, 2004; Banerjee *et al.*, 2007; Quillen *et al.*, 2005). As these outflows are inextricably linked with protostellar evolution, it is helpful to outline the picture which has emerged of this process before continuing with the description of the jets themselves. We examine where our scenario fits in the big picture, before going on to examine the observational properties and theoretical understanding of young stellar objects (YSOs) and their outflows.

1.2 Jets in the Context of Star Formation

Starting from our own galaxy, the Milky way, the only galaxy where we can directly observe outflows. We see that there is a traceable pattern of collapse from the spiral arms down to the scale of the star-disk system (see fig. 1.4). This is termed **fragmentation** and states, in a word, the propensity of gas to "clump" on basically any scale from the megaparsec scales of the cosmological universe right down to the Jeans scale, the smallest scale where the always-attractive force of gravity is able to strongly determine the gas evolution. As described in Schulz (2005), this multi-scale process can be divided into the following broad phases directly affecting star formation:

- 10 kpc - the scale of the spiral arms of the Galaxy, the initial compressions due to spiral waves in the galactic plane are readily visible
- 1 kpc - diffuse HI clouds observed in 21 cm line

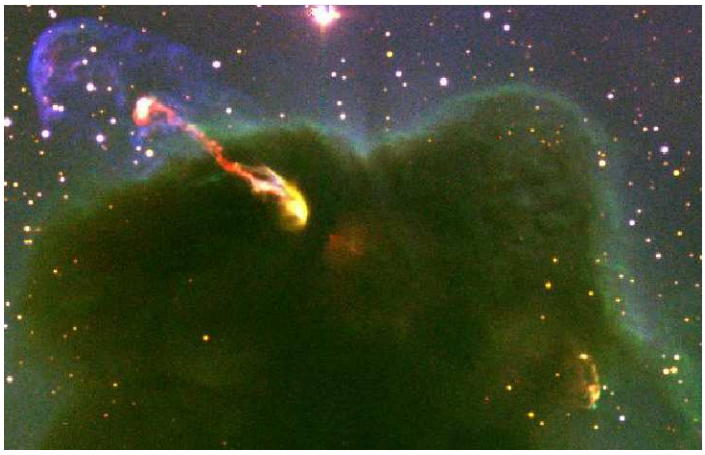

Figure 1.2: The bipolar outflow HH46/47, seen in optical wavelengths in an image from the ESO New Technology telescope, with SII, OII and Hα in red, blue and green respectively. The beam is lit up in SII as it protrudes from a dense molecular core, while the OII atomic emission marks the interaction of the bow-shock with the more diffuse gas outside the core.

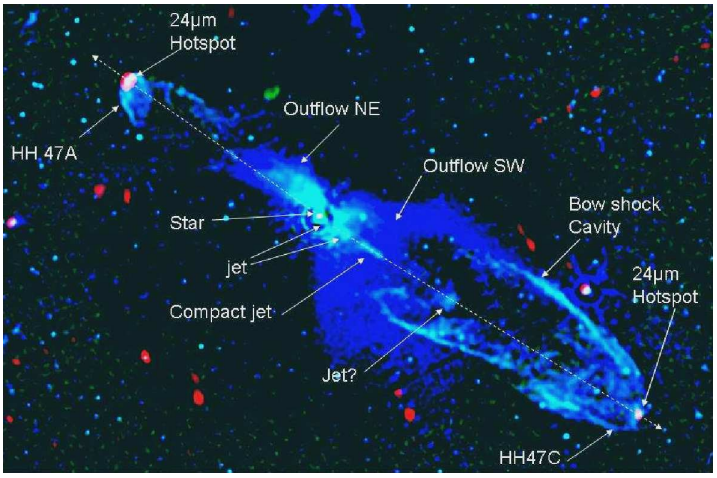

Figure 1.3: The bipolar outflow HH46/47 in infrared wavelengths. Viewing the same source in infrared wavelengths reveals the counterjet moving into and through the cloud (Velusamy *et al.*, 2007).

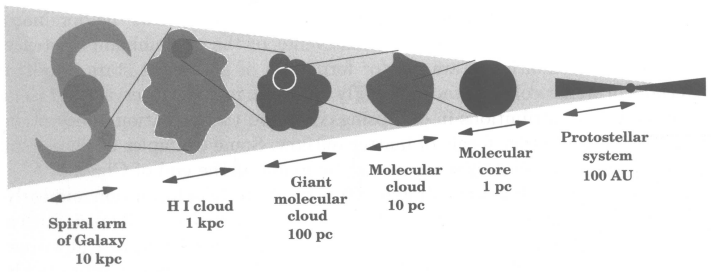

Figure 1.4: Schematic diagram of the process of fragmentation (Schulz, 2005)

- 100 kpc - giant molecular clouds
- 10 pc - molecular clouds
- 0.1 pc - molecular cores
- 100 AU - protostellar scale

Analysis of star clusters in nearby galaxies shows a correlation between star age differences and inter-star distance, suggesting that smaller, denser regions form stars quickly within larger more diffuse regions where stars form over a longer time scale (Efremov & Elmegreen, 1998).

On the small end of this cascading cycle of fragmentation is the **pre-stellar core**, often modelled as a thermally supported Bonnor-Ebert sphere (as some evidence indicates that the turbulent support present in the more diffuse cloud on larger scales is absent in the cores, see Kirk *et al.* (2009)). These cores have a typical length of 0.15pc, and have been deduced statistically to take some 3.0×10^5 years to form a protostar (Kirk, 2007).

1.2.1 Classification of Young Stellar Objects (YSOs)

As summarised in Schulz (2005), a classification scheme has emerged for protostars, dividing what appears to be a diverse range of observed objects into a more manageable arrangement of phases, see figure 1.5. This scheme divides the protostars into classes, namely Class 0, I, II or III. These stages are preceded by a long timescale collapse of a cold dense core inside a molecular cloud. This core is finally considered to harbour a Class 0 protostar when the process of accretion has become established enough that the accretion disk starts to form. In this class, most of the system's mass is still actually in the disk gas, and the central core is still cold with a temperature less than 100K. The SED of these objects is that of a cold black body, observable in the sub-millimeter wavelengths.

The next stage, the Class I object, represents a more evolved object, with the disk taking the more flattened form and the central object now having accreted much more matter, so that more of the matter is contained in the protostar than in the surrounding disk and ambient gas. However, the surrounding gas and disk are still dense enough to cause heavy dust extinction of the optical wavelengths, so that Class I central objects are observed mainly with the infrared wavelengths. This stage lasts

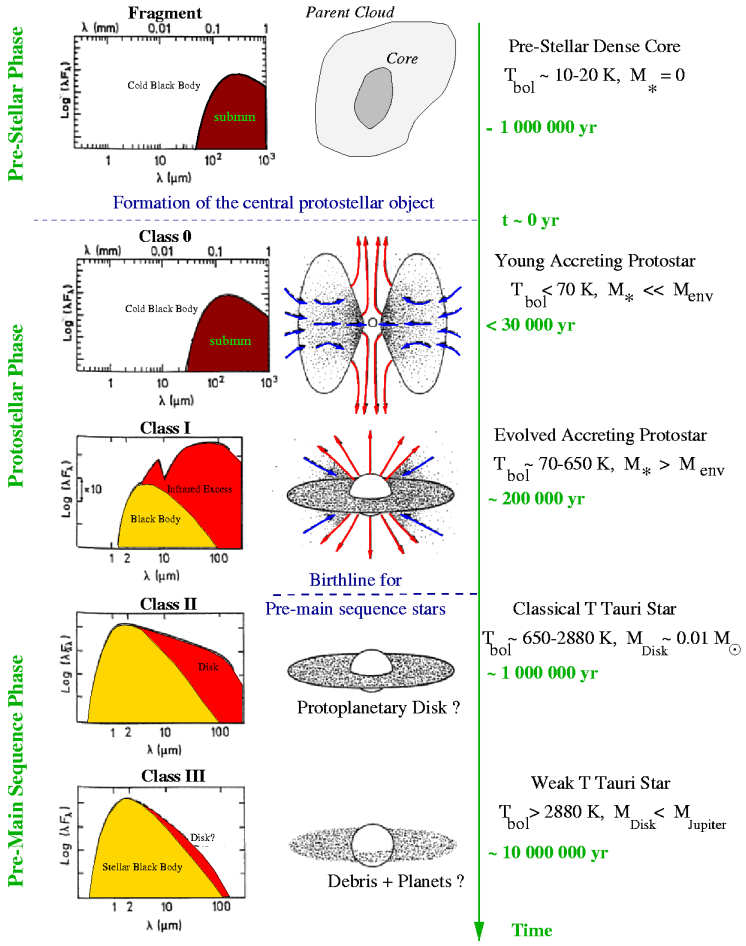

Figure 1.5: Pre-main sequence stages of a typical star's evolution O'Connell (2005), showing the progression from the cold disk-dominated Class O sources towards the pre-main sequence Class III star.

for about the first 200,000 years or so of the protostar's lifetime, leading to the end of the protostellar phase and the beginning of the pre-main sequence Class II phase.

The Class II phase is distinguished from the Class I phase by the fact that the stellar wind has by now blown off most of the surrounding gas (except for the accretion disk), and by the temperature, which will have risen to some thousands of Kelvin. These objects are also known as Classical T Tauri stars, named after the first object of this type to be discovered.

Class III represents the most advanced stage of the pre-stellar phase between 1 and 10 million years, with only a small amount of matter (mainly debris) remaining in the disk, and with the central object having reached a bolometric temperature of over 3000 K.

With these classifications of the protostars, and the many objects with outflows already discovered, an empirical model relating to the properties of the outflows to each evolutionary phase has developed (see fig 1.2.1). The outflow activity appears to decline with progressing age. Bontemps *et al.* (1996) compared the outflow strength, via measurements of as CO momentum flux of the outflow, with the age as measured

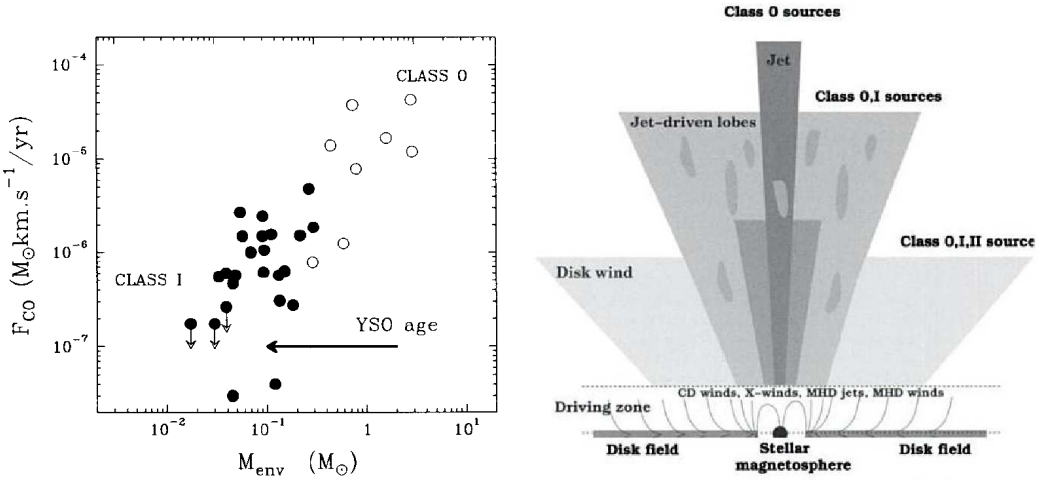

Figure 1.6: Outflow properties as a function of age. Measurements of the strength of the outflow versus the protostellar age, inversely proportional to the envelope mass, which gets accreted over time. The right panel shows the classification picture emerging from such measurements (Schulz, 2005)

by the mass in the protostellar envelope, and found a strong correlation: the objects with the fastest and most collimated associated jets are the Class 0 objects, with the Class I (and Class II) sources displaying progressively slower and less collimated jets.

The class of object we will mainly deal with in this thesis is the Class 0 phase, i.e. young (of the order of 10^4 years) deeply embedded sources, such as HH211 (see figure 1.7).

1.3 Observational Properties and Constraints

The observed protostellar jets have a number of features and properties that we can use to characterise them.

- Firstly, protostellar jets are **bipolar**; in very many cases both a jet and its counterjet are observed, however, in some cases the counterjet may be obscured by dust if it propagates into a more dense part of the molecular cloud. In these cases, the counterjet can often be seen in infrared wavelengths, as in the case of HH46/47 (see Fig 1.3).

- Jets are also seen to occur for a wide range of **propagation lengths**, ranging from a couple of hundred AU to the parsec scale (200,000 AU), though the jets we try to model are more usually in the range 8,000 to 30,000 AU.

- Jets are highly collimated, with very small **opening angles** (around 1 or 2 degrees) and length-to-width ratios ranging from 5 up to 100 in the case of HH111.

- Many HH objects, though not all, display periodic arrangements of brighter emission or **knots** along the beam of the jet due to either instabilities in the flow or,

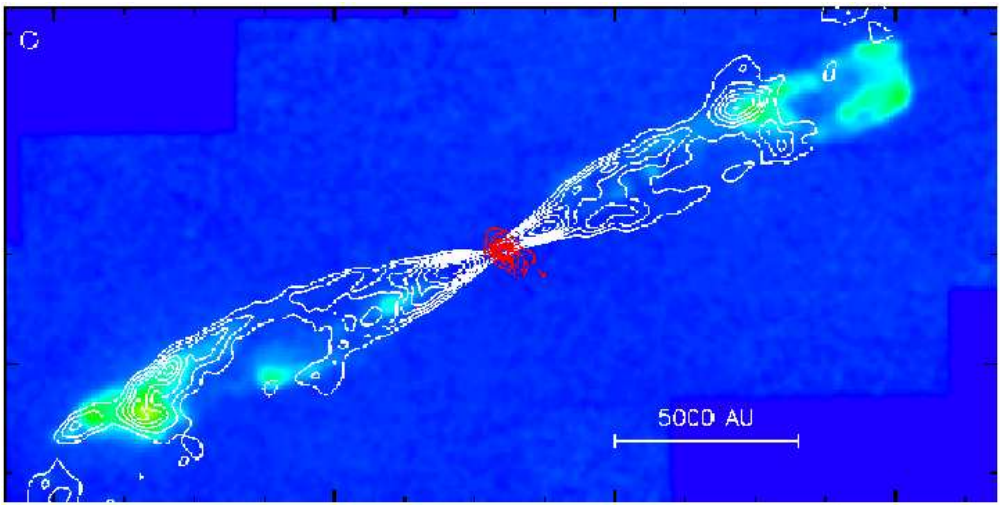

Figure 1.7: HH211, archetypal example of a molecular outflow from a Class 0 protostar The H_2 2.12μm emission intensity is shown in blue-green, while the white contours represent the CO component moving slower than 10km s^{-1}(Gueth & Guilloteau, 1999)

according to a view gaining ever more traction in the community, periodicity in the velocity of the outflow.

- Jets have **high propagation speeds**, typically in the range 100-200km s^{-1}, and are highly supersonic, with Mach numbers of around 20-80.

- Many, if not all protostellar outflows have a prominant bright emission or "hotspot" at the furthest extremity, usually in strong optical line emission from ionised atomic species such as SII and OII.

- This strong emission region is usually accompanied by an associated **bow shock region**, an extended region of emission leading back from the head of the jet, named for its resemblance to the form taken by water deflected from a ship's bow.

- Jet beams, particularly optical jets, can display a significant degree of **ionisation**, which tends to decrease gradually along the jet as electrons recombine (Bacciotti & Eislöffel, 1999). A crucial parameter due to the fact that the electron density is our primary means of determining gas densities in the jet beam.

- **Temperature** - Typical beam temperatures are in the range of 10^3-10^4 K, although the knots along the jet can reach significantly higher temperatures.

- **Density** - Most protostellar jets are thought to be overdense, having a density between 1 and 20 times that of the ambient medium, and in the range 10^3-10^4cm^{-3}.

- Depending on the inclination angle of the jet with the plane of the sky, **blue- and red-shifting of the lobes** may be observed

- Important for questions such as jet launching, collimation, and transport of angular momentum from the star-disk system **rotation** has recently been observed in some

jets, e.g. Coffey *et al.* (2004) and progress is continuing rapidly in this area Woitas *et al.* (2005); Coffey *et al.* (2008).

- Momentum transfer, average **mass fluxes** within jets are estimated to range between $10^{-}9$ to $10^{-}5$ $M_{\odot}$ yr^{-1}.

1.3.1 Observations of Molecular Outflows

The H_2 molecule, because of its lack of a dipole moment, is an unsuitable molecule to observe gas at low temperatures, compared with other molecules such as CO. However, it has in recent years been emerging as a key observable in protostellar jets. Its ro-vibrational transition lines, such as the 1-0S(1) line, have the dual benefits of being in the infrared, thus escaping the strong extinction of optical lines, and of being rather high energy transitions, making them ideal tracers for shock excitation.

The protostellar jet sources which emit in the infrared, seem to fall into three morphological categories. Although it is unclear what exactly the cause for the differing appearances is, the author thinks it may be helpful to classify these infrared jets in the following way:

A Arrowhead-type emitters such as HH212, where sharp angular bows are seen, sometimes several in succession, moving out from the central source and expanding.

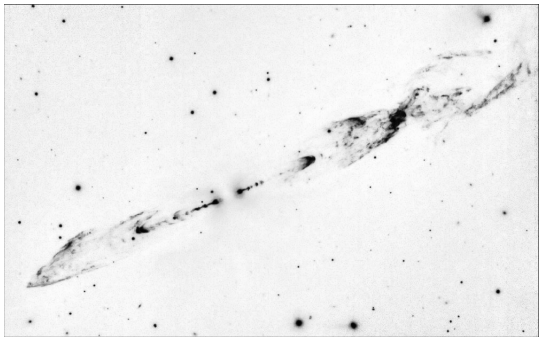

B Clumpy emitters such as HH211. These display less symmetric, often thicker and more irregularly shaped regions of emission, sometimes with distinct "gaps" between the emitting regions, as in the case of HH211.

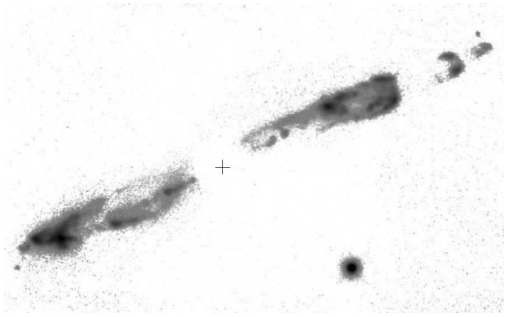

C Shell-type emitters such as HH46/47 (the only known example to date), where one single continuous shell molecular emission extends backwards from the head of the jet without any apparent disruption or clumping.

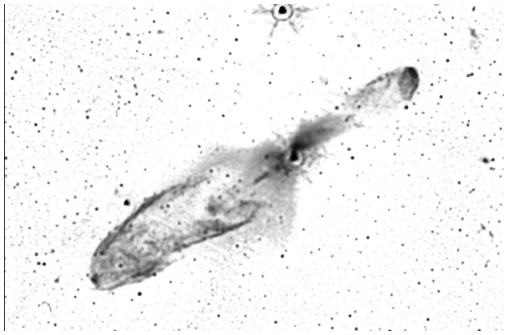

Many of these sources have, in addition to the H_2 emission, coincident CO emissions. What are the causes for these differences in the types of emission? Are they due to macroscopic properties such as the density profile of the core, density contrast of the jet with respect to the medium, dynamical properties (velocity, magnetic pressure) or microscopic aspects of the flow, such as shock chemistry? Interestingly enough, some infrared jets do not appear to have this bow-shock structure. For example the jet in the Carina Nebula, HH666, emits strongly in the FeII infrared lines (see fig 1.8), seeming to follow the beam gas, while lacking any H_2 emission Smith *et al.* (2005). In this particular case, the strong radiation field seen hitting the surface of the cloud could also be responsible through photodissociation of the molecular material in the outer layers of the cloud.

1.4 Jet Propagation - Theory

Following the detection of this infrared emission, several types of matter outflow have been proposed in an effort to explain the observed jet characteristics, and form the basis for most of the simulation work done. On the macroscopic level, the main candidates can be broken down into two categories; the "turbulent entrainment" model, and the jet-driven shock (or "prompt entrainment" model). In the entrainment model, the emission is supposed to originate from environmental gas (mostly molecular) swept up and carried along by the jet motion, and subsequently excited through ablation by the internal working surfaces of the jet. In the shock models, the ambient molecular material encountered by the jet's bow is shocked and emits directly. Within this category there is debate as to whether the shock heating in question is due to the standard J-type shock (i.e. "jump" type) or the more complex C-type ("continuous") shocks (see fig 1.12 and section 1.4.1

In figure 1.4, the main categories of outflow model are shown. The stellar wind model, consisting of a wide angle wind pushing out an envelope of compressed gas was suggested by Snell *et al.* (1980) (see fig 1.9) to explain an observed molecular outflow in L1551, and developed by Canto & Rodriguez (1980) to explain the terminal shock.

The jet driven outflow model (reference) on the other hand assumes an already collimated jet outflow which drives a bow-shock into the medium, and explains quite easily the formation of a hotspot by means of the Mach disk, where the jet material is reverse-shocked. Lee *et al.* (2000) compared the ability of these models to reproduce the position-velocity diagrams of observed jets, and found that the wind-driven model produced a remarkable match for the outflow near VLA 05487's source, but falls short in explaining the emissions in sources where H_2 bow-shocks are clearly observed. Jet-driven models (see fig 1.10), on the other hand, face challenges in reproducing the wide-angle outflows often associated with the bow-shocks and knots that they reproduce well, as well as uncertainties in the exact nature of the shock excitation mechanism. Circulation, or "transit" models deviate from the common assumption of a dipolar magnetic field, and examine the possibility of outlows in a quadrupolar magnetic topology, a detailed description is given in Lery (2007).

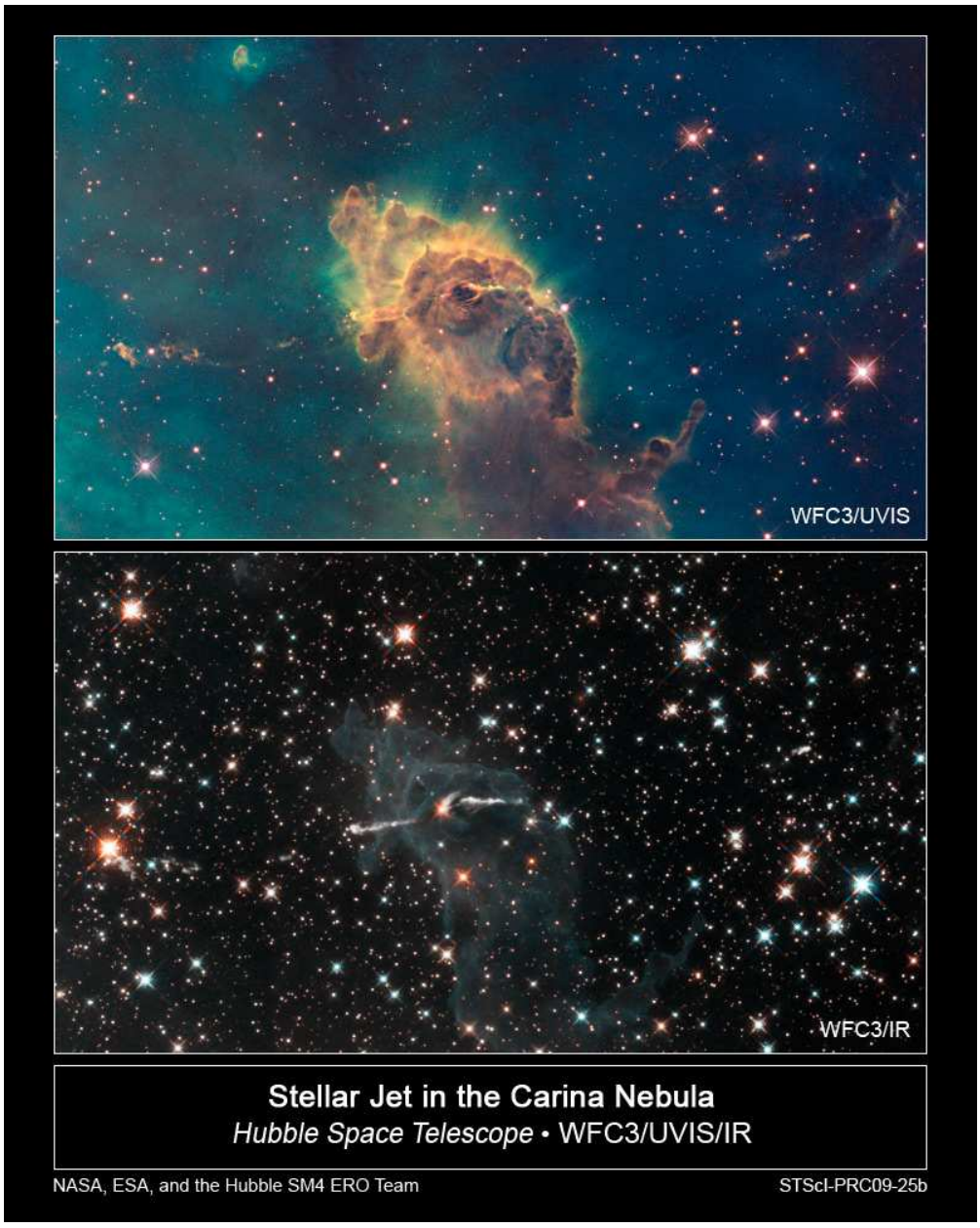

Figure 1.8: An infrared jet, but no H_2! The Carina Nebula is host to a large episodic bipolar jet visible in infrared in the lower panel. The infrared emission is however from FeII lines and not H_2

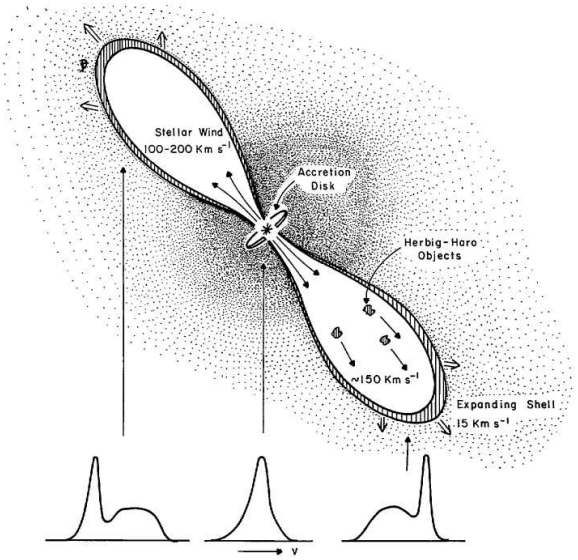

Figure 1.9: Schematic of the stellar wind model proposed by Snell *et al.* (1980), which explains some observed features but has setbacks.

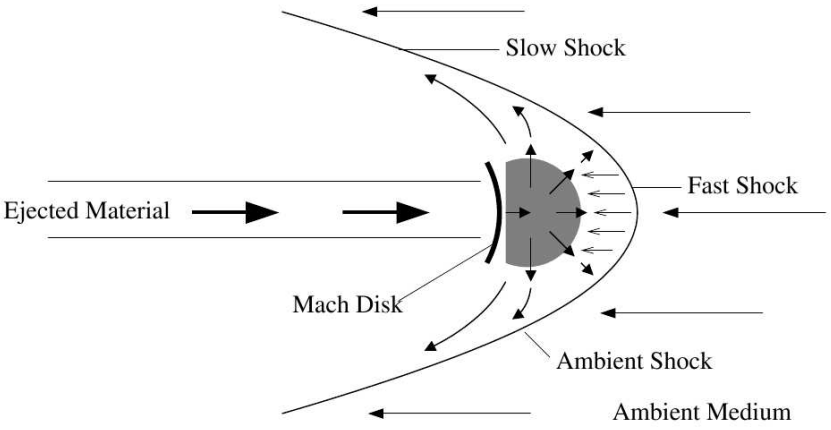

Figure 1.10: Schematic diagram of jet-shocked ouflow model , which intuitively seems to make sense as a model and reproduces many features.

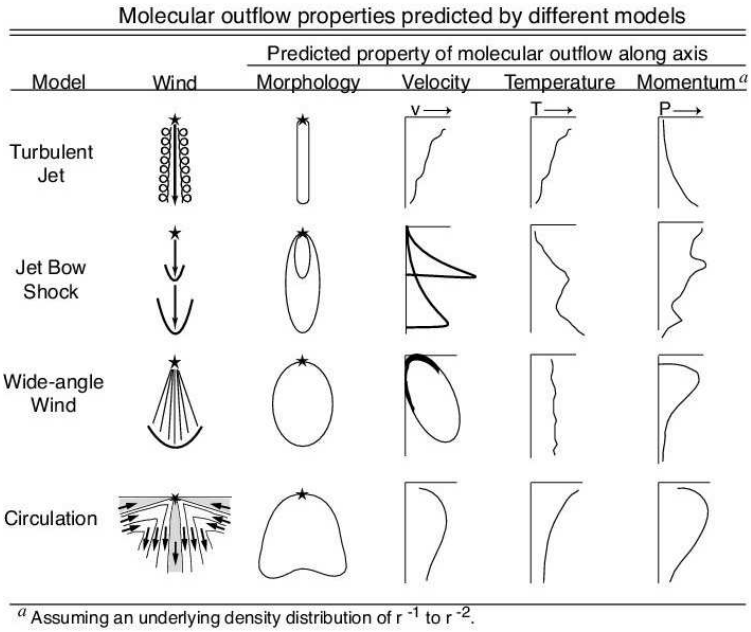

Figure 1.11: Summary of outflow model types and their characteristics.

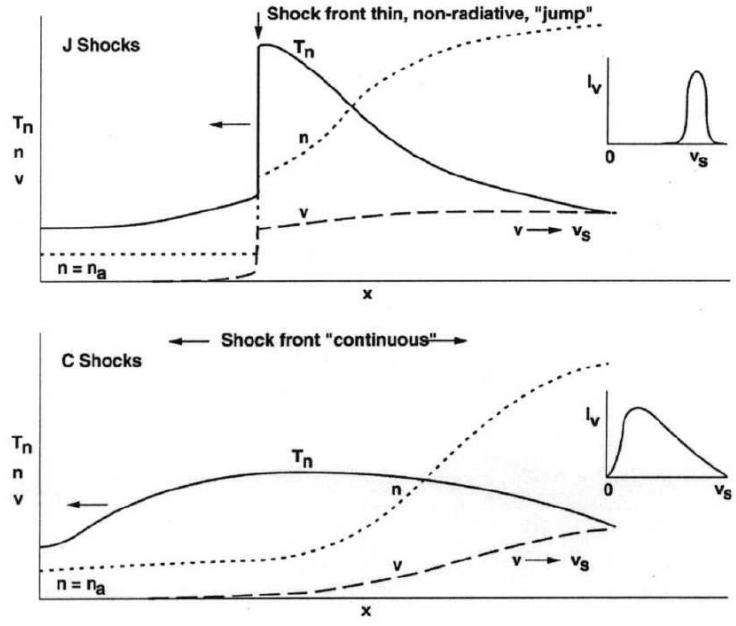

Figure 1.12: Schematic of J-shock and C-shock structures from Hollenbach (1997)

1.4.1 J-shocks and C-shocks

As described in Draine (1980), shocks in an ionised gas can be classified into three types:

- jump-type shocks, where the flow variables undergo large changes on a length scale comparable to the mean free path, which we effectively view as a discontinuity. Hollenbach & McKee (1989)
- jump-type shocks with "precursors", arising from magnetosonic disturbances propagating faster than the shock speed.
- C-type shocks where collisions between the ions and neutrals causes the temperature to rise gradually, possibly providing conditions conducive to molecular emission without dissociation occurring.

The debate about which type of shock is the origin of the molecular emissions is still under intense debate, with evidence for both types of shock being presented. Gredel (1996) and Giannini *et al.* (2002) for example, have invoked J-shocks as sources of the emissions in HH1 and HH43 respectively on the grounds that the line ratios of H_2 lines better fit excitation diagrams. There has also been work to the contrary, for example in (O'Connell, 2005), where the author uses a C-shock model to reproduce certain flattened bow shapes which have been observed, such as the ones near the head of HH211 (fig 1.7). This has been countered by geometrical arguments as illustrated in figure fig 1.13. Whether one or other type of shock occurs is a matter of the physical conditions present in the gas. For sufficiently high magnetic field strengths and sufficiently low ionisations in the pre-shock medium C-shocks are thought to occur even in fairly fast shocks up to $60\,\mathrm{km\ s^{-1}}$ (Le Bourlot *et al.*, 2002). Until these quantities can be constrained, J-type and C-type shocks compete to explain the observed bow-shock emissions.

1.4.2 Chemistry and Cooling

The motivation for the inclusion of non-ideal effects in simulations is twofold: firstly there's the need to examine the significant effect of the radiative cooling on the dynamics and energy balance of the flow, and secondly the use of the information about the chemical composition of the gas for diagnostic purposes, as one can then make reasonable estimates for line emissions, which are in fact the very means by which we observe the sources of interest. It is for this reason that extensive effort is being put into modelling chemistry in simulations, as documented in section 1.4.4.

When it comes to prediction of the molecular emissions described in section 1.3.1, the questions to ask boil down very simply to "Is there H_2? Is it hot enough to emit?". While for the atomic chemistry the matter of abundances is in some ways straightforward - one assumes solar abundances of metals for star-forming regions, and the concentrations of the various various ionised species are heavily dependent on the temperature and electron fraction - the case of molecular chemistry is a little more complicated. This is due to the fact that there is some degree of uncertainty about the molecular fraction which is dependent on the history of the accreted gas. Some recent theoretical work has been done (see Panoglou *et al.* (2009b,a)) to estimate

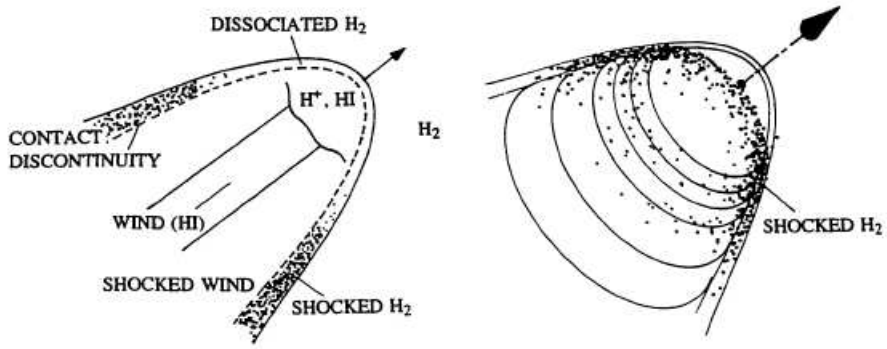

Figure 1.13: Appearance of dissociative J-type bow-shocks. A schematic diagram from Bally & Lane (1990) showing how a dissociating J-type bowshock seen at an angle may reproduce the arc-like H_2 emission observed in sources such as HH211.

the amount of H_2 surviving the accretion process by following the chemistry and temperature evolution of gas along a steady state accretion solution and accounting for both collisional and photo-dissociation mechanisms. This author finds that for the Class O sources that we consider, an appreciable fraction of H_2 exists in the flow itself, and that the flow may even be mostly molecular. This is very significant for our work, as it means that the emitting H_2 does not have to come solely from the surrounding ambient medium.

1.4.3 Jet Characterisation and Parameters

As with any area of physics, from the perspective of jet modelling, we first need to reduce the complicated system with all its intricate details of instabilities, microphysics etc. to a simplified, manageable model in order to obtain insight as we work towards a unified overview of the workings of our astrophysical scenario.

As the picture of jet morphology and dynamics has gradually become clearer, certain parameters have been identified as critical in the determination of the large scale structure and evolution of protostellar jets. Foremost among these these parameters are:

- the **density ratio,** η between the jet and the ambient medium,

$$\eta = \frac{\rho_{jet}}{\rho_{ambient}} \tag{1.1}$$

- The **plasma beta** (β), which is a measure of the relative strengths of the thermal and magnetic pressure terms, and is formulated in CGS units as

$$\beta = \frac{p_{therm}}{p_{mag}} = \frac{8\pi p_{therm}}{B^2} \tag{1.2}$$

- The **Mach number** of the jet beam. In hydrodynamics we have only the thermal Mach number, whereas in magnetohydrodynamics we have in addition the Alfven, fast-, and slow Magnetosonic Mach numbers.

With the addition of chemistry and cooling, there are two other parameters which are also of interest

- The **ionisation**, X_e of the gas, a factor in determining the strength of atomic cooling lines.
- The **molecular fraction**, X_{H2}, which determines directly the amount of molecular cooling, and changes in which will add dissociation or formation source terms.
- The **cooling parameter**, χ, which is a measure of the ratio of the cooling length to the jet radius. This parameter seems to have lost favour in the community since the early days possibly because, with the introduction of non-equilibrium chemistry and cooling, this quantity varies significantly based on the chemistry, density and shock velocity.

In simulations these are generally imposed or controlled by means of the initial conditions. These can be likened to components of a sort of input/output system, where the input represent the supposed conditions of the outflow upon reaching the large, observationally resolvable domain after emerging from the obscured and so far unresolved central launching and collimation region of the protostar.

1.4.4 Jet Simulations

Possibly the first attempt to realistically simulate a jet was that of Norman *et al.* (1982), where in order to investigate the propagation of radio jets the authors employed a grid of 60x240 zones, beginning a field of study which continues to this day (Carvalho *et al.*, 2005; Gaibler *et al.*, 2009). In a way, extragalactic jets were more suitable subjects for investigation in the early days, being light, adiabatic, and not having so many observables such as line emission to worry about.

The simulation of *protostellar* jets also has a long, if not quite so long, history of its own, and presents its own unique challenges. Protostellar jets have densities much larger than those of the extragalactic sources, with a host of strong cooling processes and physical phenomena that go beyond the ideal physics to which hydrodynamics is best suited. The velocities and temperatures are high enough to stimulate many chemical reactions, yet not so high that the gas is fully ionised. Several epochs and generations of star formation and supernovae have created an enriched interstellar medium filled with elements such as carbon, silicon and oxygen, and dust grains are consequently ubiquitous in molecular clouds. Magnetic fields are present, but the low levels of ionisation may make some of assumptions made in magnetohydrodynamics questionable and for some questions multi-fluid methods may need to be employed.

Nevertheless with the increasing amount of observational data and the availability of the computational resources to do so, the use of simulations to investigate protostellar jets began in earnest in the early 90s and research in this area has been progressing steadily since. Blondin *et al.* (1990) carried out early simulations of cooling jets and catalogued a series of important qualitative observations contrasting the radiative jets from their adiabatic counterparts (see fig 1.15), which were summarized as follows:

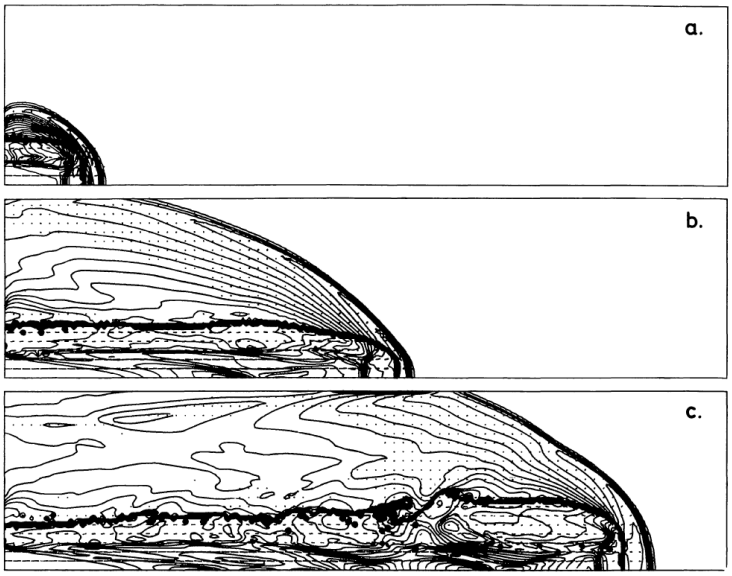

Figure 1.14: A piece of history, the first jet simulation. Adiabatic simulation of an underdense extragalactic jet ($\eta = 0.1$) from Norman *et al.* (1982), where features such as the bow-shock, Mach disk, backflow, contact discontinuity and internal shocks in the beam were identified.

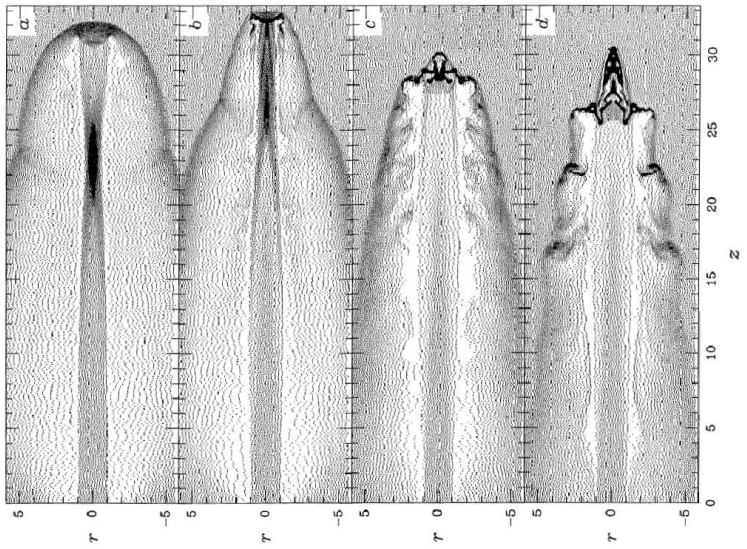

Figure 1.15: Effect of variation of cooling parameter on jet in the work of Blondin *et al.* (1990). The cooling parameter was varied from ∞ (left, the adiabatic case) thru' 2.2, 0.55, and 0.22.

- The formation of a dense shell of material at the head of the jet, behind the leading bow shock.
- A reduced pressure in the shocked matter behind the overall bow shock, leading to a more compact structure.
- The action of a dynamic instability in the dense shell at the head of the jet, triggered by variations in the cooling in different parts of the shock. These instabilities develop over time, causing the structure to break up into smaller clumps, which may later coalesce. This feature is however strongly enhanced by the axisymmetric geometry.

Building on this work, several authors proceeded to experiment with jet inflow conditions in an effort to reproduce the observed jet morphologies, adding conditions such as variations of the inflow velocity to stimulate the production of working surfaces in the jet, varying the direction of the inflow to represent precession (Biro & Raga, 1994; Biro *et al.*, 1995). It was also soon realized that magnetic field effects could play a significant role in the dynamics of the jet propagation, particularly the collimation and stability properties (Cerqueira *et al.*, 1997; Frank *et al.*, 1998).

Some authors recognized the need for non-equilibrium chemistry and cooling effects and gradually began increasing the range of physical processes included using ever more detailed cooling models and chemistry. Stone & Norman (1993) included hydrogen ionisation in an effort to reproduce the radiative knots along jet beams. Beginning with the atomic processes being modelled in lighter atomic jets and gradually increasing in density, the foundation was being laid for the step to simulations of non-equilibrium simulation of **molecular** jets.

Probably the first serious attempt at modelling molecular chemistry and cooling in jets was in Suttner *et al.* (1997), where a chemical network modelling the basic dissociation and formation (by dust) of H_2 was implemented in simulations in 1, 2 and 3 dimensions. This work also made clear some limitations of the 2-dimensional models when compared with the 3d models, such as the appearance of overdense clumps of gas close to the axis of the jet. Subsequent work has built on these results with focussed investigations into diverse questions, such as the effect of the jet "nozzle" (Völker *et al.*, 1999), outflow kinematics (e.g. Smith *et al.* (1997); Keegan (2005)) and jet rotation (Smith & Rosen, 2007).

Some of the parameters introduced in section 1.4.3 have a well understood effect on classical adiabatic flows, but to date, the effects of variations of the chemical parameters on the structure of the flow, and vice versa, need further investigation. As we will see later, even a modest change in some of these quantities can effect changes in the overall flow properties equivalent to that of the dynamical properties above.

Due to our single-fluid model, it is impossible to reproduce C-shocks in our simulations. We must therefore make the most of the information we can obtain from the J-shock physics in our results and use this in what ways we can, to contribute to the issue of molecular emission from C-shocks and J-shocks. Our question is about how and whether the emission in molecular outflows can be accounted for by J-shock excited molecular hydrogen. Although for a single, static shock it has been debatable whether J-type shocks could excite the H_2 without dissociating it, it is evident that

the highly time-dependent nature of protostellar outflows may lead to more complicated situations than just the propagation of a single shock. In particular, the presence of internal working surfaces raises the possibility of more complicated situations, such as successive re-shocking of already "lightly" shocked material behind the bow-wings.

1.5 Aims and Outline of the Thesis

Newly forming stars, despite their ubiquity, are still rather difficult to observe and study. They are usually deeply embedded inside thick molecular clouds laced heavily with dust, which blocks most radiation from our observations. Class 0 source outflows, although also embedded within these clouds, propagate far enough from the accreting envelope that their infrared emissions can escape, giving us a vital glimpse at the earliest stages of star formation. With recently available observations from infrared telescopes we now have an important tool with which to study these young stars and constrain models of their formation. Our aim is to use our models in conjunction with these observations to make judgements about what may and may not be occurring behind those clouds.

In this thesis, we present our work on the numerical simulation of protostellar jets interacting with the molecular ambient medium, and discuss the implications of our findings in the context of the ongoing debate on the origin of the infrared molecular emissions. We review the effects of chemistry and cooling in general on the morphology and propagation of jets, as well as probing in more detail the observable features of our results through the use of synthetic emission maps. We investigate in detail the effect of magnetic fields on the observable structure of outflows.

In chapter 2, a detailed description of the physical model and parameters used in modelling the jets is given, together with an explanation of the numerical methods used to carry out the simulations. Due to the necessity of making simplifications in any model and the limitations of computational resources, these are discussed and justified also in this chapter.

Chapter 3 details the test problems used in developing the model of the system and validating the operation of the code in implementing the model. Tests are chosen in such a way as to isolate as much as possible the different aspects of the code operation, so that we can, for example, examine the time integration independently of the spatial resolution and vice versa. The practical aspects of running the large scale simulations are also dealt with.

In Chapter 4 we present the results of our simulations, with analysis of the simulation data and discussion of the conclusions that can be made from this data. We show our findings on the role of magnetic fields and other parameters in shaping the jets we see. Finally in Chapter 5 we summarise our investigation in the wider context of jet research. We discuss the implications of our results and outline the further directions that may be taken in future.

2 Methods

In this chapter we describe the model used to carry out the tests and simulations presented later. The physical model is described first, with each of the various themes of gas dynamics, chemistry, and cooling described separately. This is followed by the description of the corresponding numerical aspects of the implementation of each theme of the physical model. Finally the jet model and means of visualisation are described.
It should be noted that over the course of this PhD work, the methods used have evolved, both in terms of the physical model itself (the chemical species, reactions and cooling terms considered), and the numerical implementation of the model (i.e. different integration schemes). For clarity we present the model in its latest and most complete form, any differences to particular variants of the code used in subsequent results will be noted.

2.1 Hydrodynamics/Magnetohydrodynamics

Our model is based on a hydrodynamic or magnetohydrodynamic (MHD) fluid model, where the plasma conditions of the jet material and its surrounding medium are treated as an ideal compressible gas or fully ionised plasma. The use of ideal MHD requires in principle an infinite conductivity, in order to neglect a parabolic diffusion term in the induction equation. In practice, however, what is required in order for our calculations to be valid is that the time scale for this diffusion of the magnetic field be sufficiently larger than the dynamical timescale of the system we consider. This condition does not require total ionisation of the gas, and in fact very low levels of ionisation can be sufficient, depending on the dynamical timescale considered. In order to estimate this diffusion time we use the formula from Spitzer (1978):

$$t_D = 5.0 \times 10^{13} \frac{n_e}{n_H} \text{years} \tag{2.1}$$

Within our jet, the ionisation varies between around 10^{-3} and 10^{-1} which is rather high, and more than enough to apply the MHD approximation. In the case of the ambient medium of the molecular core into which the jet is propagating, it may not be quite so straightforward. The ionisation in these cores may fall to quite low values, as the high densities shield the inner layers from ionising cosmic rays, and ionising radiation from the forming protostar has yet not reached a significant level. Recent observations of chemically mature cores have been deduced by Miettinen *et al.* (2009) to have ionisations in the region of 10^{-7} which, using equation 2.1 implies a diffusion time of $5{\times}10^6$ years, significantly longer than our propagation times of a few hundreds of years. Other authors have noted, however, that for larger parsec scale jets, ambipolar diffusion effects may become significant (Frank *et al.*, 1999). We must also accept that as the conditions in each cloud may vary, there does exist the possibility that the approximations for MHD are not always fully valid, and that a multi-fluid approach may be necessary to model the C-shocks (see section 1.4.1) that would occur in such settings. However, we approach the problem from the assumption that the physics of MHD is in operation, and we interpret our results from this perspective.

The systems of conservation equations can be expressed in differential form as

$$\frac{\partial \mathbf{U}}{\partial t} = -\nabla \cdot \mathbf{T}(\mathbf{U}) + \mathbf{S}(\mathbf{U}) \tag{2.2}$$

where $\mathbf{U}$ denotes the state vector of conserved quantities and $\mathbf{T}(\mathbf{U})$ is a tensor containing the fluxes of the state variables. $\mathbf{S}(\mathbf{U})$ comprises the source terms, for example viscous, diffusive, geometrical (in the case of non-cartesian geometries) and thermal losses, which are zero in the ideal adiabatic case. For the hydrodynamic (HD) case, the conserved variables and their fluxes are represented by

$$\mathbf{U} = \begin{pmatrix} \rho \\ \rho\mathbf{v} \\ E \end{pmatrix}, \qquad \mathbf{T}(\mathbf{U}) = \begin{pmatrix} \rho\mathbf{v} \\ \rho\mathbf{v} \otimes \mathbf{v} + p\mathbf{I}(E+p)\mathbf{v} \end{pmatrix}, \tag{2.3}$$

with the primitive pressure variable related to the total energy density E via the equation of state

$$E = \frac{p}{\Gamma - 1} + \frac{\rho v^2}{2} \tag{2.4}$$

In the magnetohydrodynamic (MHD) case, the addition of the magnetic field, with its induction equation and contribution to the pressure, brings the system to

$$\mathbf{U} = \begin{pmatrix} \rho \\ \rho\mathbf{v} \\ \mathbf{B} \\ E \end{pmatrix}, \qquad \mathbf{T}(\mathbf{U}) = \begin{pmatrix} \rho\mathbf{v} \\ \rho\mathbf{v} \times \mathbf{v} + p\mathbf{I} - \mathbf{B} \otimes \mathbf{B} \\ \mathbf{v} \otimes \mathbf{B} - \mathbf{B} \otimes \mathbf{v} \\ (E + p + \frac{B^2}{2})\mathbf{v} - (\mathbf{v} \cdot \mathbf{B})\mathbf{B} \end{pmatrix}, \tag{2.5}$$

which must be solved with the additional constraint on the divergence of the magnetic field,

$$\nabla \cdot \mathbf{B} = 0 \tag{2.6}$$

The equation of state gains an extra pressure term from the magnetic field to take

the form

$$E = \frac{p}{\Gamma - 1} + \frac{\rho v^2 + B^2}{2} \tag{2.7}$$

In addition the evolution of the vector of chemical abundances $\mathbf{X}$ is solved via

$$\frac{\partial(\rho \mathbf{X}_i)}{\partial t} + \nabla \cdot (\rho \mathbf{X}_i \mathbf{v}) = \rho \mathbf{S}_i \tag{2.8}$$

where $\mathbf{S}_i$ represents the net creation or destruction of a given species through chemical reactions. The engine of our code is the finite volume magnetohydrodynamical code PLUTO, which solves these systems of equations on static or adaptive grids (using the Chombo Adaptive Mesh Library). A variety of finite volume Godunov-type solvers, such as Roe, HLL and HLLC can be used to solve the HD/MHD equations in cartesian, cylindrical and spherical coordinates. A complete description is given in Mignone *et al.* (2007).

2.2 Chemistry & Cooling

In addition to the hydrodynamic solver used to simulate the jet gas, we have implemented a chemical network to simulate the gas chemistry and calculate the amount of cooling from optically thin atomic and molecular line emission processes. This adds to the options for cooling already available in PLUTO, which already has both a simplified single level atomic cooling module and a detailed multi-ion non-equilibrium atomic cooling module, as well as interfaces for the application of tabulated cooling losses. The atomic modules are described and compared in Rossi *et al.* (1997) and Tesileanu *et al.* (2008).

These cooling losses comprise the source term $\mathbf{S}(\mathbf{U})$ in equation 2.2. As no viscous, diffusive or other dissipative processes are included in our model, this is a scalar term affecting only the energy equation and has the form

$$\mathbf{S}(\mathbf{U}) = \begin{pmatrix} 0 \\ 0 \\ \mathbf{\Lambda}(\rho, \mathbf{X}, T) \end{pmatrix}, \tag{2.9}$$

where the source term $\mathbf{\Lambda}$ is dependent on the parameters and chemical abundances X of the gas as described in section 2.2.4 below. The action of this source term on the pressure couples the chemistry tightly to the gas physics.

2.2.1 Chemical Species & Reactions

Our approach has been to start with the dominant gas-phase reactions for the destruction and formation of molecular hydrogen presented in Abel *et al.* (1997) and modify as appropriate for the highly molecular conditions of the molecular core, with the aid of the stationary J-shock test problem outlined in section 3.1.

The following species are treated in the model, to varying extents of detail: HI, HII, H2, C, O, OH, CO, H2O, He, and dust. The abundances (by mass fraction) of the hydrogenic species are calculated in a non-equilibrium time-dependendent manner, according to the algorithm described in section 2.2.2. Helium is assumed to be completely inert as regards the chemistry and is considered only in terms of its mass

Table 2.1: Summary of the chemistry reaction set Time dependent hydrogen reactions are first, followed by the rates for the equilibrium reactions (1a-6a). T is the temperature in Kelvin, T_{eV} is the temperature in electron-volts, $T_{300} = T/300$, $T_5 = T/1 \times 10^5$ and $T_2 = T/100$

#	Reaction	Rate Coefficient (cm^3s^{-1})	Source[a]
1.	$HI + e^- \rightarrow HII + 2e^-$	$k_1 = 5.85 \times 10^{-11} T^{0.5} \exp(-157,809.1/T)/(1.0+T_5^{1/2})$	1
2.	$HII + e^- \rightarrow HI + h\nu$	$k_2 = \exp(-28.61303380689232$	2
		$-0.7241125657826851 \ln(T_{eV})$	
		$-2.026044731984691 \times 10^{-2} \ln(T_{eV})^2$	
		$-2.380861877349834 \times 10^{-3} \ln(T_{eV})^3$	
		$-3.212605213188796 \times 10^{-4} \ln(T_{eV})^4$	
		$-1.421502914054107 \times 10^{-5} \ln(T_{eV})^5$	
		$+4.989108920299513 \times 10^{-6} \ln(T_{eV})^6$	
		$+5.755614137575758 \times 10^{-7} \ln(T_{eV})^7$	
		$-1.856767039775261 \times 10^{-8} \ln(T_{eV})^8$	
		$-3.071135243196595e \times 10^{-9} \ln(T_{eV})^9)$	
3.	$H_2 + e^- \rightarrow 2H + e$	$k_3 = 4.4 \times 10^{-10} T^{0.35} \exp(-102,000.0/T)$	3
4.	$H_2 + HI \rightarrow 3HI$	$k_4 = 1.0670825e \times 10^{-10} T_{eV}^{2.012} \times$	2
		$(\exp(4.463/T_{eV})^{-1}((1 + 0.2472T_{eV})^{3.512})^{-1}$	
5.	$H_2 + H_2 \rightarrow H_2 + 2HI$	$k_5 = 1.0 \times 10^{-8} \exp(-84,100/T)$	4
6.	$HI + HI \xrightarrow{dust} H_2$	$k_6 = 3.0 \times 10^{-17} \sqrt{T_2}(1.0 + 0.4\sqrt{T_2 + 0.15} + 0.2T_2 + 0.8T_2^2)$	5
1a.	$OI + H_2 \rightarrow OH + HI$	$2.32 \times 10^{-12} T_{300}^{1.93} \exp(-3940/T)$	6
2a.	$OH + HI \rightarrow OI + H_2$	$6.60 \times 10^{-13} T_{300}^{1.53} \exp(-2970/T)$	6
3a.	$OH + CI \rightarrow CO + HI$	$1.11 \times 10^{-10} T_{300}^{0.5}$	6
4a.	$CO + HI \rightarrow OH + CI$	$1.11 \times 10^{-10} T_{300}^{0.5} \exp(-77700/T)$	6
5a.	$OH + H_2 \rightarrow H_2O + HI$	$8.80 \times 10^{-13} T_{300}^{1.95} \exp(-1429/T)$	6
6a.	$H_2O + HI \rightarrow OH + H_2$	$7.44 \times 10^{-12} T_{300}^{1.57} \exp(-9140/T)$	6

[a]REFERENCES. – (1) Cen (1992); (2) Abel *et al.* (1997); (3) Galli & Palla (1998); (4) Woodall *et al.* (2007); (5) Hollenbach & McKee (1979); (6) Smith & Rosen (2003)

effect, i.e. its effect on the mean molecular weight and thus the equation of state. A classic parameterised treatment of dust from Hollenbach & McKee (1989) is chosen in order to model the effect of surface reformation of H_2 on the overall chemistry. The remaining molecular and atomic species consisting of carbon and oxygen are treated according to the method described in Smith & Rosen (2003) using an equilibrium approximation; they are assumed to be at all times in equilibrium with the molecular component of the hydrogen gas, as the reactions governing these species are known to be faster than the hydrogenic reactions (***ibid***).

Table 2.1 shows a summary of the reactions and their rates. These reactions are included to represent the core chemistry of H_2 and the aim is to account for the evolution of two main chemical quantities; the **ionisation fraction**, and the **molecular fraction**, which between them essentially determine the total amount of cooling from molecular and atomic processes. To accomplish this, the reactions chosen are basically those which determine the rates of the two corresponding processes, the ionisation/recombination of HI (determined by reactions 1 & 2), and dissociation/formation of H_2 (reactions 3-6). The main difference from some primordial chemistry models is the addition of the H_2-H_2 dissociation reaction which, due to the high molecular fraction in the ambient medium, is a very important cooling and dissociation mechanism immediately behind the shock front.

Dust is also an important factor in H_2 chemistry at the temperatures and densities

considered, and although we see the effect of its opacity quite clearly whenever optical observations of areas of high column densities of gas are made, reliable information on the size and composition of dust particles is difficult to obtain. Therefore, for many purposes, relatively antiquated parameterised treatments for estimating the amount of dust-catalyzed H_2 formation such as that of Hollenbach & McKee (1989) are still commonly used in simulations. This treatment does not deal with issues such as grain survival in shocks, so for shocks having the speeds of greater than 60km s^{-1} or so required to destroy grains, large inaccuracies in the H_2 formation rate are inevitable. However on the timescales of the simulations we carry out, it is the degree of dissociation of molecular hydrogen in hot gas, and not so much its formation in cool gas, which is of most importance for our comparisons - in parts of the flow cool enough and dense enough to allow the re-formation of H_2, the temperatures are not high enough to excite the ro-vibrational lines of interest to us.

2.2.2 Time Integration

We use the reactions in Table 2.1 to formulate a set of rate equations for the evolution of the species HI, HII and H_2 in time. The rate equations for a chemistry network have the general form

$$\frac{\mathrm{d}n_i}{\mathrm{d}t} = C_i(T, n_j) - D_i(T, n_j)n_i \tag{2.10}$$

where the coefficients C_i and D_i, for the creation and destruction of the species respectively, are obtained by examining, for each species, all of the reactions and seeing where the species appears on the right hand side (created) or the left hand side (destroyed) or both. These coefficients have the form

$$C_i(T, n_j) = \sum_{j,k} k_{j,k} n_j n_k \tag{2.11}$$

$$D_i(T, n_j) = \sum_{j} k_{i,j} n_j \tag{2.12}$$

We evolve the the system in terms of the **mass fraction, $\mathbf{X}$**[1] , which will be used to represent chemical abundances in this work, where for example a fully molecular gas would have $\mathbf{X}_{\mathrm{H}_2} = 1$, and not 0.5 as per some other measures of abundance. This is to better deal with practical considerations when allowing the relative amounts of species with different molecular weights to change (In contrast to the atomic case, where the fractions of ions of a given species do change, but the relative abundances of given atomic species are held fixed, e.g. at solar abundances). The mass fraction is related to the number density by

$$n_i = \frac{\mathbf{X}_i \rho A_H}{M_i m_H} = \frac{n \mathbf{X}_i}{M_i} \tag{2.13}$$

where m_H denotes the proton mass, A_H is the abundance of hydrogen, M_i the mass of species i in atomic mass units and n denotes the number of hydrogen nuclei. In order

[1]Note - During the course of this text, the terms X_e and X_{HII} will be used interchangeably. The electron mass is in no way accounted for:- the term X_e is taken to mean "the number of electrons corresponding to the HII ions having mass fraction X_{HII}"

to evolve the system in equations 2.10 and 2.12 in terms of mass fractions, one can substitute for n_i in equations 2.10 and 2.12 using eq. 2.13, to get the new equations

$$\frac{n}{M_i}\frac{\mathrm{d}\mathbf{X}_i}{\mathrm{d}t} = C_i^*(T, \mathbf{X}_j) - D_i^*(T, \mathbf{X}_j)\frac{n}{M_i}\mathbf{X}_i \tag{2.14}$$

and

$$C_i^*(T, \mathbf{X}_j) = \sum_{j,k} k_{j,k} n^2 \frac{\mathbf{X}_j}{M_j}\frac{\mathbf{X}_k}{M_k} \tag{2.15}$$

$$D_i^*(T, \mathbf{X}_j) = \sum_{j} k_{i,j} \frac{n}{M_j}\mathbf{X}_j \tag{2.16}$$

and making cancellations where possible. These equations must be solved in conjunction with the pressure equation in order to properly follow the chemistry and temperature of the gas. The pressure equation is updated with a loss calculated from the cooling terms described in section 2.2.4

$$\frac{\mathrm{d}p}{\mathrm{d}t} = -(\gamma - 1)\mathbf{\Lambda}(\rho, \mathbf{X}, T) \tag{2.17}$$

2.2.3 Numerical Method

The PLUTO code evolves the source step and the homogeneous part of equation 2.8 separately using operator splitting, while maintaining second-order accuracy (Tesileanu *et al.*, 2008). Therefore in our cooling module we are concerned directly with only the time evolution of equations 2.14 and 2.17.

The modelling of non-ideal effects in time-dependent, multi-dimensional problems poses formidable numerical challenges, both in terms of accuracy and performance. As the microphysics of gas reactions and cooling losses are not accounted for in the formalism of fluid dynamics, depending on the gas conditions and reaction rates, the timescales involved will often not be resolved by the CFL timestep used to resolve the fluid motion.

The main requirement for us is that the code reproduce the chemical evolution, while still being reasonably economical for use in large-scale simulations. For this purpose we employ a semi-implicit first-order BDF (Backward Differentiation Formula) Euler method, as described in Anninos *et al.* (1997), to integrate the chemistry and cooling in step. This method allows stability to be maintained while taking a larger timestep than possible with explicit solvers, albeit at first order accuracy, in "stiff" zones in the flow where the rates of change in the chemical variables and/or cooling are much faster than those on the fluid scale. The chemistry and cooling are evolved on a substep of the fluid timestep, chosen to limit the maximum fractional change in species abundances or pressure to 10% in a given step. The chemical species are evolved in turn according to

$$\frac{n}{M_i}\mathbf{X}_i^{t+\Delta t} = \frac{C_i^{*t+\Delta t}\Delta t + \frac{n}{M_i}\mathbf{X}_i^t}{1 + D_i^{*t+\Delta t}\Delta t} \tag{2.18}$$

where the pseudo-implicit values for the coefficients $\mathrm{C}_i^{*t+\Delta t}$ and $\mathrm{D}_i^{*t+\Delta t}$ are calculated from the relevant species abundances and the value of the related reaction rate at the

current temperature. The new species abundances are used as they become available, otherwise the ones from the current timestep are used. These functions of temperature are usually provided as fits for experimental data or theoretical calculations, and as can be seen in Table 2.1, they are mostly expressed as exponential functions, which are in practice computed using costly expansions. Therefore, for computational efficiency, the tables are instead calculated (in increments of 50 Kelvin) at the beginning of the program, and table lookups are performed to interpolate the rate's value at a given temperature.
The pressure equation eq. 2.17 is similarly discretised as

$$p^{t+\Delta t} = p^t - \Delta t(\gamma - 1)\mathbf{\Lambda}^{t+\Delta t}(\rho, \mathbf{X}^{t+\Delta t}, T) \tag{2.19}$$

and evolved in the same substep using the newly computed species fractions.
Based on the total fractional variation of the species and pressure over the course of the fluid timestep, a cooling timestep is also calculated to limit the fractional change to 10%, which is later checked against the advection timestep and will limit the global timestep accordingly.

2.2.4 Cooling Terms

The cooling losses due to the molecular and atomic processes are calculated from the species concentrations and the density and temperature using various cooling functions from the literature. Although the main interest of this work is the effect of molecular cooling, we must also include some treatment of the atomic cooling losses, as our gas reaches temperatures of up to 10^5 K in shocks of over 100 km s^{-1}.

2.2.4.1 Atomic Cooling

We have included the cooling contributions for several atomic processes, described below, which dominate the cooling in regions of high temperature and significant ionisation. Figure 2.1 shows a comparison of the different cooling terms as a function of temperature for a chosen density and chemical composition in a "slab" of gas. Although not intended to give a real indication of cooling in a gas (as the chemical composition is held constant independently of the temperature), this technique does allow a clear comparison of the relative magnitudes of the different cooling terms for given conditions. The Lyman-α term is the principle atomic coolant above 10^4K, especially when there's a significant level of ionisation. The following expressions are used to compute the losses[2]:

Collisional excitation cooling from the excitation (mainly of the Lyman-α line) of atomic hydrogen by electrons, (**?**)

$$\mathbf{\Lambda}_{ceH} = n_e n_H 7.5 \times 10^{-19} \exp(-118348/\mathrm{T})(1 + \sqrt{\mathrm{T}_5}) \tag{2.20}$$

Collisional ionisation cooling

$$\mathbf{\Lambda}_{ciH} = n_e n_H 1.27 \times 10^{-21} \sqrt{\mathrm{T}} \exp -157809.1/\mathrm{T} \tag{2.21}$$

[2] T in Kelvin, T_3=T/10^3K, T_5=T/10^5K, T_6=T/10^6K, all terms yield loss in erg cm^{-3}s^{-1}

Radiative Recombination cooling

$$\mathbf{\Lambda}_{reHII} = n_e n_{HII} 8.70 \times 10^{-27} \sqrt{\mathrm{T}} \mathrm{T}_3^{-0.2} (1 + \mathrm{T}_6^{0.7}) \tag{2.22}$$

OI fine structure line at 63μm as given in Smith & Rosen (2003), where the spontaneous transition from the LTE population of the $^3\mathrm{P}_1$ level is calculated using

$$\mathbf{\Lambda}_{OI} = n_O \frac{2.82 \times 10^{-18}}{1/f_H + A_{10}/r_L} \tag{2.23}$$

where

$$\begin{aligned} A_{10} &= 8.95 \times 10^{-5} \\ f_H &= \frac{0.6 \exp(-228/\mathrm{T})}{1 + 0.6 \exp(-228/\mathrm{T}) + 0.2 \exp(-326/\mathrm{T})} \\ r_L &= r_H + r_{H_2} \\ r_H &= [4.37 \times 10^{-12} \mathrm{T}_{0.66} 0.6 \exp(-228/\mathrm{T}) \\ &\quad + 1.06 \times 10^{-12} \mathrm{T}^{0.8} 0.2 \exp(-326/\mathrm{T})](n_H + 0.48 n_H) \end{aligned}$$

Gas-grain cooling caused by the transfer of energy via collisions from the gas to the dust, which at around 15K is much cooler is treated again using the parameterised expressions from Hollenbach & McKee (1989). Again, some inaccuracy is introduced as this term does not allow for grain destruction in fast shocks, and this can be seen in figure 2.1, where higher losses are attributed to dust cooling at improbable temperatures.

$$\mathbf{\Lambda}_{grain} = 3.8 \times 10^{-33} \sqrt{\mathrm{T}} (\mathrm{T} - \mathrm{T}_{dust}) [1 - 0.8 \exp(-75/\mathrm{T})] n^2 \tag{2.24}$$

where n is the total number of nuclei.

2.2.4.2 Molecular Cooling

For the losses from molecular hydrogen we include terms for cooling from collisional excitation of ro-vibrational modes of H_2 by HI and H_2, as well as cooling and heating from dissociation and formation, respectively, of H_2. The commonly used assumption for an ortho:para ratio of 3:1 for H_2 has been used where required.

H_2 ro-vibrational excitation cooling This type of cooling is typically calculated from a weighted average depending on the gas density, which bridges the effective cooling between the values for the simplified limits of very low densities, where the H_2 is all in the ground vibrational state, and the high density regime, where the H_2 is fully collisional and in LTE. We use the expression from Hollenbach & McKee (1979) for the high density limit

$$\mathbf{\Lambda}_{H_2}^{LTE} = \mathbf{\Lambda}_{H_2 vib}^{LTE} + \mathbf{\Lambda}_{H_2 rot}^{LTE} \tag{2.25}$$

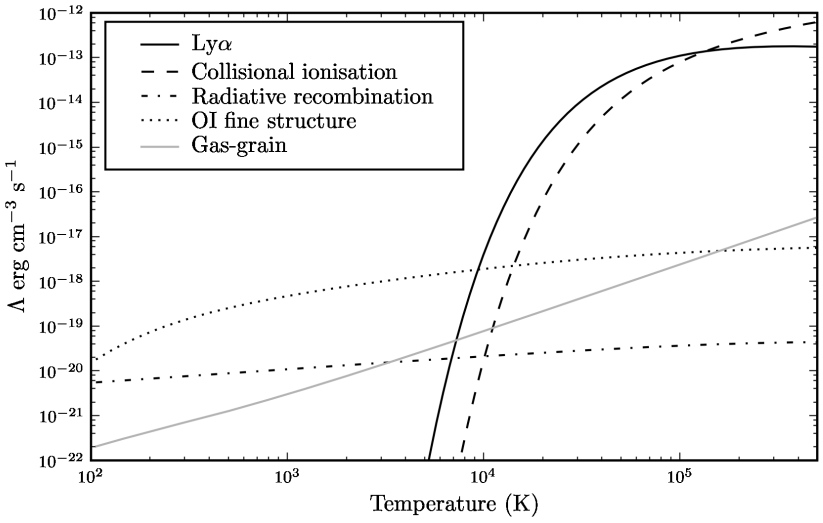

Figure 2.1: Cooling emissivities for atomic processes for a slab of partially molecular gas: X_{HI}=0.48,X_{HII}=0.02 and X_{H_2}=0.50, with $n_{H_{tot}}$ (the number of hydrogen *nuclei*) equal to $10^4 cm^{-3}$.

with

$$\mathbf{\Lambda}^{LTE}_{H_2 vib} = 6.7 \times 10^{-19} \exp(-5.86/T_3) \tag{2.26}$$

$$+ 1.6 \times 10^{-18} \exp(-11.7/T_3) \tag{2.27}$$

$$\mathbf{\Lambda}^{LTE}_{H_2 rot} = \left(\frac{9.5 \times 10^{-22} T_3^{3.76}}{1.0 + 0.12 T_3^{2.1}} \right) \exp\left[(-0.13/T_3)^3 \right]$$

$$+ 3.0 \times 10^{-24} \exp(-0.51/T_3) \tag{2.28}$$

For the low density limit for collisions with HI & H_2 we use the expressions from Glover (2008), which gives a comprehensive review of H_2 chemistry and cooling.

$$\mathbf{\Lambda}_{H_2}(n \to 0) = n_H \mathbf{\Lambda}^{HI}_{H_2}(n \to 0) + n_{H2} \mathbf{\Lambda}^{H_2}_{H_2}(n \to 0) \tag{2.29}$$

where

$$\mathbf{\Lambda}^{HI}_{H_2}(n \to 0) = \begin{cases} \text{dex}^3[-24.311209 \\ \quad +3.5692468\log(\mathrm{T}_3) \\ \quad -11.332860\log(\mathrm{T}_3)^2 \\ \quad -27.850082\log(\mathrm{T}_3)^3 \\ \quad -21.328264\log(\mathrm{T}_3)^4 \\ \quad -4.2519023\log(\mathrm{T}_3)^5] & \mathrm{T} < 1000K \\ \\ \text{dex}[-24.311209 \\ \quad +4.6450521\log(\mathrm{T}_3) \\ \quad -3.7209846\log(\mathrm{T}_3)^2 \\ \quad +5.9369081\log(\mathrm{T}_3)^3 \\ \quad -5.5108047\log(\mathrm{T}_3)^4 \\ \quad +1.5538288\log(\mathrm{T}_3)^5] & \mathrm{T} > 1000K \end{cases} \tag{2.30}$$

(2.31)

$$\mathbf{\Lambda}^{H_2}_{H_2}(n \to 0) = \begin{cases} \text{dex}[-23.962112 \\ \quad +2.09433740\log(\mathrm{T}_3) \\ \quad -0.77151436\log(\mathrm{T}_3)^2 \\ \quad +0.43693353\log(\mathrm{T}_3)^3 \\ \quad -0.14913216\log(\mathrm{T}_3)^4 \\ \quad -0.033638326\log(\mathrm{T}_3)^5] \end{cases} \tag{2.32}$$

(2.33)

Finally the total cooling from H_2 is calculated from

$$\mathbf{\Lambda}_{H_2} = n_{H2}\frac{\mathbf{\Lambda}^{LTE}_{H_2}}{1 + \mathbf{\Lambda}^{LTE}_{H_2}/\mathbf{\Lambda}_{H_2}(n \to 0)} \tag{2.34}$$

H_2 dissociation cooling of H_2 are obtained by simply multiplying its binding energy by the destruction rate (and thereby assuming that the binding energy is radiated away)

$$\mathbf{\Lambda}_{H_2Diss} = 4.48eV\mathbf{D}_{H_2}(\mathbf{X}_{H_2}, \rho, T) \tag{2.35}$$

H_2 formation heating is similarly treated by multiplying the binding energy by the formation rate

$$\mathbf{\Lambda}_{H_2Form} = 4.48eV\mathbf{C}_{H_2}(\mathbf{X}, \rho, T) \tag{2.36}$$

The rest of the terms for cooling from metals are the ones described in Smith & Rosen (2003) and references therein

[3] "dex" = "10 to the power of"

CO rotational and vibrational cooling

$$\mathbf{\Lambda}_{CO} = \mathbf{\Lambda}_{CO_{rot}} + \mathbf{\Lambda}_{CO_{vibH_2}} + \mathbf{\Lambda}_{CO_{vibHI}} \tag{2.37}$$

where the cooling due to collisional excitation of rotational modes by HI & H_2 is (McKee *et al.*, 1982)

$$\mathbf{\Lambda}_{CO_{rot}} = n_{CO} n \frac{k\mathrm{T}\sigma v_T}{1 + n_a/n_{cr} + 1.5(n_a/n_{cr})^{0.5}} \tag{2.38}$$

where

$$\begin{aligned} v_T &= \sqrt{8k\mathrm{T}/\pi m_{H_2}} \\ n_{cr} &= 3.3 \times 10^6 \mathrm{T}_3^{0.75} cm^{-3} \\ \sigma &= 3.0 \times 10^{-16} \mathrm{T}_3^{-0.25} cm^{-2} \\ n_a &= 0.5(n_H + \sqrt{2} n_{H_2}) cm^{-3} \end{aligned}$$

and the vibrational mode cooling, also from collisions with HI & H_2 (Neufeld & Kaufman, 1993)

$$\mathbf{\Lambda}_{CO_{vibH_2}} = 1.83 \times 10^{-26} n_{H_2} n_{CO} \mathrm{T} \exp(-3080/\mathrm{T}) \exp(-68/\mathrm{T}^{1/3}) \tag{2.39}$$

$$\mathbf{\Lambda}_{CO_{vibHI}} = 1.28 \times 10^{-24} n_H n_{CO} \mathrm{T}^{1/2} \exp(-3080/\mathrm{T}) \exp(-(2000/\mathrm{T})^{3.43}) \tag{2.40}$$

H_2O rotational and vibrational cooling

$$\mathbf{\Lambda}_{H_2O} = \mathbf{\Lambda}_{H_2O_{rot}} + \mathbf{\Lambda}_{H_2O_{vibH_2}} + \mathbf{\Lambda}_{H_2O_{vibHI}} \tag{2.41}$$

$$\begin{aligned} \mathbf{\Lambda}_{H_2O_{rot}} &= (n_{H2} + 1.39 n_H) n(H_2O) \lambda_3 \\ \lambda_3 &= 1.32 \times 10^{-23} (\mathrm{T}_3)^{\alpha} \\ \alpha &= 1.35 - 0.3 \log(\mathrm{T}_3) \end{aligned} \tag{2.42}$$

$$\mathbf{\Lambda}_{H_2O_{vibH_2}} = 1.03 \times 10^{-26} n_{H_2} n(H_2O) \mathrm{T} \exp(-2325/\mathrm{T}) \exp(-47.5/\mathrm{T}^{1/3}) \tag{2.43}$$

$$\mathbf{\Lambda}_{H_2O_{vibHI}} = 7.40 \times 10^{-27} n_H \lambda_3 n(H_2O) \mathrm{T} \exp(-2325/\mathrm{T}) \exp(-34.5/\mathrm{T}^{1/3}) \tag{2.44}$$

OH rotational and vibrational cooling

$$\mathbf{\Lambda}_{OH} = 2.84 \times 10^{-28} n_{OH} n \mathrm{T}^{3/2} \tag{2.45}$$

Molecular losses are completely dominant in areas with temperatures under around 10^4K, although in hot zones with a significant molecular fraction, H_2 dissociation cooling can still be very effective, and this is an important effect in our particular scenario of a jet impinging on a fully molecular cloud. Finally to illustrate the amounts of cooling from atomic and molecular terms and the effect of ionisation on their relative

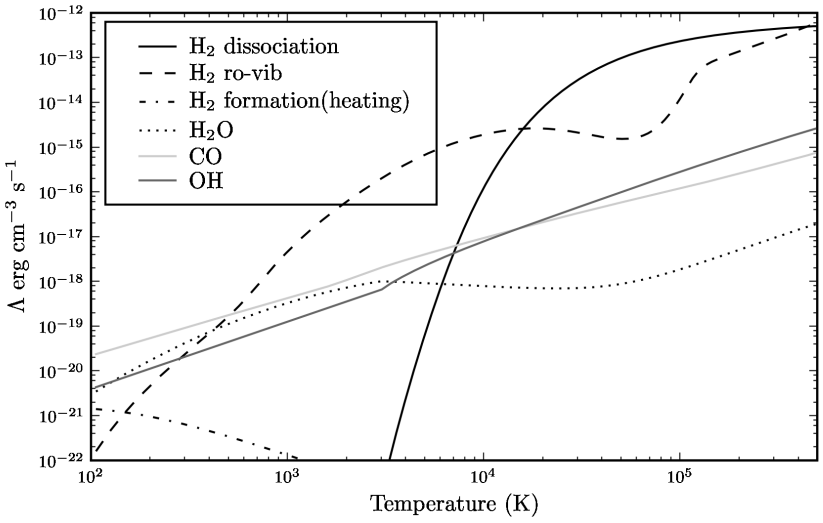

Figure 2.2: Cooling emissivities for molecular processes for a slab of partially molecular gas: X_{HI}=0.48,X_{HII}=0.02 and X_{H_2}=0.50, with $n_{H_{tot}}$ (the number of hydrogen *nuclei*) equal to $10^4 cm^{-3}$.

importance, figure 2.3 shows together the dominant atomic and molecular cooling terms for a gas with 2% ionisation. The effect of increasing the ionisation to 10% is seen in figure 2.4 for example.

2.2.5 Treatment of the Adiabatic Index

In dealing with a gas chemistry network which can have both monatomic and diatomic species, one is immediately presented with the issue of how to treat the adiabatic index, γ, of the gas, which directly influences the equation of state,

$$p = \frac{k_B T}{\mu m_p}\rho = (\gamma - 1)\rho\epsilon \tag{2.46}$$

and thus the behaviour of the gas. In the particular case of Riemann solvers, this manifests itself in the calculation of the characteristic speeds of the gas, affecting the fluxes and intermediate states. In standard hydrodynamical codes the gas is generally assumed to be a monatomic ideal gas, with $\gamma = 5/3$. A diatomic gas, such as H_2, on the other hand, has a value of γ 1.4 at low temperatures, decreasing to below 1.3 at higher temperatures as the vibrational modes of the hydrogen molecule become excited. Calculating the value of γ for a gas containing a mixture of atomic and molecular hydrogen therefore requires a temperature-dependent calculation of the γ-value for H_2 and a weighting of the values for the atomic and molecular components according to their abundance. (One would proceed, for example, using) This can be done according to the method in Yoshida *et al.* (2006), although we note that there is a mistake in equation 15 of aforementioned paper, where a weighting corresponding to each species abundance appears to be missing. First of all one would calculate the temperature-dependent γ value of the molecular hydrogen from

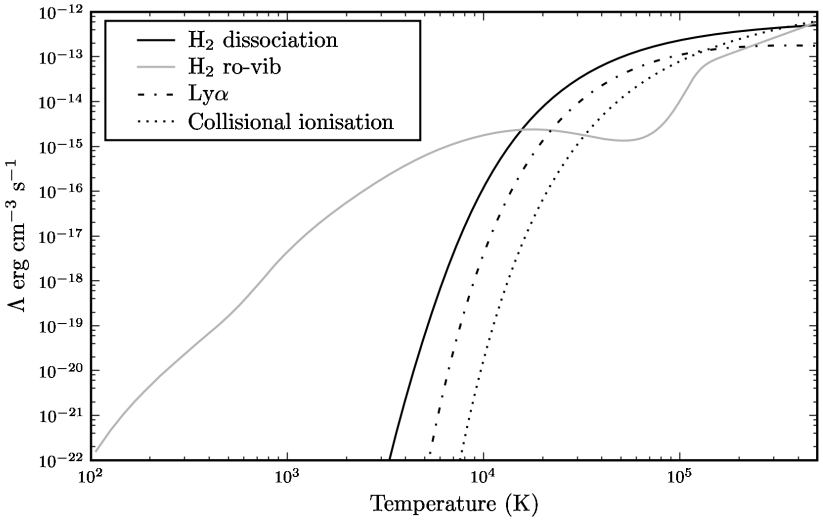

Figure 2.3: Cooling emissivities for molecular processes for a slab of partially molecular gas: X_{HI}=0.48,X_{HII}=0.02 and X_{H_2}=0.50, with $n_{H_{tot}}$ (the number of hydrogen *nuclei*) equal to $10^4 cm^{-3}$.

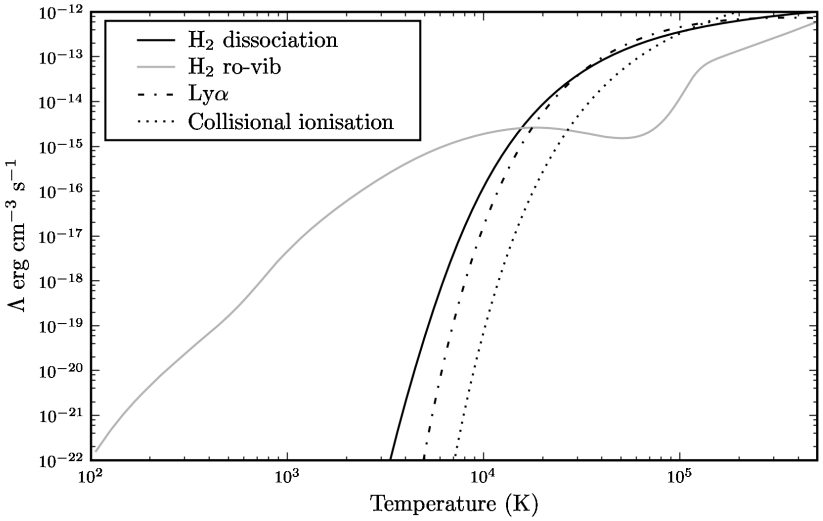

Figure 2.4: Cooling emissivities for molecular processes for a slab of partially molecular gas: X_{HI}=0.40,X_{HII}=0.10 and X_{H_2}=0.50, with $n_{H_{tot}}$ (the number of hydrogen *nuclei*) equal to $10^4 cm^{-3}$.

$$\frac{1}{\gamma_{H_2} - 1} = \frac{1}{2}\left[5 + 2x^2 \frac{e^x}{(e^x - 1)^2}\right] \tag{2.47}$$

whereupon one can then calculate the total γ using

$$\frac{1}{\gamma - 1} = \mu \left[\sum_i \frac{X_i}{A_i} \frac{1}{\gamma_i - 1}\right] \tag{2.48}$$

However, before carrying out such an implementation, one must first consider its cost, effectiveness, and even correctness. Although such a method would indeed yield a more correct γ-value for the gas mixture in conditions where the rotational and vibrational modes have had enough time to reach the level of excitation corresponding to the temperature of the gas, in cases where the gas has just been shocked, the method would produce an incorrect γ-value. This is because the gas that passes through shock gets rapidly heated, but this energy goes predominantly into the translational degrees of freedom of the gas. It is only with time that energy goes into the rotational and vibrational degrees of freedom of the gas through collisions. Flower *et al.* (2003) maintains that therefore the adiabatic index of the post-shock gas has close to the ideal monatomic value of 5/3, and that in order to calculate correctly its evolution as the gas adjusts one would have to model the rotational and vibrational levels of the hydrogen molecules in a time-dependent manner.

Given that this is impractical for large-scale simulations, one must decide between calculating the adiabatic index in a way that it is more correct for equilibrated parts of the domain but incorrect in the immediate post-shock regions, or to use the standard value of 5/3 which is correct for the post-shock and predominantly atomic parts of the flow but incorrect for the equilibrated parts of the flow with a significant fraction of molecular matter. In this case, as the shock regions and their effect on the molecular hydrogen content of the ambient gas are of primary importance here, we opt for the more relevant, and also simpler, policy of keeping the normal γ-value of 5/3 for our simulations. This is somewhat fortunate because, in the case of the PLUTO code, some straightforward, but not-quite-trivial modifications would have to be made in the code for each solver we wish to use in our simulations in order to incorporate the alternative γ-value.

2.3 Simulation Setup

The jet is modelled as a simple sinusoidally time-dependent gas inflow, which enters a quiescent ambient medium in 2-dimensional cylindrical symmetry, as shown in figure 2.6. A reflective/axisymmetric boundary condition is used on the z-axis in the hydro- and magneto-hydrodynamic simulations respectively. These simulations are carried out for a propagation distance of 5000AU which, although not quite up to the scales of many of the observed molecular outflows, still reaches a level which is comparable, especially with respect to the scales of the chemical and cooling lengths. The reason for this propagation distance of 5000AU is partly to do with performance, given that the computational power required increases approximately exponentially for a jet simulation with AMR as described in section 3.5. The approach of using a lower resolution or overall density in an effort to simulate jets to larger distances is

also used in the field, however we choose to model the "real" parameters as closely as possible, albeit at the cost of overall scale.
The jet inflow velocity varies sinusoidally about a mean value of 122km s^{-1} with an amplitude of one quarter, i.e. between 92 and 153 km s^{-1}, with a period of 11 years. The beam density, pressure and velocity are injected with a smoothed top-hat profile in order to avoid an unphysical sharp gradient and any associated numerical difficulties. This profile has the form

$$f(r) = \frac{1.0}{\cosh(\left(\frac{r}{0.1}\right)^3)} \tag{2.49}$$

All runs keep a beam density equivalent to n = 10^4 cm^{-3}, where n is the total number of nuclei (hydrogen and helium). The average mass loss rate then has a value

$$\dot{\mathbf{M}} = \pi r_{\rm jet}^2 \rho < v_{\rm jet} > = 8.79 \times 10^{17}\,{\rm gs}^{-1} = 1.4 \times 10^{-8}\,{\rm M}\odot\,{\rm yr}^{-1}, \tag{2.50}$$

which is in the range 10^{-9}-10^{-5} M$\odot$ yr^{-1} of observed mass loss rates.
In order to implement a particular value of η, the density of the ambient medium is obtained by dividing its density by the appropriate factor. In other words, as η is increased, the absolute density of the ambient medium is decreased. A purely poloidal magnetic field is implemented, existing in the whole domain and injected with the beam matter. Again we choose the value of the field strength in order to yield the desired β-parameter, as computed with respect to the pressure of the beam gas. The constraint on the divergence of the magnetic field (eq. 2.6) is treated using the Powell 8-wave option in PLUTO. This method is not in the same league as more advanced methods, such as the FCT method, but makes the implementation of magnetic fields less complicated, and keeps the divergence of B under control in the majority of the domain, see fig. 2.5.

Table 2.2 lists the parameters which are in common for all subsequent runs, unless otherwise noted.

2.3.1 Hardware

For these runs, which were run in parallel using MPI, we used the HLRB II supercomputer, based on SGI's Altix 4700 platform, installed at the Leibniz Rechenzentrum (LRZ) Muenchen. As described in section 3.5 we used a varying number of proces-

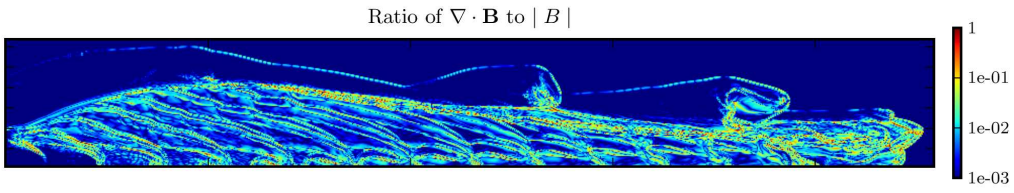

Figure 2.5: Divergence of B in an MHD simulation. In the majority of the domain the divergence of B is less than a percent or two. However, some zones do show an appreciable fraction of the field strength.

Average jet velocity	v_j	122 km s$^-$1
Beam time variation period	t_j	14.3 yr
Beam internal mach number	M_{int}	23
Beam external mach number (w.r.t. ambient)	M_{int}	102
Jet density (number of nuclei)	n_H	1×10^4 cm^{-3}
Jet temperature	T_{jet}	2000 K
Ambient temperature	T_a	100 K
Jet radius	r_{jet}	188 AU
Jet domain (length)	z_{dom}	5000 AU
Poloidal magnetic field (in MHD runs)	$B_\parallel$	30-120 μG

Table 2.2: Parameters common to all runs (except where noted otherwise).

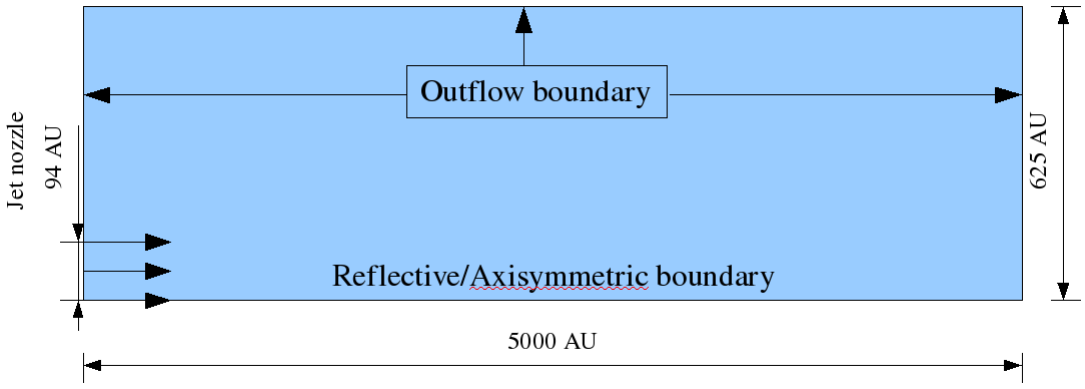

Figure 2.6: Schematic diagram of the jet and domain setup.

sors at different stages of the runs, typically starting them with 32 or 64 processors and continuing at 128 or 256 processors. The typical CPU consumption per run was between 5 and 10 thousand CPU hours.

2.3.2 Observable quantities

The simulations produce a large amount of raw data, composed of the state variables and the time dependent chemical species fractions. On top of this, the equilibrium species fractions and emission data are computed. In order to make some sense of all the information we also calculate some derived quantities. Below we list the quantities that we use to examine and organise the data for visualisation.

Physical and chemical variables ρ, T, **X**, give us direct information on the values of the variables on the spatial domain.

Derived physical quantities β, Mach number, are parameters which help to explain the behaviour of the gas.

Emissivities and integrated emission maps (surface brightness) for molecular and atomic lines: $H_2$1-0S(1) and $H_2$2-1S(1) ro-vibrational lines, CO 1-0 & CO 32-31 rotational transitions, OI 63μm fine structure line. These quantities are necessary in order to be able to compare our model with the actual observational data. We choose the 1-0 and 32-31 lines as they populate differently according to

temperature. The CO 1-0 line is a mainstay of mm-wave observational astronomy as a tracer of cold molecular material. The CO 32-31 line is admittedly a rather obscure transition, but allows us to probe a different temperature regime than the cold molecular component, i.e. the shocked gas. This transition has heretofore been observed spectroscopically, but will soon be spatially resolvable with the Far Infrared Space Telescope (FIRST) (Maret *et al.*, 2001). For several years now we have been getting excellent views inside molecular cores in the the H_2 ro-vibrational lines from the Spitzer space telescope. Unfortunately this great telescope is near the end of its useful life, having recently run out of coolant, but with new and upcoming telescopes such as the Infrared Space Observatory (ISO), the Stratospheric Observatory for Infrared Astronomy (SOFIA), the Next Generation Space Telescope (NGST) and Herschel, observations in these lines will only improve. The H_2 emissions are calculated in statistical equilibrium using a 3-level model for the vibrational levels of the molecule, while the rotational levels in each vibrational level are assumed to be in LTE. For the CO emissions we use the treatment of McKee *et al.* (1982), solving for the first 50 rotational levels of CO. The surface brightnesses are calculated from the emission maps, by integrating along the line of sight according to the axisymmetric geometry of the simulation. For this calculation, the jet is assumed to be in the plane of the sky. The surface brightnesses are slightly smoothed with a gaussian filter, but not convolved with the seeing of a particular telescope. The highest densities reached in our simulations are of the order of $10^6 \mathrm{cm}^{-3}$, and the lines are all assumed to be optically thin.

Profiles, or 1D cuts, of all of the above across and along the jet to enable a better side-by-side comparison of the effect of the input parameters.

Mass-Velocity and Line-Profiles As well as the direct visualisation of the data, it is often useful to check aggregated quantities, such as the Mass-velocity relation, and the Intensity velocity relation. These are essentially histograms, showing how much mass (or emitting mass) is travelling at a given velocity. They are important because they are one of the means by which we can judge that our model is matching observations, or other models, on a fairly fundamental level. The range between maximum and minimum velocities) is divided into several bins. Then, for each cell in the domain, the volume is calculated and the amount of the volumetric quantity is added to the appropriate bin, giving a distribution of mass or intensity against velocity.

3
Testing & Validation

Our aim in this chapter is to show that the model described in the previous chapter, consisting of the combined hydro- & magnetohydrodynamics solver and cooling module, reproduces properly the gas physics of the astrophysical scenario we are interested in, at the resolutions used in our simulations. We do this in a series of incremental steps by carrying out a set of tests on the code, each chosen to isolate a separate aspect of the model or code, each building on the results of the previous one, to arrive at a conclusion on the performance of the code as a whole.

3.1 Chemistry and Cooling Verification - Stationary J-shock Comparison

The first question we ask ourselves, before delving into the issues of numerical implementation, is whether the chemical and cooling model, i.e the chosen set of reactions and cooling rates as distinct from the solution method, accurately reflects the chemistry and cooling of the gas. In other words we wish to first ascertain the accuracy of the *model* in isolation from the accuracy of *algorithm* calculating it, before going on to examine the time evolution and the effect of spatial resolution.
To answer this question and gain information on how to constrain or augment the set of reactions and cooling terms included, we first carried out a comparison of the result from our model with that from a more complex chemical model (see Flower *et al.* (2003); Flower (2007)), using the simple test problem of a stationary J-shock. This is an ideal problem for comparing the choice of chemical and cooling terms, as well as for carrying out parameter studies as, yielding static output, it allows one to examine the evolution calmly and in detail.

3.1.1 Setup

The scenario describes a steady flow of an incoming gas of given properties (density, velocity, temperature etc.), which passes through a shock at a given speed. A

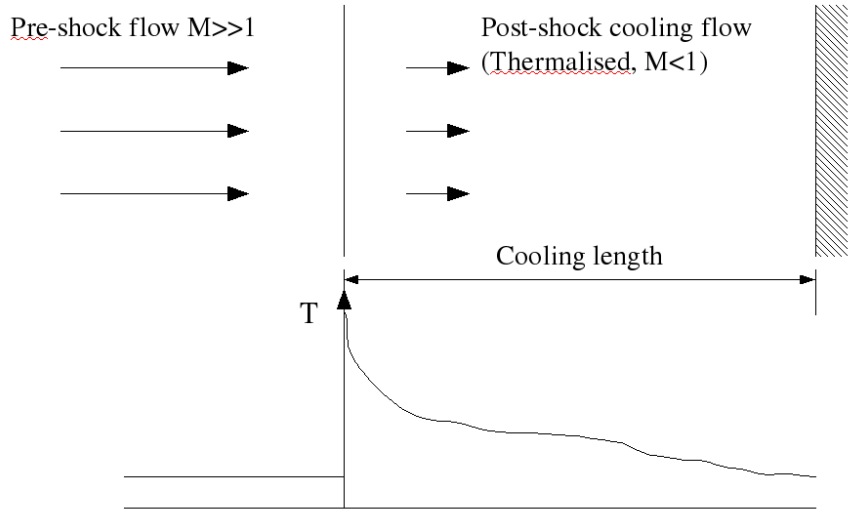

Figure 3.1: Schematic diagram of a stationary shock configuration The incoming gas is shocked, thermalised and cools as it flows steadily away from the shock. In the mathematical treatment of sectionthe wall is not actually necessary.

schematic example of this is shown in figure 3.1. The jump conditions for the hydrodynamic shock are evaluated in order to get the appropriate post-shock parameters, and these parameters are used as initial conditions for the solution of the post-shock flow via the steady fluid equations. The numerical treatment elaborated here is adapted from Massaglia *et al.* (2005), with the only difference being the chemical equations integrated in parallel with the fluid velocity. Starting with the 1D fluid equations and taking the magnetic field to be transverse to the direction of the fluid motion, a steady state condition is enforced by setting the time derivatives to zero, leaving us with the continuity, momentum and induction equations

$$\frac{\mathrm{d}}{\mathrm{d}x}(\rho v) = 0 \tag{3.1}$$

$$\frac{\mathrm{d}}{\mathrm{d}x}\left(\rho v^2 + p + \frac{B_y^2}{2}\right) = 0 \tag{3.2}$$

$$\frac{\mathrm{d}}{\mathrm{d}x}(B_y v) = 0, \tag{3.3}$$

which, when integrated, yield the following Rankine Hugoniot conditions relating quantities before and after the shock

$$\rho v = C_0 \tag{3.4}$$

$$C_0 v + p + \frac{B_y^2}{2} = C_1 \tag{3.5}$$

$$v B_y = C_2 \tag{3.6}$$

These relations allow us to always express the density, magnetic field and pressure in terms of the velocity, which along with the vector of the species fractions, is the only dependent variable we will need to solve for. The main equation to be solved for the

evolution of the gas is the steady state energy equation in primitive form

$$v\frac{\mathrm{d}p}{\mathrm{d}x} + \gamma p\frac{\mathrm{d}v}{\mathrm{d}x} = -(\gamma-1)\Lambda(T,\rho,\mathbf{X}) \tag{3.7}$$

where the cooling term Λ represents the optically thin losses from the atomic and molecular emissions. In order to be able to evaluate this term, we must also evolve the chemistry along the flow. The energy equation is solved by rearranging eq. 3.5 and 3.6 to get the pressure in terms of the integration constants and substituting to get equation 3.7 completely in terms of v.

$$\frac{\mathrm{d}v}{\mathrm{d}x} = \frac{-(\gamma-1)\Lambda(T,\rho,\mathbf{X})}{\gamma C_1 - C_0 v(1+\gamma) + \frac{C_2^2}{v}(1-\frac{\gamma}{2})} \tag{3.8}$$

This equation must be solved numerically. The cooling term Λ is dependent on the species fractions, which must also be integrated in parallel with the energy equation. They are solved according to their rate equations with a small alteration. In this stationary scenario, the time and spatial variable are essentially equivalent and are related by the expressions

$$t = \int \frac{\mathrm{d}x}{v}, \qquad \frac{\mathrm{d}}{\mathrm{d}t} = v\frac{\mathrm{d}}{\mathrm{d}x} \tag{3.9}$$

The rate equations (eq 2.10) for the species are thus solved as normal by replacing d/dt with vd/dx,

$$v\frac{\mathrm{d}n_i}{\mathrm{d}x} = C_i(T,n_j) - D_i(T,n_j)n_i \tag{3.10}$$

and the cooling losses are calculated at each step from the species fractions and temperature. The system $[v,\mathbf{X}]$ is integrated explicitly in the x-direction, starting immediately behind the shock and moving backwards with the post-shock flow. This was carried out using the ODE solvers from the Gnu Scientific Library (GSL, see e.g Gough (2009)).

The initial post-shock conditions are taken from the normal Rankine Hugoniot procedure for the region immediately at the shock. For this, the shock is treated as a pure discontinuity as determined by the true conservative MHD system or Euler equations, where the shock region is assumed small enough that the loss term is considered not to have taken effect. Denoting the upstream (pre-shock) flow primitive variables $(\rho_1, v_1, B_{y1}, p_1)$ and the post-shock, or downstream variables by $(\rho_2, v_2, B_{y2}, p_2)$ we have

$$\rho_1 v_1 = \rho_2 v_2 \tag{3.11}$$

$$\rho_1 v_1^2 + p_1 + \frac{B_{y1}^2}{2} = \rho_1 v_2^2 + p_2 + \frac{B_{y2}^2}{2} \tag{3.12}$$

$$v_1 B_{y1} = v_2 B_{y2} \tag{3.13}$$

The upstream velocity and magnetic field can be expressed in terms of the (upstream) density and pressure by writing them in terms of the Mach number and plasma beta

respectively

$$v_1 = M_1 c_s, \qquad B_{y1}^2 = \frac{8\pi p_1}{\beta_1} \tag{3.14}$$

where as usual $c_s^2 = \gamma p/\rho$. Upon substitution one arrives at the following expressions for the post-shock quantities in terms of the pre-shock quantities

$$\frac{\rho_2}{\rho_1} = r \tag{3.15}$$

$$\frac{v_2}{v_1} = \frac{1}{r} \tag{3.16}$$

$$\frac{B_{y2}}{B_{y1}} = r \tag{3.17}$$

$$\frac{p_2}{p_1} = 1 + \gamma M_1^2 (1 - \frac{1}{r}) + \frac{1}{\beta_1}(1 - r^2) \tag{3.18}$$

where X is the positive root of the following quadratic equation

$$2(2-\gamma)r^2 + \gamma[2\beta_1 + (\gamma - 1)\beta_1 M_1^2 + 2]r - \gamma(\gamma+1)\beta_1 M_1^2 = 0 \tag{3.19}$$

For the hydrodynamic case, the above procedure still applies, one sets B_y to be zero and the formulae simplify accordingly.

3.1.2 Comparison of Results

Having set up the problem accordingly, we first chose the parameters corresponding the test case used in Flower *et al.* (2003), namely that of a "fully-dissociative" J-shock propagating with a velocity of 25km s^{-1} into a fully molecular gas with density $n_H = 10^4 cm^{-3}$ and temperature of 15K, with no magnetic field present. Here we outline the details of the comparison.

3.1.2.1 Qualitative agreement

The first thing to check was whether we had qualitative agreement between our model and the reference model. The main things to look for here were the amount and rate of H_2 dissociation, and the general temperature evolution in time. This particular shock speed is actually a sort of "turning point" in terms of the type of shock chemistry which arises; a small increase or decrease in the shock speed leads to a rather different evolution. This is due to the highly sensitive balance between the temperature, dissociation, and cooling of the molecular gas behind the shock, and is discussed in section 3.1.2.2 below. Because of this, we find that with our reaction set the results of Flower *et al.* (2003) are reproduced for a slightly higher velocity than 25km s^{-1}, closer in fact to 30km s^{-1}. Figure 3.3 shows the dissociation reaching similar levels (i.e. practically complete) as the reference model, and at similar times. This was achieved after some tweaking of the reaction set, in particular with the modification of the H_2-H_2 dissociation reaction and the dust-catalyzed H_2 formation reaction. Figures 3.2 and 3.3 for example show a before-and-after the dust reaction was added.

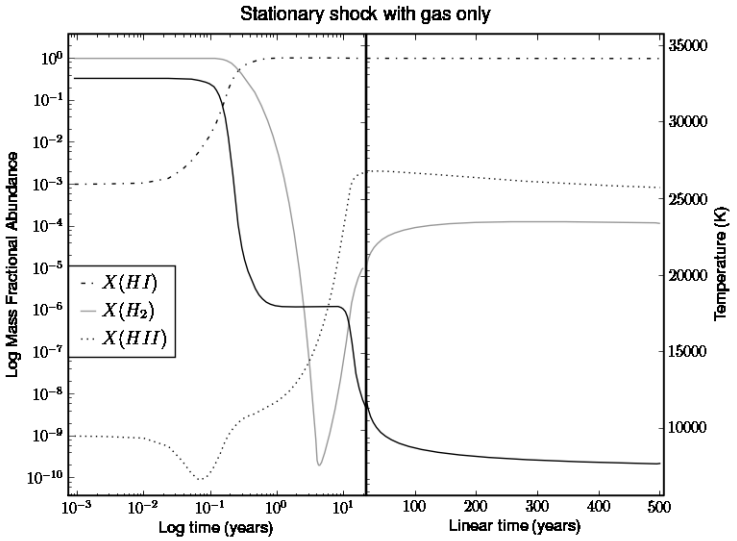

Figure 3.2: Profile of the post-shock flow for a stationary hydrodynamic shock with velocity 25km s^{-1}, pre-shock density n(H) = $10^4 cm^{-3}$ and temperature 15K. The shock can be thought of as being located on the very left axis, with the steady flow moving to the right along the x-axis. Shown are the mass fractions and temperature. The left panel shows the first 10 years in logarithmic scale, the remainder of the flow is displayed in the right panel with a linear scale.

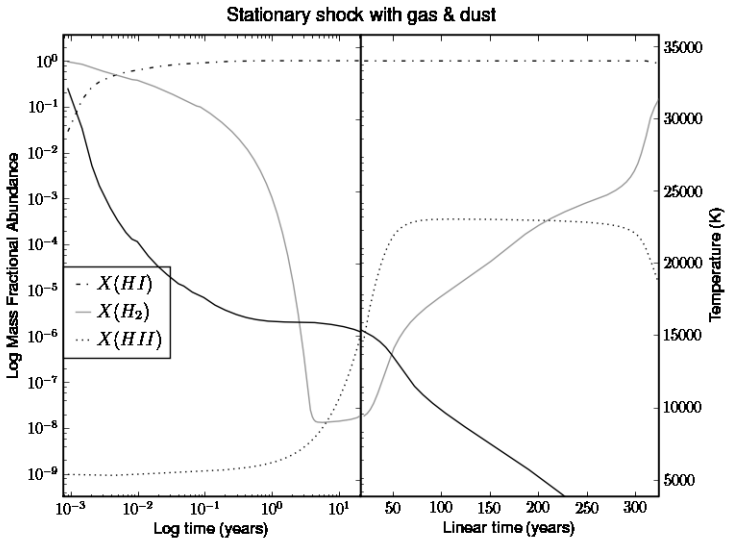

Figure 3.3: Stationary shock with modified chemistry and cooling Shock profile for the same shock parameters, but with the addition of dust formation of H_2 and some previously omitted cooling terms (such as H_2-H_2 dissociation cooling, important in the fully molecular pre-shock gas), which lead to much faster cooling and H_2 reformation behind the shock.

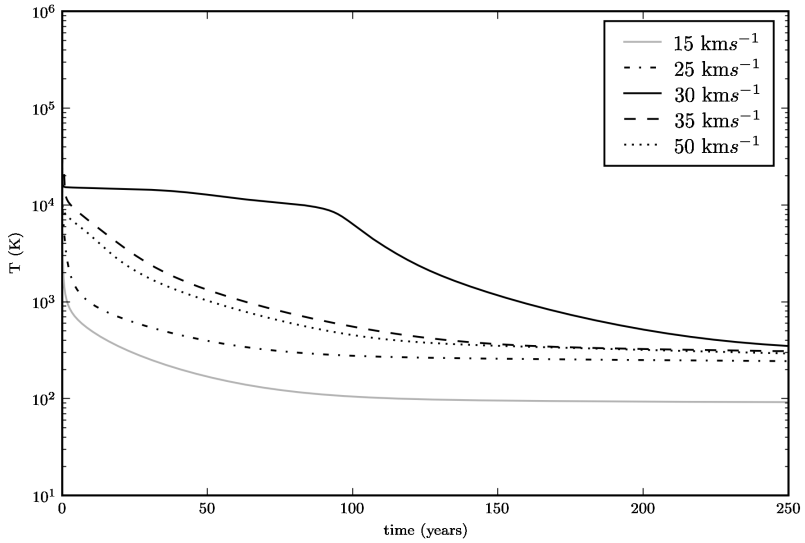

Figure 3.4: Temperature evolution with time for different shock speeds A linear scale is used to show the large scale evolution.

3.1.2.2 Cooling length & Cooling time

The next important aspect of the flow to compare is the cooling length, and its dependence on the shock speed. Looking at the shock's physical structure in terms of the temperature evolution and cooling width (see figure 3.4) we see that there is a clear and dramatic maximum for the cooling width for shocks with a velocity of about 30km s^{-1}, reproducing the observation in Flower *et al.* (2003) (albeit at a slightly different velocity). This rather counter-intuitive observation means, in simple language, that heating the gas by increasing the shock speed doesn't necessarily increase the cooling length! This is attributed to the fact that the increased temperature of the gas causes a higher level of ionisation (see also figure 3.6). The resulting abundance of electrons, through collisional excitation of atomic hydrogen, cause a stronger contribution to the cooling from Lyman α emission, resulting in the observed return to a shorter cooling length. For shock speeds lower than 30km s^{-1}, the shorter cooling length occurs because the survival of most of the molecular hydrogen, due to the lower shock temperature, allows fast cooling through the ro-vibrational losses of eq. 2.2.4.2.

The cooling time similarly varies with the shock speed, and forms the next part of our comparison. In figure 3.5 we show the cooling times for the evolution of the temperature towards 8000K and 400K. The cooling time for temperatures lower than this, towards 100K are significantly longer than those in Flower *et al.* (2003), suggesting some difference in the energy balance of the gas at low temperatures. The cooling rates we use seem to be less effective at those temperatures at countering the effect of H_2 formation heating than the rates used in that paper (we use the same method of computing the formation heating as those authors.) This is one area that could warrant further investigation, but the regions of the computational domain expected to cool to those temperatures are not extensive, and the difference is not expected to have significant dynamical or observational effects in the regime

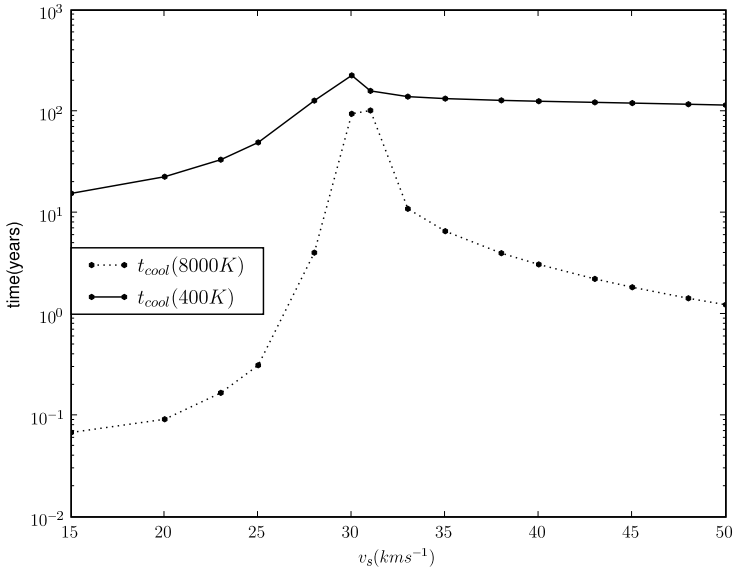

Figure 3.5: The cooling times for a range of shock speeds, to temperatures of 8000 K and 400K

we consider.

3.1.2.3 Ionisation & H_2 dissociation

Figure 3.6 shows the extent of dissociation and ionisation caused by shocks of various speeds. A sharp increase in the highest level of dissociation reached is seen as the shock speed varies from 25km s^{-1} to 30km s^{-1} followed, again somewhat counterintuitively, by an increase in the amount of H_2 surviving the shock. This is a consequence again of the higher ionisation for the higher temperatures causing atomic cooling to bring the temperature down before the H_2 can be fully dissociated.
We note that the minimum H_2 for our model does reach a somewhat lower value than that in the reference model. This minimum value is essentially a balance between two dominant reactions at that turning point in the post-shock flow; on the one hand there is the destruction of H_2 by the two main dissociation reactions (reactions 4 and 5 in Table 2.1), on the other hand the formation of H_2 on dust grains. This is quite a fine balance, depending acutely on the temperature evolution up to this turning point, and the resultant difference in the minimum H_2 fraction can thus be readily attributed to the particularities of the choice of dissociation rates and H_2 formation rate. The ionisation is also seen to be slightly higher in our model, and it is this, with its corresponding effect on the atomic cooling and temperature evolution, which causes the minimum H_2 abundance at shock velocities above 35km s^{-1} to rebound also somewhat higher than in the comparison model.
This all illustrates quite clearly how in such a nonlinear system, non-equilibrium chemistry can affect the temperature, which can then feed back to affect the chemistry.

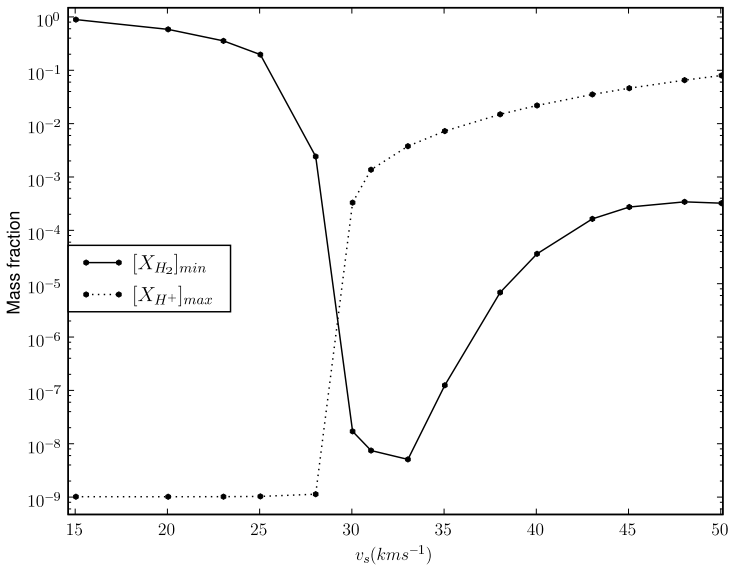

Figure 3.6: The minimum fractional abundance of H_2 and the maximum abundance of H^+ reached during the evolution of the post-shock flow towards equilibrium.

3.2 Time Evolution - 0D Time dependent equilibrium convergence

After having validated the chemical and cooling model our next question is, how are the rate equations and cooling step being integrated in time? Given that our treatment of the chemistry and cooling is local, in that there is no spatial dimension to the equations being solved, it is desirable to find a means of testing the module's operation without interference from spatial aspects of the problem. By considering a single parcel of gas, with no advection terms, we can analyse the operation of just the time dependent aspects of the code to which our module is directly relevant, namely the chemical and thermal properties.

3.2.1 Setup

The test consists of taking the same pre-shock gas chemical compositions, representing gas in a typical molecular cloud core, considered in the stationary shock problem of section 3.1 and imposing suddenly the post-shock physical conditions (namely the temperature and density) as the initial condition of the gas. This is of course then a situation which is out of equilibrium chemically, and the reactions will drive the gas in time towards chemical and thermal equilibrium, until the floor cooling temperature is reached and the reactions governing the species at that temperature are in equilibrium. The objective here is to check that the algorithm used in the large scale time dependent simulations presented later, which uses a larger timestep or subtimestep necessarily larger than can be afforded in single-point tests, is able to effectively reproduce the chemical and cooling evolution of the gas.
This is similar to the stationary shock scenario, the only change being no compres-

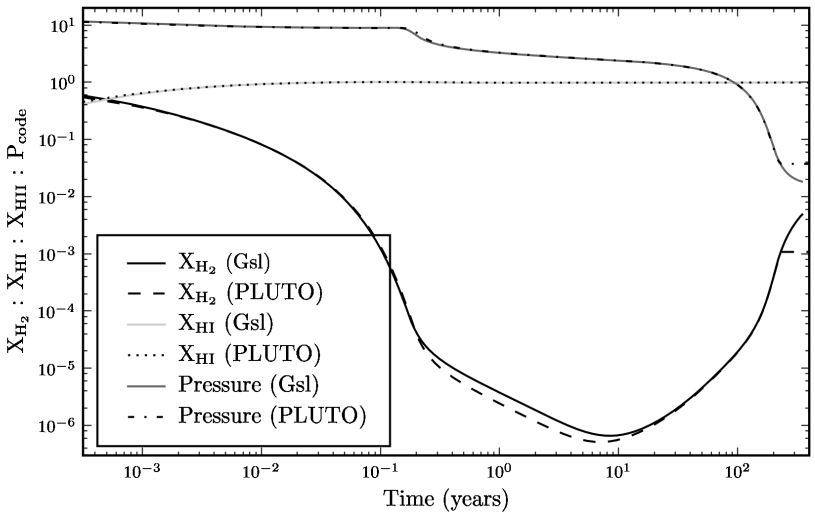

Figure 3.7: Comparison of solver time evolution with reference model The chemical variables and pressure as evaluated by our chemistry and cooling network are compared with the same model as computed using the GSL ODE solvers to very high accuracy. The basic evolution

sion occurs during the evolution as there is no flow. The reference code this time is our implementation of our chemical model using the GSL ODE integrators using an adaptive timestep with a very low tolerance (i.e. high accuracy), and the implementation being tested is our module as implemented within the PLUTO code. The problem is set up in PLUTO for the minimum number of points in one dimension with the velocity set to zero, in this way we represent the parcel of gas we wish to consider.

3.2.2 Comparison and Discussion

We find the time evolution of the chemistry and pressure to be well reproduced by the module in general. Figure 3.7 shows the evolution matching the reference solution very closely, up to the point where the gas cools to the cutoff temperature in the module, at which point the solutions diverge. The performance is of course highly dependent on the timestep. In order to test the accuracy of the solver, we switch off the code's adaptive time step described in section 2.2.3 and force the timestep to different values (though not affecting the internal substepping cycles of the module). We define as a metric for the accuracy the average relative error

$$\epsilon = \sum_i \left(\frac{\mid \mathbf{X}_i - \mathbf{X}_i^{\mathbf{ref}} \mid}{\mathbf{X}_i^{\mathrm{ref}}} \right) \tag{3.20}$$

where $\mathbf{X}_i$ is the solution calculated with our time dependent solver, and $\mathbf{X}_i^{ref}$ is the solution from the GSL solver. A similar approach is used by Tesileanu *et al.* (2008) to evaluate the accuracy of the explicit solver developed for their non-equilibrium atomic module, though the error parameter is defined slightly differently. Figures 3.8 and 3.9 show the error introduced for two different timesteps. A timestep of $1{\times}10^5$ (code

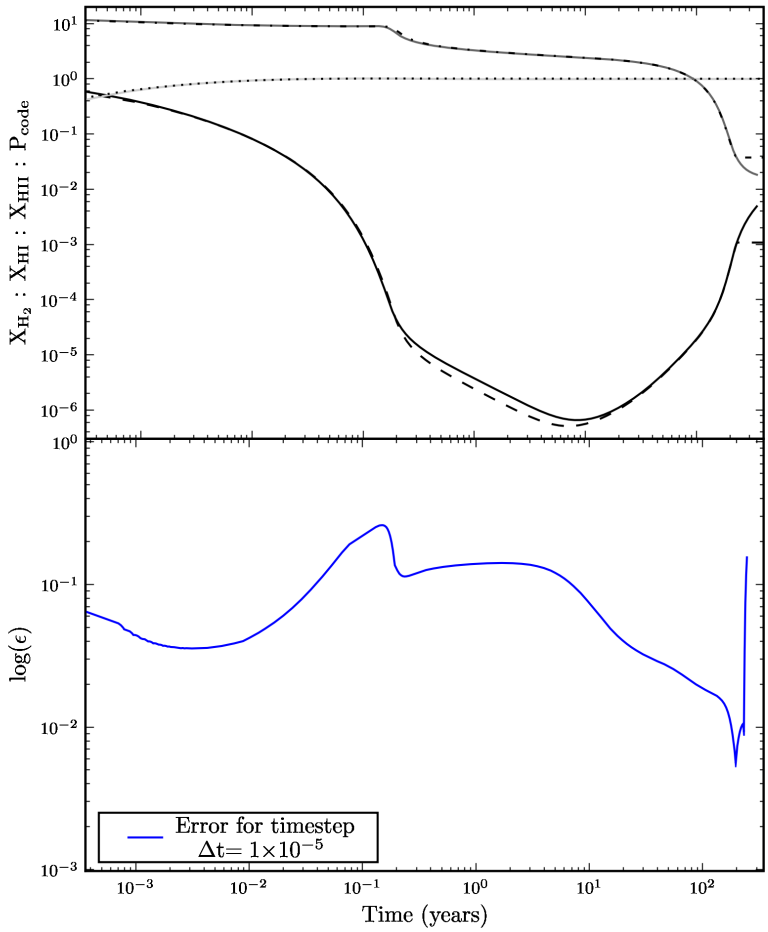

Figure 3.8: Accuracy with respect to the reference solution. The timestep of 1×10^{-5} yields an accuracy which fluctuates around 10%. The decrease towards the end is due to the species reaching equilibrium and having lower rates of change.

time units) is accurate to within 10% which for our purposes is reasonable, given the performance benefit from having a larger timestep (in these tests 1 or 2 orders of magnitude greater than the explicit solver) and light algorithm. The inaccuracies in the case of figure 3.9 are unlikely to occur, as the adaptive timestep step shorten if necessary. Also, in one of our typical AMR simulations the timestep on the coarse grid varies between 1×10^{-5} and 1×10^{-4}. With four levels of refinement always covering the stiffest regions of the flow, this corresponds to a timestep of a few 10^{-6} which means we are assured of accuracy to at least 10%.

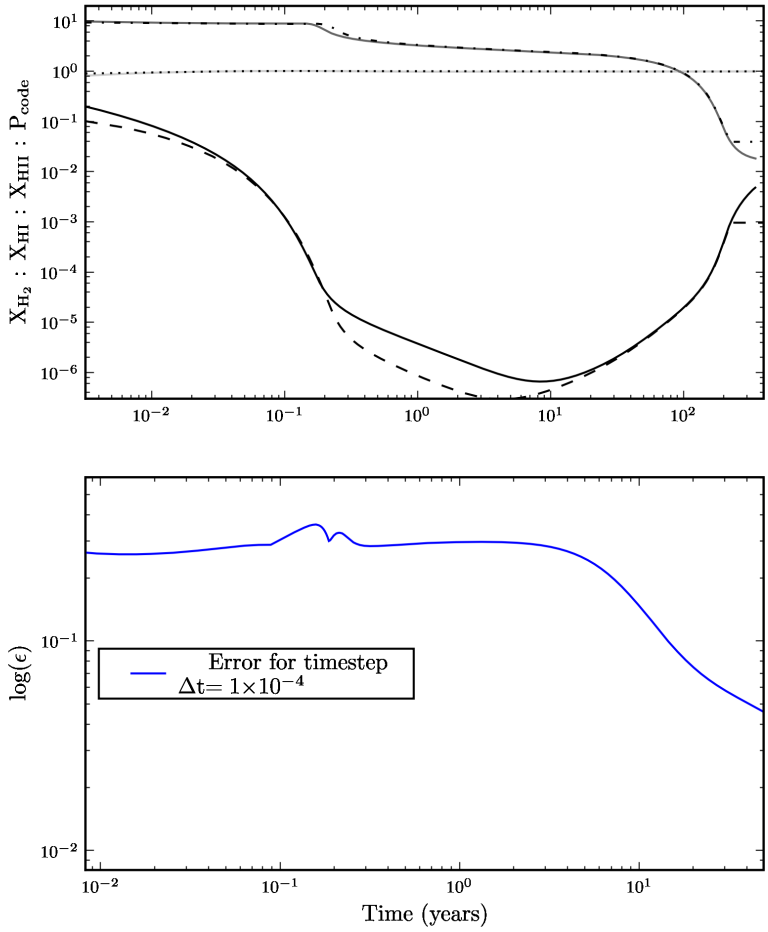

Figure 3.9: Comparison of solver time evolution with reference model Here the effect is shown of increasing the timestep from that used in figure 1.8 by a factor of 10 to 1×10^{-4}. The error reaches up to 20%, though the chemical and pressure evolution are still reproduced reasonably.

3.3 Spatial and Time Evolution - 2D planar J-shock

The last link in the chain from model to simulation is the time dependent J-shock test. So far we have seen the chemistry and cooling code working under somewhat "pleasant" conditions and performing quite well. The chemistry and cooling routine working in the 0D test case must only reproduce the post-shock chemical and thermal evolution of a parcel of stationary gas with no physical or dynamical forces involved. However, when we simulate time dependent jets in a spatial domain, a new range of resolution issues and dynamical extremes faces us. Gas flows are colliding at highly supersonic speeds and rapid compression and heating, expansion and cooling, occur over very short timescales and distances. It is of considerable importance to be able to ascertain the level of reliability of the code in such settings.

3.3.1 Setup

In order to ensure that our code is working okay in the exact conditions of a multi-dimensional simulation, we test the full time dependent code, PLUTO and the cooling module in conjunction with the Chombo libraries, in a 2D cartesian geometry. The logical way to proceed is to try to reproduce the same shock chemistry as we obtained in the stationary shock case from section 3.1. In order to generate a stationary shock we use one of the boundaries as a "piston", by using reflective boundary conditions to represent a wall (see fig. 3.1), starting the gas flowing against the wall at the desired shock speed (equivalent to a piston moving into the gas). As the shock moves out from the wall in the beginning, the actual shock speed will then of course be greater than the desired shock speed, until the shock passes the cooling length. At this point, the shock loses pressure support and will be driven back (with the relative speed between the shock and the inflowing gas reduced) by the incoming gas to the cooling length, where it basically remains in the stationary state where the total post-shock pressure balances that of the incoming flow.

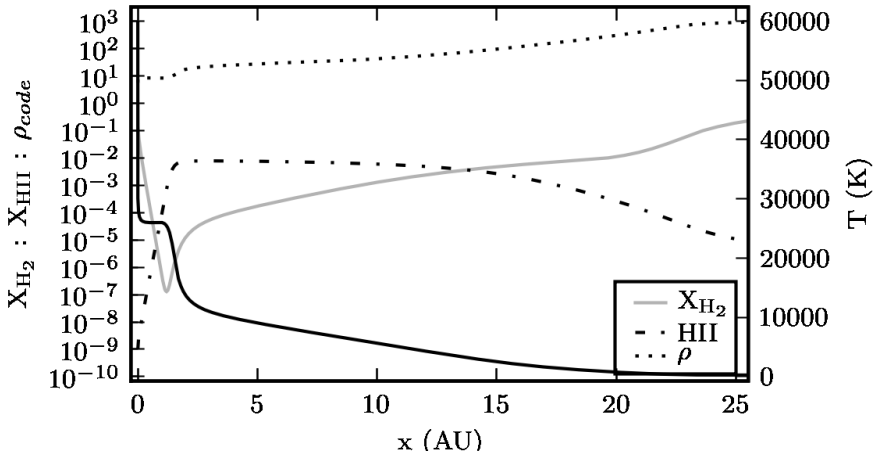

Figure 3.10: Reference solution for 2D planar shock test Solution from the stationary code using the GSL solvers, for a 35 km s^{-1} shock.

3.3.2 Comparison with Stationary Shock

We run this problem with the same initial conditions as the stationary shock problem in section 3.1.2, but with a shock speed of 35 km s^{-1}. The reference solution is shown in figure 3.10. The time dependent code is run at resolutions of 0.3 AU per grid cell, similar to those used in the large scale simulations in Chapter 4. Comparing the 1D stationary solution with the final steady state of the 2D time dependent solution in figure 3.11 we see a rather good reproduction of the post-shock chemistry, with the amounts of ionisation and dissociation in the right region. The cutoff temperature implement in the time dependent module does affect the end state of the gas, as the corresponding residual pressure of this cutoff temperature will not allow the gas to compress as much as it would otherwise. Also the reformation of H_2 gets curtailed, slowing down at an abundance of around 10%. The temperature in the sharp peak immediately at the shock is not correctly reached, for two unavoidable reasons. reasons. One is that this temperature occurs in a region smaller than the grid size, and so is averaged over the spatial extent of the cell and over the cell time step. The other reason is that the shock in a spatial code is never really a true theoretical shock. It is usually resolved by two or three points, in which cooling losses are already being incurred even as the gas is heating up. The only way to improve this is to drastically increase resolution, but the gains of doing so are probably not significant. In any case, the temperature evolution from 20,000 K onwards is reasonably good, and the fact that the chemical evolution afterwards is correct means that the time resolution is being handled sufficiently well.

It is interesting to note that the shock propagates out cleanly, numerical errors are not enough to perturb the shock front. If, however, we introduce a perturbation at the inflow boundary condition, we do see a completely turbulent nature to the shock front in figure 3.12, which has the potential to significantly affect the chemical and temperature properties through mixing.

3.4 Resolution Study

In order to decide on a resolution suitable for carrying out our large scale simulations, we have two criteria. First, the solution should converge, i.e. increasing the resolution should not alter the solution significantly. Secondly, the chosen resolution should not be too expensive, in other words, we should not waste CPU time on a resolution which doesn't improve the solution from the standpoint of what we are trying to investigate.

The tests carried out up to this point in the previous sections go some way towards assuring us that the resolution is sufficient to reproduce the gas physics and chemistry to the extent we require. However, we must also check the correct resolution to use in the setting of an actual simulation, as the performance constraints are critical here. To this end we run a test simulation using successively higher resolutions until we reach a reasonable convergence. For the simulations carried out in Chapter 4, we need to ensure that not only the physical evolution of the gas is evolved correctly, but also that the chemistry is reproduced.

Figure 3.13 shows the test simulation for 4 different resolutions, with both the density and H_2 fraction plotted. The first, although reproducing the basic jet shape and

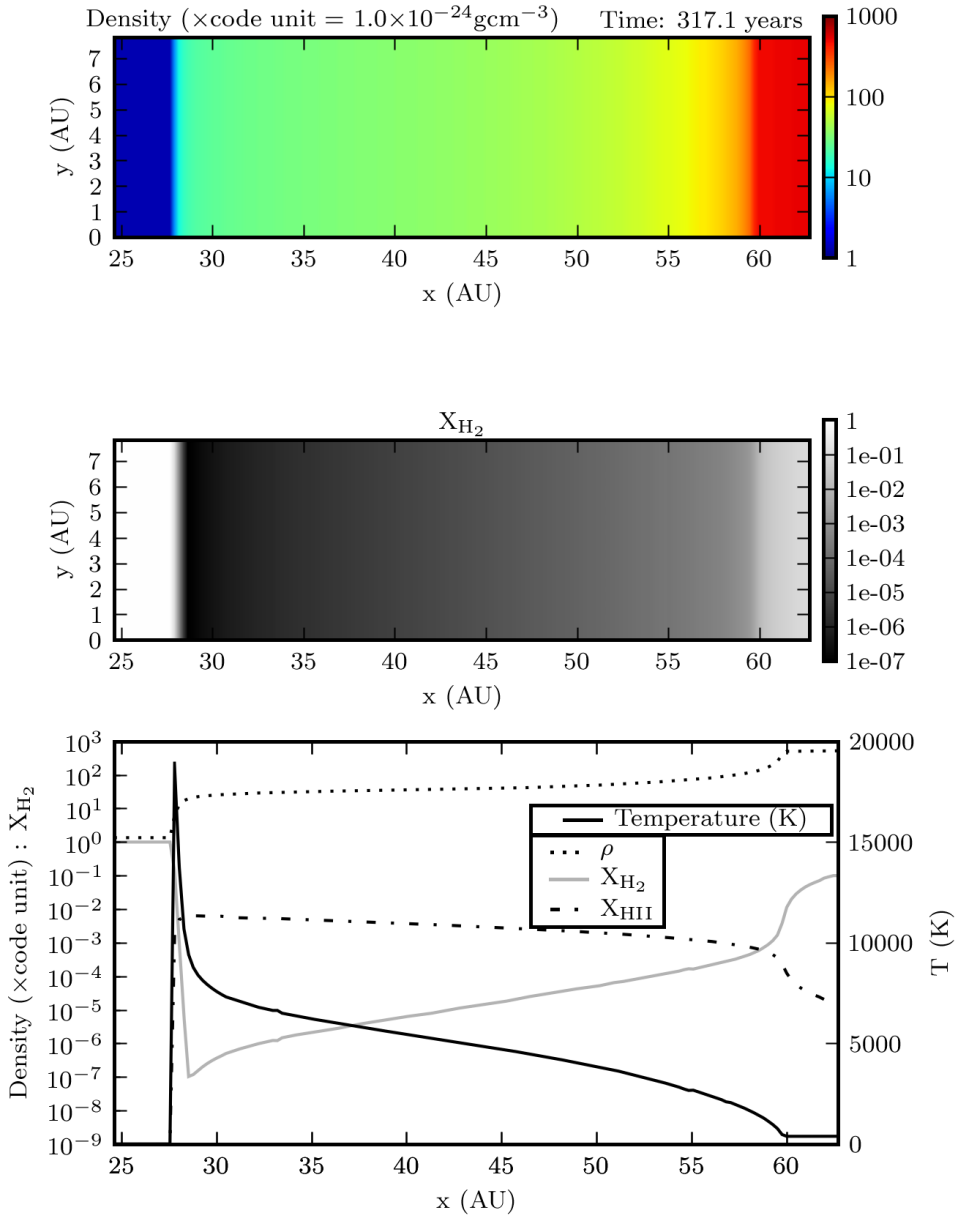

Figure 3.11: 2D planar shock test An inflow of gas from the left collides with a reflective boundary on the right, and a shock propagates outwards. Here is shown the steady state result.

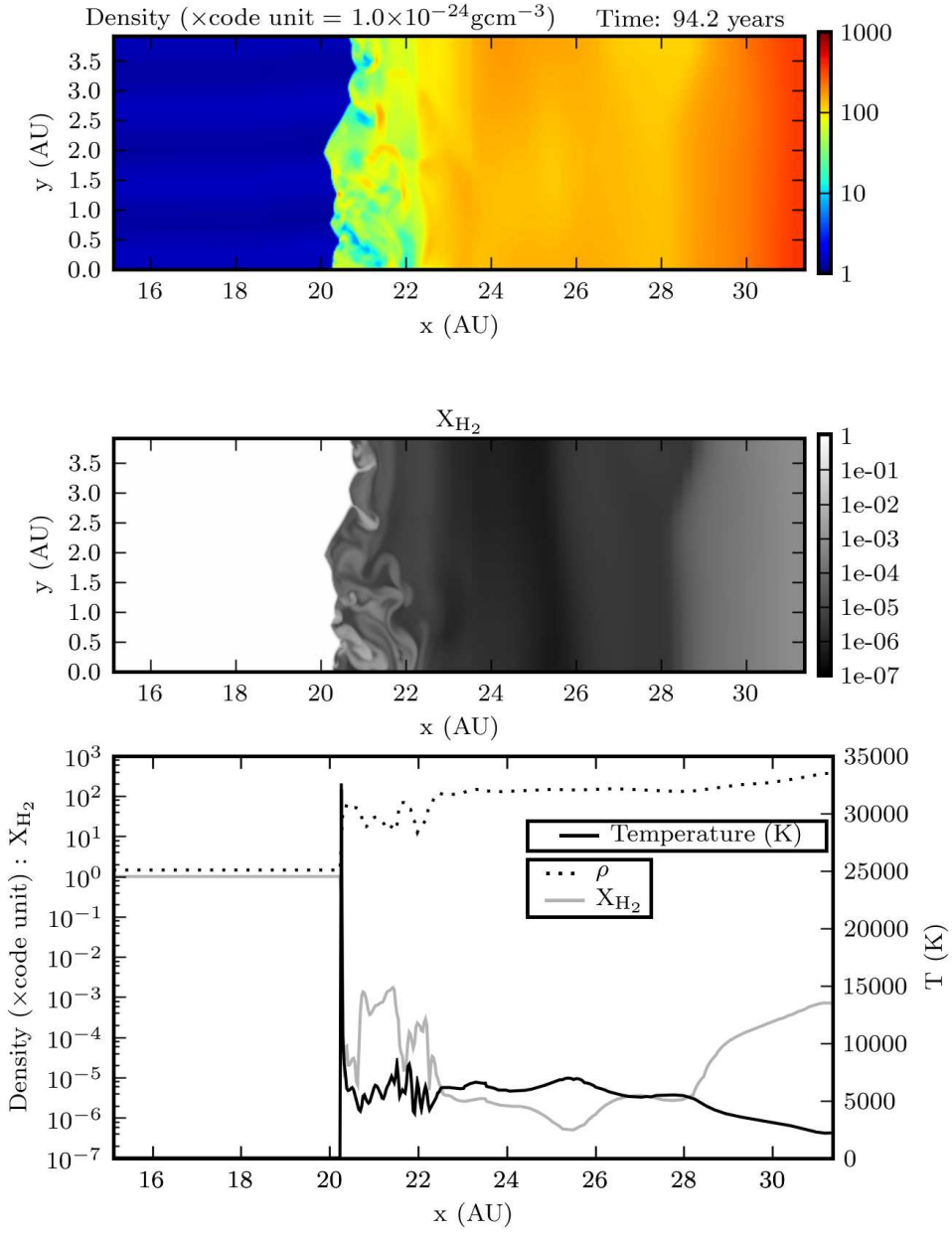

Figure 3.12: 2D planar shock test with perturbation (for different parameters). Here an inflow perturbation (sinusoidal variation of 10% of the density) has been introduced to a planar shock, disrupting it to cause turbulent mixing. The profile is just a section, not the average over the whole width.

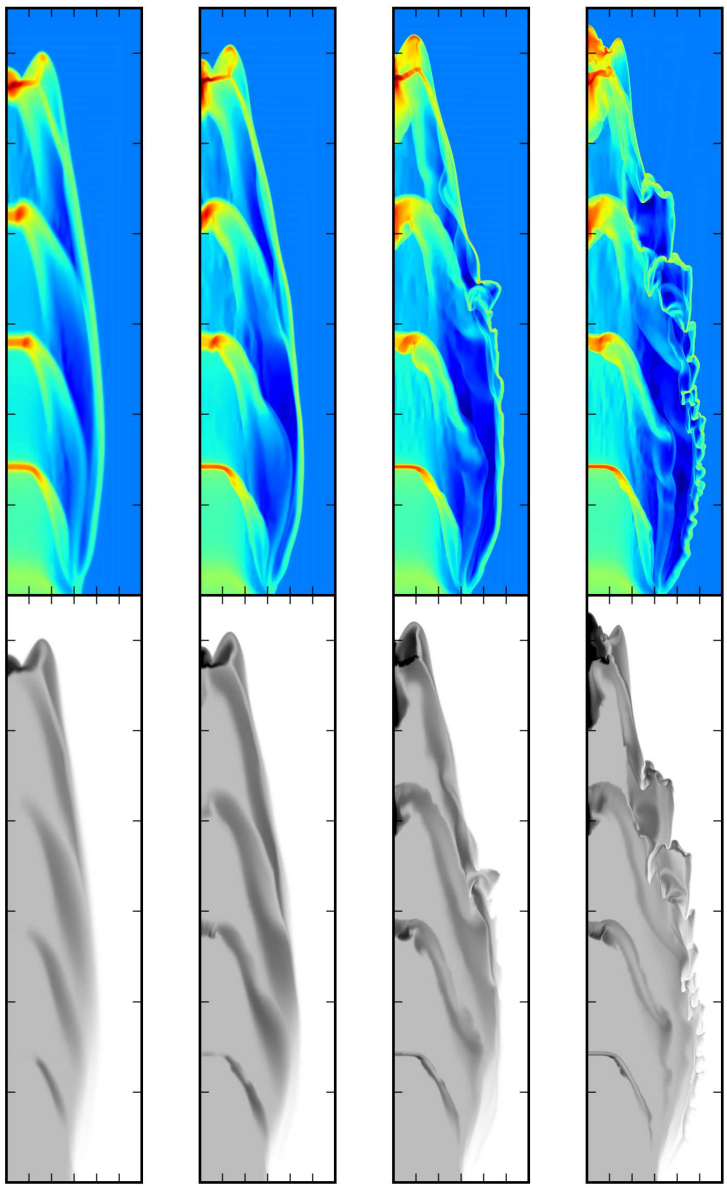

Figure 3.13: Resolution test showing density and molecular fraction for four different resolutions. From left to right the resolutions are (in AUs per grid zone): 2.44, 1.22, 0.61 and 0.305. The third one (0.61) is used in the production simulations in Chapter 4.

speed, is clearly poor as regards the chemistry, with no dissociation in the knots. The second, with double the resolution at 1.22 AU per gridpoint, is much better, with the knots visible. In the last two, we see differences in the lateral bow-shock, where the cooling instabilities are appearing more quickly, though in the lower resolution case they do eventually develop.
For the inner part of the jet, i.e. the head and knots, there is however pretty good convergence for the chemistry and the propagation length and width of the bow-shock. For this reason, in the end we compromise between performance and resolution, choosing the third of these resolutions for our production simulations. This involves, for the 5000AU domain, a base grid of 512x64 grid points, with 4 levels of binary refinement, bringing the equivalent resolution to 8192x1024 for the domain.

3.5 Scalability and "Macroscopic Testing"

Although the detailed examination of any code in order to ascertain its reliability is of the utmost importance, we always keep in mind the final goal of large-scale multi-dimensional simulations. In addition to the previously described detailed tests and comparisons in 1 and zero dimensions, we also evaluate, albeit necessarily at a lower level of depth, the properties of the code in action at larger scales and in 2 and 3 dimensions. We are concerned with the performance of the code under such conditions for two reasons. First, despite the fact that the code may have been validated in more limited and focussed scenarios such as the 1-dimensional shock propagation described in section 3.3, when we move to multi-dimensional scenarios the dynamics are different. The range of shock speeds in different parts of the domain is considerable in a time-dependent jet flow, and some aspects of the code may be tested more than in the simpler problems (for example if lower density regions occur from vortical motion). Secondly, the execution of batches of large simulations requires a significant amount of resource budgeting, organisation and optimisation. Examination of the performance properties of the code is necessary to avoid excessive waste of computing resources and real time.

Unlike uniform grid jet simulations, in AMR codes the number of points simulated changes during the simulation. For the case of jet simulations, the refined area increases as the jet propagates along the axis, see figure 3.14. Although this non-uniform computational load slightly complicates performance estimations, heuristic estimations of the CPU consumption for a larger scale jet simulation can nonetheless be made by observing the amount of wall time required for e.g. the jet head to propagate a given distance, at various stages of a smaller scale simulation. As the jet advances through the domain in an essentially linear manner, one can extrapolate the trend to estimate the consumption for the larger scale simulations.

To this end, we use the usual Unix system commands to obtain the creation time of each output. Plotting the "real time" against the "simulation time" (roughly corresponding with the jet length as it propagates linearly with a fairly constant velocity) we see the evolution of the required CPU time versus the jet length. As seen in figure 3.15 the increase in the slope represents a marked increase in the amount of CPU time needed per physical time unit in the simulation as it proceeds.

This also leads to complications in evaluating the scalability of the code (i.e. the

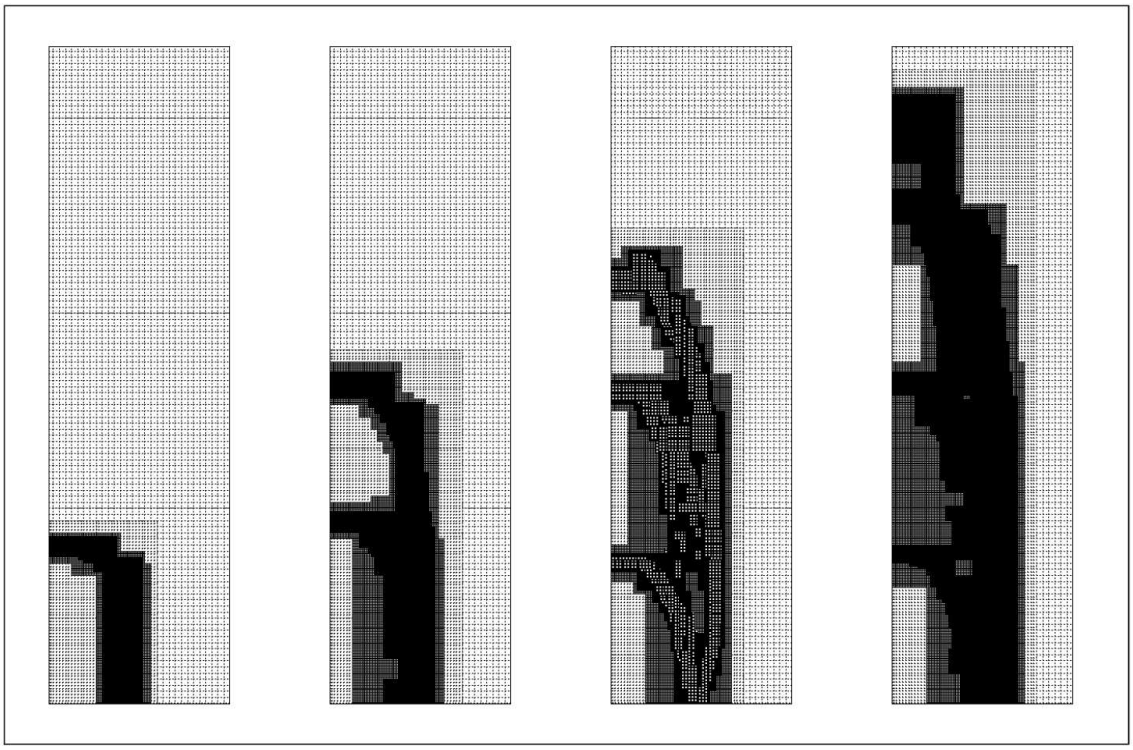

Figure 3.14: Illustration of Mesh Refinement load. As the jet propagates in the z-direction the refined area increases, with a corresponding increase in the number of points to be computed.

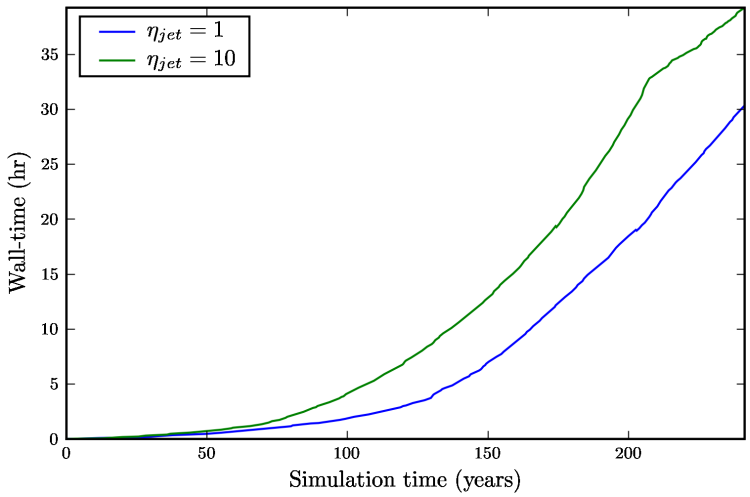

Figure 3.15: Required wall-time as a function of jet propagation time for typical simulations of over-dense and equal density jets propagating to 5000AU and 3900AU respectively. An overdense jet fills the domain faster and the computational load increases faster than for the light jet. However the physical distance traversed in the computational domain by the light jet in the given time is consequently less.

increase in performance gained by increasing the number of processors). Although it is necessary to have a large number of CPUs in the later stages of the simulation, adding more processors in the early stages is not helpful and may actually slow the program down with excessive communication cost. In practice, we found the best way to work with the performance properties of the AMR code in this particular simulation scenario was to use the somewhat low-tech procedure of starting the jobs with a low number of processors, where an excessive number of processors would be wasteful, and run the later stages of the jobs with a larger number of processors, using the "restart" function of the PLUTO code.

3.6 Summary

To summarise this chapter, we have presented the range of tests we used to bring the chemical and cooling model as it existed "on paper", to an implemented and validated module within the PLUTO-Chombo code.
These tests illustrate the workings of the main processes in the chemistry, and the effect of real-life constraints of time and spatial resolution on the quality of the solutions obtained.

4
Jet Simulations

In order to answer our questions on the factors affecting emission from shocks of J-type in protostellar outflows, we have carried out several simulations, with the aim of probing the effect of several key jet parameters expected to have an influence on the behaviour of emission-relevant aspects of the gas.
The chapter is divided as follows: The first section examines in detail a typical simulation run and uses various visualisation and diagnostic methods to examine the data. This "typical" simulation is used as a point of reference thereafter, in the main results section where we present our findings on the role of each of the four quantities independently considered in our study. These quantities are the magnetic field strength, the density ratio of the jet to the ambient medium, the ionisation and the H_2 content of the jet inflow. Finally, we consider what the four studies mean as a whole for the modelling of properties of Class 0 jets.

4.1 Results: Analysis of the Control Case

We begin by describing our reference run and analysing its properties in detail. This particular set of parameters will serve as a control, to be used as a reference case (referred to by the name "REF") against which the rest of the simulation runs will be compared. First, we state the parameters used in the run, then we describe the general features.

4.1.1 Parameters of the Control Case

For this run we specify three parameters in addition to those in Table 2.2, and which will vary from run to run. These are:

- **Density contrast,** $\eta = 10$. The beam is overdense with respect to the ambient gas by a factor 10. The beam density in Table 2.2 is held constant while the ambient gas is set to one tenth of that density, i.e. to $1{\times}10^3\,\mathrm{cm}^{-3}$.

- **Molecular fraction, $\mathbf{X}_{H_2} = 0.10$.** 10% by mass of the gas is molecular.
- **Ionisation, $\mathbf{X}_e = 0.01$,** or 1% ionisation in the gas.

In addition, the magnetic field strength will be varied in the MHD runs. The set of parameter studies was run without the metal cooling terms. However the data were post-processed to calculate the abundances of the metal species in equilibrium with the molecular hydrogen, and these abundances are used to calculate the CO emission lines.

4.1.2 Physical Features

Figure 4.1 shows the progression of the jet through the domain The first thing to remark upon is the morphology of the jet as seen in the density plot. The jet displays many of the classic hallmarks of a radiating jet. As described in section 2.3, the jet gas enters with a sinusoidally varying velocity, and shocks form almost immediately to produce "knots", as expected due to the nonlinearity of the equations. The first knots are decelerated by the ambient medium and are caught up by subsequent knots. This kinetic energy is thermalised and much of it radiated away, and a dense cool region forms at the head of the bow, becoming essentially ballistic with respect to the ambient gas. We see also very quickly the onset of the cooling instabilities in the bow-shock first documented by Blondin *et al.* (1990) and subsequently analysed by Dgani *et al.* (1996) (these instabilities are seeded by a perturbation which starts at the head of the jet and travels back along the bow-shock). The bow-shock is much slower laterally than towards the head, with the result that the molecular material of the medium goes largely un-dissociated and remains available for cooling, with the result that the post-shock gas cools rapidly and a thin, compressed layer builds up as successive reverse shocks reach the initial post shock region.
Looking now inside the jet, the excavation of an underdense cavity or "cocoon" is evident in the area between the jet and the bow-shock. Figure 4.2 shows, for the same simulation, the other main physical quantities, with the jet having reached the end of the domain of 5000 AU after just under 230 years. With the aid of the temperature and pressure plots, it can be seen that the development of this cavity is due to the pressure expansion of the gas in the cavity, from the velocity vectors. The gas is continually reshocked and heated by the internal working surfaces propagating from the knots, which ensures that the gas remains pressurised. The knots themselves are in turn overpressurised with respect to the rest of the material inside the cocoon, and they are seen to expand gradually as they travel along the beam.
We also see, looking at the velocity vectors, that there is little in the way of turbulence in the cocoon gas. As the jet is overdense and overpressurised with respect to the ambient medium, the motion of the jet gas is uniformly directed along the jet axis and outward. Another factor contributing to this is the ability of the gas to radiate away its kinetic energy, cooling and becoming compressed. The profiles across the jet in figure 4.3 show in more detail the density structure. Particularly evident is the underdense nature of the cocoon, and the survival of the H_2 in the narrow region between the initial bow-shock and the high temperature region which has been heated by several successive reverse-shocks from the internal working surfaces of the knots.

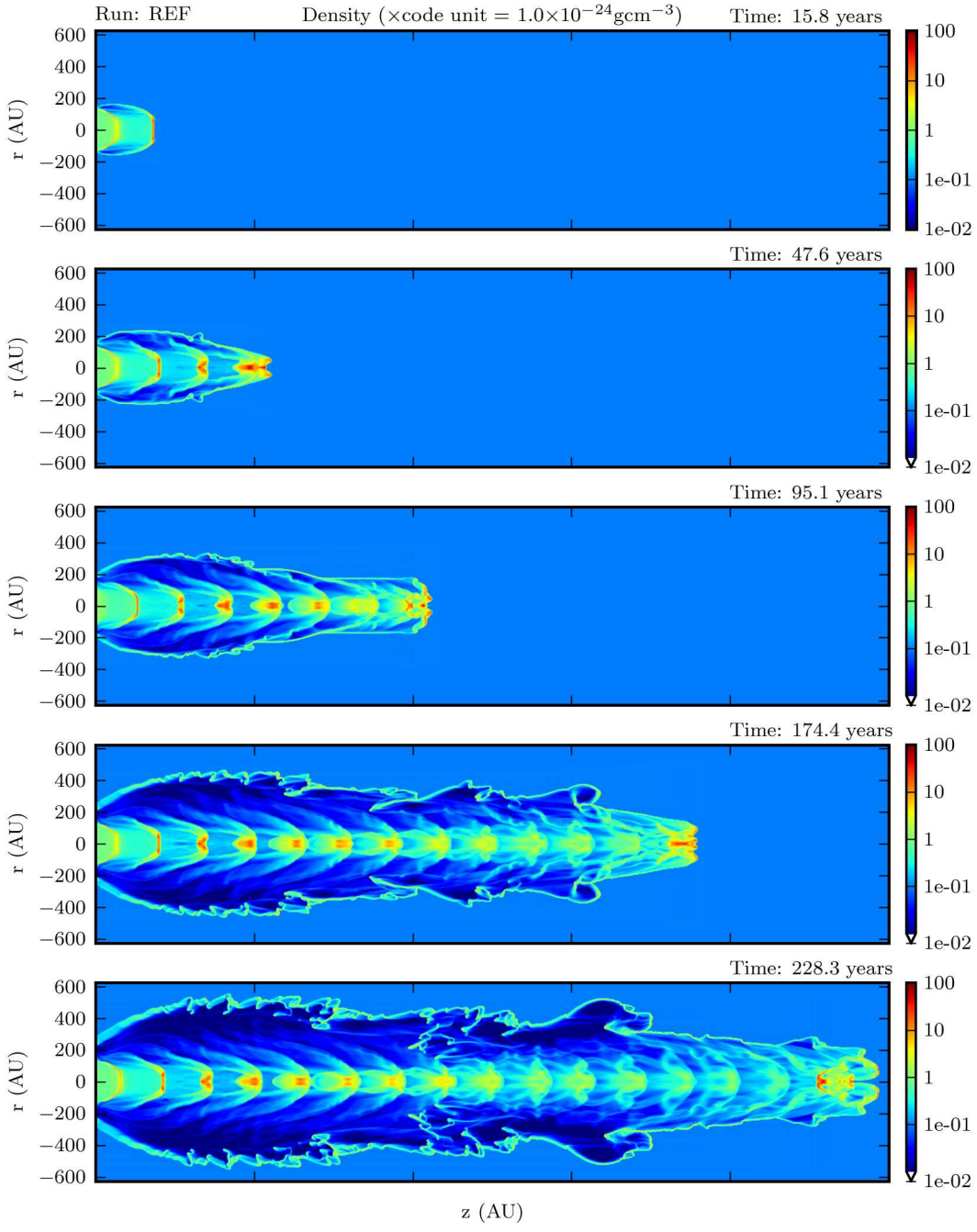

Figure 4.1: Run: REF time evolution. Time development of the density for the jet as it progresses through the domain. Our reference hydrodynamic solution has beam parameters X_{H_2}=0.1 & X_e=0.01 and η=10. The solution displays the typical features of a cooling jet, most notably the "deflated" bow shock, cooling instabilities in the bow, and a build-up of dense cooled matter at the head.

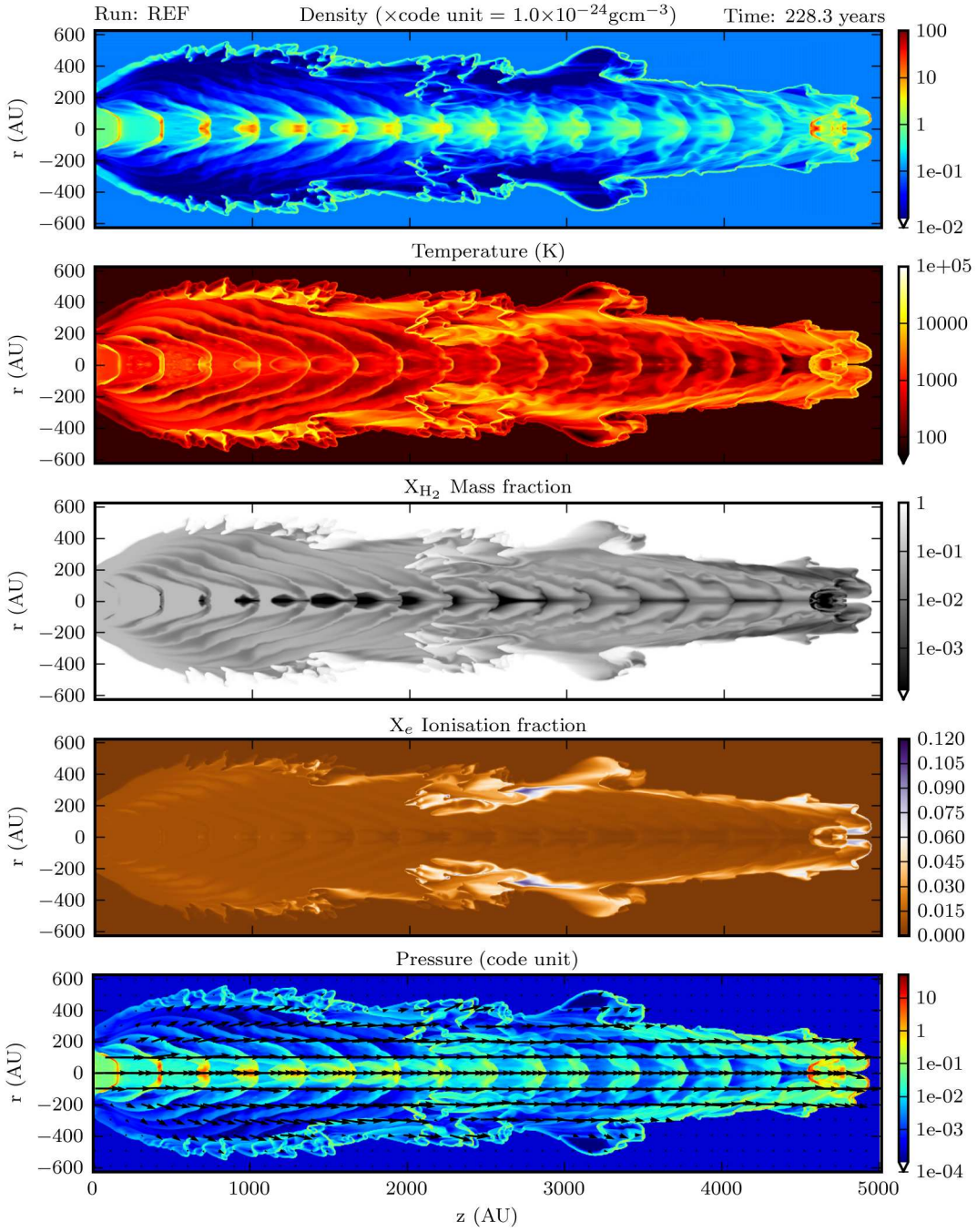

Figure 4.2: Run: REF $\eta = 10$ Plotted this time are (top to bottom): density ρ, Temperature, X_{H_2}, X_e and pressure, with velocity vectors (normalised to highest velocity of 150 km s^{-1}). The vectors show the pressure expansion of the jet beam.

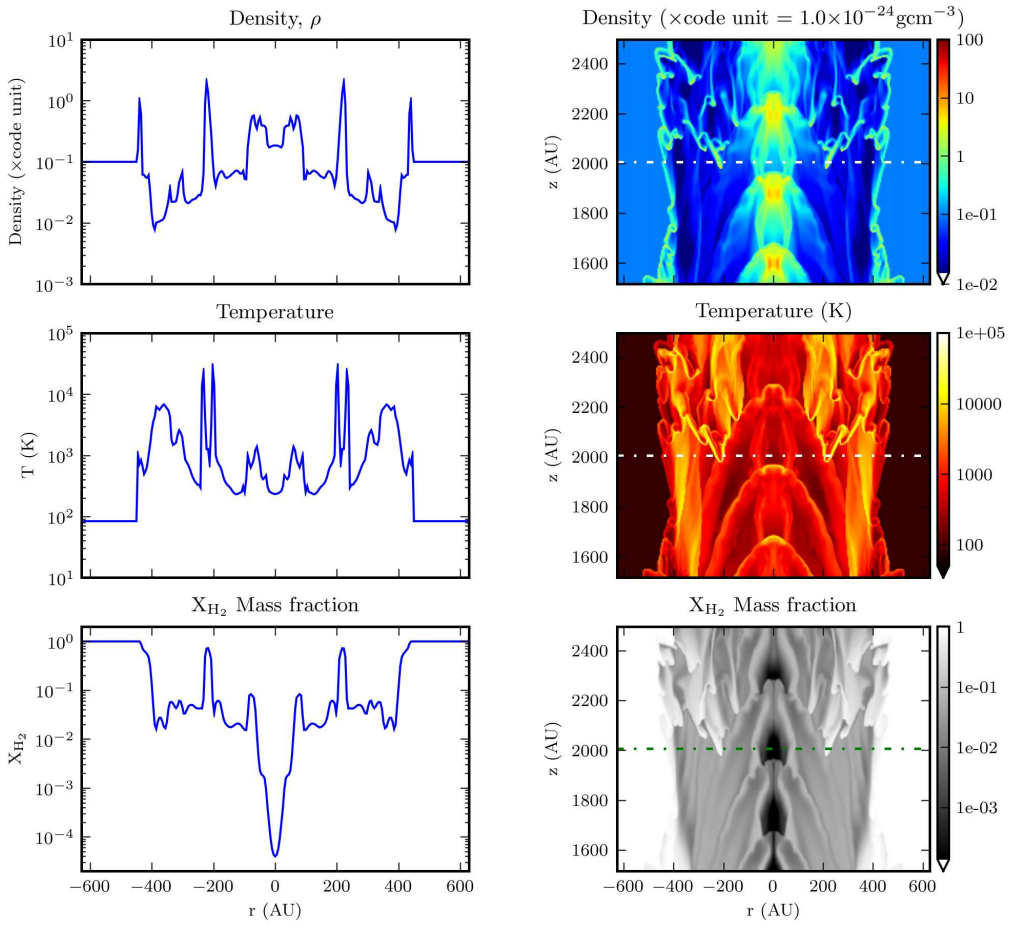

Figure 4.3: Run: REF $\eta = 10$ Profiles across a slice of the jet for (top to bottom): density ρ, Temperature and X_{H_2}.

4.1.3 Emission maps

Using the density, temperature and H_2 abundance, we calculate the emissivity and surface brightness of the gas in several emission lines, see figure 4.4. The first important thing to notice here is in that the H_2 ro-vibrational emission does not occur in the initially shocked region behind the bow show. The H_2 survives, but it is not hot enough to emit in the 1-0S(1) ro-vibrational line, which is quite a high energy transition. The lower energy CO rotational transitions, on the other hand, do emit significantly in this region. The higher CO 32-31 transition is seen in more areas of the jet, although it is also strongest at the bow area. There appears to be no emission at the knots, however, the regime there appears not agreeable with the routine used to solve for the levels, so we treat this area as faulty data and do not make any conclusions based on it.

Conversely, in the hot, reverse-shocked region just inside the cocoon, the gas is over an order of magnitude hotter at around 10,000 K and despite the fact that the density

and H_2 fraction are lower, there is significant emission from H_2, while there is little or none from CO. Looking at the integrated column of emission from H_2, we see that the strongest emission occurs near the tip of the jet, and also at a section in the middle, with several pronounced gaps in between.
Looking to the physical variables plotted in figure 4.2, we can try to explain why this is so. At the tip of the jet, the matter is hot *and* dense, even though the H_2 abundance is not that high (a few percent). There is enough of this H_2, as well as newly shocked H_2 from the ambient medium that can emit before it all dissociates, to account for the significant emission.
At the middle of the jet, it is quite clear from the plot of the H_2 fraction that a significant amount of matter from the ambient medium is being **entrained**, with "fingers" or chunks of the matter entering the jet cocoon. Here, the internal working surfaces of the knots, interact with or "ablate" these fingers of ambient matter, shocking the mostly molecular gas and causing it to emit quite strongly. Some of this matter is also quite dense, as seen in figure 4.3, and in time-dependent videos of the plots, reveal themselves to be sections of the cooled layer of bow-shocked matter that have broken off in an instability and moved into the flow. The matter is also seen to be significantly ionised in the plot of the ionisation fraction, reaching a levels of about 5%.
Figure 4.5 shows the profiles for some of the predicted emissions. Here we see that the CO emission is strongest in the immediate post-shock region of the bow, as well as in the entrained matter, whereas the H_2 emission is strongest (in this particular section of the jet) in the entrained matter. The CO emission profile has a single peak of emission at the entrained clump, whereas the H_2 emission has a double-peaked structure, where the sides of the clump are being ablated by the internal shocks. Also shown in figure 4.5 is the column-integrated H_2 emission. Most of the emission seen on the integrated map is from the strong double peaks of emission at the surface of the entrained matter. Although the line-of-sight integration process necessarily smears this emission across the centre of the plot, the "limb-brightening" effect is apparent in the column-integrated emission plot. We note that the brightness predicted matches approximately the scale of the observations of McCaughrean *et al.* (1994) of the young Class 0 source HH211. The OI 63μm line emission seen in blue contours in figure 4.4 traces the regions where atomic losses are occurring. This emission is much more localised at the knots of the jet where the high temperatures occur, and with a sufficient ionisation fraction.

4.1.4 Mass-Velocity and Line-velocity profiles

By means of a check, to compare our results with other works, we use the mass velocity diagrams and line velocity profiles described in section 2.3.2. Figure 4.6 shows these quantities for the simulation REF. The mass-velocity relation reproduces what has been found in other works (Downes & Cabrit, 2003). Looking at the features in the plot of the total mass, we see that most of the gas is in low velocities of under 20 km s^{-1}, representing un-dissociated, swept-up molecular hydrogen from the ambient medium, as noted by that author. This fairly dense shell of cooling material follows the bow-shock at low velocities and constitutes a large portion of the matter due to the cylindrical geometry and being at a large distance from the jet axis. The

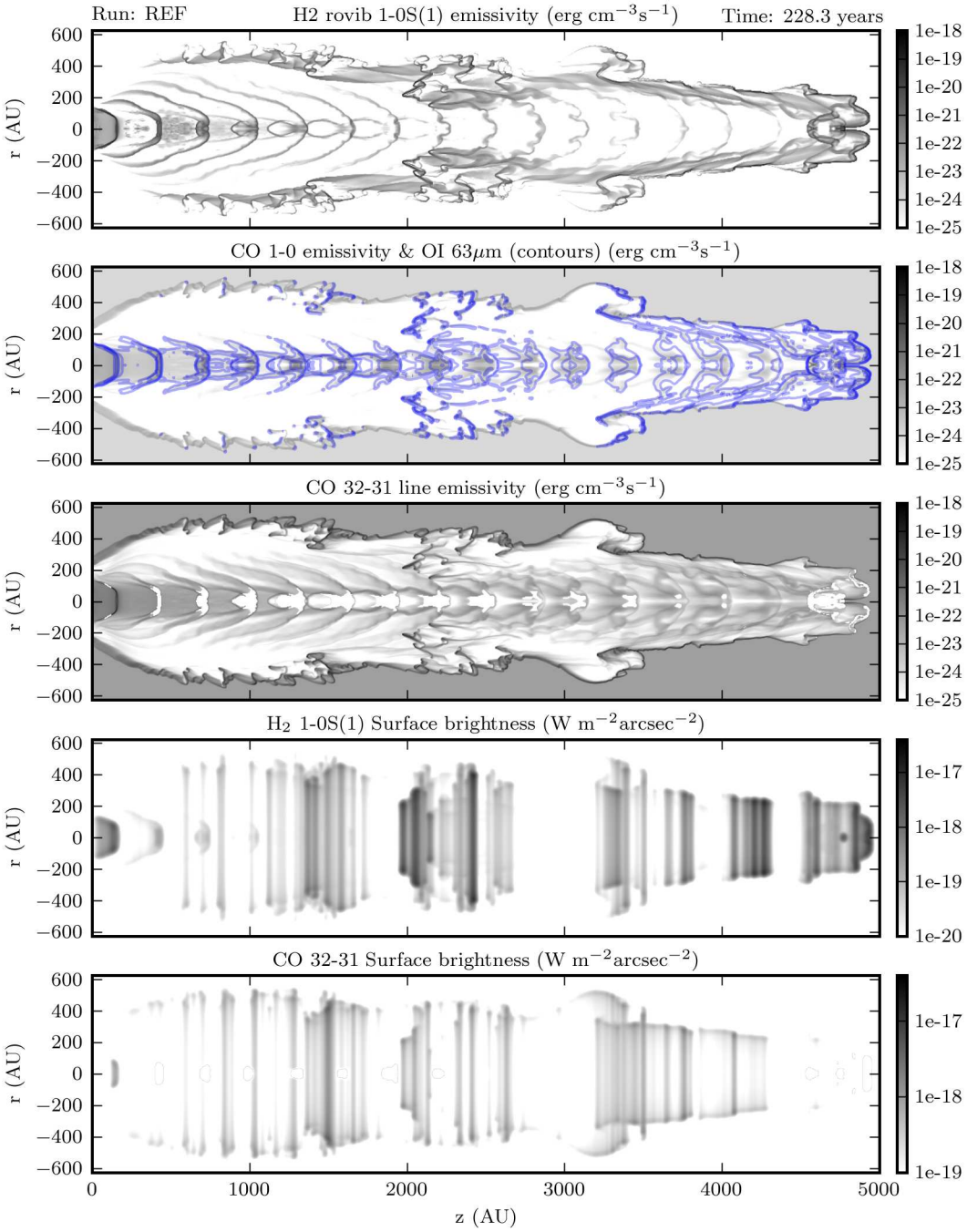

Figure 4.4: Run: REF $\eta = 10$ Our reference hydrodynamic solution, with X_{H_2}=0.1, X_e=0.01, η=10. Plotted are (top to bottom): H_2 ro-vibrational line 1-0S(1) emissivity, CO 1-0 rotational line emissivity with OI 63μm line emission in contours at emissivities of $[10^{-20}, 10^{-19}, 10^{-18}10^{-17}]$ erg cm^{-3}s^{-1}, CO 32-31 rotational line emissivity, H_2 line 1-0S(1) and CO 32-31 rotational line surface brightnesses in W m^{-2}arcsec^{-2}

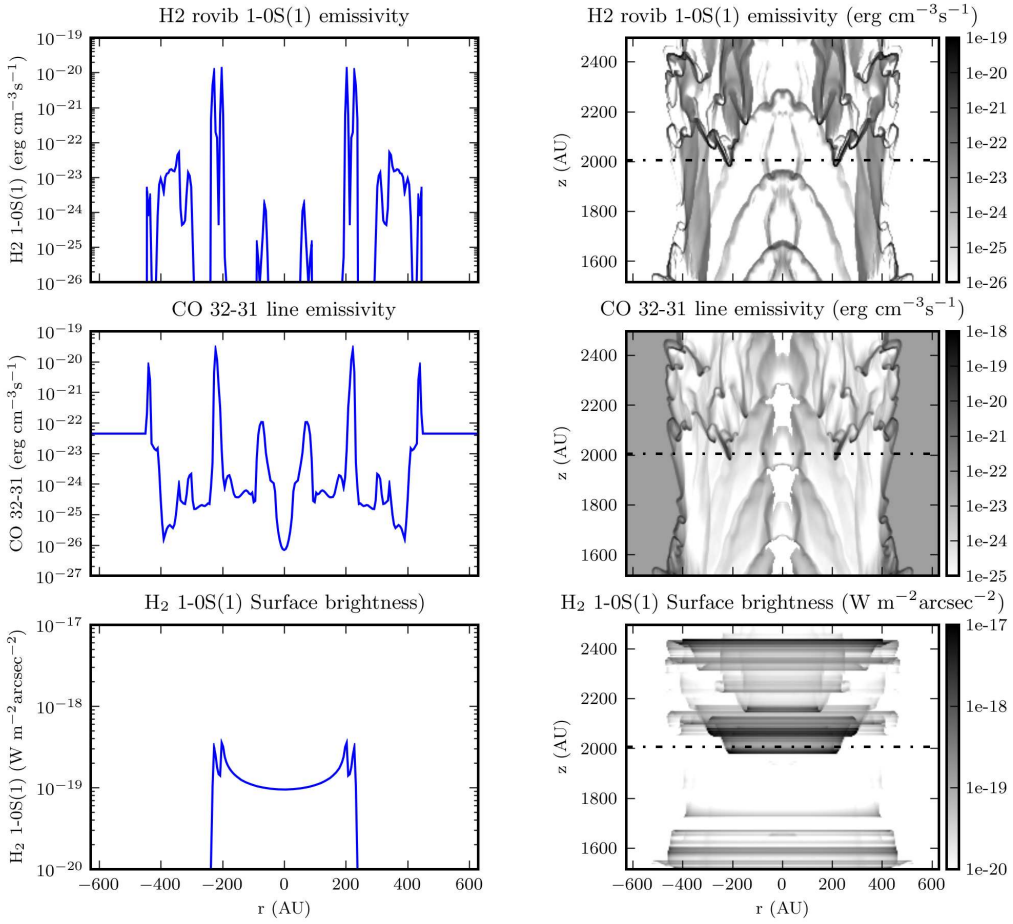

Figure 4.5: **Run: REF** $\eta = 10$ Profiles for (top to bottom): H_2 emissivity, CO 32-31 emissivity, and H_2 1-0S(1) column density.

next prominent feature is the anvil-shaped peak at high velocities. This represents the fast, dense beam matter travelling at between 92 and 150 km s^{-1}, and this range is in fact visible in the graph.

The mass-velocity diagram also yields some insight into the chemical properties of the gas. Notably, the majority of the mass at low velocities is molecular, while the high velocity matter is predominantly atomic. The turning point between molecular-dominated and atom-dominated gas is seen to be at a velocity of between 20 and 30 km s^{-1}. This follows from the turning point for shock velocities which cause a temperature rise sufficient to dissociate H_2 being around this value, as seen in section 3.1.2.1. The peak in the molecular matter at high velocities is due to ambient matter encountered near the head of the jet and accelerated, some of which survives into cooler post-shock regions.

The ionisation of the matter doesn't change hugely. From its 1% injection value (in this run) the ionisation gets to a maximum of around 10 or 12% as seen in

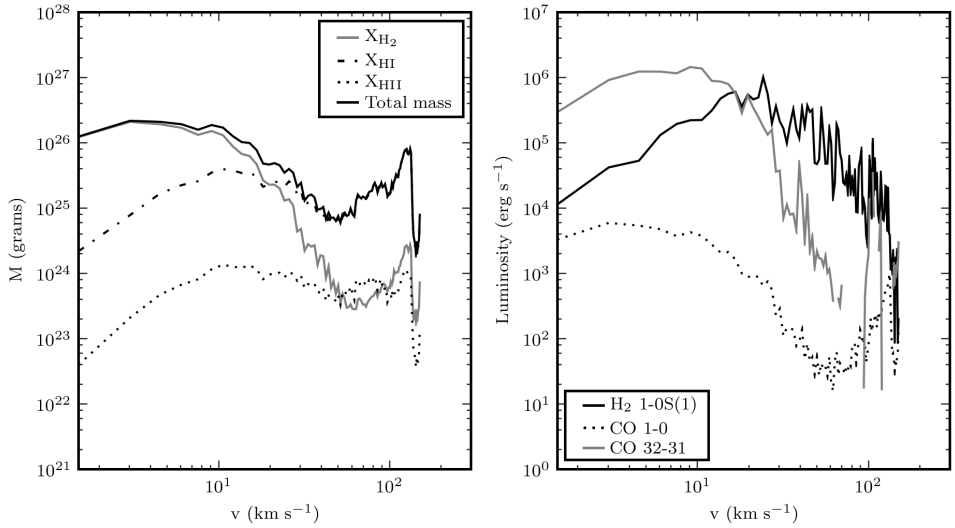

Figure 4.6: Mass-velocity and Line profiles for REF ($\eta = 10$) The left panel shows the amount of mass in the total domain as a histogram function of the velocities, while the intensities of the H_2 1-0S(1) and CO 1-0 32-31 lines are displayed in the right panel.

figure 4.2. The gentle peak in the ionisation at around 10 km s^{-1} is initially somewhat surprising. However, it seems to originate from the ionisation which occurs on the lateral flanks of the jet, for example at around 1500-2000 AU, where the internal shocks continually collide against the post bow-shock region, the temperatures are high, and the velocities low. The line-velocity profiles for both of the CO emission lines shows a sharp trough at around the dissociation point of 30 km s^{-1} reflecting the strong dependence of the equilibrium CO abundance on the molecular fraction of hydrogen. Our result for the line-velocity relation of the H_2 line, differs somewhat from the pattern, in that there is simply a definite peak around the dissociation shock velocity, with the emission gradually reducing towards higher velocities. This contrasts with the results of Downes & Cabrit (2003), who find the H_2 line profile having a similar behaviour to the other quantities with a trough and peak shape. It is unclear why this is the case, given that the mass of molecular hydrogen is in agreement. We note, however that the densities in our simulations are an order of magnitude higher, and that this, in conjunction with our neglecting projection effects, could account for the difference.

4.2 Results: Analysis of the Test Cases

In this section we present our findings on the role of density, magnetic field, molecular fraction and ionisation on the properties of interest to us, such as the extent of entrainment, survival of molecular hydrogen in the beam and the effect on the emission strength and distribution. Consigning the large amount of plots to Appendix A we refer to them from this chapter, highlight the salient points and supplement them with additional specific plots where needed.

Run	X_{H2}	X_e	► η ◄	β
ETA_A	10%	1%	5	-
REF	10%	1%	10	-
ETA_B	10%	1%	20	-
ETA_C (light)	10%	1%	10	-

Table 4.1: Summary of runs used to examine the effect of the density ratio η. The first three runs have a beam density equivalent to n = $10^4\,\mathrm{cm}^{-3}$, where n is the total number of nuclei (hydrogen and helium), while ETA_C has a jet density of $10^4\,\mathrm{cm}^{-3}$.

4.2.1 Density ratio

We next examine the effect of the density on the jet structure. Table 4.1 shows the values of η for which simulations were run. In order to vary the density contrast between the jet and the ambient medium, one has three choices; to vary the jet density; vary the ambient density; or, vary both. For most of the runs in our study we vary the *ambient* density. In our reference run, REF, the beam gas has a number density of $10^4\,\mathrm{cm}^{-3}$ (all nuclei) and the ambient medium, has a number density of $10^3\,\mathrm{cm}^{-3}$ for a density contrast $\eta = 10$.

In the table, the runs ETA_A, REF, and ETA_B can be grouped together as they are directly comparable, having identical parameters except for their η values of 5, 10 and 20 respectively. Examining these runs first in figures A.1, A.2 and A.3, perhaps the first thing to notice is the expected change in the advancement of the head of the jet. With increasing η, the jet can plough through the medium with more ease. This is reflected in the expression estimating the relation of the speed of the jet head to the speed of the jet beam (which is the same in all these runs)

$$\frac{v_h}{v_j} = \frac{\sqrt{\eta}}{1+\sqrt{\eta}} \tag{4.1}$$

with v_h the velocity of the head of the jet and v_j the beam velocity. Eq. 4.1 is derived by balancing the momentum of the jet gas and incoming ambient gas in the frame of the head of the jet.

Apart from this, however, there is a very important difference in the results from these runs, namely the changes in the H_2 plot, where we see that the entrained fingers of ambient material described in section 4.1.3 are more prominent the $\eta = 5$ case and less so in the $\eta = 20$ case. This fairly straightforward observation does suggest that the density ratio of the jet with respect to the ambient gas is responsible. However, we have increased the *absolute* density of the ambient medium, which may also be responsible. In an effort to clarify, we include another simulation ETA_C, with the same parameters as REF, except with *both* the jet and ambient densities reduced by a factor of 10. Comparing the plots of the H_2 fractions for ETA_C (fig. A.4) and REF (fig. A.2), it does indeed seem that somewhat more ambient matter enters the cocoon in the case of REF. However, on comparing both ETA_A (η=5) and ETA_C with REF, the effect of the density contrast seems more dramatic than that of the absolute density. However we would surmise that a combination of (a) a low value of η and (b) a high density ambient medium (in an absolute sense), can contribute to stronger entrainment.

The corresponding emission plots for REF and ETA_C cannot be directly compared,

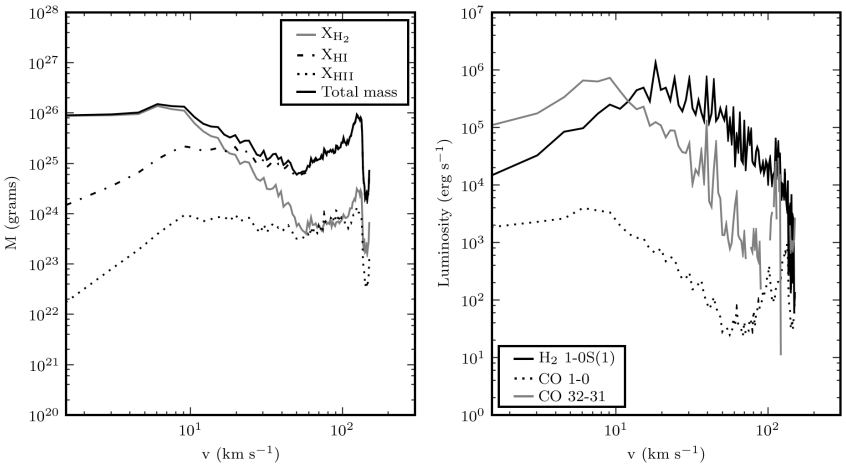

Figure 4.7: Mass-velocity and Line profiles for ETA_B ($\eta = 20$).

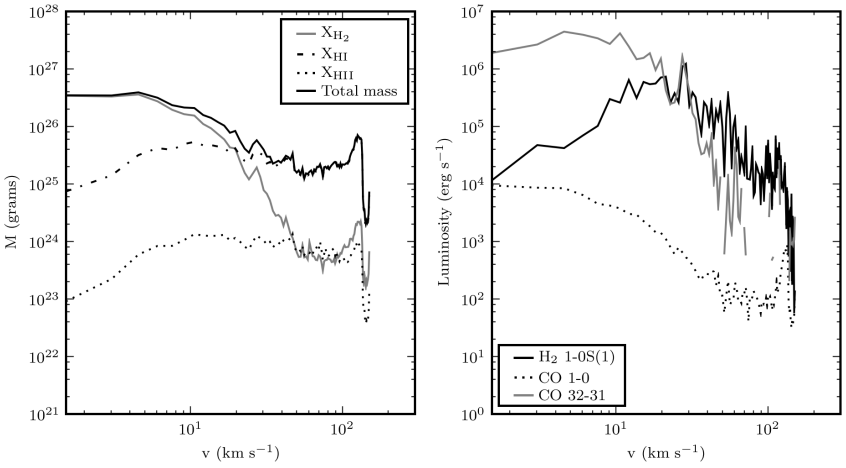

Figure 4.8: Mass-velocity and Line profiles for ETA_A ($\eta = 5$).

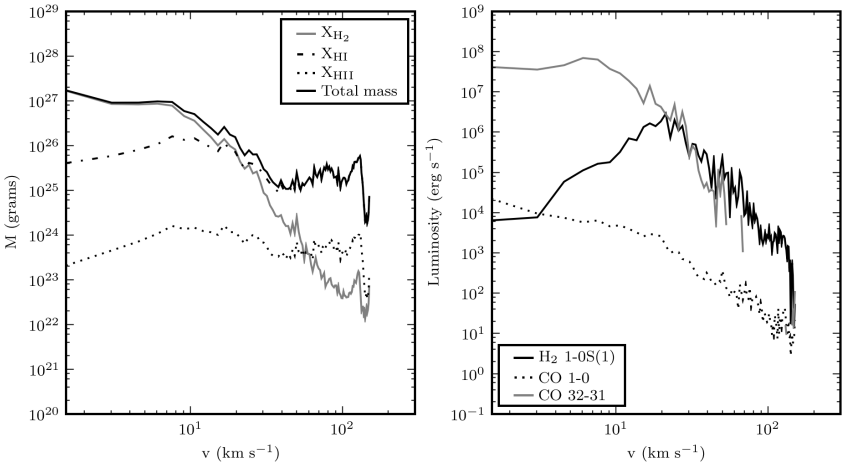

Figure 4.9: Mass-velocity and Line profiles for ETA_E ($\eta = 10$, X_{H_2}=1%)

as the lower densities in ETA_C will naturally emit less, all other parameters being equal. We do make some observations on the lighter ETA_C jet, however. In the density and pressure plots it is apparent that there is less expansion of the knots as they travel towards the head of the jet, than in the heavier jets considered, and the cocoon remains much hotter, presumably because the lower density gas has a longer cooling time. Also interesting is the dramatic increase in the amount of post-shock ionisation, which can probably be attributed to the lower densities meaning less cooling in the post-shock material, and slower cooling timescales, allowing more ionisation to take place (despite longer ionisation timescales, which should also be longer, however).
In the emission plots, the raw emissivity of the H_2 line has a different structure, due to the temperature in the cocoon, this manifests itself in the column integrated plot, where the ETA_C jet has a broader tip than the heavier REF jet. The high temperature in the ETA_C cocoon is also apparently much more hostile to CO emission than the REF jet. This could possibly be used as an observational constraint on the jet density, for example in the case of HH211 (see figure 1.7), where Gueth & Guilloteau (1999) report both high velocity CO emission in what we take to be the beam, and a low velocity component where the bow wings of our model are.
Turning again to the mass-velocity diagrams and line profiles for these simulations (figures 4.6, 4.7, 4.8 and 4.9) we see that the information from the mass velocity diagrams varies very little with changes in η in terms of the behaviour of the atomic and molecular mass. The line profiles, however, particularly for CO emission, do show a very strong dependence on the density contrast, with a much stronger slow CO component for jets with a lower value of η. We note that the run ETA_E in figure 4.9 does have a lower initial value of the molecular fraction in the beam. However this difference should not affect the result for the low velocity component too much, as that lack of molecular material from the initial condition should affect only the high velocity component. We can therefore say that the observation of a stronger low velocity component for lower values of η holds.

4.2.2 Ionisation of the Jet Beam

Run	X_{H2}	► X_e ◄	η	β
ION_A	10%	0.1%	10	-
REF	10%	1%	10	-
ION_B	10%	3%	10	-
ION_C	10%	10%	10	-

Table 4.2: Summary of simulations with varying Ionisation X_e in the beam

Having seen the effect of the relative densities of the jet and ambient medium on the entrainment and emission, we now turn to the chemical properties of the jet matter to see what dependencies exist of the jet morphology and observables on the chemical composition arise. In this section we investigate the role of the ionisation in determining the evolution of the jet. Table 4.2 shows the runs used to see the effect of varying the ionisation fraction, from X_e=10^{-3} to X_e=10^{-1}, while again maintaining all other parameters unchanged. Examining the morphology of the runs in the density plots of figures A.9, A.10, A.11 and A.12 it is evident that there is a significant direct relation between the ionisation fraction and the rate of progression of the jet head -

as the ionisation is increased, the distance traversed in the given time is larger - by some 15% over the range of ionisations covered. The head of the jet is also steadily taking a narrower shape during this progression, coincident with a tendency of the knots to expand less as they travel down the jet beam.
The reason for these observed differences becomes evident when we look at the plots of the H_2 fraction, where it is seen that as the ionisation is increased, the amount of molecular matter remaining in the beam also increases. This is attributable to the fact that the higher the ionisation, the more electrons are available for atomic recombination cooling in the knots of the jet beam, as calculated by our term in equation 2.22. Figures 4.10 and 4.11 illustrate the change in value of cooling term. This extra cooling then reduces the amount of H_2 which will be dissociated, making it also available for cooling. The stronger cooling in the beam reduces the pressure in the knots without them having to expand towards pressure equilibrium.

Looking at the plots of the ionisation, one can see that in the cases with strong ionisation in the injected beam gas, recombination occurs along the beam as it cools down. Therefore we can say that the cooling responsible for the knots remaining compact, and the head consequently also, is the molecular cooling. The reduced expansion of the knots and head of the jet, can then readily explain the increase in the rate of propagation of the jet head, by decreasing the surface area in contact with the ambient medium. This gives a causal progression from the initial chemical composition, to its effect on the pressure, to the observed feature.
As mentioned, in the runs with a highly ionised jet inflow (REF, ION_B, and ION_C), the ionisation decreases, implying that the initial ionisation is somehow out of equilibrium. This is not surprising as, without concrete knowledge of the ionisation fraction, we have imposed the values ad hoc. In the knots, which are dense, this recombination occurs quickly, while outside the beam, the process of recombination is much slower due to the lower densities, and the ionisation remains fairly high for the duration of the simulation.
However, in the low ionisation case ION_A, we see *ionisation* occurring in the knots, as the high temperatures and densities cause collisional ionisation of atomic hydrogen. This gives us then some idea of what levels of ionisation should be existing on the scale of the propagating jet, whatevever was happening in the launching region. Looking at figure 4.12, we can see the ionisation in the cases with 1%, 3% and 10% decreasing along the jet (until the Mach disk where it spikes again) while in the case with 0.1% it increases. One can estimate from this graph that the ionisation appropriate for this particular flow is in the region of 0.2-0.3%. Again, this is for the particular parameters chosen, for a higher velocity, different pulsation frequency, or higher H_2 fraction we could expect a different value of the ionisation. Surprisingly, we do not observe a large increase in the atomic emissions apart from the radiative recombination, and the strength of the OI line remains essentially unchanged with ionisation. The emissions (figures A.13, A.14, A.15 and A.16) for the runs with varying ionisation thus show more the results of the indirect effects of the ionisation on the H_2 fraction and the morphology of the jet.

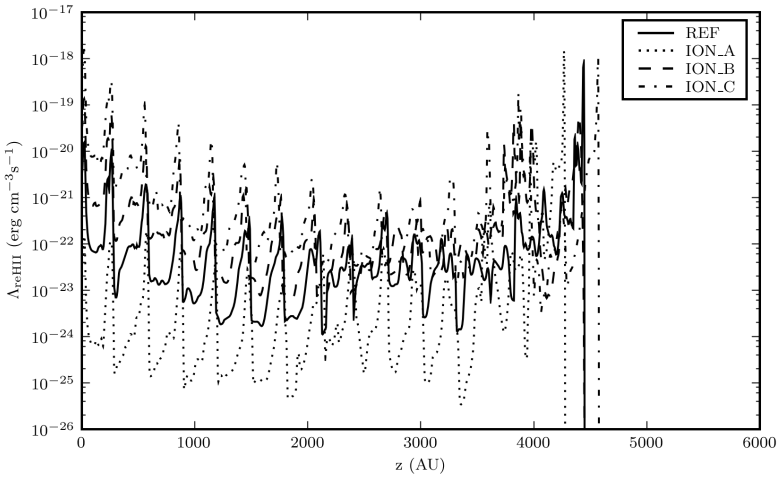

Figure 4.10: Radiative recombination cooling along the jet beam for the different values of the ionisation fraction in our runs.

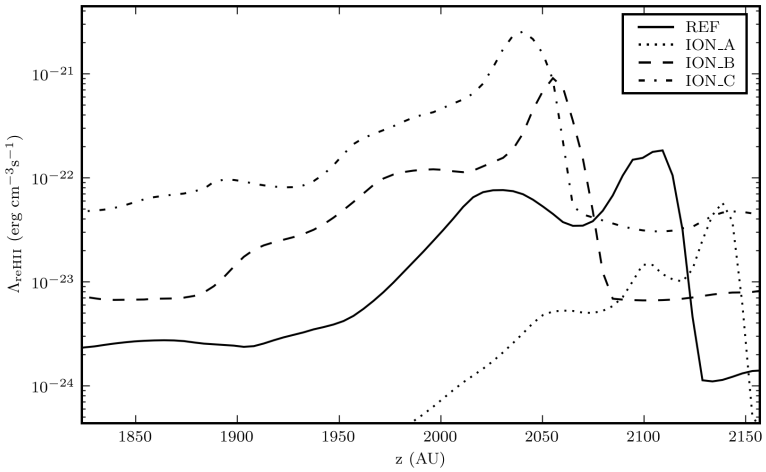

Figure 4.11: Close-up view of radiative recombination cooling in the jet beam for the different values of the ionisation fraction.

Run	► X_{H2} ◄	X_e	η	β
MOL_A	1%	1%	10	-
MOL_B	5%	1%	10	-
REF	10%	1%	10	-
MOL_C	33%	1%	10	-
MOL_D	50%	0.001%	10	-

Table 4.3: Summary of runs varying the molecular fraction $\mathbf{X}_{H2}$ in the beam

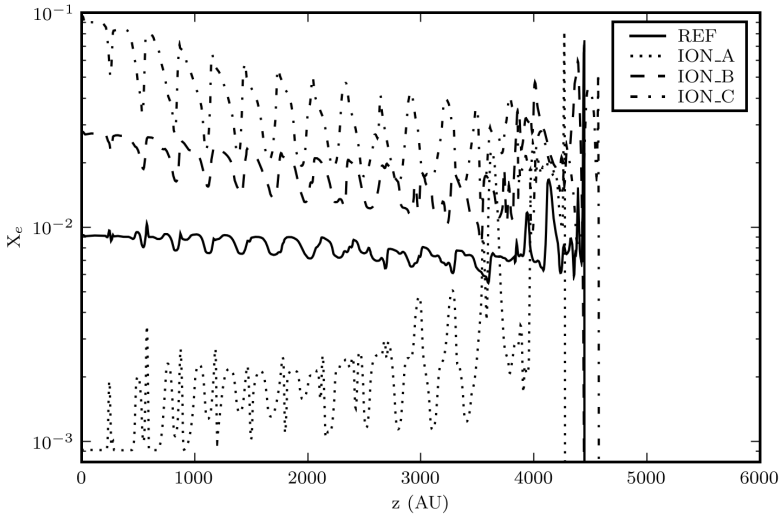

Figure 4.12: Ionisation fraction along the beam for different ionisation fraction. Runs with an ionisation which is too high for the prescribed temperature tend to recombine, while ION_A appears to be initially under-ionised

4.2.3 H_2 content of the Jet Beam

Another factor in our astrophysical scenario which it is difficult to constrain is the fraction of molecular material in the gas. What is clear is that molecular material is observed in the jet itself at the beginning stages of Class 0 jet outflows, as evidenced in the HH46/47 counterjet (figure 1.3), and dramatically in the HH212 jet (figure 1.1). From the observations it seems that the beam matter is usually visible in the infrared close to the source, but further away from the source the emission appears to come instead from entrained matter. As mentioned in section 1.4.2, there are indications that significant amounts of H_2 survive the accretion and ejection process, although this is based on steady flow models. We therefore use our simulations to examine the properties of jets with varying fractions of H_2 in the flow. Table 4.2.3 lists the runs with different values of the H_2 fraction, where all except for MOL_E were initialised with a jet beam having an ionisation of 1% as in REF. MOL_E was given a lower ionisation in order to model a neutral molecular outflow.

Again examining the morphology first (figures A.17, A.19, A.18, A.20 and A.21), we see from the density plots a similar progression in the features as seen previously with increasing ionisation, this time from directly increasing the molecular coolant, rather than indirectly preserving it via recombination cooling. Now, as the range of H_2 considered is rather large, we see a correspondingly large degree of change in the structure of the jet. Particularly evident, as we go from 10% to 33% H_2, is the change seen in the form of the knots, which instead of expanding, collapse to form dense bullet-type structures. The jet is also seen, after an initial period of expansion, to emerge as much a narrower outflow, with a cold ballistic head ploughing through the ambient medium. Looking at the chemical properties, as the H_2 fraction of the injected gas is decreased, we see a higher amount of dissociation in the beam, with essentially all of the H_2 in MOL_A being dissociated by the time the beam gas

reaches the Mach disk. This is again because of the amount of the molecular material available for cooling, so that there is a sort of non-linear dependence here, with the amount of H_2 surviving in the beam being dependent on the initial amount present in the initial inflow.
The most striking effects of increasing the amount of molecular material are seen in the emission plots (figures A.22, A.23, A.24, A.25 and A.26), as we move from the low molecular abundances in MOL_A, MOL_B and REF, to the runs with a high molecular fraction. In the highly molecular case, the H_2 emission becomes more intermittent and narrow, reflecting the narrower morphology of the jet. Also, as in the other simulations discussed up to now, the emission originates predominantly from the head of the jet and at the points where ambient matter interacts with the jet cocoon. It is only at the beginning of the flow (the first 1000 AU or so that the H_2 knots are visible, thereafter they disappear as the beam gas cools. In the CO emission, however, the knots stay visible in the cases with a high molecular fraction in the beam, travelling along the beam and gradually catching up with the head of the jet. The other emission from the interactions of the ambient matter with the internal working surfaces remains longitudinally almost stationary, only moving outwards from the axis gradually as the cocoon slowly expands.
Looking again to the mass-velocity and line-profile plots, we compare the low molecular fraction case REF (fig. 4.13) with the high molecular fraction case MOL_D (fig. 4.14). Immediately apparent in the mass-velocity relation is the much lower slope of the decrease in the H_2 fraction in MOL_D, where the cooling in the knots is allowing more H_2 to survive there. In the line-profiles, a similar decrease in the slope of the CO 32-31 line occurs, and our observation of the CO bullets is reflected in the high velocity peak in this emission.

4.2.4 Magnetic Field strength

Run	X_{H2}	X_e	η	$\blacktriangleright \beta \blacktriangleleft$	$B_\parallel$ (μG)
REF	10%	1%	10	∞	0
BETA_A	10%	1%	10	22.6	30
BETA_B	10%	1%	10	5.6	60
BETA_C	10%	1%	10	1.4	118
BETA_D	10%	1%	20	∞	0
BETA_E	10%	1%	20	2.8	83

Table 4.4: Summary of runs varying the strength of the magnetic field with β defined as the ratio of the magnetic pressure with respect to the thermal pressure in the beam.

We now examine the effect of a moderate poloidal magnetic field on the properties of the jet-driven outflow. The poloidal field will be transverse to the lateral bow-shock, and so is expected to experience compression with the shocking of the gas. Taking as a starting point the hydrodynamic control run REF, we investigate the effect of successively stronger magnetic fields, ranging from 30 μG to just under 120 μG as listed in table A.4. As the magnetic β parameter is dependent on the square of the magnetic field strength, this represents a broad range in the extent of the physical effect we expect to see.
First we compare the state variables from the pure hydrodynamic run REF (fig. A.27)

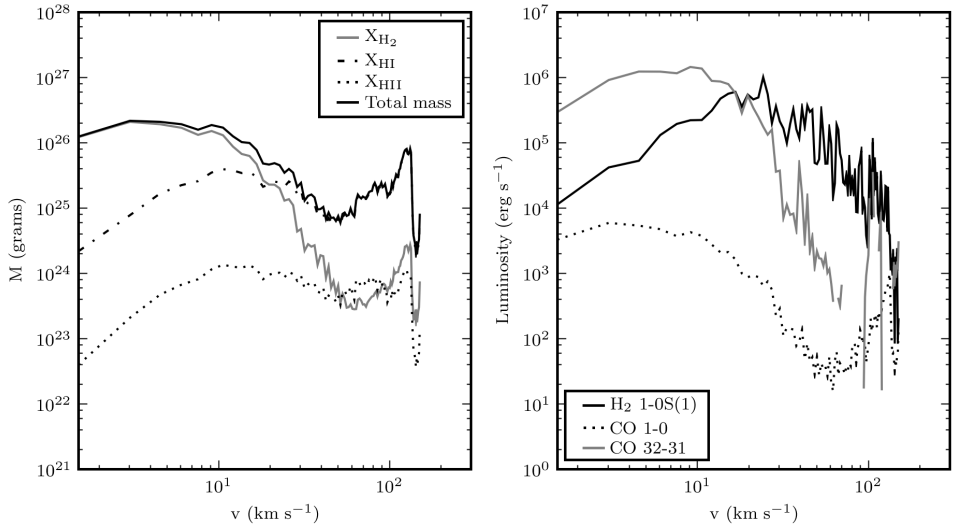

Figure 4.13: Mass-velocity and Line profiles for REF. The CO intensity is marked by a predominantly low velocity component.

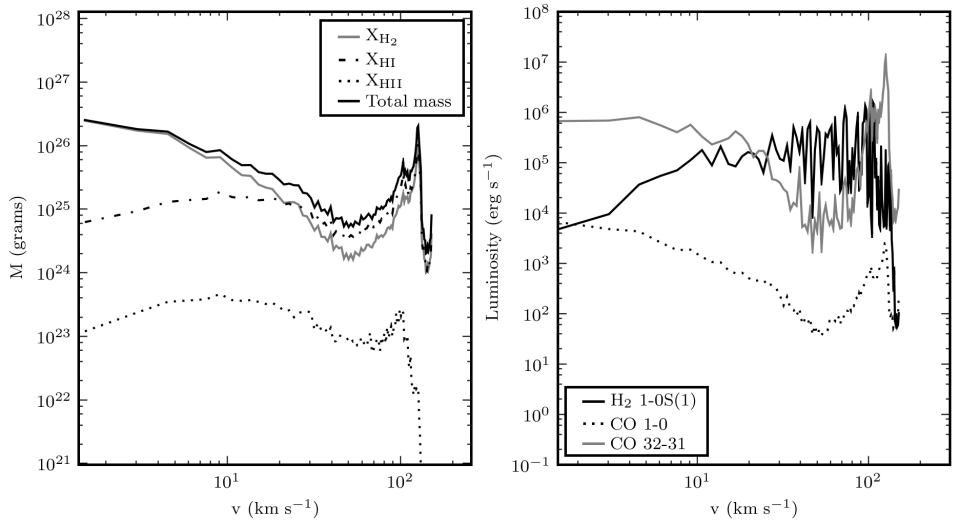

Figure 4.14: Mass-velocity and Line profiles for MOL_D. Apart from the less extreme reduction in the molecular mass at velocities above 20-30 km s^{-1}, an extremely high contribution to the CO intensity, due to the molecular bullets, is seen at the beam velocity.

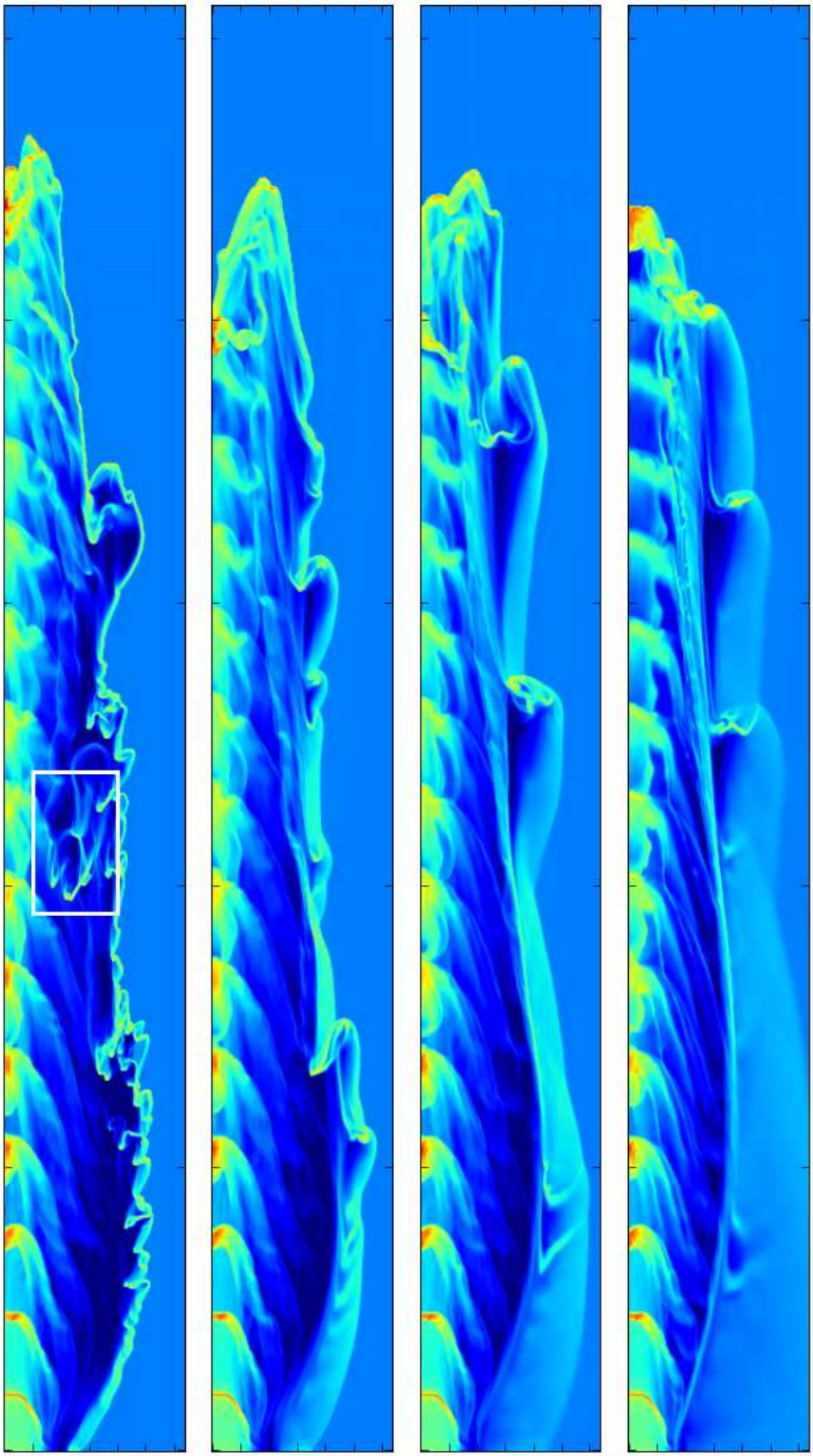

Figure 4.15: Comparison of densities for different β. From left to right: REF ($\beta = \infty$), BETA_A ($\beta = 22.6$), BETA_B ($\beta = 5.6$), BETA_C ($\beta = 1.4$). The white box shows pieces of the cooled bow-shock layer, disrupted by instabilities and drifting inside the cocoon. These are then ablated by the internal working surfaces.

with those of BETA_A (fig. A.28) which has a magnetic β parameter of 22.6 with respect to the beam pressure of the jet. Even with this relatively moderate magnetic field, the impact on the structure of the jet is quite strong. The magnetic field stabilises the bow-shock, and much fewer instances of cooling instability occur, as seen in the density plot.
The entrainment as traced by the molecular fraction, seen at the middle part of REF, is mostly absent in the MHD case. Also visible in the MHD case is a definite thickening of the cooling region behind the weak lateral bow-shocks, whereas these are completely collapsed in the hydrodynamic case. There are also noticeable differences in the column-integrated H_2 emissions (figures A.37 and A.38). The emission in the magnetohydrodynamic case is much more intermittent and "smoother" than the hydro case, apparently due to the fewer interactions between the ambient gas and the cocoon gas at instabilities in the bow. Also apparent is the reduction in the CO 32-31 emission, which seems coincident with the broadening of the thin cooling layer at the bow-shock.
Looking to the next MHD simulation, BETA_B (fig. A.29), with a stronger magnetic field ($\beta = 5.6$) we see a continuation of the trend; less instability in the bow-shock, a further broadening of the lateral bow-shock, and the cocoon almost completely sealed off from ambient matter. What is also becoming apparent, looking at the temperature plot, and the H_2 emissivity (fig. A.39) plots, is the transformation of the inner surface of the cocoon from a rough, distributed area being heated by the internal working surfaces, to a thinner, smoother high temperature layer between the cavity and the lateral shock area. The column integrated emission shows a more uniform region of emission along the jet as a consequence of this stable, hot region. The CO 32-31 emission is further attenuated, in correlation with the further expanded outer bow-shock. Also evident is the narrowing of the cocoon itself with increasing field strength, as the magnetic pressure balances the cocoon pressure.
This is continued in the most strongly magnetic simulation, BETA_C with $\beta = 1.4$ (figures A.30 and A.40) where the emissions have a completely different character to the hydrodynamic case. The smooth, extended emission from the inner surface of the cocoon is present, though somewhat weaker than in the less strongly magnetic BETA_B. The emission at the head of the jet is broad and extended, and a little bit away from the head of the jet there is a simple clean arc-like shock, unlike the more common situation in these simulations where we generally see emission from more complicated interactions between matter at the head of the jet or, as discussed previously, between the internal working surfaces of the knots and the interface between the jet cavity and the ambient matter. This is what is referred to as "prompt entrainment" - ambient matter is shocked, accelerated and moves with the jet. Looking at the H_2 plot one can see that at the fast leading shocks the molecular matter gets dissociated, while further back where the shock hits the ambient matter obliquely, the degree of dissociation gets lower. Another interesting feature in the emissions as one progressively increases the magnetic field is the change in the atomic line emission, which for the strongly magnetic case BETA_C neatly traces the edge of the inner cavity. However, this observation is of limited use given that Class O sources are generally not visible in optical lines.
Figure 4.15 illustrates very simply the morphological changes described above. In order to see how the magnetic field causes such an effect on the morphological and

emission properties of the jet, figure 4.17 shows the magnetic variables. Here the magnitude of the magnetic field |B| shows the reason for the broadening of the bow-shock, with the ambient field, mostly transverse to the shock, being compressed significantly. The plot of β shows low values in this region, showing that the magnetic pressure is dominating there. The plots of the Mach numbers show that the jet is almost completely supersonic, but is sub-Alfvenic in the bow region. For further detail we examine the profiles in figure 4.16. The extent of the effect of the magnetic field is apparent in the reduction in density in the initial bow-shock density compared to the REF case as the field strength is increased. The gas in the outer bow-shock in BETA_C for example, is almost an order of magnitude less dense than that in REF, and this reduction in density can account for the reduced CO emission in this area. Again this is due to the magnetic pressure, compensating for the pressure lost in the cooling, as evidenced by the trend in the β, which is reduced in this bow-shock for increasing magnetic field. In BETA_D and BETA_E (figures A.31 and A.32) we again see the effect of the introduction of a magnetic field, this time for $\eta = 20$. The combination of a high η value and strong magnetic field result in an interesting morphology. The typical unstable bow-shock of the hydrodynamic case is more or less usual, but the magnetised jet shows, apart from the normal damping of the bow-shock instabilities, a parabolic J-shock tip visible in the H_2 line, illustrating the variety of morphologies that can be produced by the jet-driven shock scenario with the adjustment of the key parameters.

4.3 Discussion

In this chapter, we presented the results of our investigation into the properties of molecular outflows as described by a pulsed jet-driven outflow model. We summarise our conclusions on the role of the density, ionisation fraction, molecular fraction and magnetic field in determining these properties.

The density contrast parameter, η, between the jet and its ambient medium is seen to have an important effect on the occurrance and amount of **entrainment** of the ambient medium. For a less overdense jet, the interface between the ambient medium and the jet cocoon is less stable and allows molecular material to enter the jet, whereupon it (in our model) is encountered by the internal working surfaces of the pulsed inflow condition, and ablated. We have seen that the shock heating arising from such interactions can produce H_2 ro-vibrational emissions of similar magnitudes to those observed in Class 0 sources such as HH211 (McCaughrean *et al.*, 1994). The largely un-dissociative lateral bow-shocks, while being too cool to excite H_2 emission, are sufficiently warm and dense to show significant amounts of CO line emissions, matching observations of low velocity CO outflows tracing what may be the bow of a jet-driven outflow in observations such as those of Gueth & Guilloteau (1999). We also see a very simple and direct correlation between a reduced density contrast and an increase in the intensity of this low velocity component of molecular CO emission.

We have seen that the key effect of varying levels of ionisation in the beam is in its effect on the molecular fraction. For the parameters we used here, a stable value for the ionisation fraction appears to occur at 2-5$\times 10^{-3}$, and if the jet is initialised with a higher or lower ionisation fraction, the gas tends to recombine (and "protect"

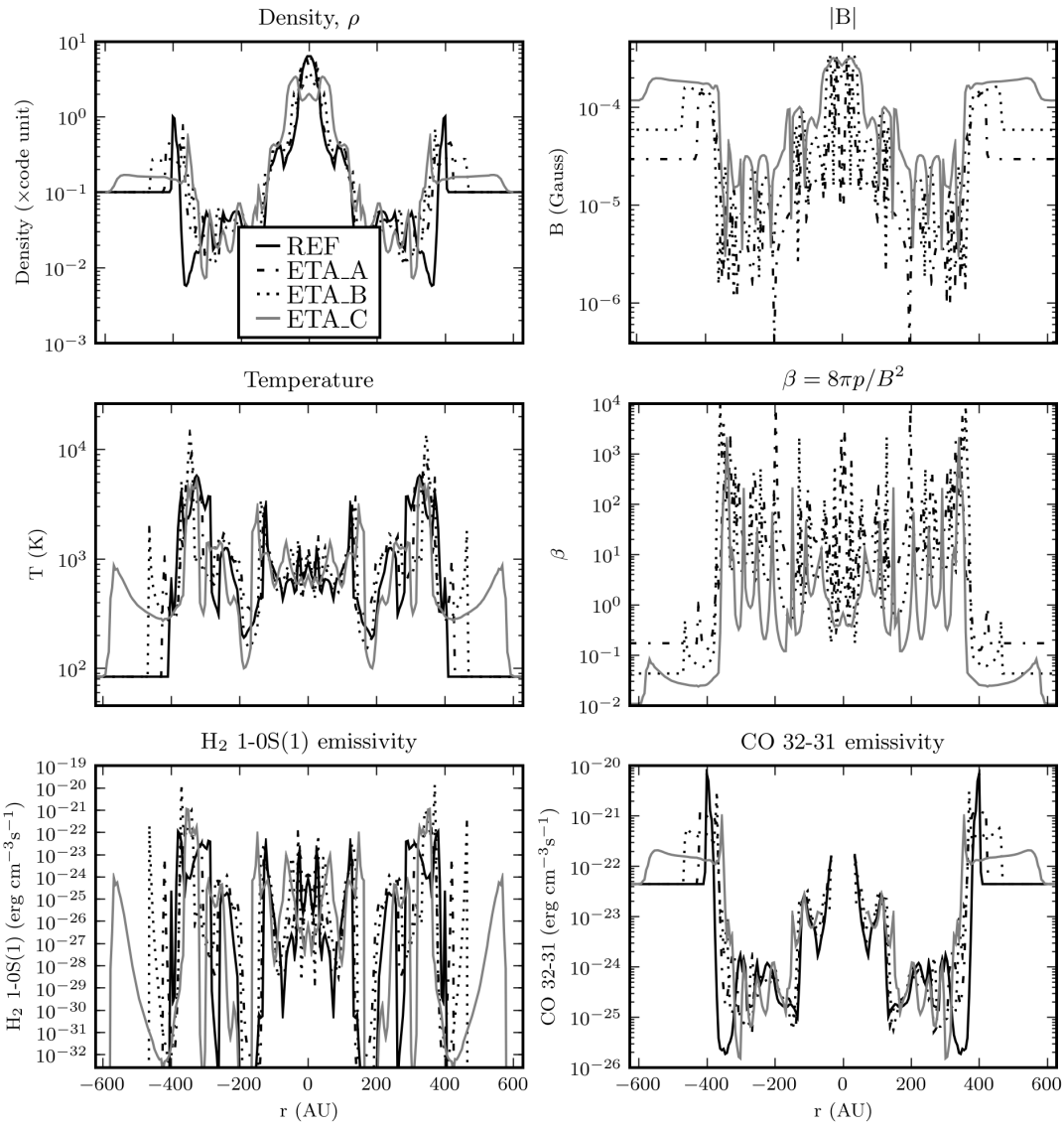

Figure 4.16: Profiles across the jet for different values of β. The profile is taken at a position of 1600 AU.

the H_2 fraction through the cooling loss incurred) or get ionised respectively to move towards this fraction. This may help constrain the ionisations in Class 0 jets.

Examining the effect of the molecular fraction on the jet, it is apparent that the strong cooling action of the molecular material leads to a more collimated jet. After an initial period of pressure expansion, heavily molecular jets are seen to develop a narrow ballistic head, and propagate somewhat faster than less molecular jets. Interestingly, highly molecular jets, consisting of one third or more of molecular material, exhibit in mass-velocity diagrams a much increased high velocity component in both molecular material and emission intensity. This is also seen in emission maps, where in addition to the emission from the interacting environment and cocoon matter, we see knots in the CO 32-31 line (they appear similarly in the CO 2-1 line) moving along the beam at roughly the jet velocity, while the emission from the lateral bows moves outwards from the axis extremely slowly. As we have seen, knots that emit

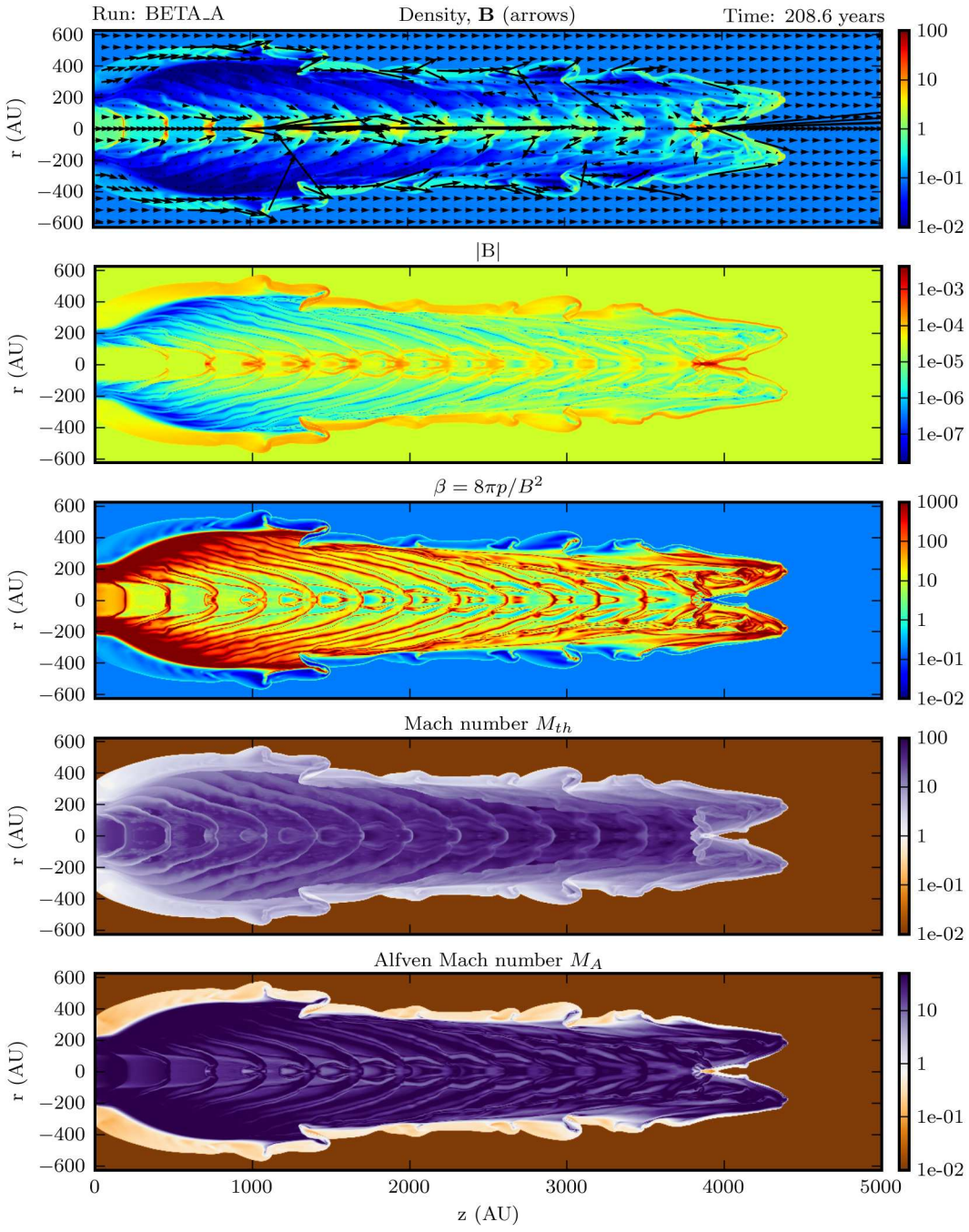

Figure 4.17: Magnetic variables for BETA_A, $\beta = 22.6$**.** Plotted are, from top to bottom: Mass density with magnetic field lines, magnetic field modulus, magnetic beta, local sonic and Alfven Mach numbers.

strongly for an appreciable distance along the jet are somewhat rare in the simulations presented here, and these CO "bullets" appear to be the only ones predicted by our model, occurring only for these high molecular fractions.

The presence of even a moderate magnetic field (in the poloidal direction) can strongly affect the physics. For the weakest case we considered, with a field strength of $30\,\mu$G, the entrainment of matter through cooling instabilities in the bow shock is almost completely suppressed. Stronger magnetic fields, of over $100\,\mu$G completely alter the appearance of the jet, by inflating the bow-shock through the action of the increased magnetic pressure in the compressed shocked matter. One of the main observationally relevant differences seen in the cases with the magnetic field is its suppression of the CO emission in these bow-shocks, due to the consequently reduced density. Although the magnetic field appears to prevent the emission of H_2 ro-vibrational lines through the mechanism of entrainment and ablation seen in the pure hydrodynamic case, observationally detectable H_2 emission is nevertheless still predicted by these simulations. The magnetic field, as we have seen, appears to favour the "prompt entrainment" mechanism for causing this emission, whereby the ambient matter is directly shocked and accelerated at the bow.

Finally, we return to our "classification" for the observed appearance of molecular outflows introduced in section 1.3.1 to see if we can hazard some statements based on our conclusions in this chapter which might help the overall picture on these infrared outflows, and on the other hand, if the overall picture can help us to unify what may seem like disparate observations. Three main categories for the observed morphologies were identified; the "arrow-shaped" objects like HH212, the clumpy, more irregular HH211-like objects, and the unique shell-type object HH46/47. From a qualitative point of view, the run most resembling the first arrow type must be BETA_E (figure A.42). The subject of the density contrast needs further investigation. However, from our investigation of the effect of the magnetic field, it seems almost certain that for this type of morphology and emission pattern, a moderate magnetic field must be playing a role. Purely hydrodynamic jets simply do not remain stable in such a manner. Similarly for the structure of our "shell-type" objects, although in this case our parameters in the MHD runs do not result in any kind of match. Possibly the single-fluid approximation is not sufficient, but further runs, for example with *low* η and a magnetic field would need to be tried in order to eliminate it as a model. The third category, the "clumpy" jets do not rule out a hydrodynamic, or at least weakly magnetic scenario. In fact the jet-driven outflow model is really beginning to look convincing in reproducing the emission from HH211 (figure. 1.7), with its intermittent H_2 emission, ovoid shaped low-velocity CO outflow and beam-shaped high-velocity CO emissions (Gueth & Guilloteau, 1999). Pertaining to the parameters in our study, then in particular we can say that for this type of jet, a high-β, high molecular fraction jet-driven outflow seems to match the observations.

5

Conclusion & Future Directions

Class 0 and Class I protostellar jets, being a proximate and visible part of the early stages of star formation, provide a valuable means to observe and constrain certain aspects of an important but hidden process. By comparing our simulations to observed Class 0&I sources, we are able to eliminate particular parameter setups, and propose alternative ones. That is what we have endeavoured to do during this thesis.

This body of work consists of three main items;

- the development and refinement of a molecular chemistry and cooling module for the PLUTO astrophysical code and its validation using a variety of tests. This module is computationally light enough to allow its use in large scale simulations, while still reproducing the chemistry quite well when compared with more sophisticated models.

- the gathering of a portfolio of test problems with which to validate the code, carry out parameter studies, and supplement the main simulation results with more detailed examination of particular sections of the flow in isolation.

- the results and analysis of large scale simulations putting this code to use in the modelling of protostellar jets with molecular chemistry and cooling.

Our results demonstrate the effect of four crucial parameters on the gas chemistry, cooling and ultimately line emission from molecules. The effect of the magnetic field, density contrast, ionisation fraction and molecular fraction on the jet physics and consequently the molecular emission, have been shown. J-shocks from jet driven outflows do appear capable of supporting emission in lines from shocked molecular material, and given the variation we have seen in the morphologies by simply varying a few parameters, it seems that the jet-driven model has quite a lot of leeway for explaining the different classes of emission we identified in section 1.3.1. We qualify this by acknowledging the lack of C-shock and magnetic precursor modelling ability with our approach, and that there is still contention between J-shocks and C-shocks

for explaining the emissions. The results of our investigations can be distilled into a few distinct points:

- A high-beta scenario supports an entrainment emission regime in outflows, where instabilities in the cooled layer of the bow shock may cause chunks of cool, dense, undissociated molecular material to drift inside the cocoon of the jet. This occurs for η values of 10, and may be more prevalent for lower values of η.
- Conversely, a low-beta scenario favours shock emission, or the so-called "prompt entrainment" regime.
- A low value of η increases the proportion of the low-velocity component of the CO emission.
- A high molecular content in Class 0 jets causes the jet-driven model to fit well with observations which indicate CO outflows tracing H_2 emission, with a high-velocity collimated component and broader low-velocity component.

The prospects for future work in this field are prodigious for two main reasons. Firstly, there is a huge range of microphysical processes waiting to be addressed in large-scale numerical simulations, particularly in the area of dust modelling, which would enable us to use the excellent SiO observations (see e.g. (Lee *et al.*, 2008)) as a further constraint. Secondly, the continuing increase in readily available computer resources, steadily makes the implementation of more of these processes feasible. Once of the most immediate additions which would be readily made with this work would be to combine the molecular cooling module with a simple atomic cooling algorithm. As the ionisation of hydrogen is already calculated within the chemical network, it is ideally suited for merging with an atomic cooling function/algorithm which accounts for the first ionisation state of the included species, such as the simple non-equilibrium (SNEq) module available with the PLUTO code. As evident in (Gålfalk, 2007), in some sources, H_2 emission knots from dissociative shocks lie well within the optical region of the bow-shock. This simple observation illustrates perfectly the need for combined atomic and molecular microphysics in simulation codes.

We have experimented with FeII lines by using the expressions from the Raymond cooling module in the PLUTO code, but found the emissivities to be extremely low, perhaps because of some error. Iron lines would be of tremendous use, as they emit in similar wavelengths to the H_2 ro-vibrational lines and can escape the core gas.

For this work, the effects of rotation were not considered, in order not to encumber the study with more complicated effects. However, having thoroughly investigated the fully 2-dimensional case, enough data has now been gathered that we could reliably distinguish rotational effects from the effects of the parameters investigated in this work. In particular, rotation is expected to lead to a decrease in the poloidal component of the field over time. However, a toroidal component of the field would still be transverse to the lateral shocks of the jet, so it would be interesting to see if similar effects to the ones seen in our simulations would occur.

Although the jet-shock model has been all but discarded as a possible mechanism for the wide angle outflows such as that near the source of HH46/47 (fig 1.3), our finding in the strongly magnetic case of broadened bow-shock wings does provoke some curiosity. To investigate, one could use a similar setup to our simulations

here, but modifying the domain to focus on the base region and vary the relevant parameters |B| and ρ_{ambient} (allowing the jet to propagate off the domain). Some experimentation with the jet inflow conditions, for example the opening angle and velocity, pulsation frequency, could increase the heating of a dense ambient medium and lead to emission.

A

Appendix A. Simulation Data

This Appendix contains the plots of the state variables and the emissions for each of the runs carried out in the study.

A.1 Density

The following pages contain the plots for the simulation runs listed in Table A.1. They are ordered on the following pages first according to plot type (state variables, emissions) and then according to their order within Table A.1.

Run	X_{H2}	X_e	$\blacktriangleright \eta \blacktriangleleft$	β
ETA_A	10%	1%	5	-
REF	10%	1%	10	-
ETA_B	10%	1%	20	-
ETA_C (light)	10%	1%	10	-

Table A.1: Summary of runs used to examine the effect of the density ratio η. The first three runs have a beam density equivalent to n = $10^4\,\mathrm{cm}^{-3}$, where n is the total number of nuclei (hydrogen and helium), while ETA_C has a jet density of $10^4\,\mathrm{cm}^{-3}$.

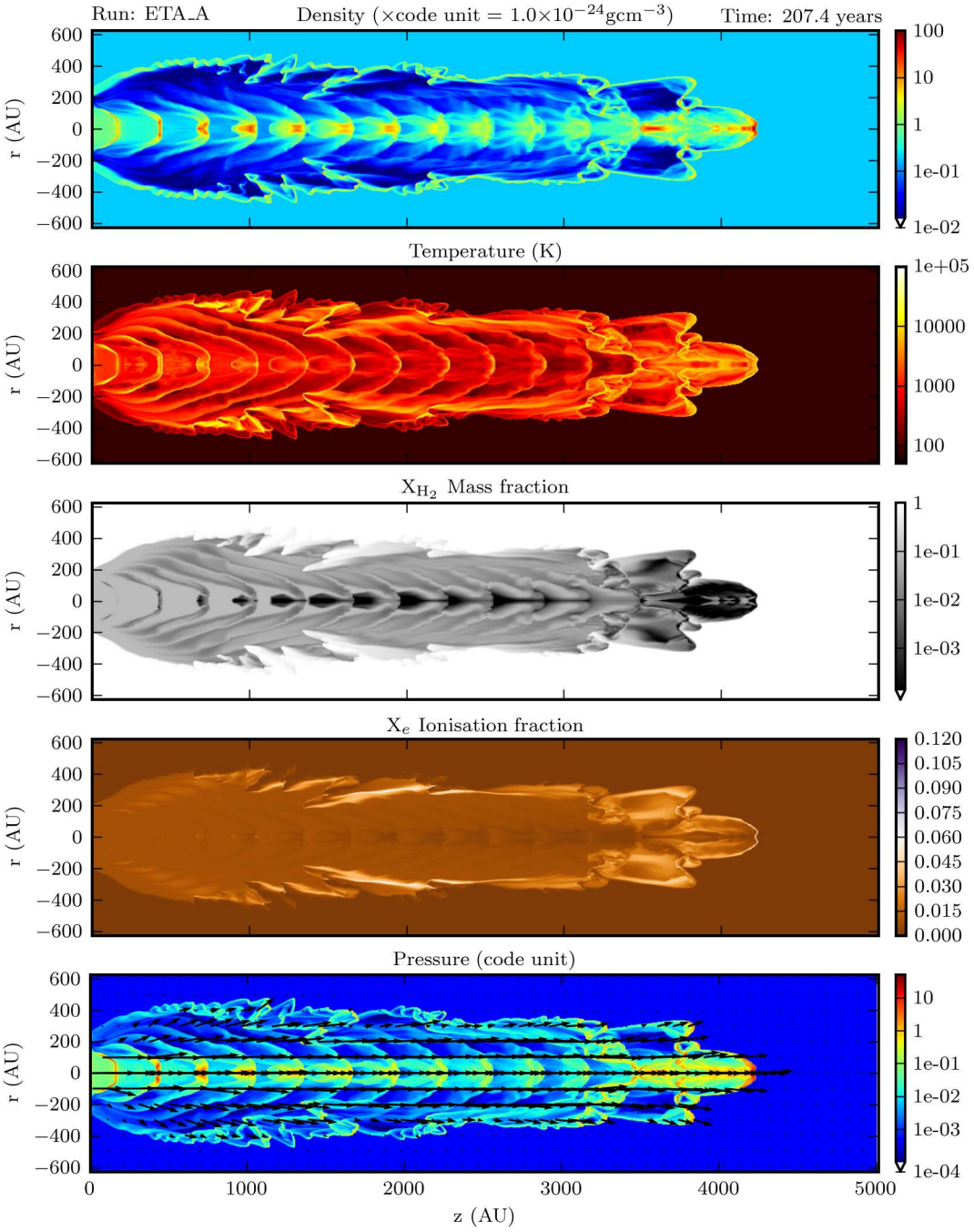

Figure A.1: Run: ETA_A $\eta = 5$ Plotted are (top to bottom): density ρ, Temperature, X_{H_2}, X_e and pressure, with velocity vectors normalised to highest velocity.

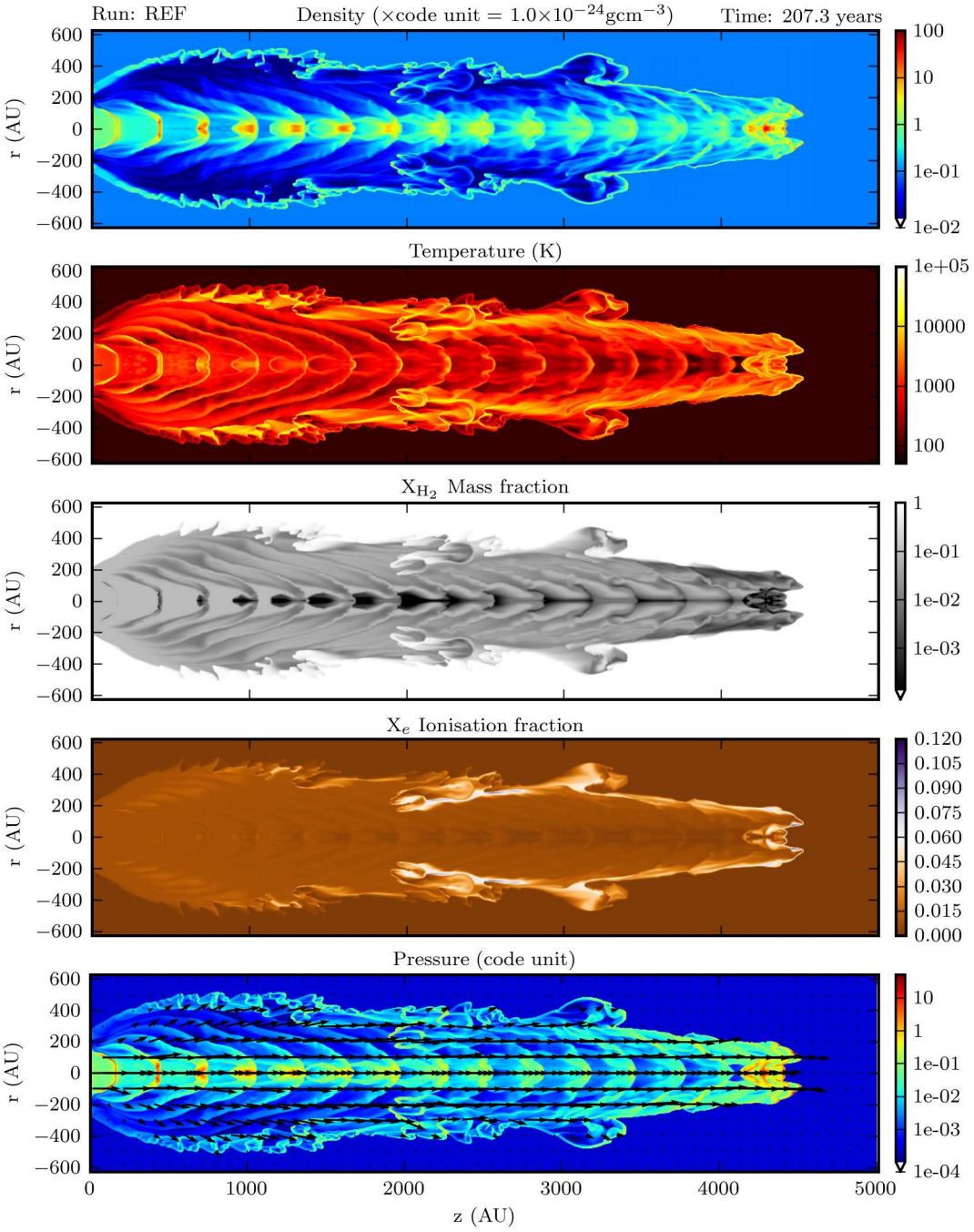

Figure A.2: Run: REF $\eta = 10$ Plotted are (top to bottom): density ρ, Temperature, X_{H_2}, X_e and pressure, with velocity vectors normalised to highest velocity.

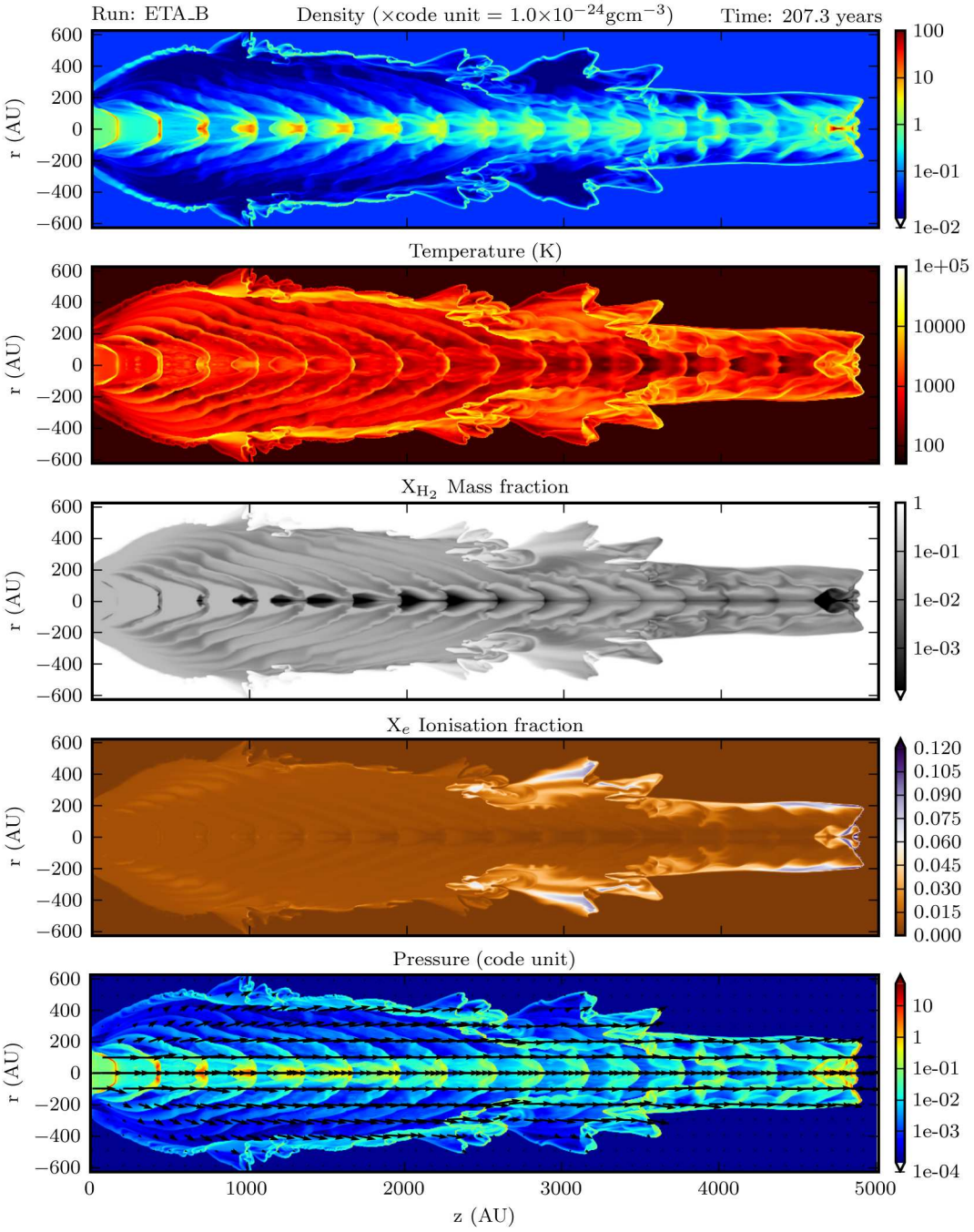

Figure A.3: Run: ETA_B $\eta = 20$ Plotted (top to bottom): density ρ, Temperature, X_{H_2}, X_e and pressure, with velocity vectors normalised to highest velocity.

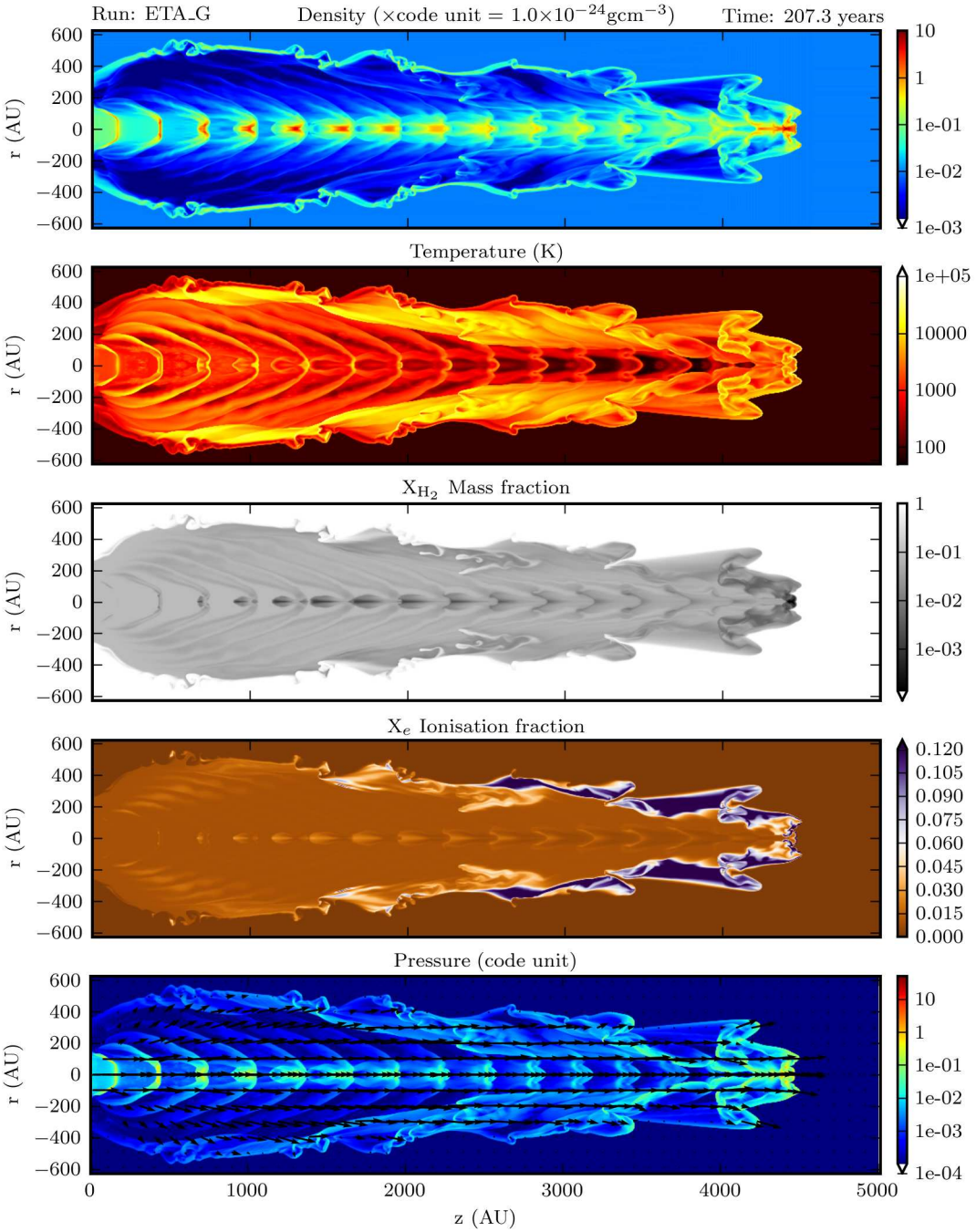

Figure A.4: Run: ETA_C (light) $\eta = 10$ Plotted are (top to bottom): density ρ, Temperature, X_{H_2}, X_e and pressure, with velocity vectors normalised to highest velocity.

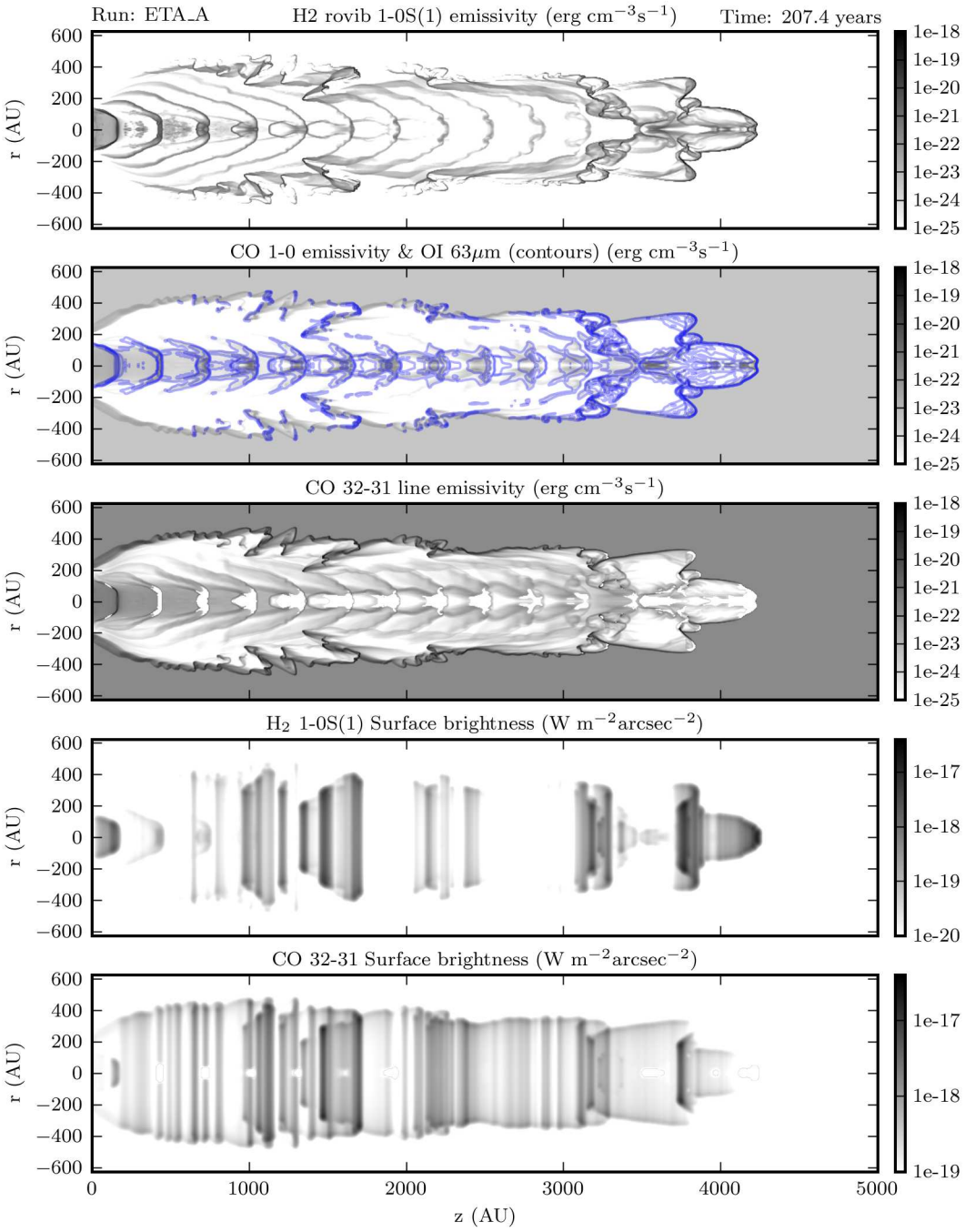

Figure A.5: Run: ETA_A $\eta = 5$ Plotted are (top to bottom): H_2 ro-vibrational line 1-0S(1) emissivity, CO 1-0 rotational line emissivity with OI 63μm line emission in contours at emissivities of $[10^{-20}, 10^{-19}, 10^{-18}10^{-17}]$ erg cm^{-3}s^{-1}, CO 32-31 rotational line emissivity, H_2 line 1-0S(1) and CO 32-31 rotational line surface brightnesses in W m^{-2}arcsec^{-2}.

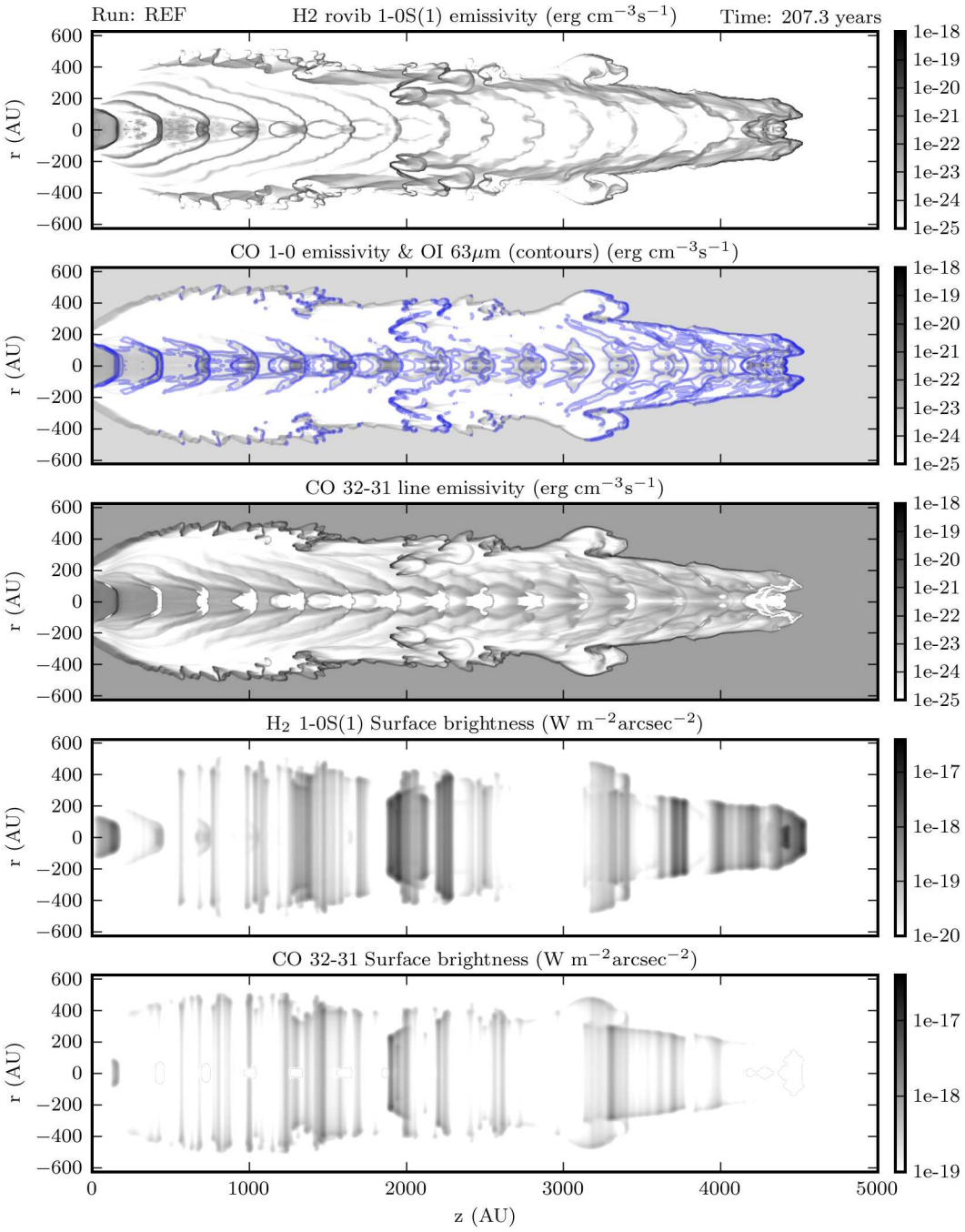

Figure A.6: Run: REF $\eta = 10$ Plotted are (top to bottom): H_2 ro-vibrational line 1-0S(1) emissivity, CO 1-0 rotational line emissivity with OI 63μm line emission in contours at emissivities of $[10^{-20}, 10^{-19}, 10^{-18}10^{-17}]$ erg cm^{-3}s^{-1}, CO 32-31 rotational line emissivity, H_2 line 1-0S(1) and CO 32-31 rotational line surface brightnesses in W m^{-2}arcsec^{-2}.

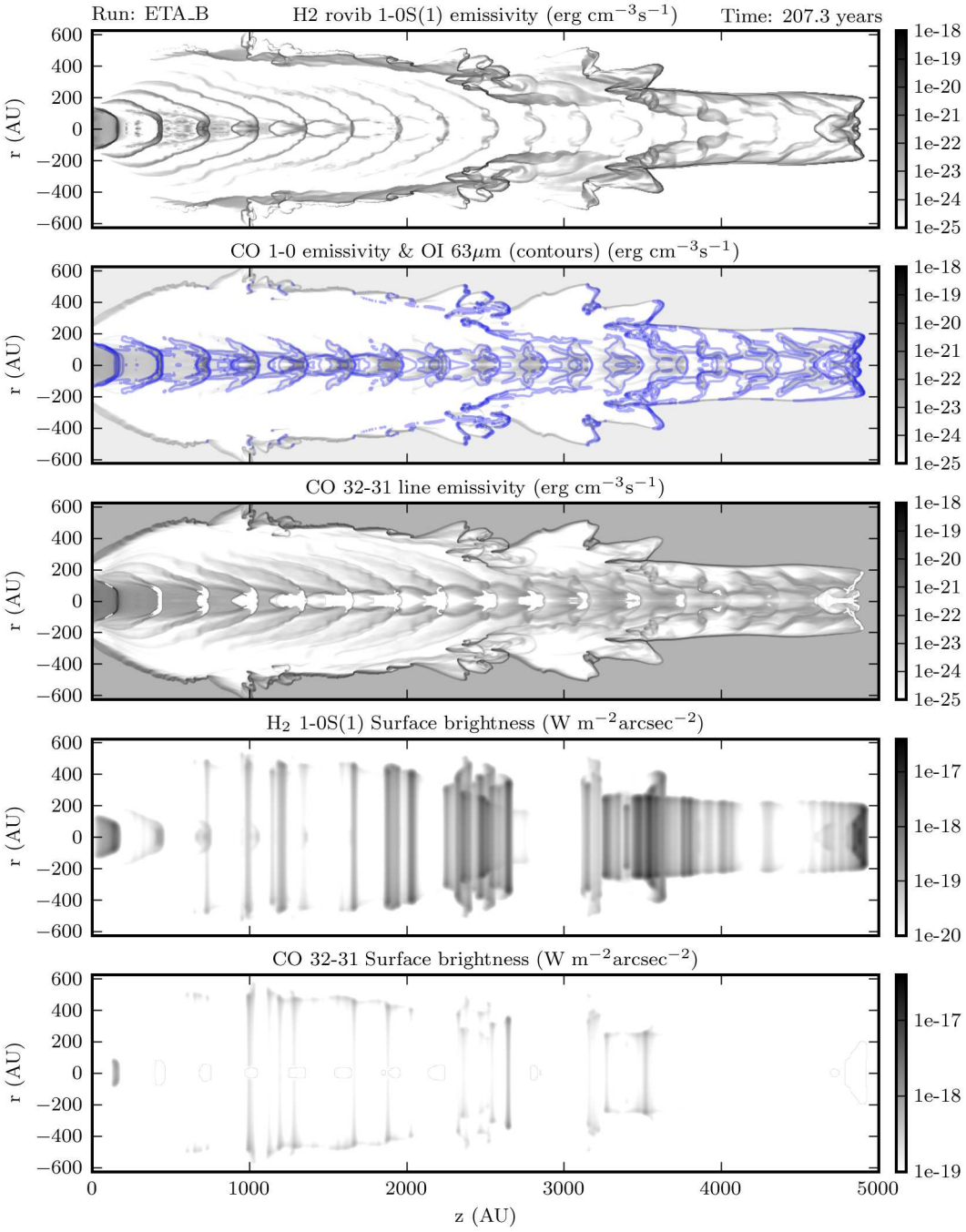

Figure A.7: Run: ETA_B $\eta = 20$ Plotted are (top to bottom): H_2 ro-vibrational line 1-0S(1) emissivity, CO 1-0 rotational line emissivity with OI 63μm line emission in contours at emissivities of $[10^{-20}, 10^{-19}, 10^{-18}10^{-17}]$ erg cm^{-3}s^{-1}, CO 32-31 rotational line emissivity, H_2 line 1-0S(1) and CO 32-31 rotational line surface brightnesses in W m^{-2}arcsec^{-2}.

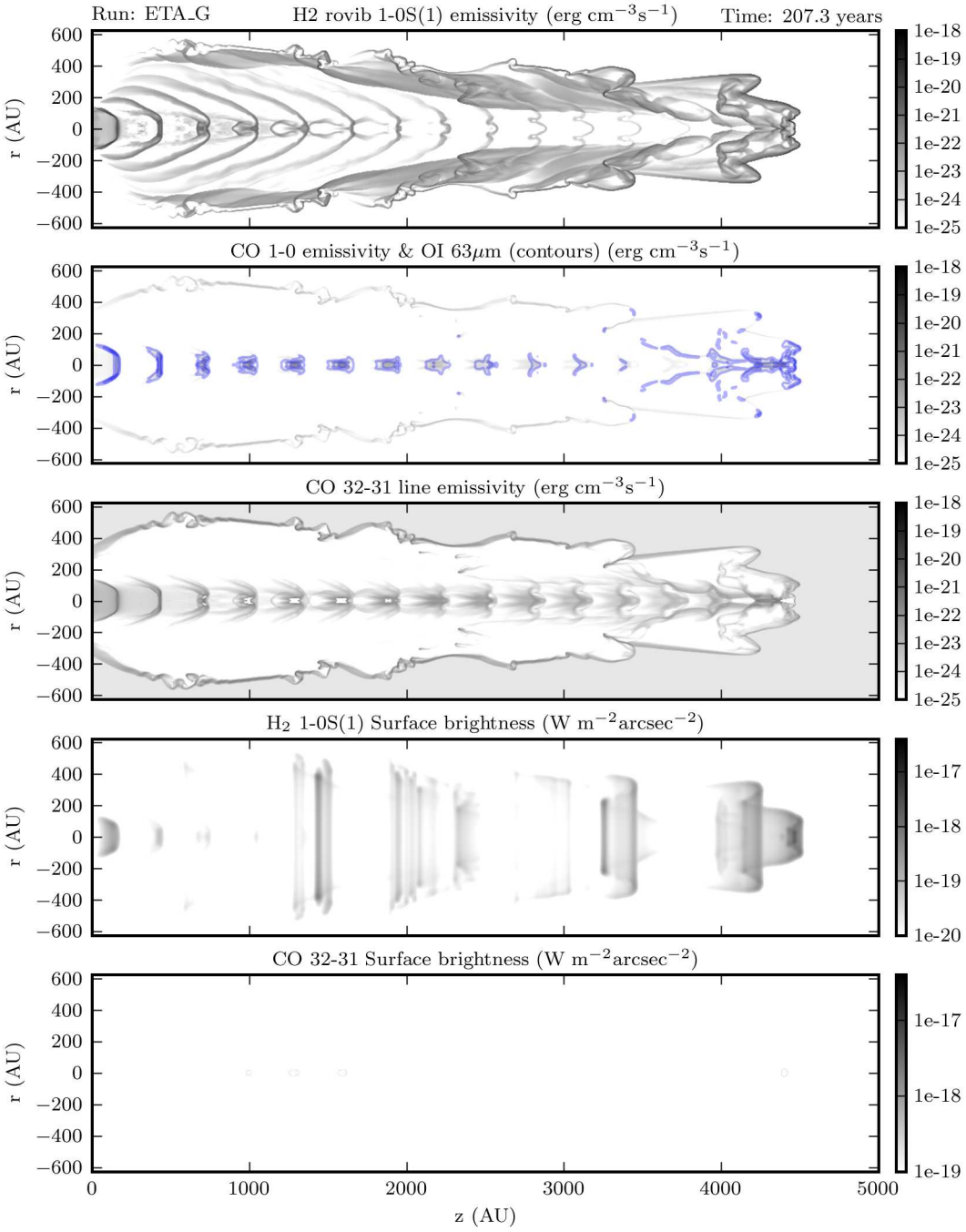

Figure A.8: Run: ETA_C (light) $\eta = 10$ Plotted are (top to bottom): H_2 ro-vibrational line 1-0S(1) emissivity, CO 1-0 rotational line emissivity with OI 63μm line emission in contours at emissivities of $[10^{-20}, 10^{-19}, 10^{-18}10^{-17}]$ erg cm^{-3}s^{-1}, CO 32-31 rotational line emissivity, H_2 line 1-0S(1) and CO 32-31 rotational line surface brightnesses in W m^{-2}arcsec^{-2}.

A.2 Ionisation

Table A.2 lists the parameters for the variation of the ionisation fraction.

Run	X_{H2}	► X_e ◄	η	β
ION_A	10%	0.1%	10	-
REF	10%	1%	10	-
ION_B	10%	3%	10	-
ION_C	10%	10%	10	-

Table A.2: Summary of simulations with varying Ionisation X_e in the beam

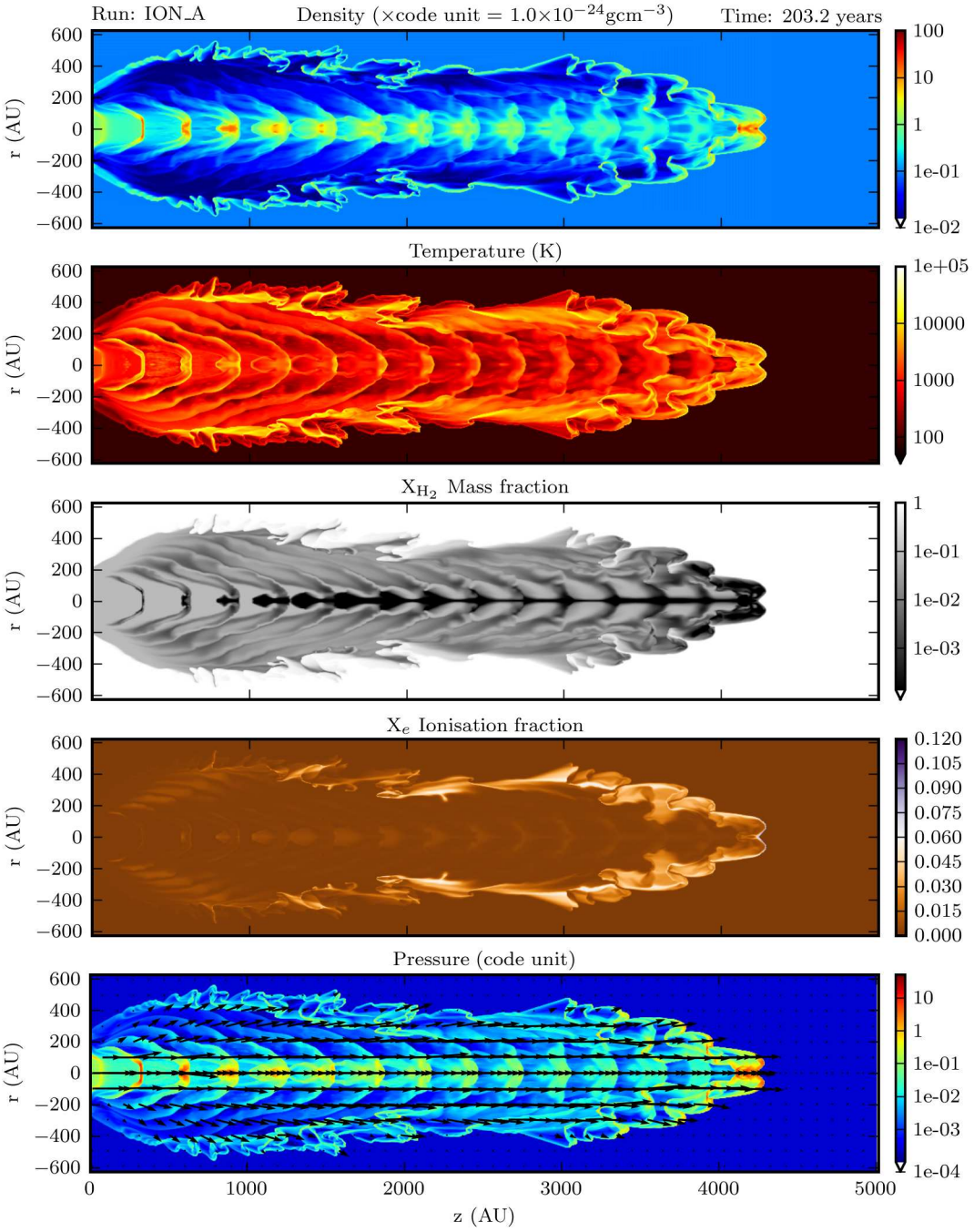

Figure A.9: Run: ION_A $X_e = 0.1\%$ Plotted are (top to bottom): density ρ, Temperature, X_{H_2}, X_e and pressure, with velocity vectors normalised to the highest velocity.

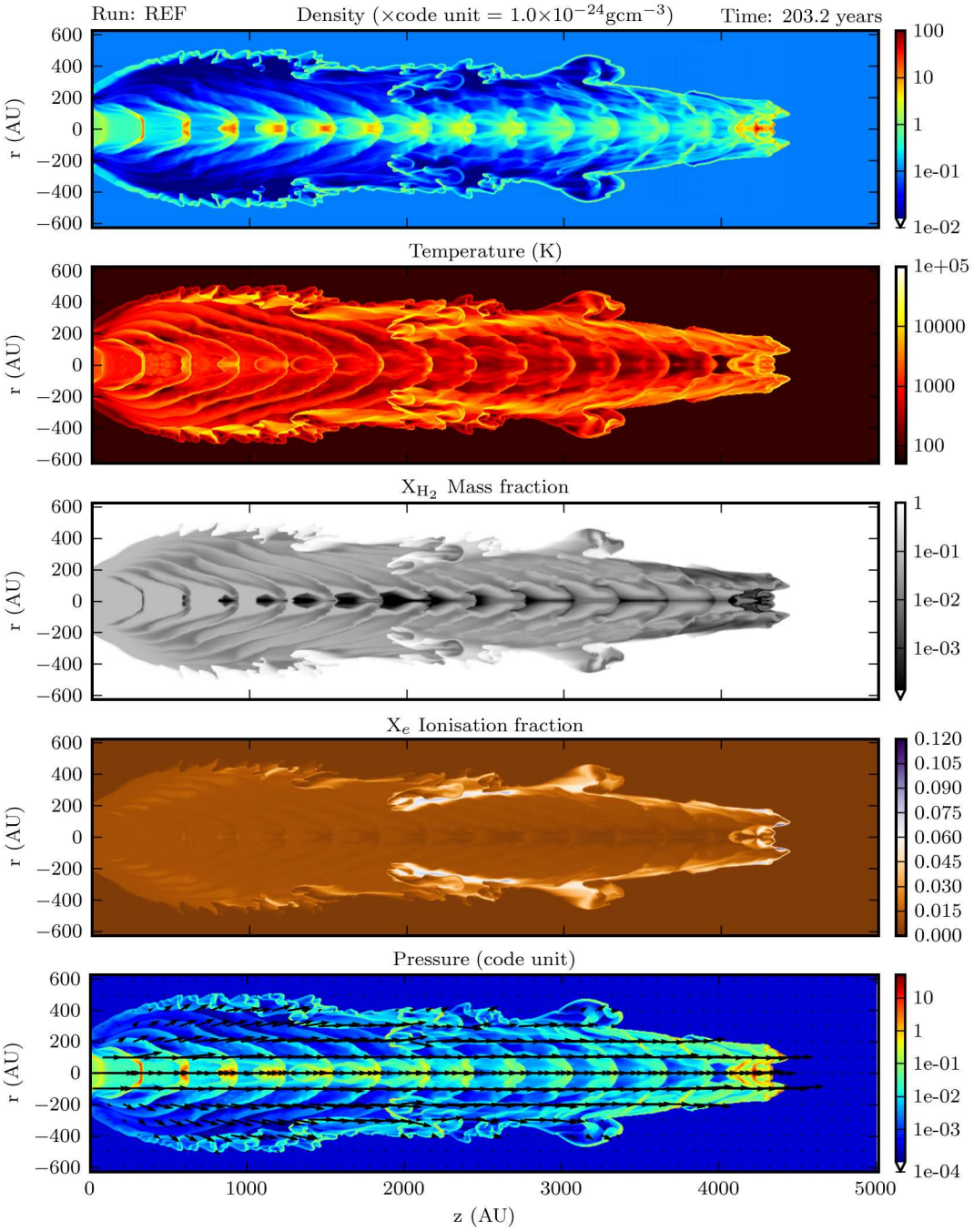

Figure A.10: Run: REF $X_e = 1\%$ Plotted are (top to bottom): density ρ, Temperature, X_{H_2}, X_e and pressure, with velocity vectors normalised to the highest velocity.

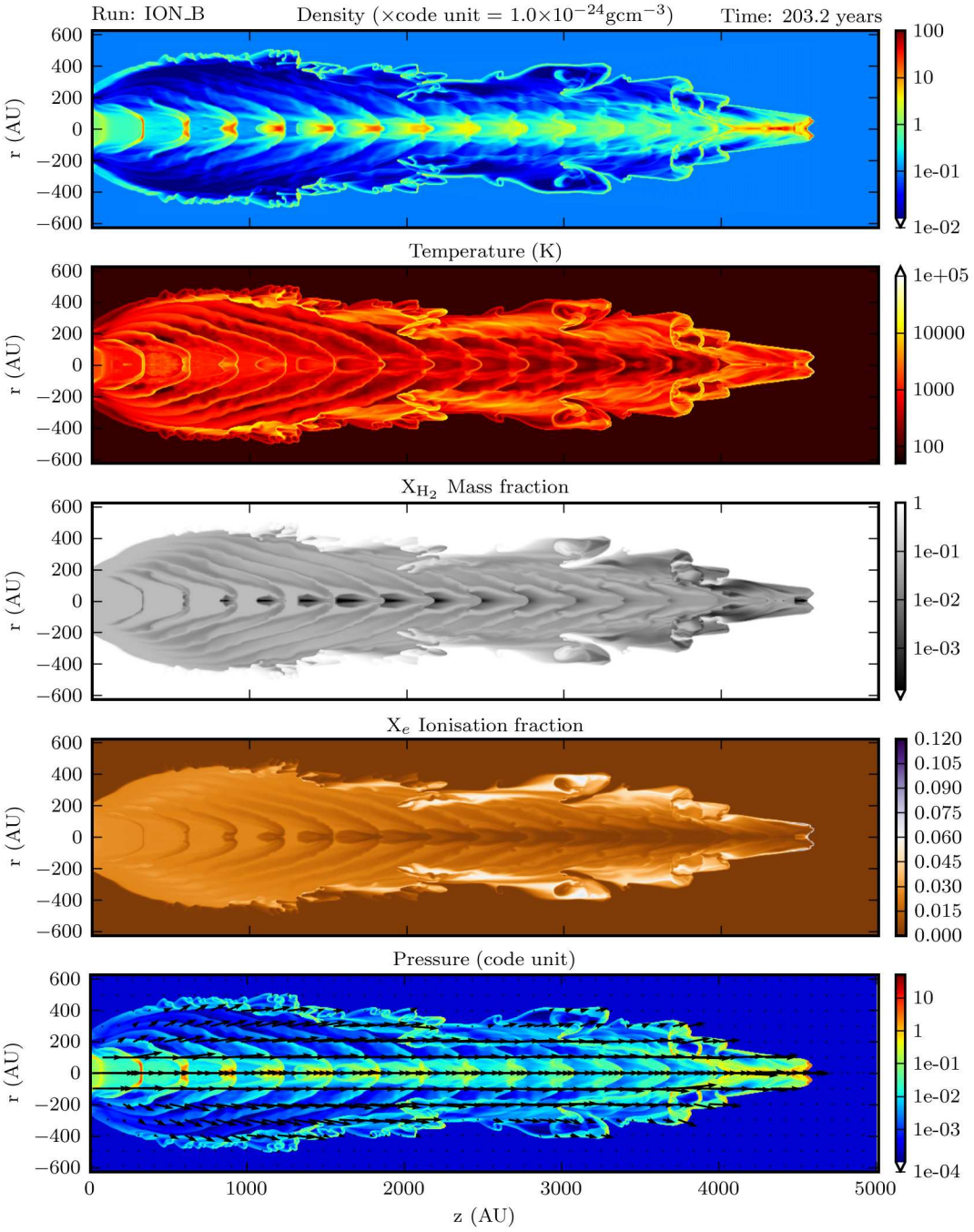

Figure A.11: Run: ION_B $X_e = 3\%$ Plotted are (top to bottom): density ρ, Temperature, X_{H_2}, X_e and pressure, with velocity vectors normalised to the highest velocity.

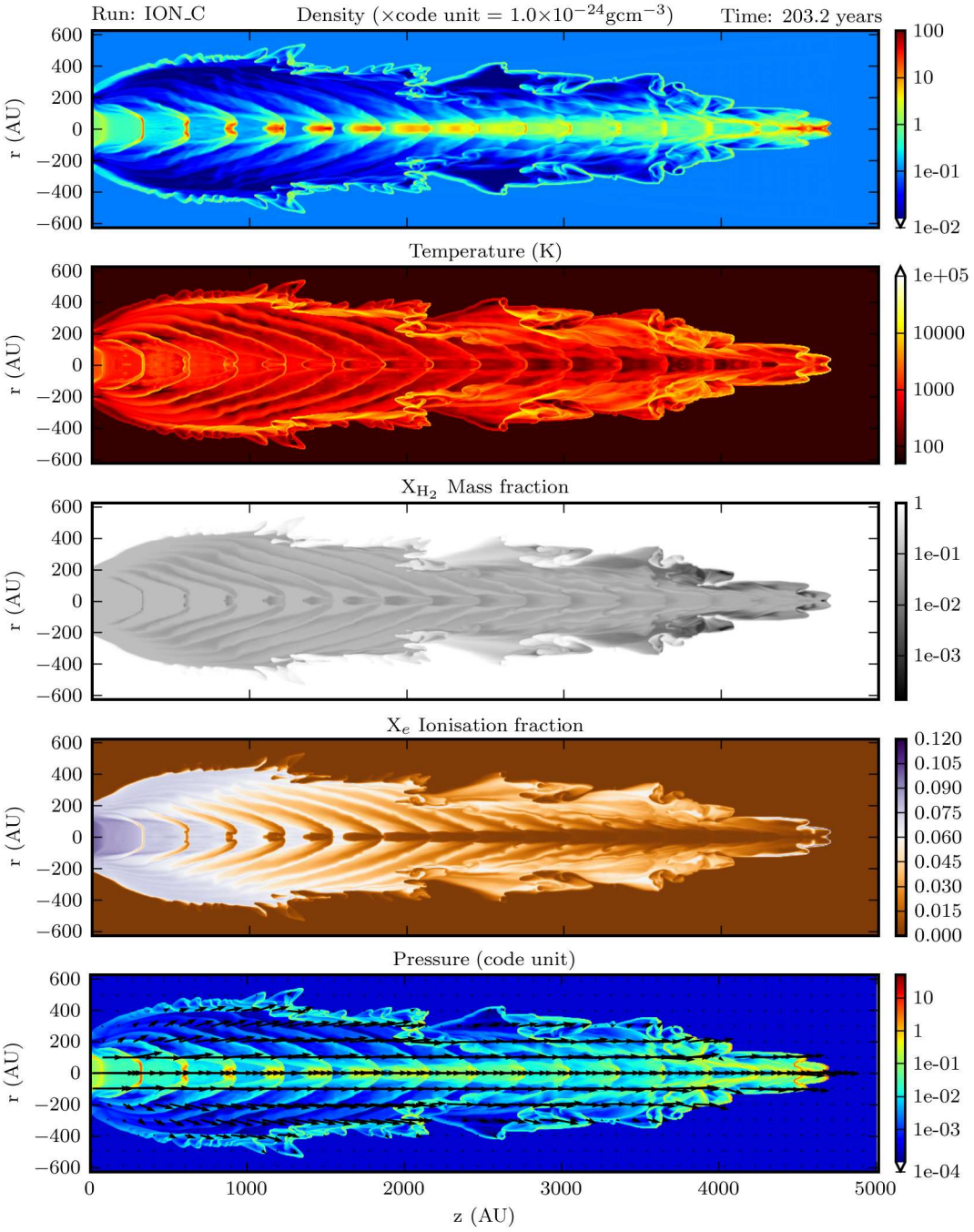

Figure A.12: Run: ION_C X_e = 10% Plotted are (top to bottom): density ρ, Temperature, X_{H_2}, X_e and pressure, with velocity vectors normalised to the highest velocity.

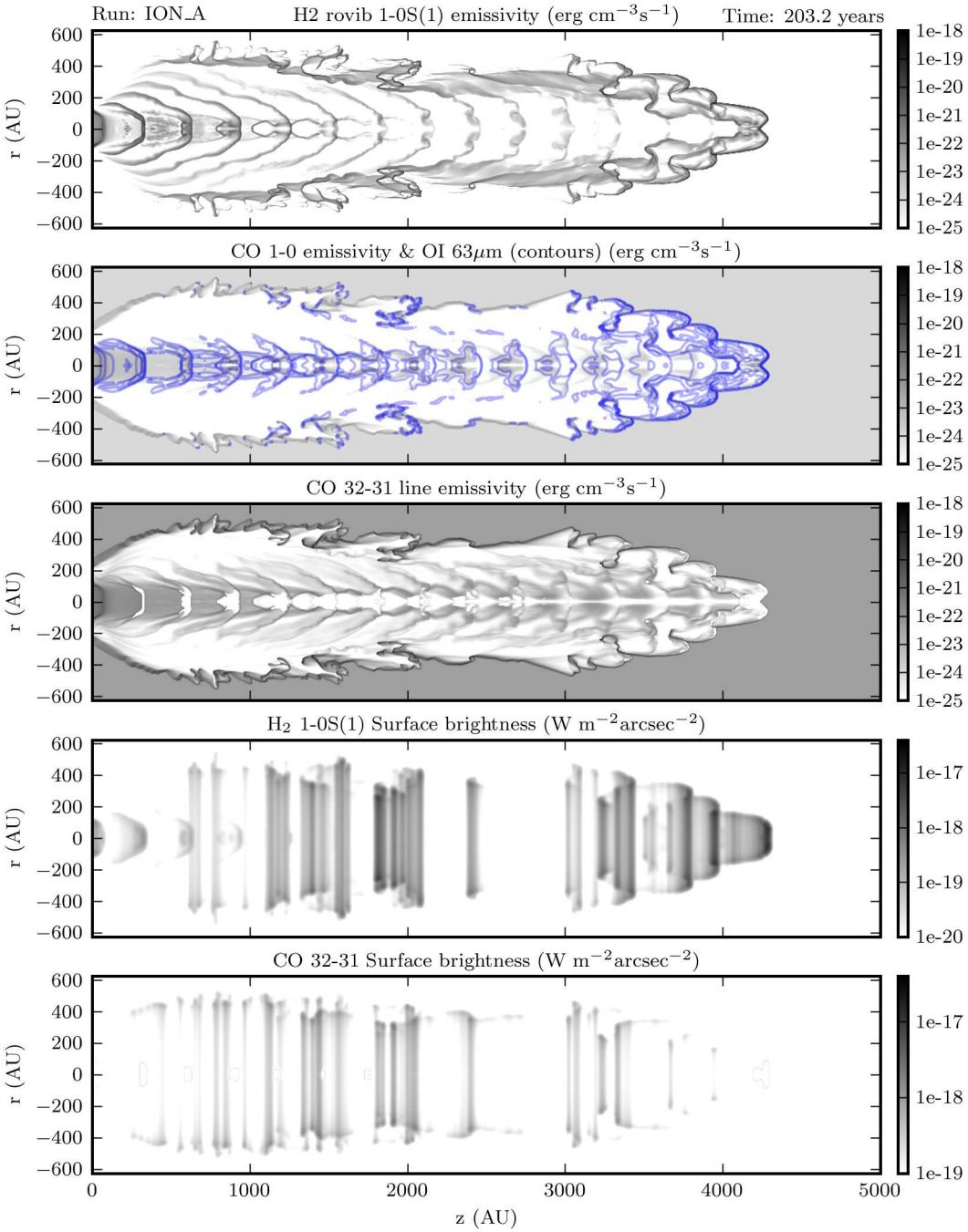

Figure A.13: Run: ION_A $\mathbf{X}_e = 0.1\%$ Plotted are (top to bottom): H_2 ro-vibrational line 1-0S(1) emissivity, CO 1-0 rotational line emissivity with OI 63μm line emission in contours at emissivities of $[10^{-20}, 10^{-19}, 10^{-18}10^{-17}]$ erg cm^{-3}s^{-1}, CO 32-31 rotational line emissivity, H_2 line 1-0S(1) and CO 32-31 rotational line surface brightnesses in W m^{-2}arcsec^{-2}.

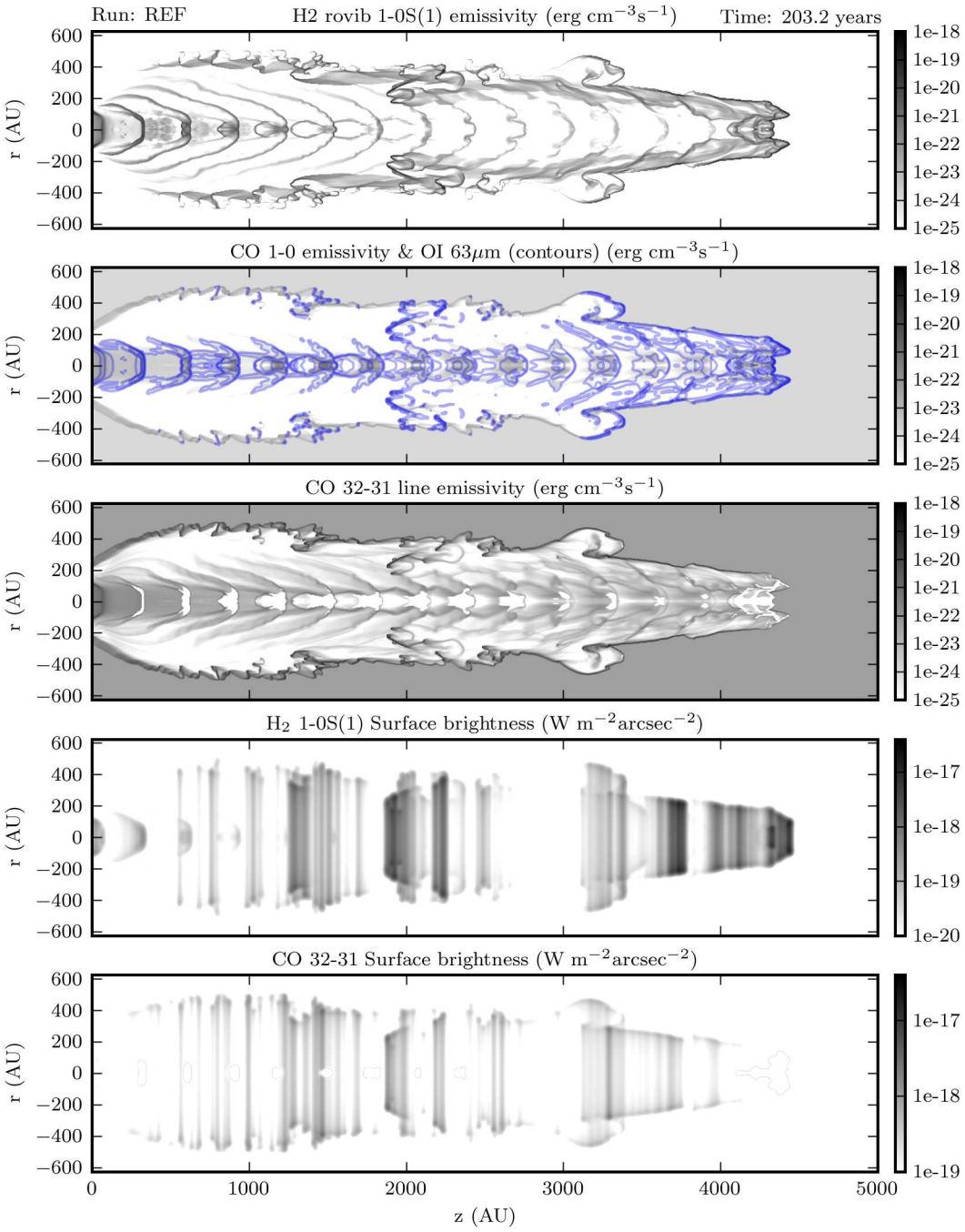

Figure A.14: Run: REF $\mathbf{X}_e = 1\%$ Plotted are (top to bottom): H_2 ro-vibrational line 1-0S(1) emissivity, CO 1-0 rotational line emissivity with OI 63μm line emission in contours at emissivities of $[10^{-20}, 10^{-19}, 10^{-18}10^{-17}]$ erg cm^{-3}s^{-1}, CO 32-31 rotational line emissivity, H_2 line 1-0S(1) and CO 32-31 rotational line surface brightnesses in W m^{-2}arcsec^{-2}.

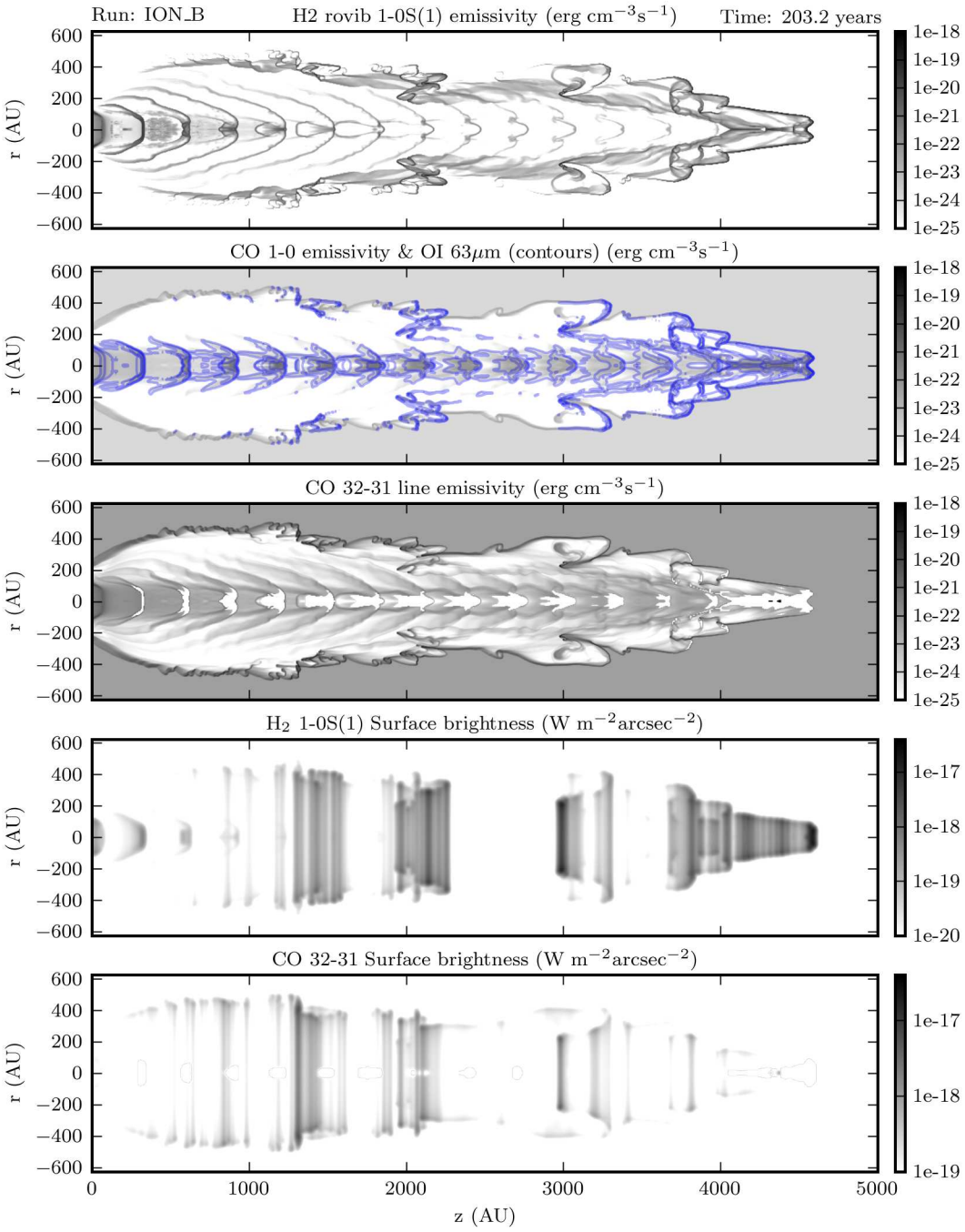

Figure A.15: Run: ION_B $X_e = 3\%$ Plotted are (top to bottom): H_2 ro-vibrational line 1-0S(1) emissivity, CO 1-0 rotational line emissivity with OI 63μm line emission in contours at emissivities of $[10^{-20}, 10^{-19}, 10^{-18}10^{-17}]$ erg cm^{-3}s^{-1}, CO 32-31 rotational line emissivity, H_2 line 1-0S(1) and CO 32-31 rotational line surface brightnesses in W m^{-2}arcsec^{-2}.

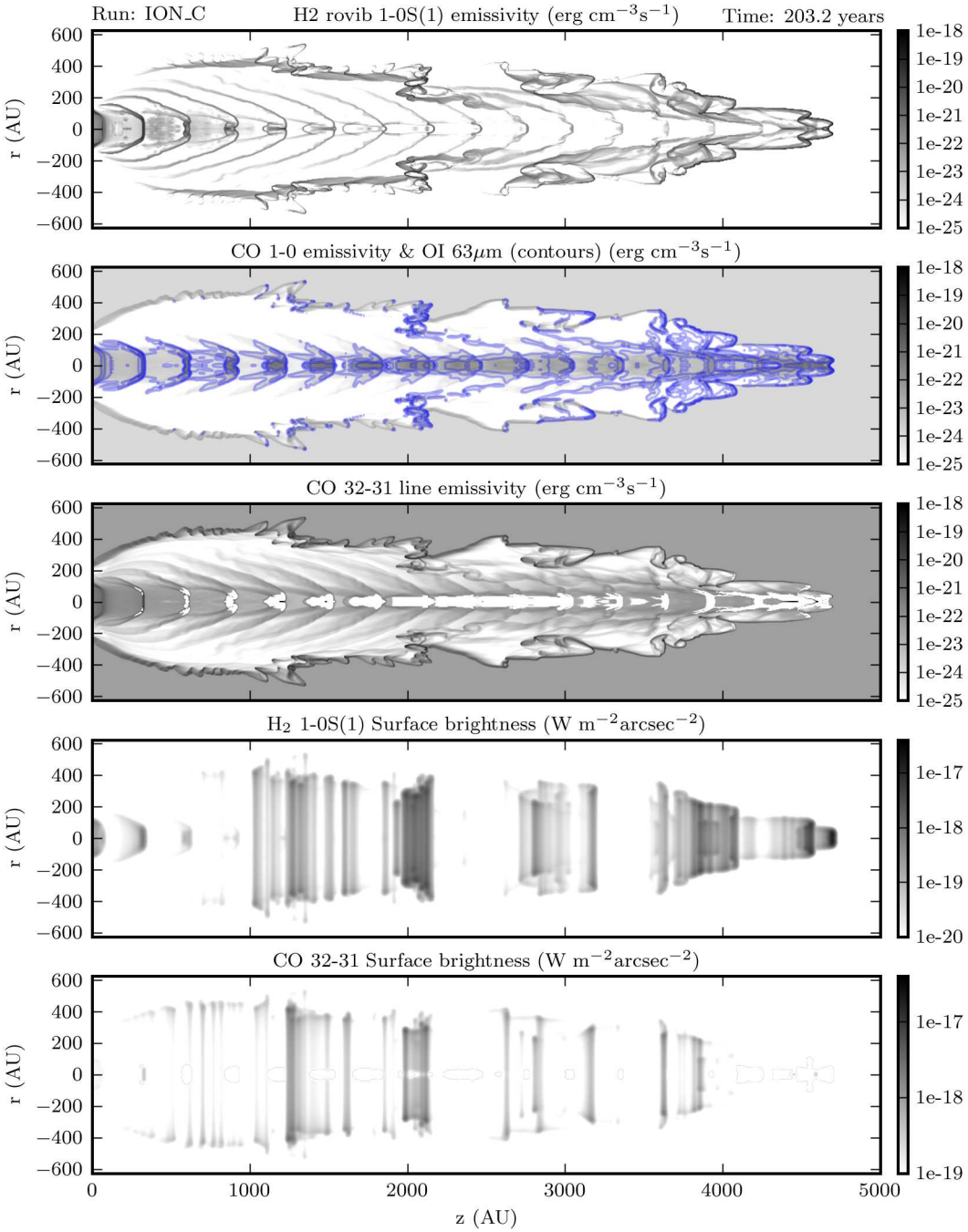

Figure A.16: Run: ION_C $\mathbf{X}_e = 10\%$ Plotted are (top to bottom): H_2 ro-vibrational line 1-0S(1) emissivity, CO 1-0 rotational line emissivity with OI 63μm line emission in contours at emissivities of $[10^{-20}, 10^{-19}, 10^{-18}10^{-17}]$ erg cm^{-3}s^{-1}, CO 32-31 rotational line emissivity, H_2 line 1-0S(1) and CO 32-31 rotational line surface brightnesses in W m^{-2}arcsec^{-2}.

A.3 Molecular Fraction

Table A.3 lists the simulations runs varying the molecular fraction X_{H_2}.

Run	► X_{H2} ◄	X_e	η	β
MOL_A	1%	1%	10	-
MOL_B	5%	1%	10	-
REF	10%	1%	10	-
MOL_C	33%	1%	10	-
MOL_D	50%	0.001%	10	-

Table A.3: Summary of runs varying the molecular fraction $\mathbf{X}_{H2}$ in the beam. All have beam ionisation fractions of 10^{-2} except for MOL_D, with an ionisation fraction of 10^{-5}.

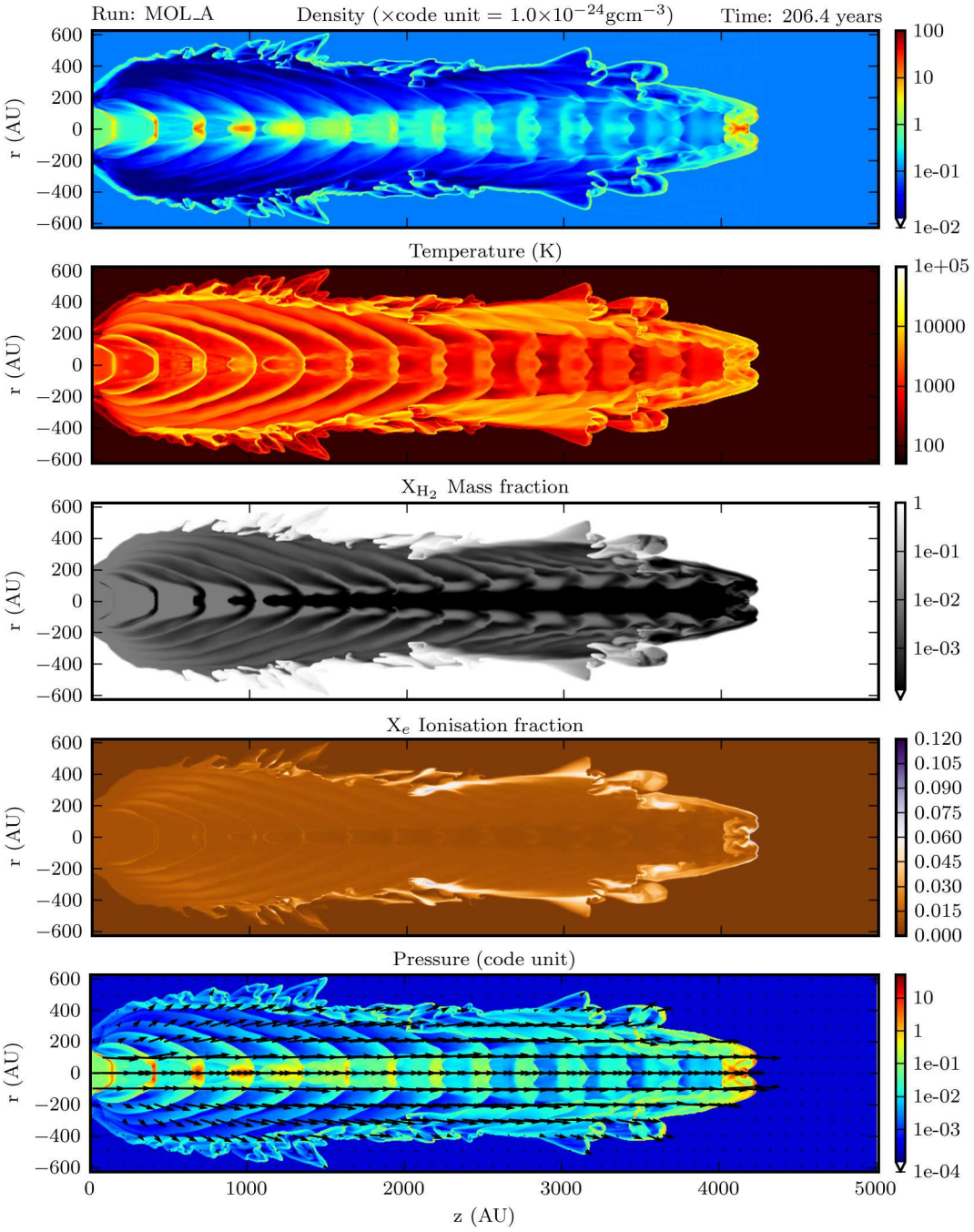

Figure A.17: **Run: MOL_A X_{H_2} = 1%** Plotted are (top to bottom): density ρ, Temperature, X_{H_2}, X_e and pressure, with velocity vectors normalised to the highest velocity.

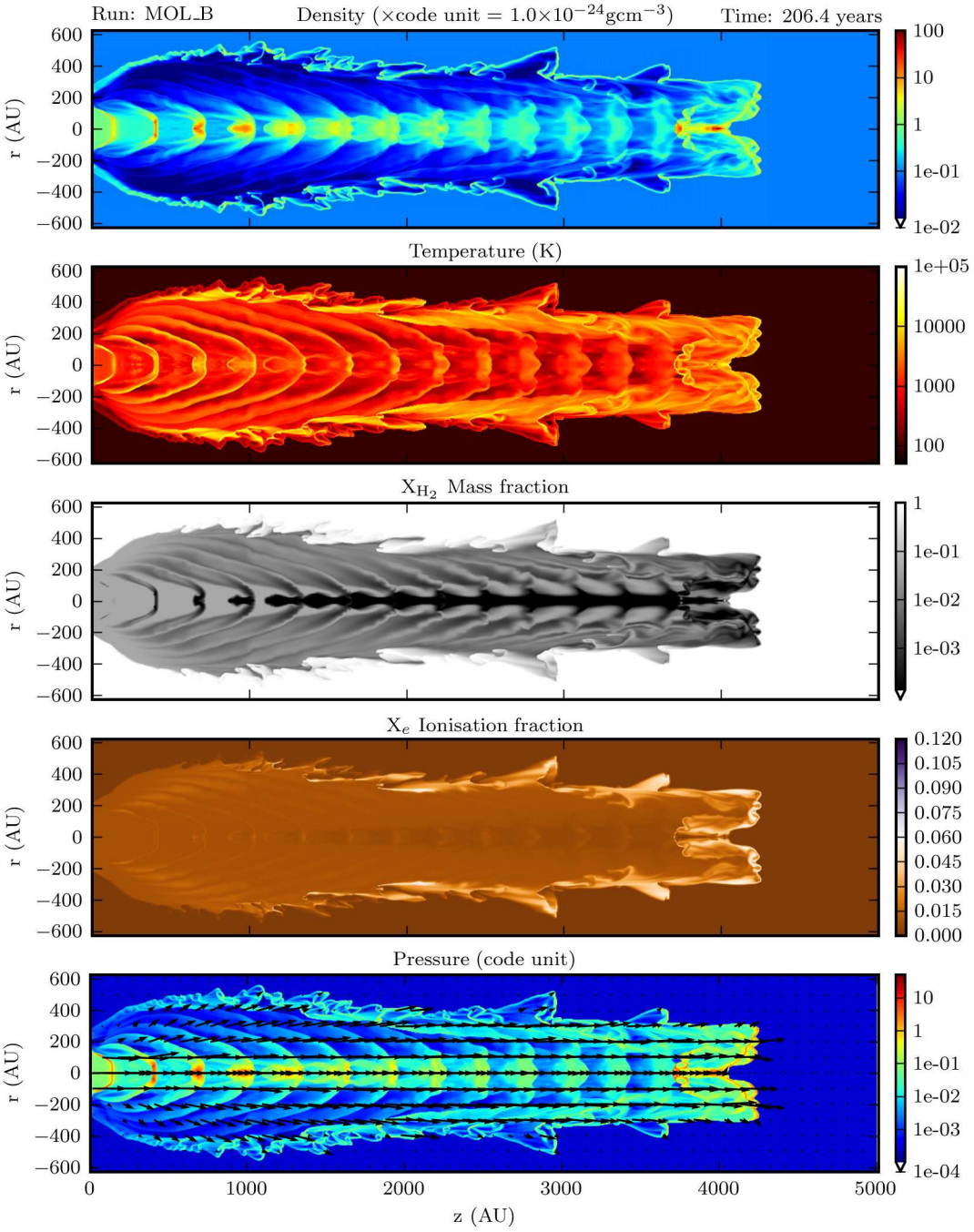

Figure A.18: **Run: MOL_B X_{H_2} = 5%** Plotted are (top to bottom): density ρ, Temperature, X_{H_2}, X_e and pressure, with velocity vectors normalised to the highest velocity.

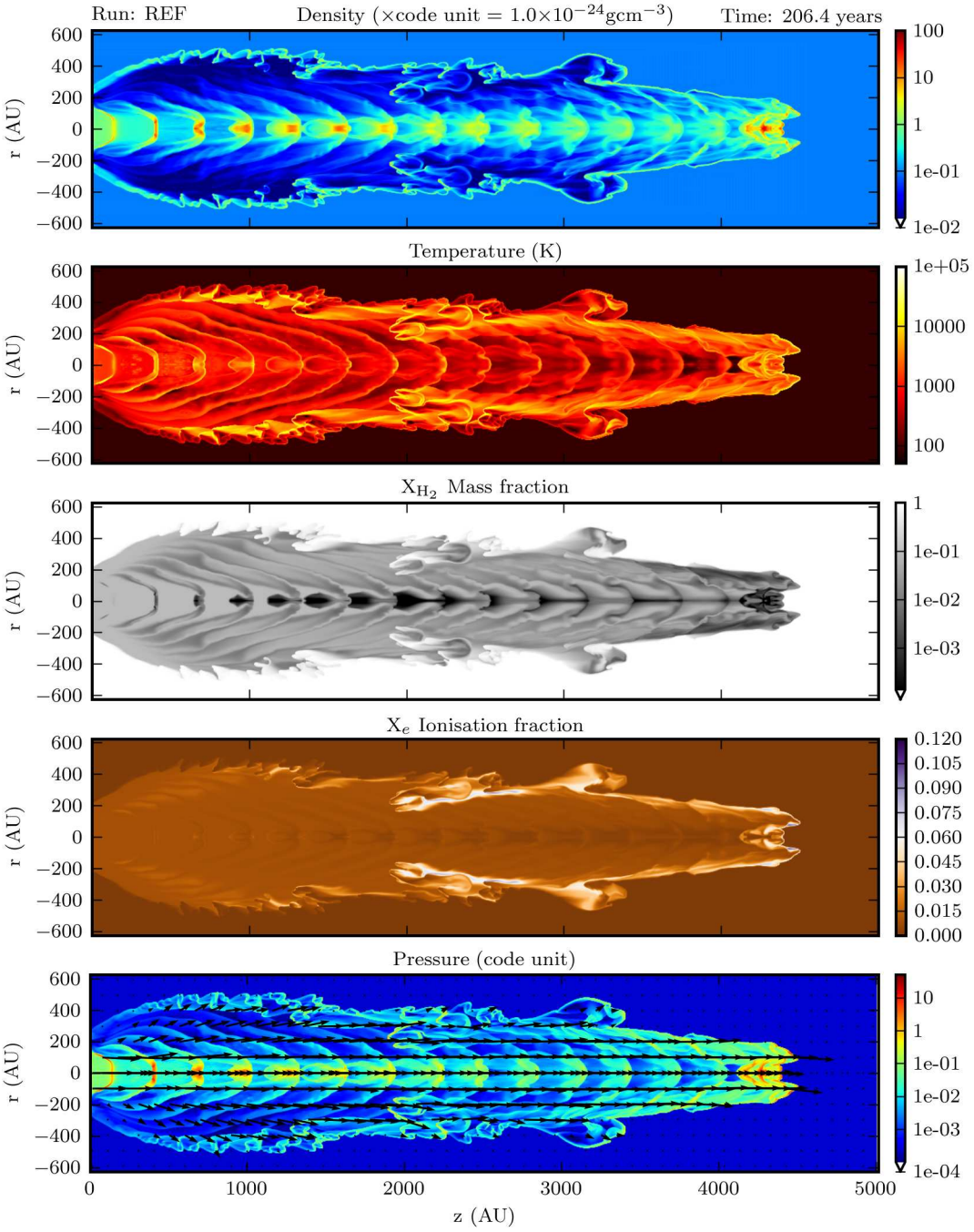

Figure A.19: Run: REF $X_{H_2} = 10\%$ Plotted are (top to bottom): density ρ, Temperature, X_{H_2}, X_e and pressure, with velocity vectors normalised to the highest velocity.

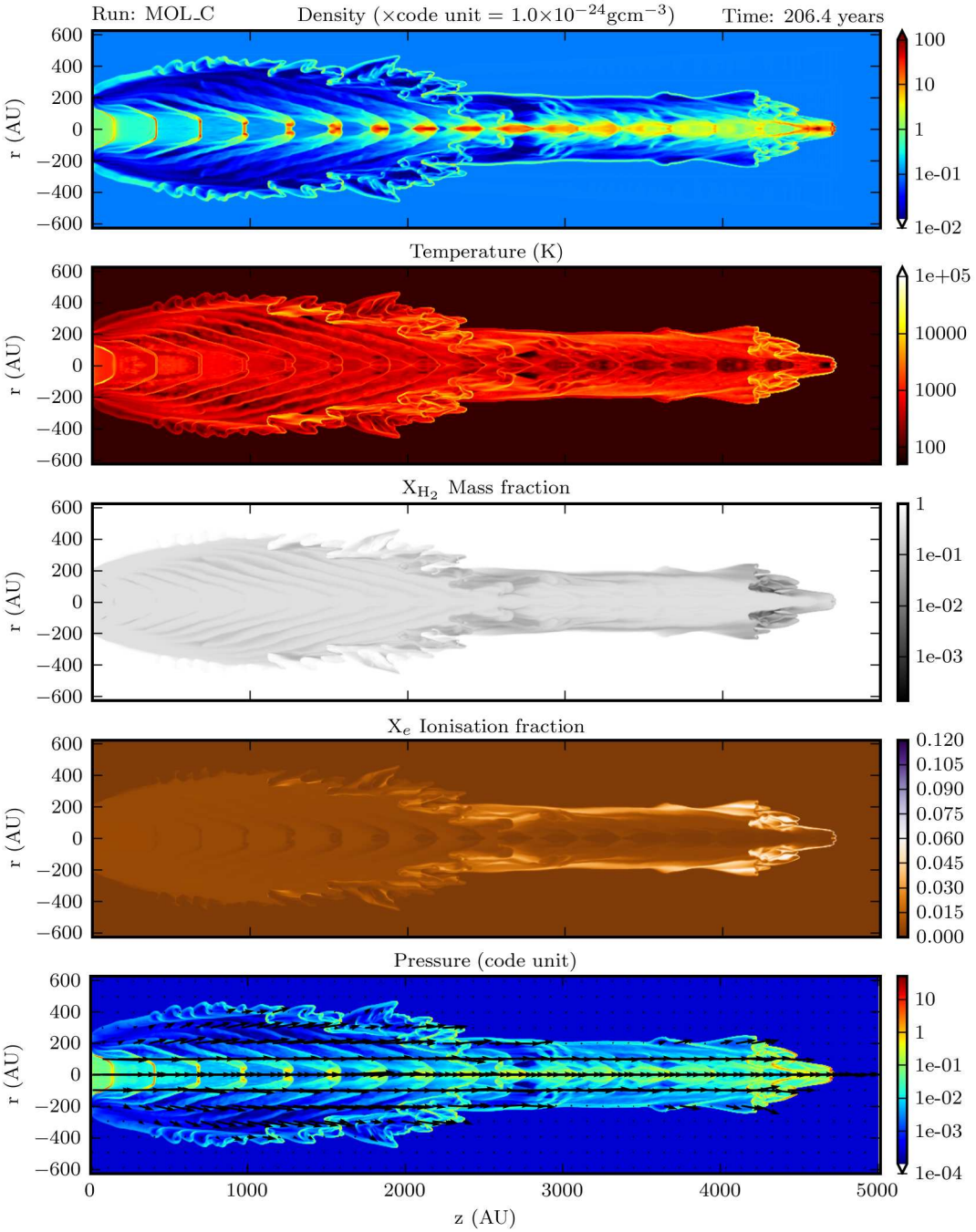

Figure A.20: Run: MOL_C X_{H_2} = 33% Plotted are (top to bottom): density ρ, Temperature, X_{H_2}, X_e and pressure, with velocity vectors normalised to the highest velocity.

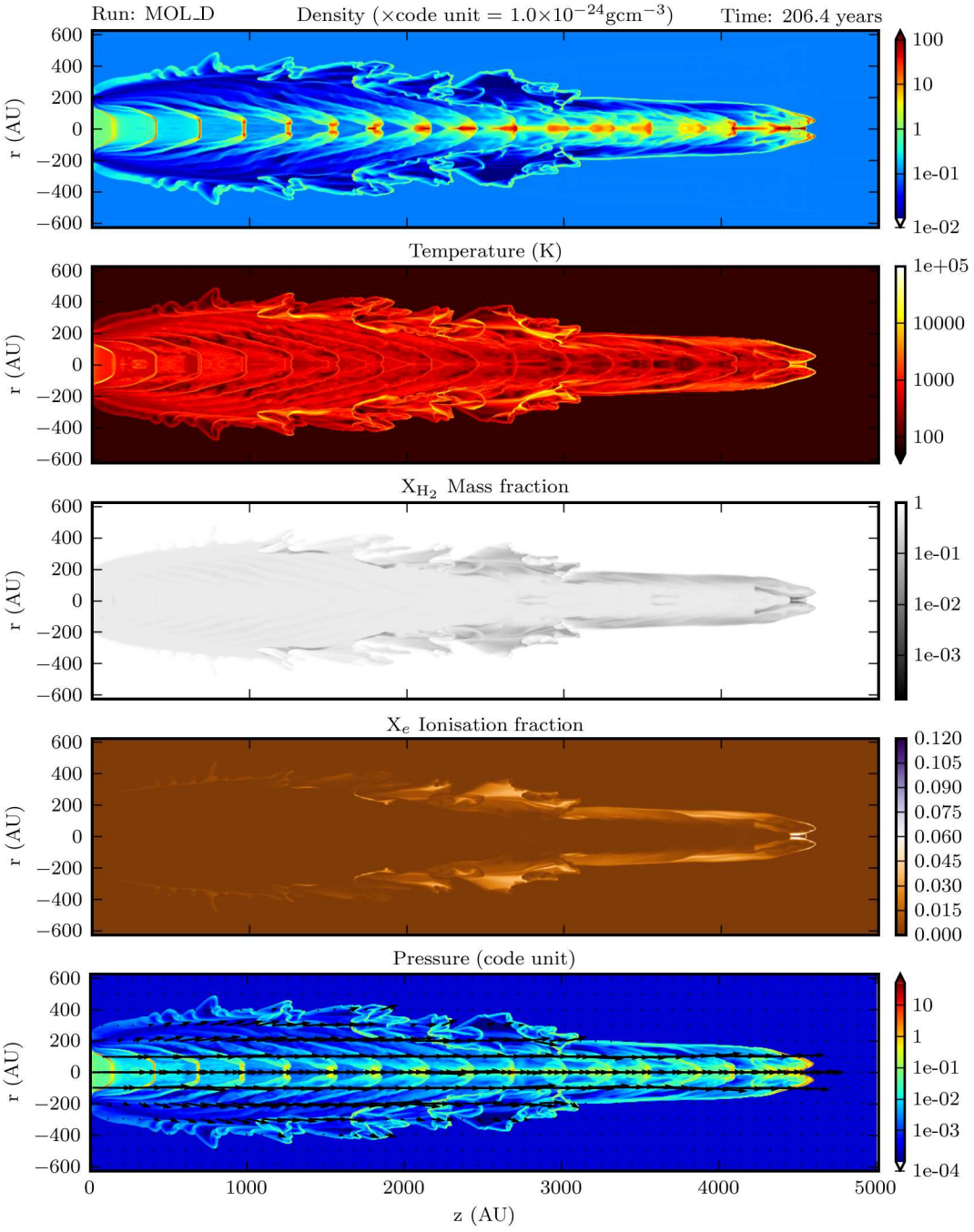

Figure A.21: Run: MOL_D $X_{H_2} = 50\%$, X_e=10^{-5} *Plottedare(toptobottom) : densityρ*, **Temperature, X_{H_2}, X_e and pressure, with velocity vectors normalised to the highest velocity.**

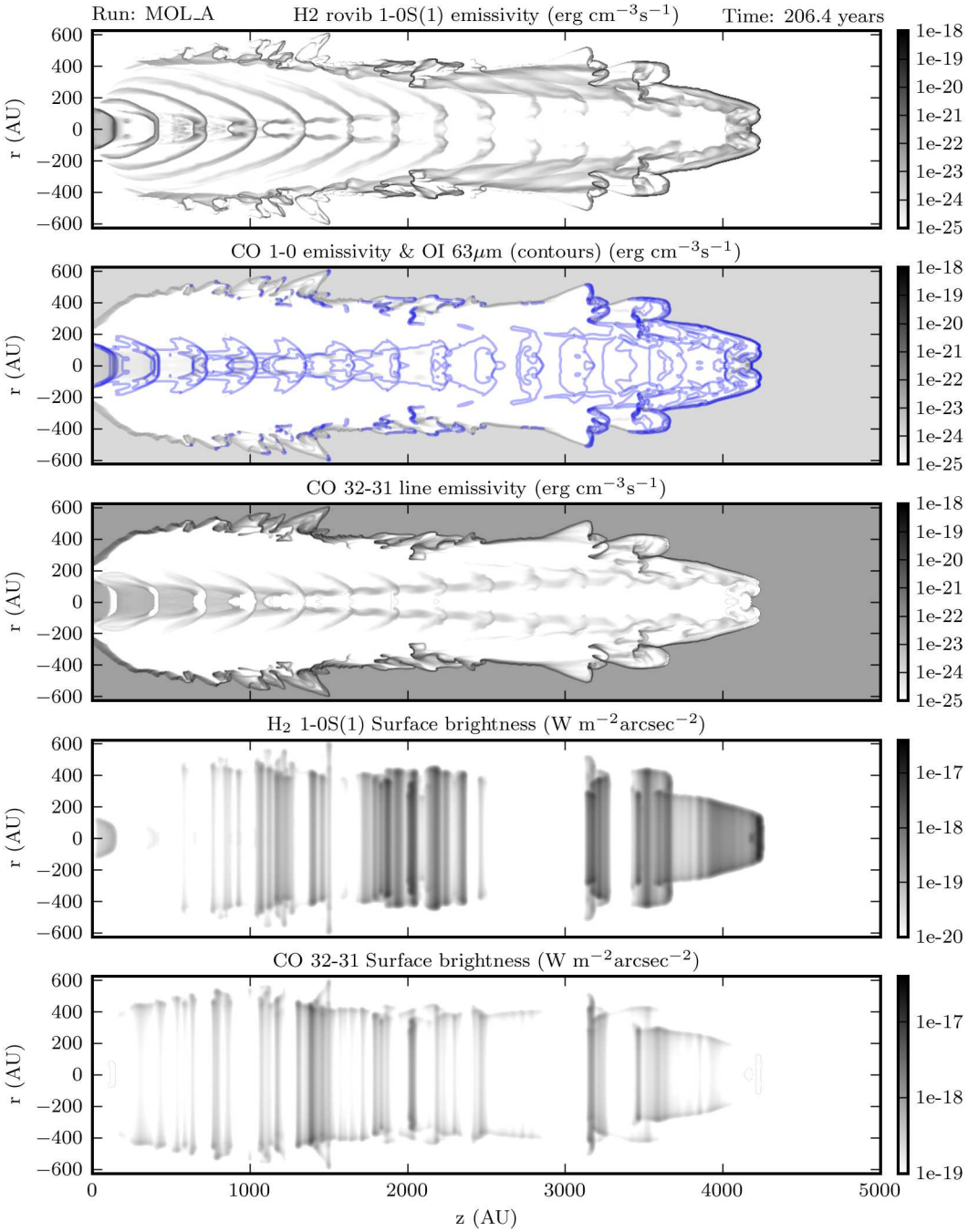

Figure A.22: Run: MOL_A $X_{H_2} = 1\%$ Plotted are (top to bottom): H_2 ro-vibrational line 1-0S(1) emissivity, CO 1-0 rotational line emissivity with OI 63μm line emission in contours at emissivities of $[10^{-20}, 10^{-19}, 10^{-18}10^{-17}]$ erg cm^{-3}s^{-1}, CO 32-31 rotational line emissivity, H_2 line 1-0S(1) and CO 32-31 rotational line surface brightnesses in W m^{-2}arcsec^{-2}.

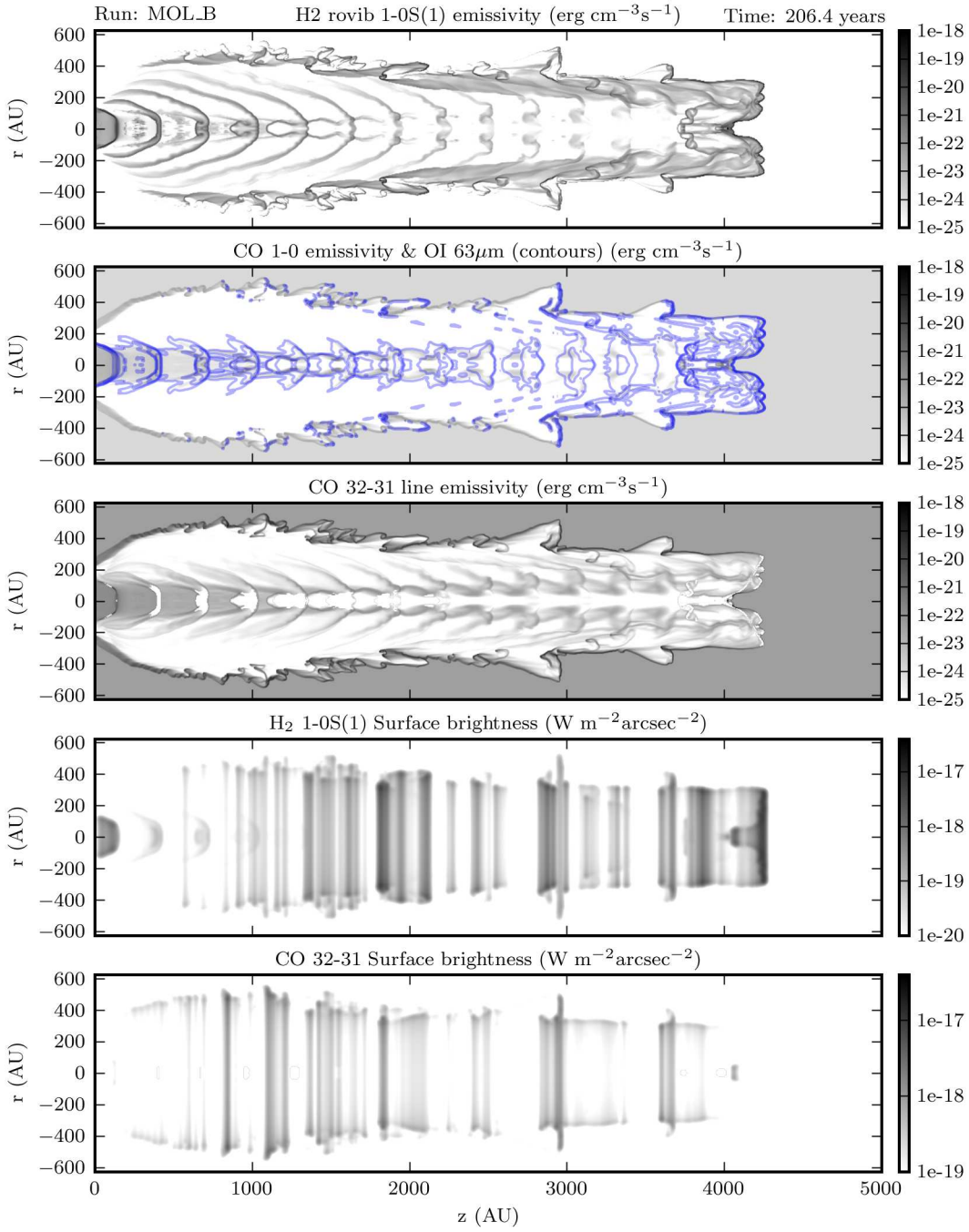

Figure A.23: Run: MOL_B $\mathbf{X}_{\mathrm{H_2}} = 5\%$ Plotted are (top to bottom): H_2 ro-vibrational line 1-0S(1) emissivity, CO 1-0 rotational line emissivity with OI 63μm line emission in contours at emissivities of $[10^{-20}, 10^{-19}, 10^{-18}10^{-17}]$ erg cm^{-3}s^{-1}, CO 32-31 rotational line emissivity, H_2 line 1-0S(1) and CO 32-31 rotational line surface brightnesses in W m^{-2}arcsec^{-2}.

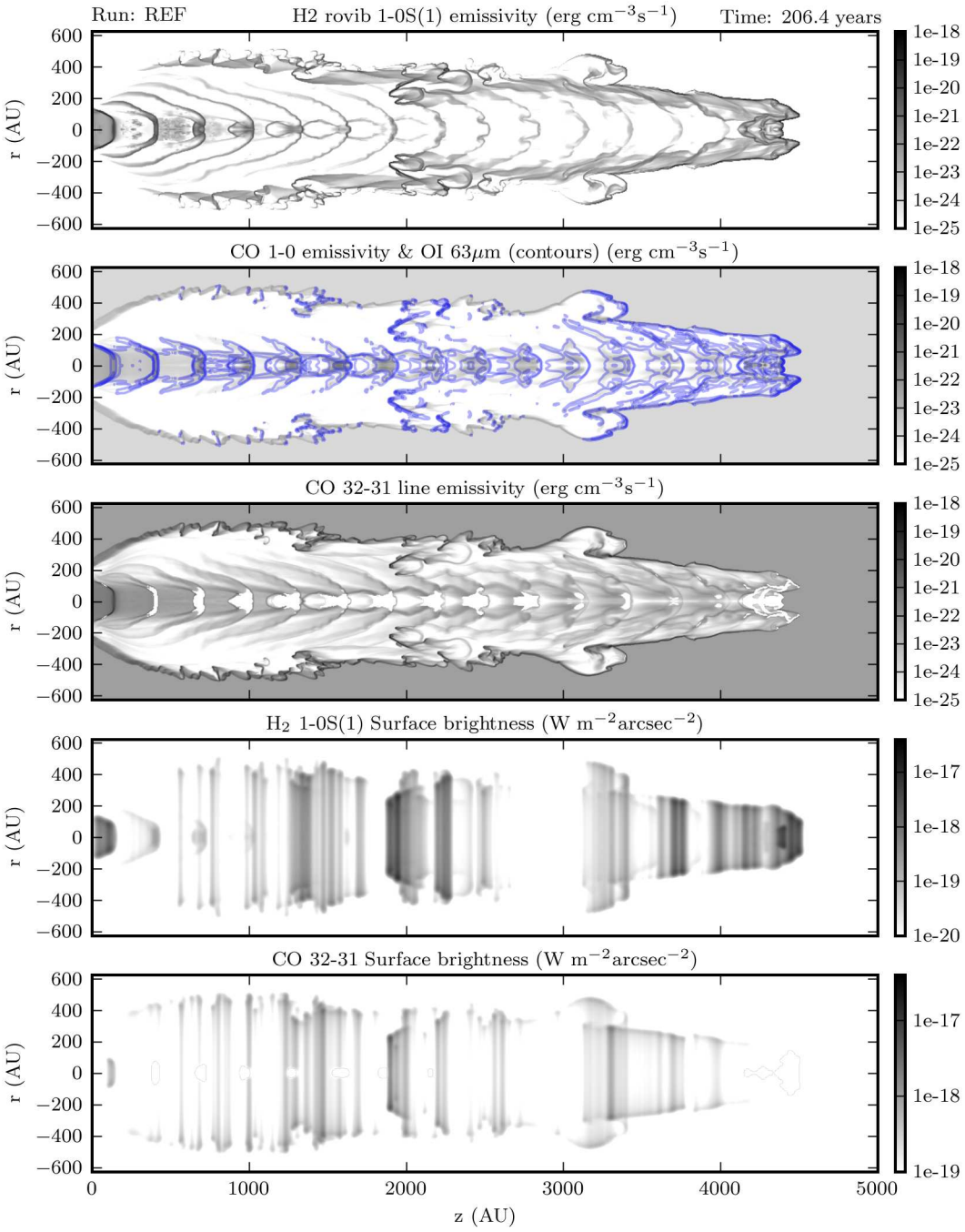

Figure A.24: Run: REF $X_{H_2} = 10\%$ Plotted are (top to bottom): H_2 ro-vibrational line 1-0S(1) emissivity, CO 1-0 rotational line emissivity with OI 63μm line emission in contours at emissivities of $[10^{-20}, 10^{-19}, 10^{-18}10^{-17}]$ erg cm^{-3}s^{-1}, CO 32-31 rotational line emissivity, H_2 line 1-0S(1) and CO 32-31 rotational line surface brightnesses in W m^{-2}arcsec^{-2}.

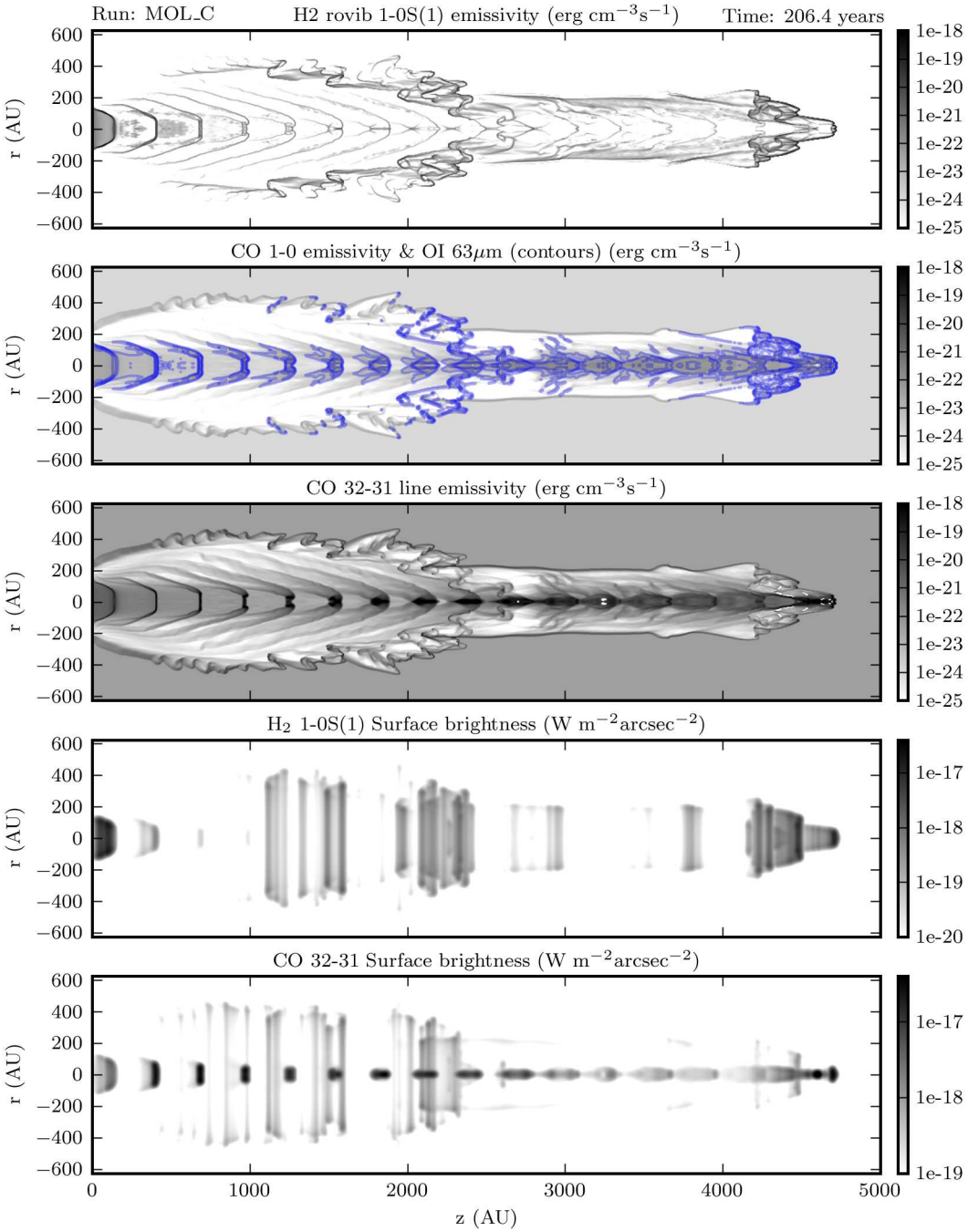

Figure A.25: **Run: MOL_C X_{H_2} = 33%** Plotted are (top to bottom): H_2 rovibrational line 1-0S(1) emissivity, CO 1-0 rotational line emissivity with OI 63μm line emission in contours at emissivities of $[10^{-20}, 10^{-19}, 10^{-18}10^{-17}]$ erg cm^{-3}s^{-1}, CO 32-31 rotational line emissivity, H_2 line 1-0S(1) and CO 32-31 rotational line surface brightnesses in W m^{-2}arcsec^{-2}.

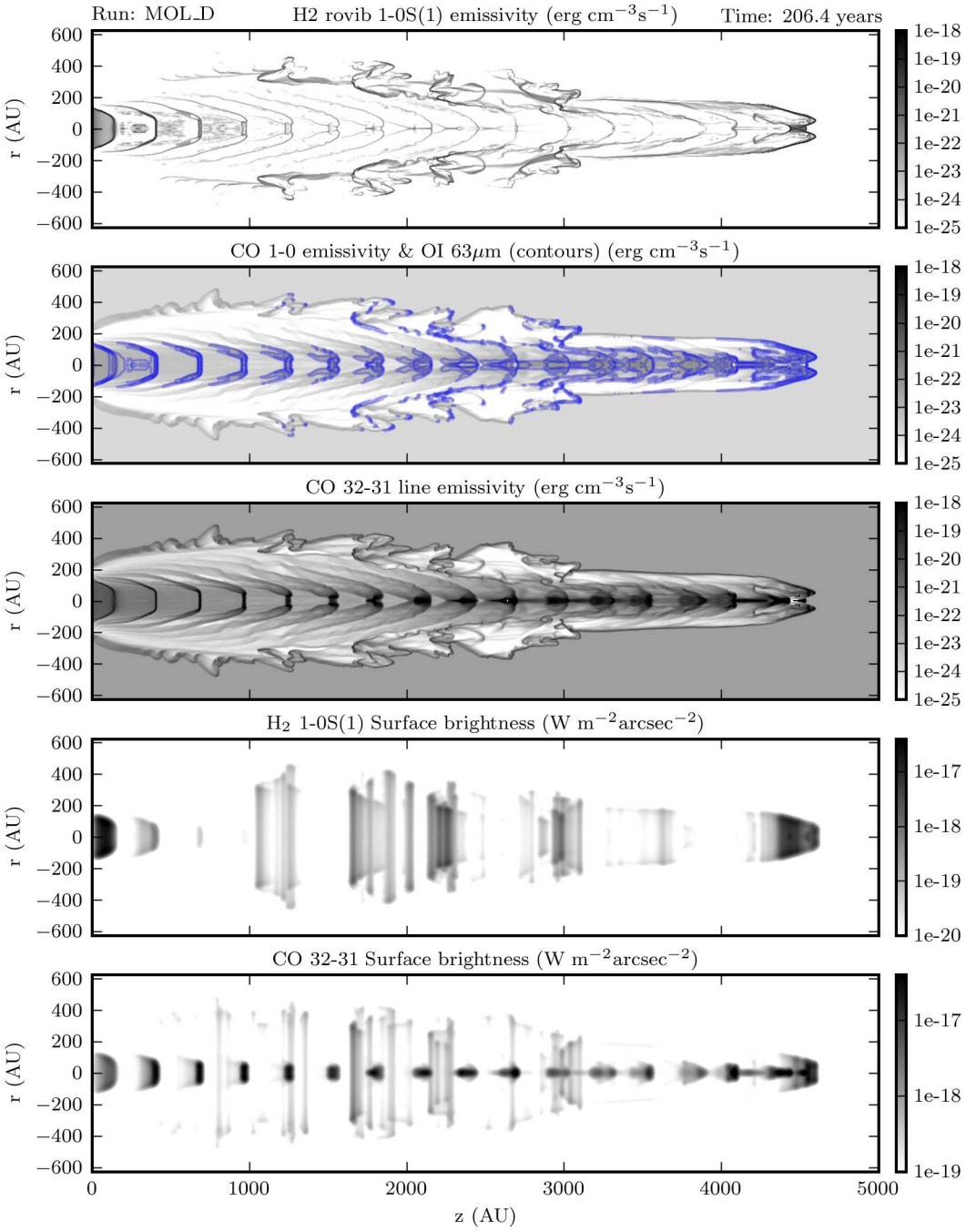

Figure A.26: **Run: MOL_D X_{H_2} = 50%** Plotted are (top to bottom): H_2 rovibrational line 1-0S(1) emissivity, CO 1-0 rotational line emissivity with OI 63μm line emission in contours at emissivities of $[10^{-20}, 10^{-19}, 10^{-18}10^{-17}]$ erg cm^{-3}s^{-1}, CO 32-31 rotational line emissivity, H_2 line 1-0S(1) and CO 32-31 rotational line surface brightnesses in W m^{-2}arcsec^{-2}.

A.4 Magnetic Field

Table A.4 shows the set of runs for examining the role of the magnetic field.

Run	X_{H2}	X_e	η	► β ◄	$B_{\parallel}$ (μG)
REF	10%	1%	10	∞	0
BETA_A	10%	1%	10	22.6	30
BETA_B	10%	1%	10	5.6	60
BETA_C	10%	1%	10	1.4	118
BETA_D	10%	1%	20	∞	0
BETA_E	10%	1%	20	2.8	83

Table A.4: Summary of runs varying the strength of the magnetic field with β defined as the ratio of the magnetic pressure with respect to the thermal pressure in the beam.

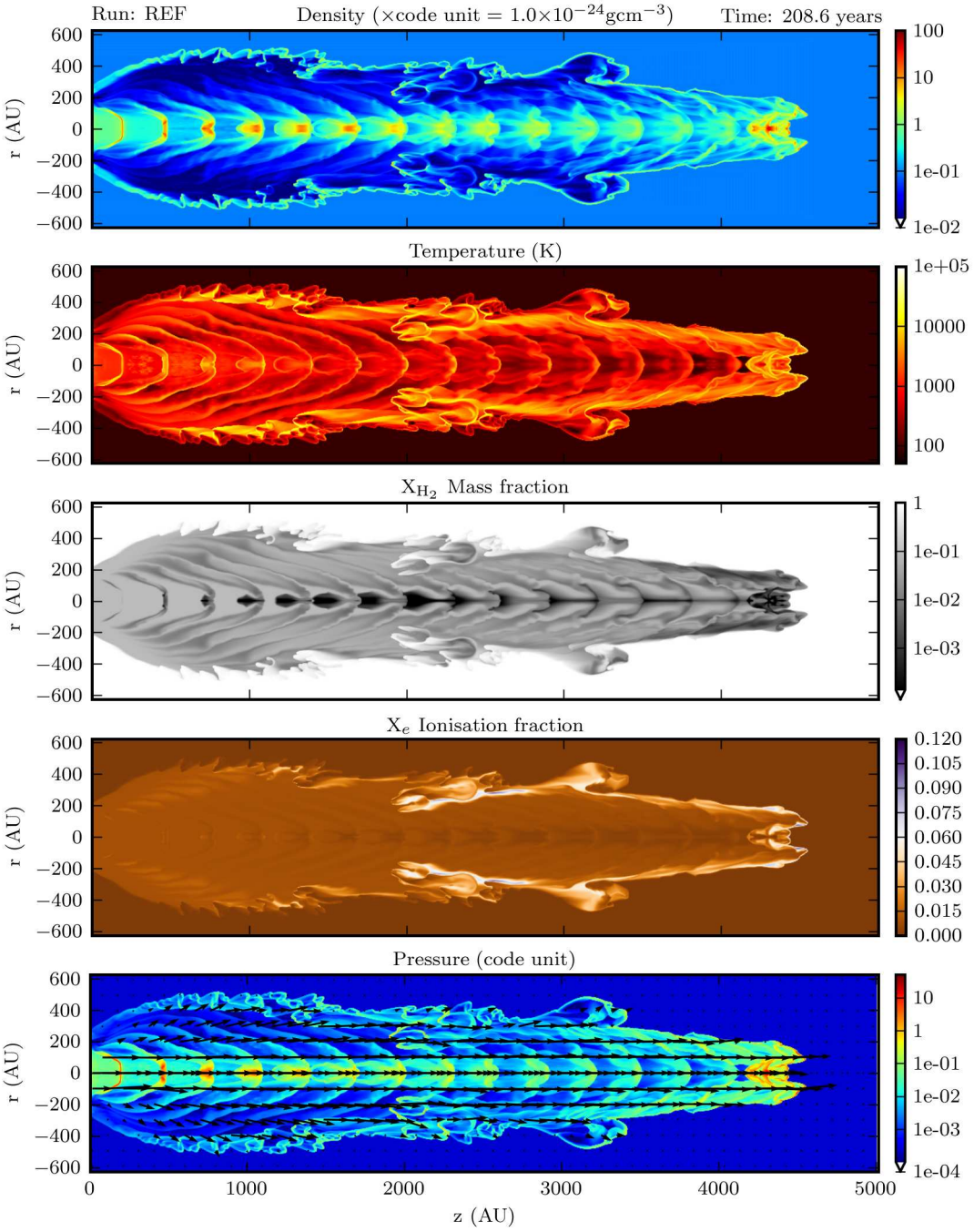

Figure A.27: Run: REF $\beta = \infty$ Plotted are (top to bottom): density ρ, Temperature, X_{H_2}, X_e and pressure, with velocity vectors normalised to the highest velocity.

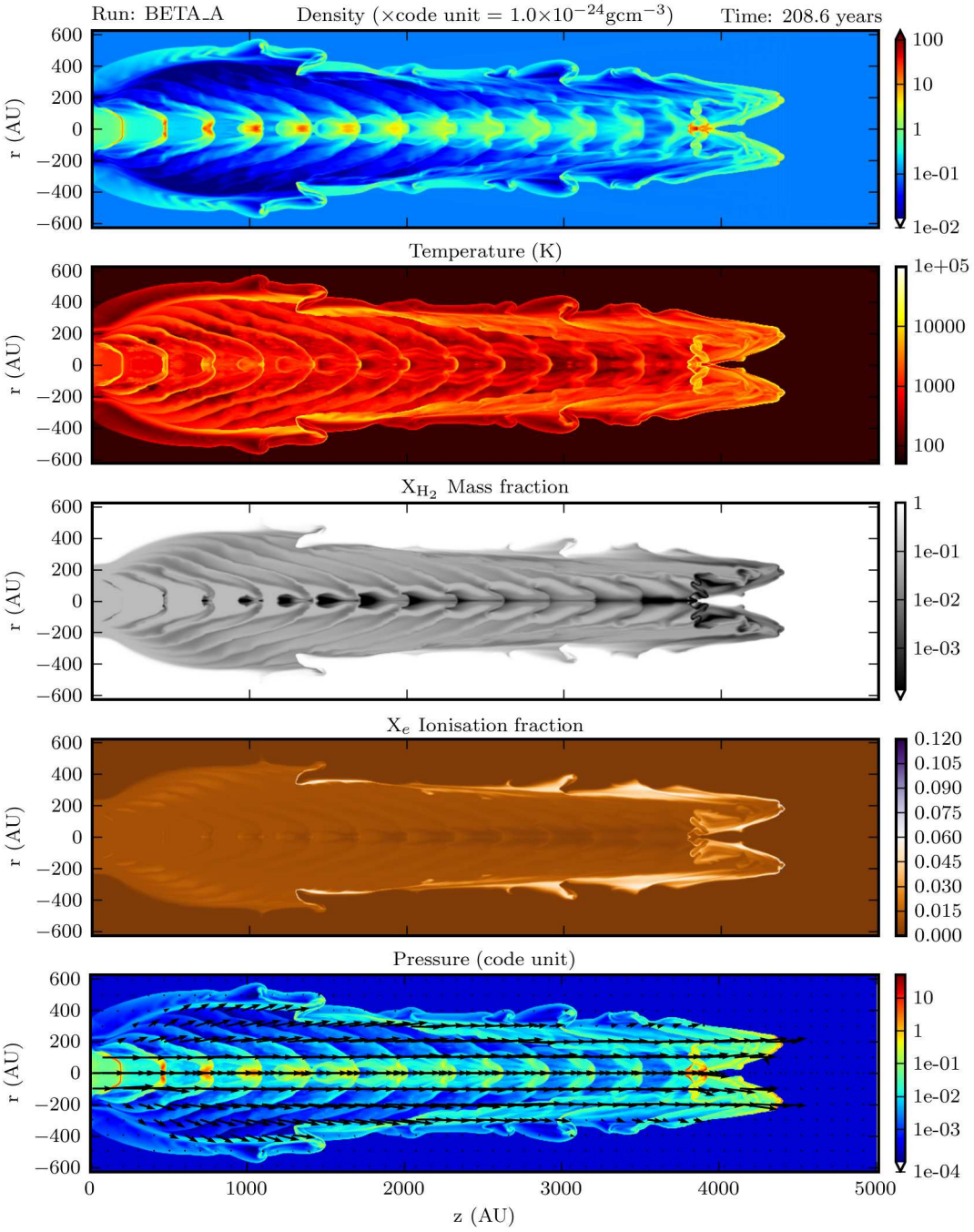

Figure A.28: Run: BETA_A $\beta = 22.6$ Plotted are (top to bottom): density ρ, Temperature, X_{H_2}, X_e and pressure, with velocity vectors normalised to the highest velocity.

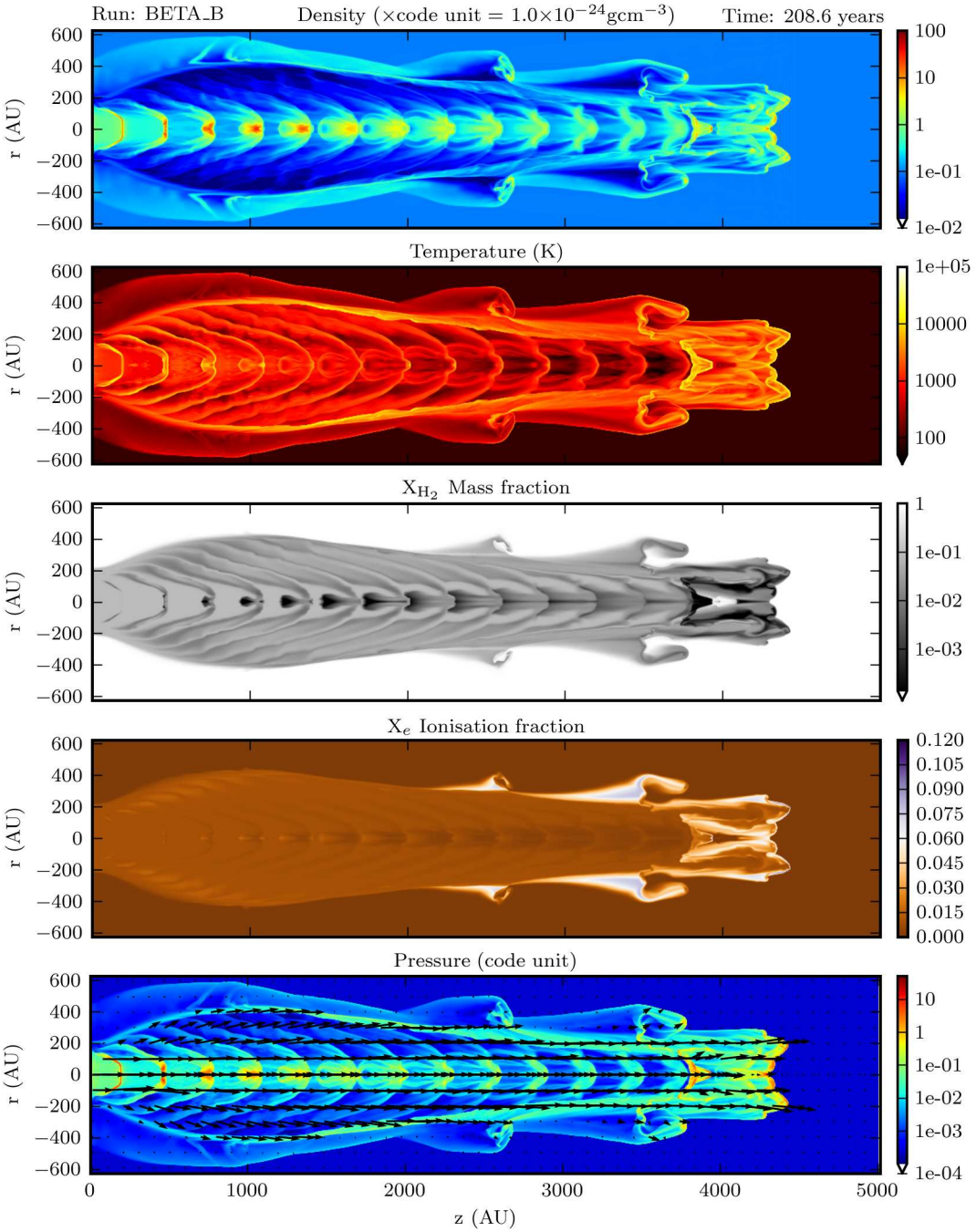

Figure A.29: Run: BETA_B $\beta = 5.6$ Plotted are (top to bottom): density ρ, Temperature, X_{H_2}, X_e and pressure, with velocity vectors normalised to the highest velocity.

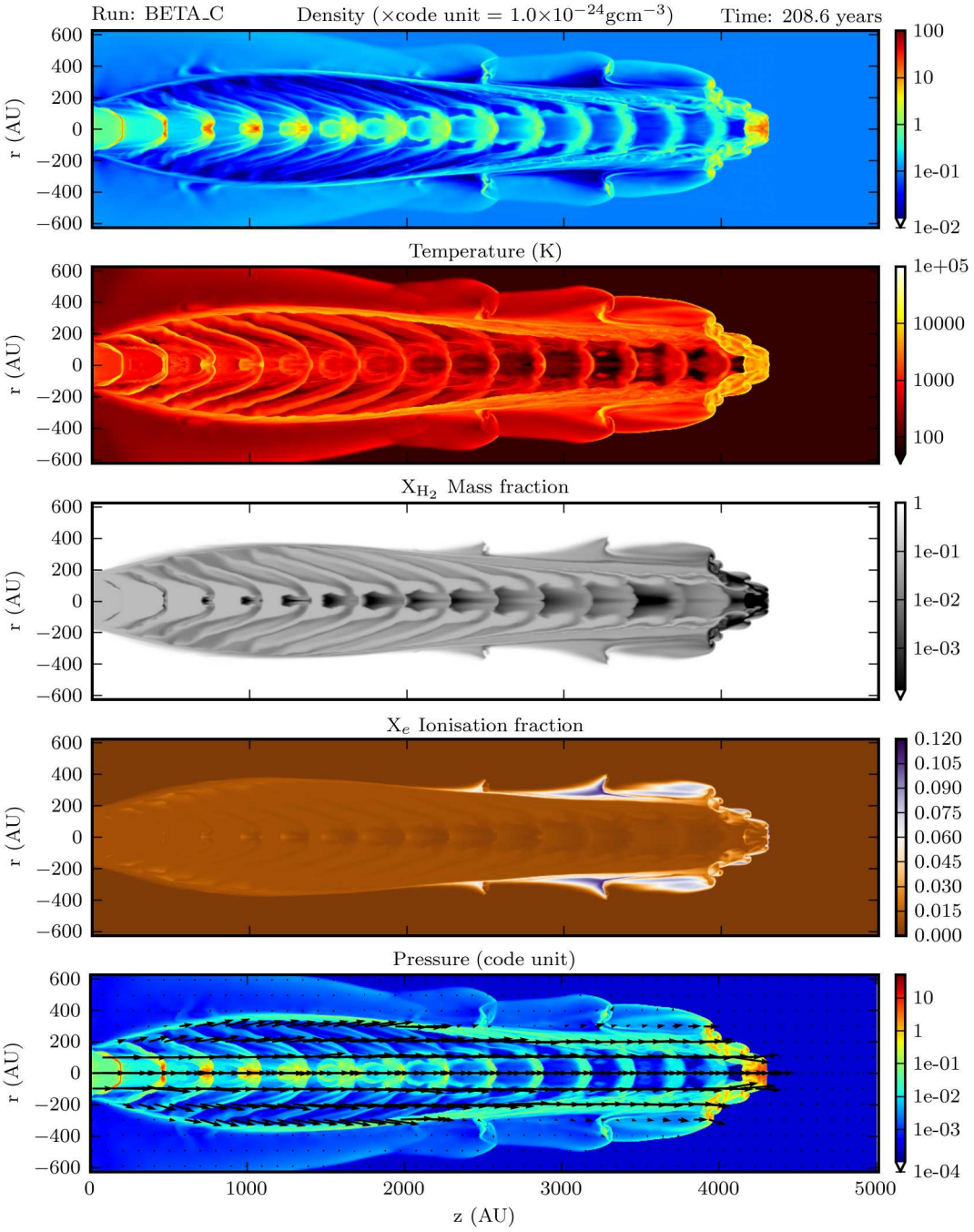

Figure A.30: Run: BETA_C $\beta = 1.4$ Plotted are (top to bottom): density ρ, Temperature, X_{H_2}, X_e and pressure, with velocity vectors normalised to the highest velocity.

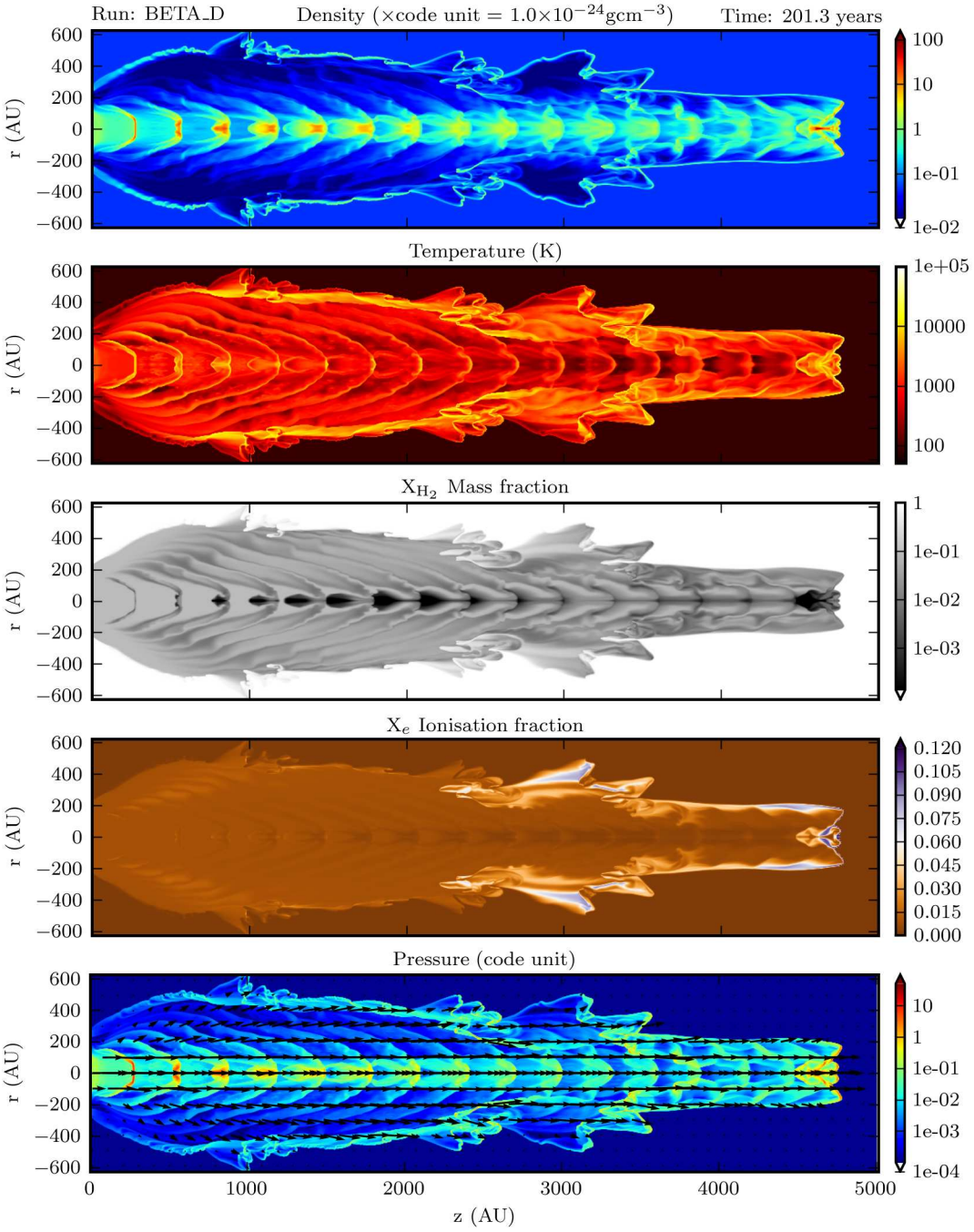

Figure A.31: Run: BETA_D $\beta = \infty$, $\eta = 20$ Plotted are (top to bottom): density ρ, Temperature, X_{H_2}, X_e and pressure, with velocity vectors normalised to highest velocity.

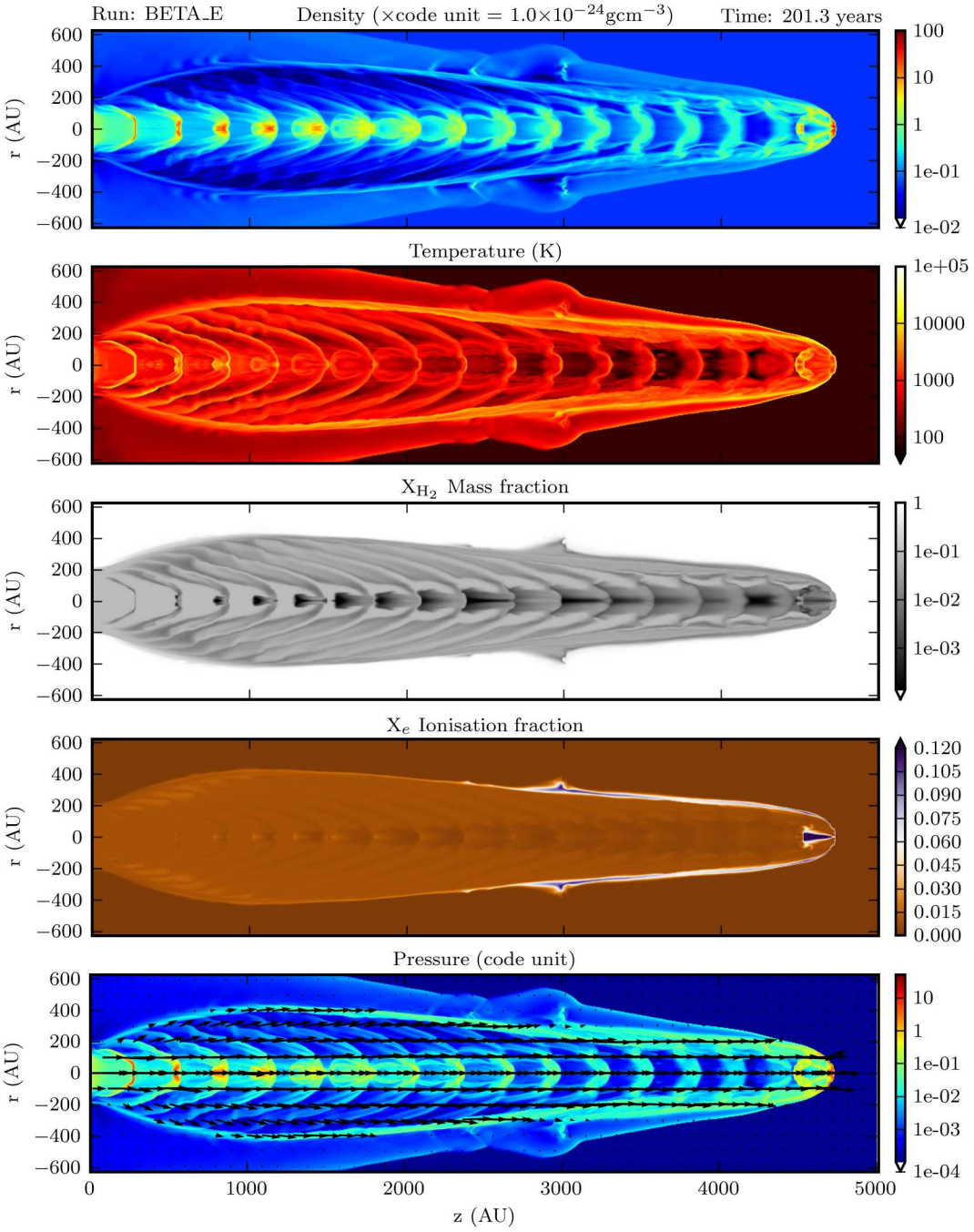

Figure A.32: Run: BETA_E $\beta = 2.8$, $\eta = 20$ Plotted are (top to bottom): density ρ, Temperature, X_{H_2}, X_e and pressure, with velocity vectors normalised to highest velocity.

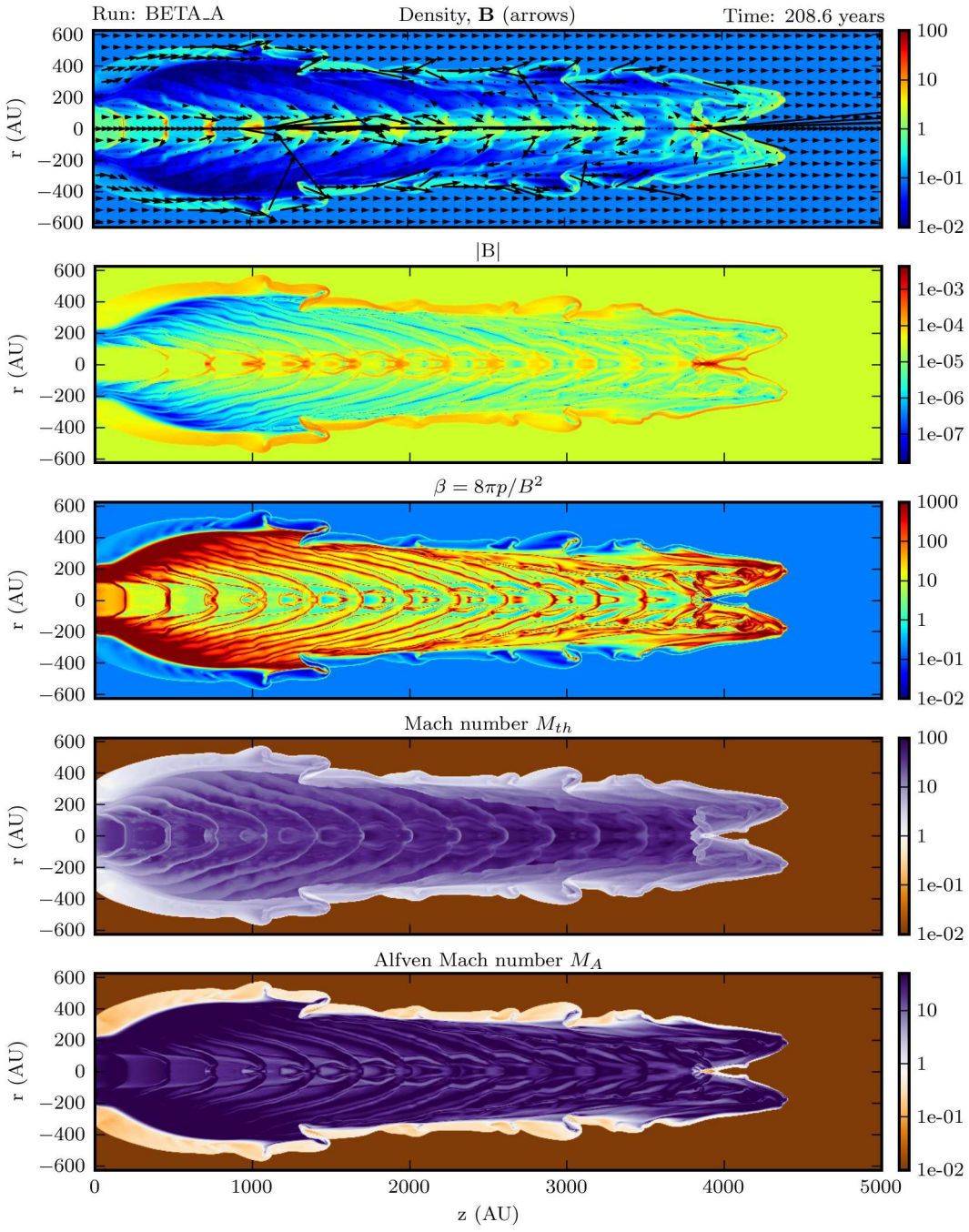

Figure A.33: Magnetic variables for BETA_A $\beta = 22.6$**.** Plotted are, from top to bottom: Mass density with magnetic field lines, magnetic field modulus, magnetic beta, local sonic and Alfven Mach numbers.

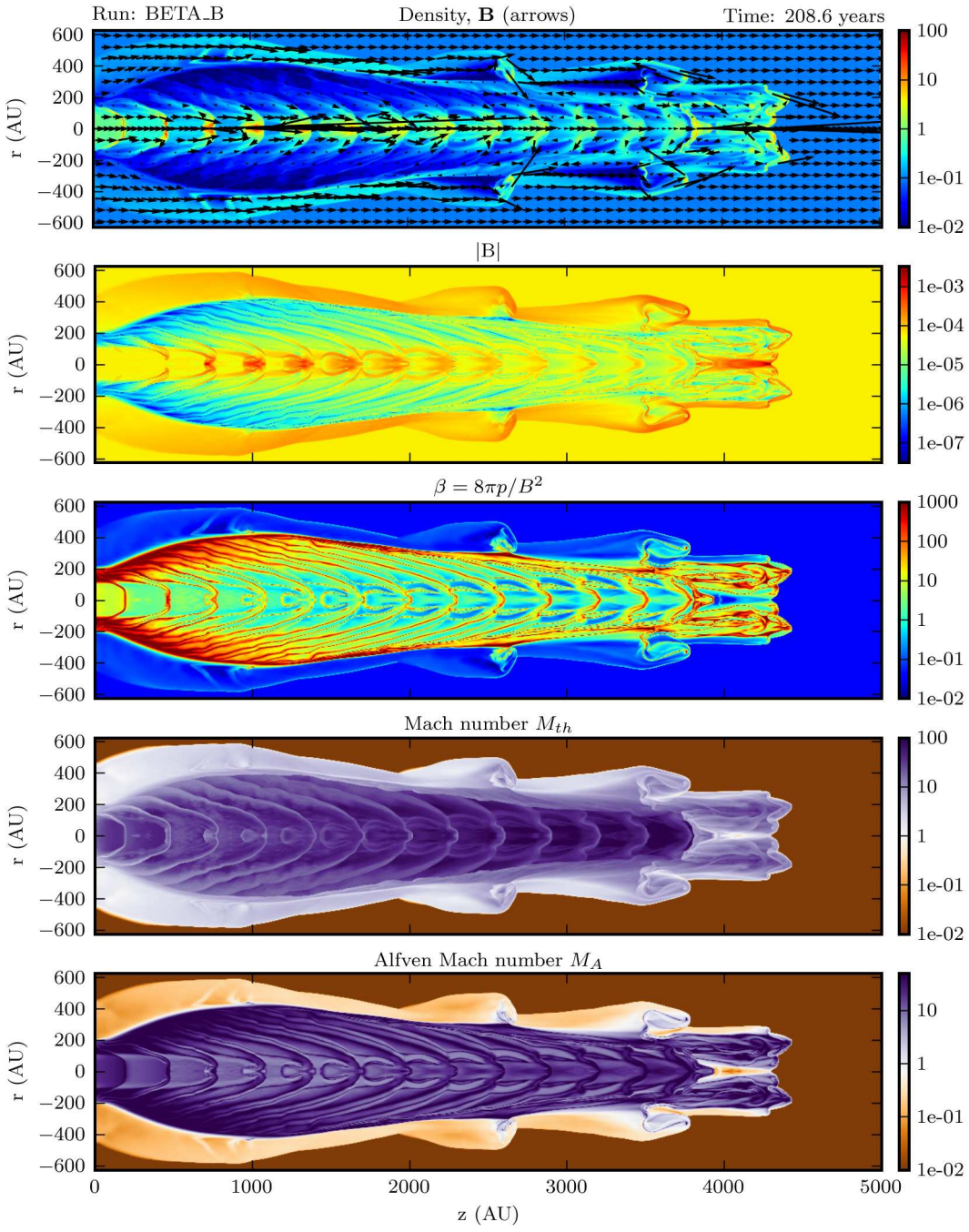

Figure A.34: Magnetic variables for BETA_B $\beta = 5.6$**.** Plotted are, from top to bottom: Mass density with magnetic field lines, magnetic field modulus, magnetic beta, local sonic and Alfven Mach numbers.

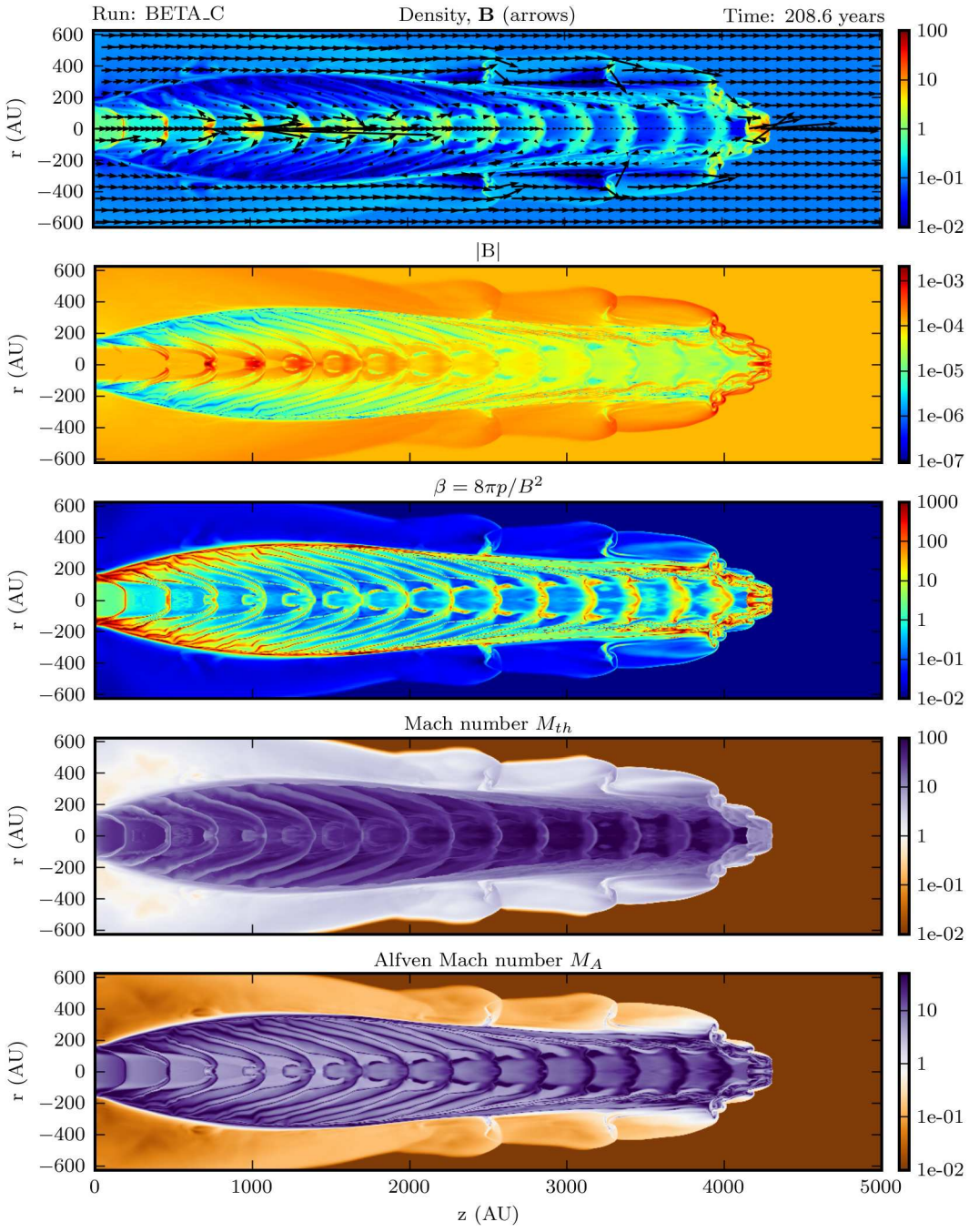

Figure A.35: Magnetic variables for BETA_C $\beta = 1.4$**.** Plotted are, from top to bottom: Mass density with magnetic field lines, magnetic field modulus, magnetic beta, local sonic and Alfven Mach numbers.

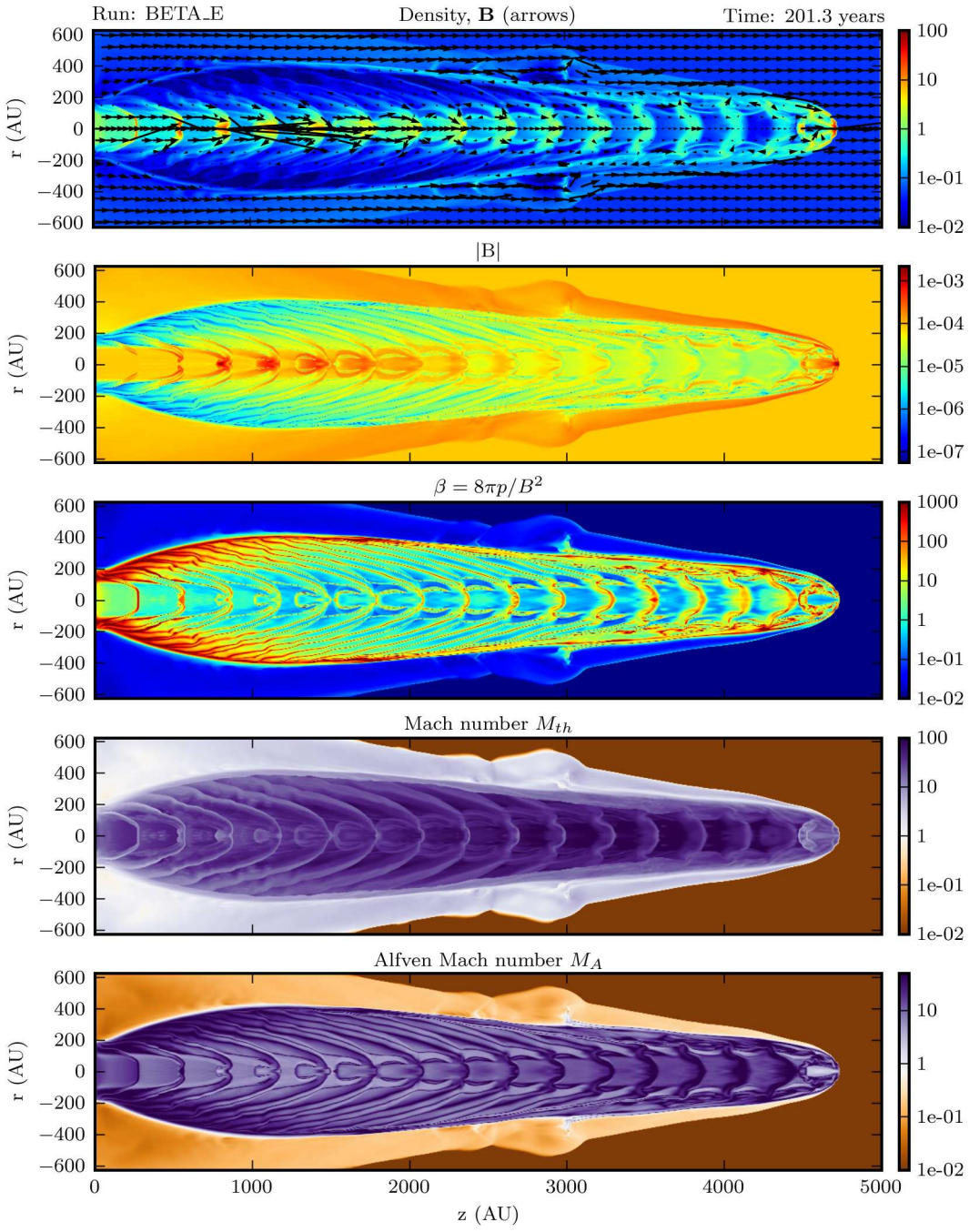

Figure A.36: Magnetic variables for BETA_E $\beta = 2.8$**.** Plotted are, from top to bottom: Mass density with magnetic field lines, magnetic field modulus, magnetic beta, local sonic and Alfven Mach numbers.

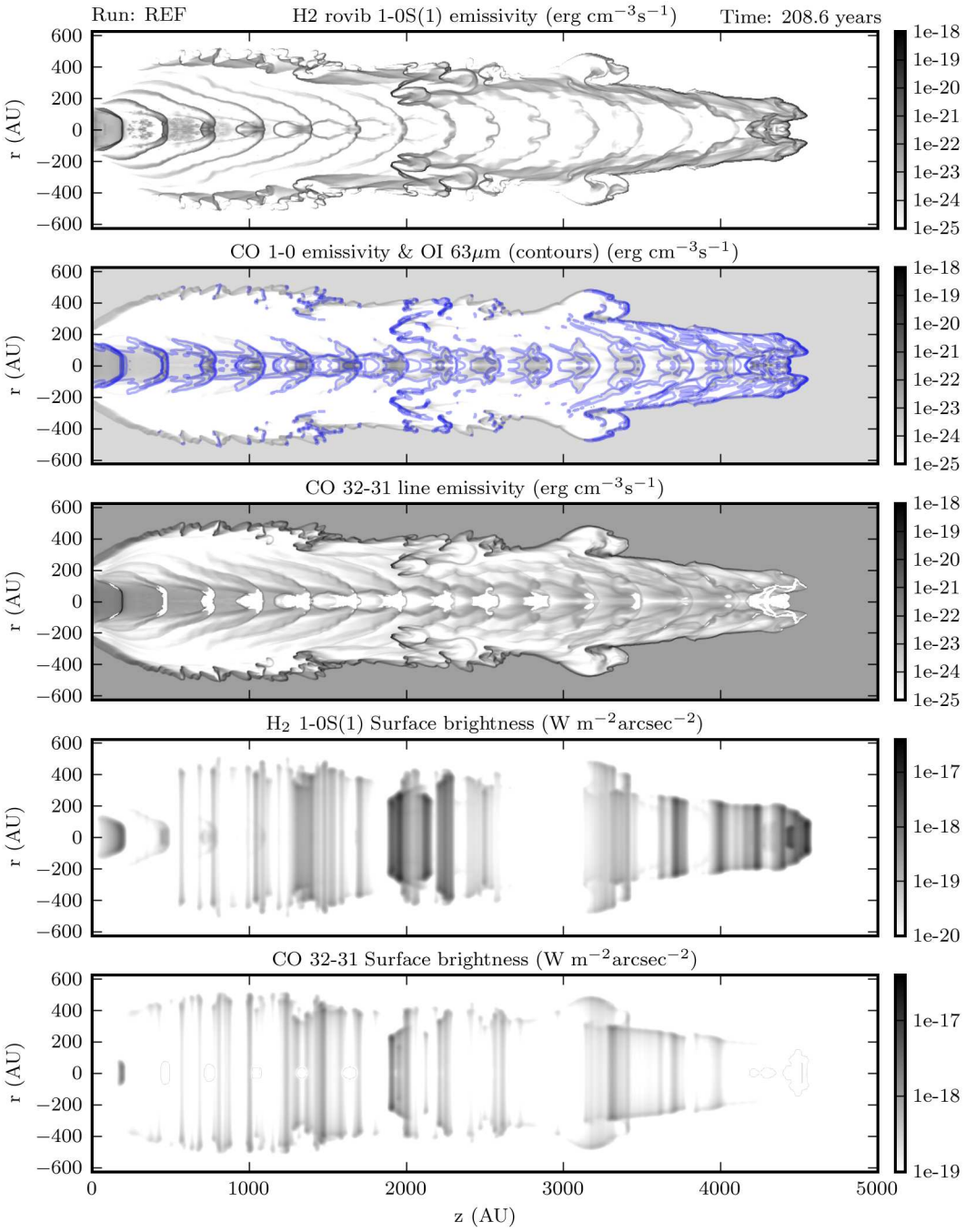

Figure A.37: Run: REF $\beta = \infty$ Plotted are (top to bottom): H_2 ro-vibrational line 1-0S(1) emissivity, CO 1-0 rotational line emissivity with OI 63μm line emission in contours at emissivities of $[10^{-20}, 10^{-19}, 10^{-18}10^{-17}]$ erg cm^{-3}s^{-1}, CO 32-31 rotational line emissivity, H_2 line 1-0S(1) and CO 32-31 rotational line surface brightnesses in W m^{-2}arcsec^{-2}.

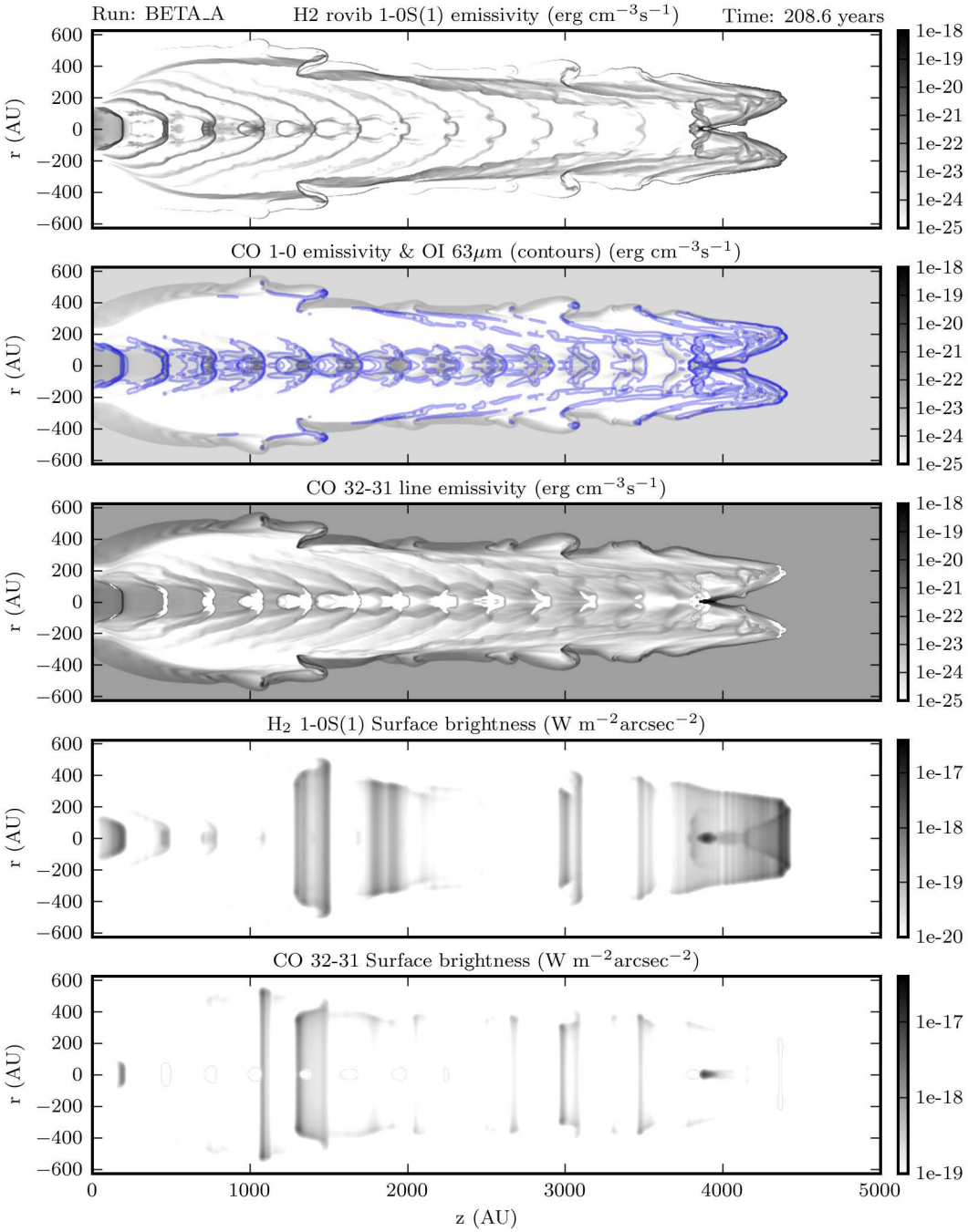

Figure A.38: Run: BETA_A $\beta = 22.6$ Plotted are (top to bottom): H_2 ro-vibrational line 1-0S(1) emissivity, CO 1-0 rotational line emissivity with OI 63μm line emission in contours at emissivities of $[10^{-20}, 10^{-19}, 10^{-18}10^{-17}]$ erg cm^{-3}s^{-1}, CO 32-31 rotational line emissivity, H_2 line 1-0S(1) and CO 32-31 rotational line surface brightnesses in W m^{-2}arcsec^{-2}.

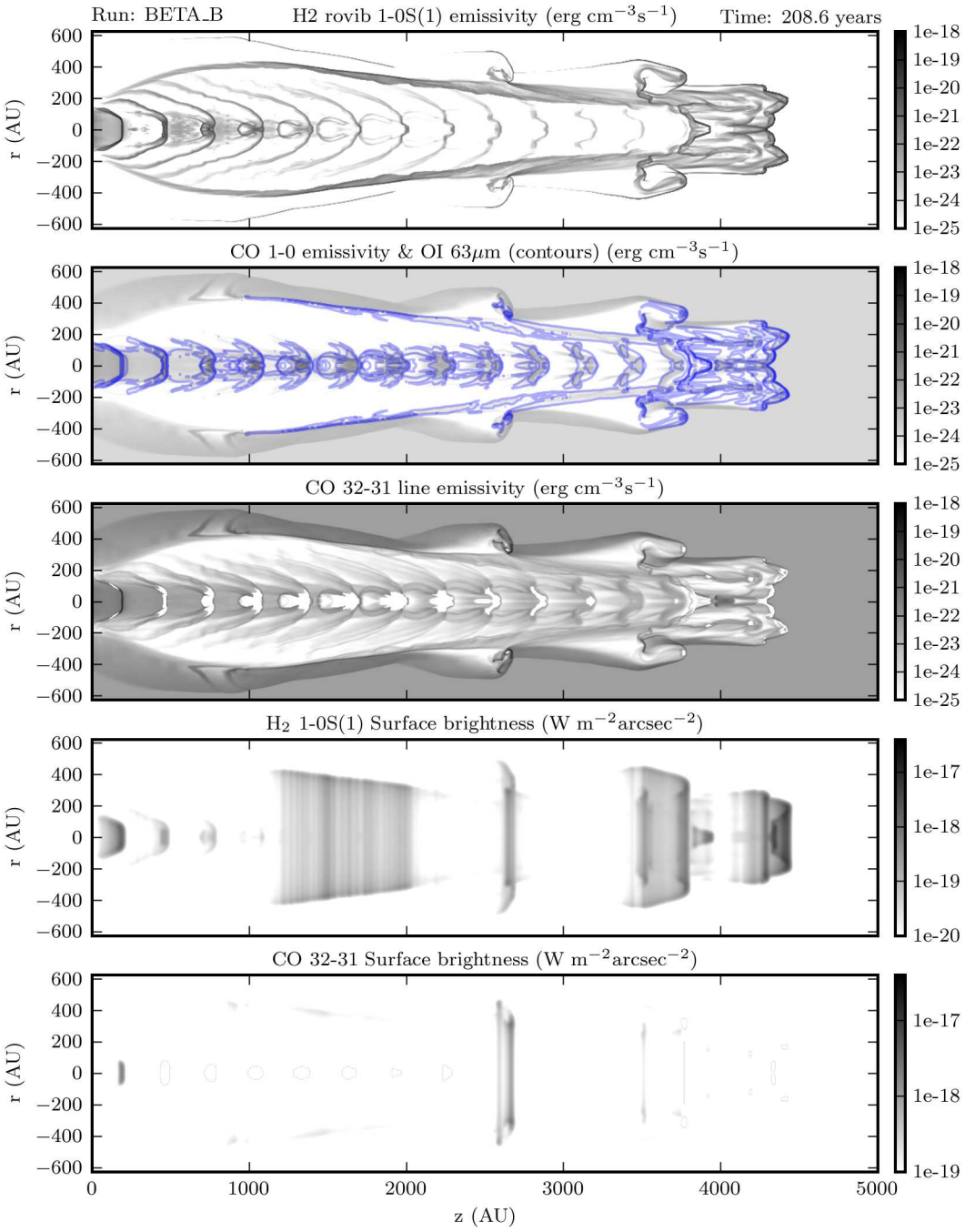

Figure A.39: Run: BETA_B $\beta = 5.6$ Plotted are (top to bottom): H_2 ro-vibrational line 1-0S(1) emissivity, CO 1-0 rotational line emissivity with OI 63μm line emission in contours at emissivities of $[10^{-20}, 10^{-19}, 10^{-18}10^{-17}]$ erg cm^{-3}s^{-1}, CO 32-31 rotational line emissivity, H_2 line 1-0S(1) and CO 32-31 rotational line surface brightnesses in W m^{-2}arcsec^{-2}.

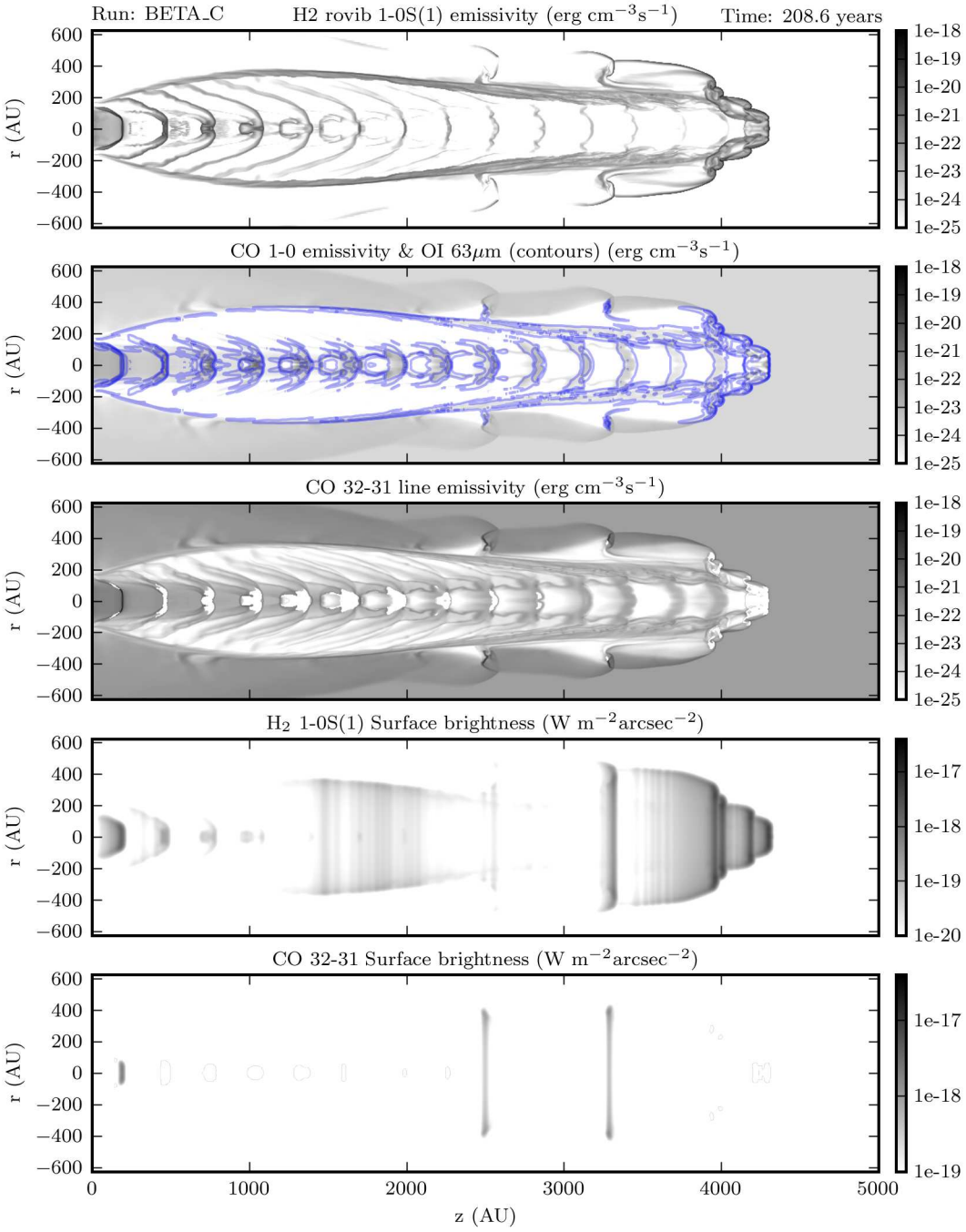

Figure A.40: Run: BETA_C $\beta = 1.4$ Plotted are (top to bottom): H_2 ro-vibrational line 1-0S(1) emissivity, CO 1-0 rotational line emissivity with OI 63μm line emission in contours at emissivities of $[10^{-20}, 10^{-19}, 10^{-18}10^{-17}]$ erg cm^{-3}s^{-1}, CO 32-31 rotational line emissivity, H_2 line 1-0S(1) and CO 32-31 rotational line surface brightnesses in W m^{-2}arcsec^{-2}.

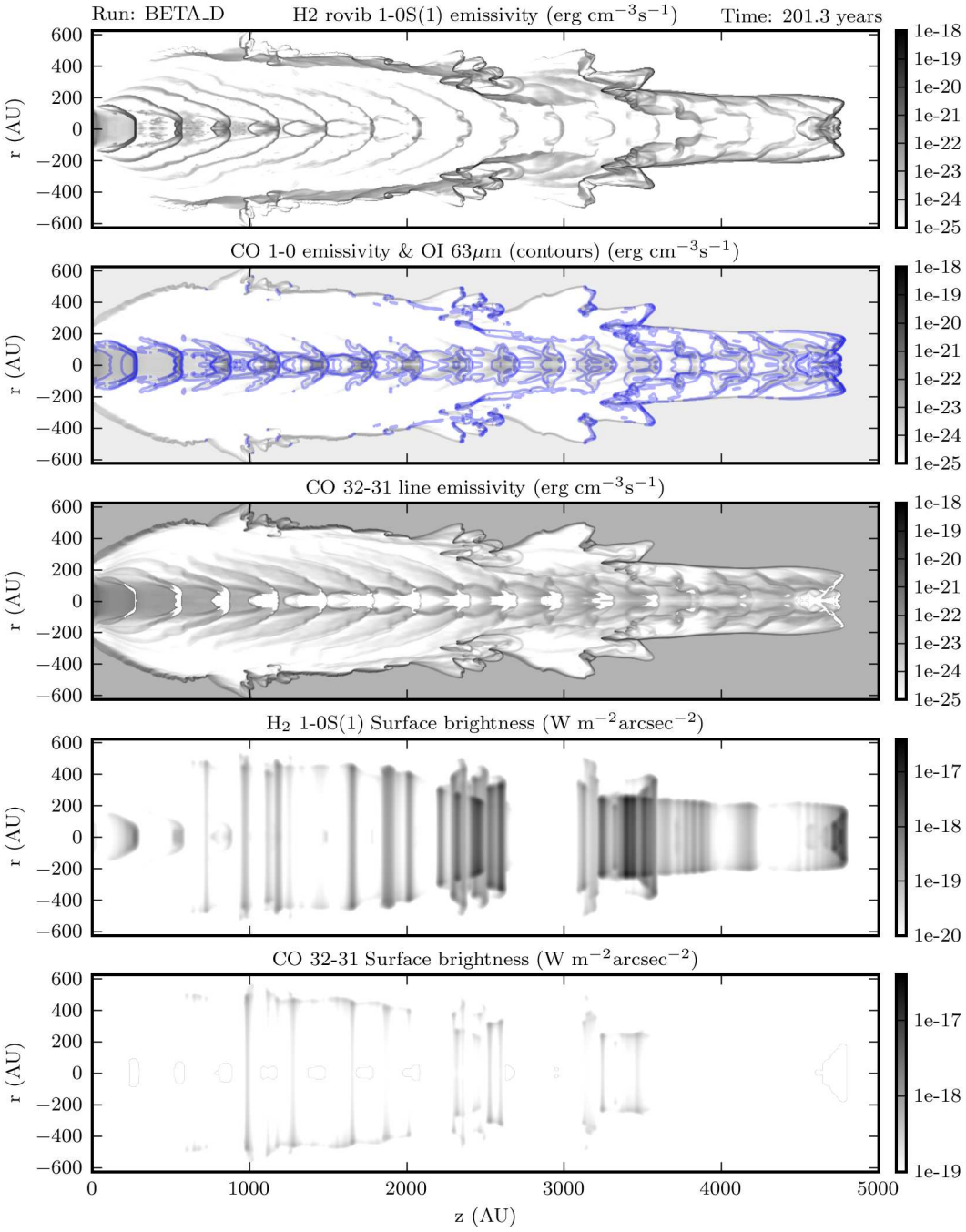

Figure A.41: **Run: BETA_D** $\beta = \infty$, $\eta = 20$ Plotted are (top to bottom): H_2 ro-vibrational line 1-0S(1) emissivity, CO 1-0 rotational line emissivity with OI 63μm line emission in contours at emissivities of $[10^{-20}, 10^{-19}, 10^{-18}10^{-17}]$ erg cm^{-3}s^{-1}, CO 32-31 rotational line emissivity, H_2 line 1-0S(1) and CO 32-31 rotational line surface brightnesses in W m^{-2}arcsec^{-2}.

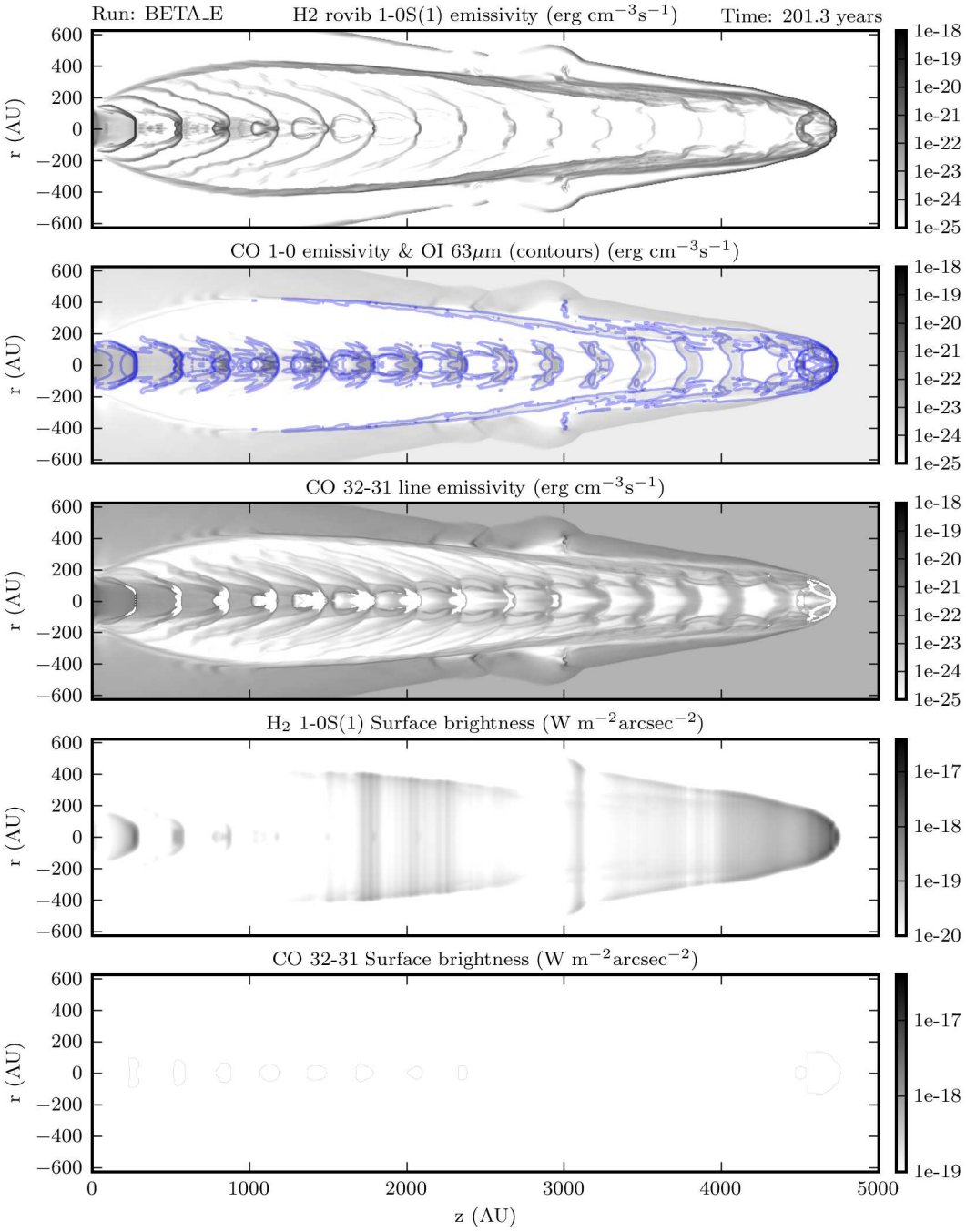

Figure A.42: Run: BETA_E $\beta = 2.8$, $\eta = 20$ Plotted are (top to bottom): H_2 ro-vibrational line 1-0S(1) emissivity, CO 1-0 rotational line emissivity with OI 63μm line emission in contours at emissivities of $[10^{-20}, 10^{-19}, 10^{-18}10^{-17}]$ erg cm^{-3}s^{-1}, CO 32-31 rotational line emissivity, H_2 line 1-0S(1) and CO 32-31 rotational line surface brightnesses in W m^{-2}arcsec^{-2}.

B

Appendix B. Additional Material

In order to give a better impression of the nature of the time dependent evolution of the jets in our simulations, we have included some videos of selected runs on a Compact Disc[1] for distribution with this thesis. These videos are:

- **REF_state.mpg & REF_emissions.mpg**
- **BETA_E_state.mpg & BETA_E_emissions.mpg**
- **MOL_D_state.mpg & MOL_D_emissions.mpg**

and are best viewed with VideoLAN's VLC player.

[1] The videos are also available for a limited time at the following web address: http://www.lsw.uni-heidelberg.de/users/josulliv/Thesis_videos/

List of Publications

- O'Sullivan, J. & Camenzind, M. (2009) Molecular Cooling in Large Scale Simulations of Protostellar Jets. *Protostellar Jets in Context, by Kanaris Tsinganos, Tom Ray, Matthias Stute. Astrophysics and Space Science Proceedings Series. Berlin: Springer, 2009.*, pp.453-458

- Cabrit, S.; Bocchi, M.; Camenzind, M.; Ciardi, A.; de Colle, F.; Downes, T.; Ferreira, J.; Frank, A.; Gracia, J.; Lebedev, S.; Marrochino, A.; Massaglia, S.; Matsakos, T.; O'Sullivan, J.; Stehl, C.; Stute, M.; Suzuki-Vidal, F.; Tesileanu, O.; Tsinganos, K.; Zanni, C. (2009) Dynamics of magnetized YSO jets: Examples of results from the JETSET network. *Magnetic Fields in the Universe II: From Laboratory and Stars to the Primordial Universe (Eds. A. Esquivel, J. Franco, G. Garca-Segura, E. M. de Gouveia Dal Pino, A. Lazarian, S. Lizano, & A. Raga) Revista Mexicana de Astronoma y Astrofsica (Serie de Conferencias)* Vol. **36**, pp. 171-178

- O'Sullivan, J. & Camenzind, M. (2008) Molecular Cooling Effects in Large-scale simulations of Herbig-Haro Objects (Poster), Physics and Chemistry of the Interstellar Medium, Arcachon France

- O'Sullivan, J. Molecular Cooling Effects in Protostellar Jets, HPC-Europa Science and Supercomputing in Europe Report 2008

Bibliography

Abel, T., Anninos, P., Zhang, Y. & Norman, M.L. (1997). Modeling primordial gas in numerical cosmology. *New Astronomy*, **2**, 181–207.

Anninos, P., Zhang, Y., Abel, T. & Norman, M.L. (1997). Cosmological hydrodynamics with multi-species chemistry and nonequilibrium ionization and cooling. *New Astronomy*, **2**, 209–224.

Bacciotti, F. & Eislöffel, J. (1999). Ionization and density along the beams of herbig-haro jets. *A&A*, **342**, 717–735.

Bally, J. & Lane, A.P. (1990). Shocked molecular hydrogen associated with herbig-haro objects and molecular outflows: The cepheus-a flow. In R. Elston, ed., *Astrophysics with Infrared Arrays*, vol. 14 of *Astronomical Society of the Pacific Conference Series*, 273.

Banerjee, R., Klessen, R.S. & Fendt, C. (2007). Can protostellar jets drive supersonic turbulence in molecular clouds? *ApJ*, **668**, 1028–1041.

Biro, S. & Raga, A.C. (1994). A numerical simulation of a variable velocity jet. *ApJ*, **434**, 221–231.

Biro, S., Raga, A.C. & Canto, J. (1995). Numerical simulation of 2d jets with time-dependent direction of ejection. *MNRAS*, **275**, 557–566.

Blondin, J.M., Fryxell, B.A. & Konigl, A. (1990). The structure and evolution of radiatively cooling jets. *ApJ*, **360**, 370–386.

Bontemps, S., Andre, P., Terebey, S. & Cabrit, S. (1996). Evolution of outflow activity around low-mass embedded young stellar objects. *A&A*, **311**, 858–872.

Canto, J. & Rodriguez, L.F. (1980). A stellar-wind focusing mechanism as an explanation for herbig-haro objects. *ApJ*, **239**, 982–987.

Carvalho, J.C., Daly, R.A., Mory, M.P. & O'Dea, C.P. (2005). Comparison of radio observations and numerical simulations of the radio lobes of cygnus a. *ApJ*, **620**, 126–144.

Cen, R. (1992). A hydrodynamic approach to cosmology - methodology. *ApJS*, **78**, 341–364.

Cerqueira, A.H., de Gouveia dal Pino, E.M. & Herant, M. (1997). Magnetic field effects on the head structure of protostellar jets. *ApJL*, **489**, –185.

Coffey, D., Bacciotti, F., Woitas, J., Ray, T.P. & Eislöffel, J. (2004). Rotation of jets from young stars: New clues from the hubble space telescope imaging spectrograph. *ApJ*, **604**, 758–765.

Coffey, D., Bacciotti, F. & Podio, L. (2008). T tauri jet physics resolved near the launching region with the hubble space telescope. *ApJ*, **689**, 1112–1126.

Davis, C.J., Froebrich, D., Stanke, T., Megeath, S.T., Kumar, M.S.N., Adamson, A., Eislöffel, J., Gredel, R., Khanzadyan, T., Lucas, P., Smith, M.D. & Varricatt, W.P. (2009). A census of molecular hydrogen outflows and their sources along the orion a molecular ridge. *Astronomy and Astrophysics*, **496**, 153.

Dgani, R., van Buren, D. & Noriega-Crespo, A. (1996). Stability analysis of bow shocks. *ApJ*, **461**, 927.

Dopita, A. (1978). The herbig-haro objects in the gum nebula. *A&A*, **63**, 237–241.

Downes, T.P. & Cabrit, S. (2003). The mass-velocity and intensity-velocity relations in jet-driven molecular outflows. *A&A*, **403**, 135–140.

Draine, B.T. (1980). Interstellar shock waves with magnetic precursors. *ApJ*, **241**, 1021–1038.

Efremov, Y.N. & Elmegreen, B.G. (1998). Hierarchical star formation from the time-space distribution of star clusters in the large magellanic cloud. *MNRAS*, **299**, 588–594.

Flower, D. (2007). *Molecular collisions in the interstellar medium: University Press, 2007 vii, 187 p. Cambridge astrophysics series, vol. 42.*

Flower, D.R., Le Bourlot, J., Pineau des Forêts, G. & Cabrit, S. (2003). The contributions of j-type shocks to the h_2 emission from molecular outflow sources. *MNRAS*, **341**, 70–80.

Frank, A., Ryu, D., Jones, T.W. & Noriega-Crespo, A. (1998). Effects of cooling on the propagation of magnetized jets. *ApJL*, **494**, –79.

Frank, A., Gardiner, T.A., Delemarter, G., Lery, T. & Betti, R. (1999). Ambipolar diffusion in young stellar object jets. *ApJ*, **524**, 947–951.

Gaibler, V., Krause, M. & Camenzind, M. (2009). Very light magnetized jets on large scales - i. evolution and magnetic fields. *ArXiv e-prints*.

Gålfalk, M. (2007). Herbig-haro flows in b335. *Astronomy and Astrophysics*, **475**, 281.

Galli, D. & Palla, F. (1998). The chemistry of the early universe. *A&A*, **335**, 403–420.

Giannini, T., Nisini, B., Caratti o Garatti, A. & Lorenzetti, D. (2002). Understanding the nature of protostellar jets through near-infrared spectroscopy: The key role of the j band proved on hh 43. *ApJ*, **570**, –33.

Glover, S.C.O. (2008). Uncertainties in h2 and hd chemistry and cooling and their role in early structure formation. *Monthly Notices of the Royal Astronomical Society*, **388**, 1627.

Gough, B. (2009). *GNU Scientific Library Reference Manual - Third Edition*. Network Theory Ltd.

Gredel, R. (1996). The excitation of molecular hydrogen in hh 1 and in hh 7 to 11. *A&A*, **305**, 582.

Gueth, F. & Guilloteau, S. (1999). The jet-driven molecular outflow of hh 211. *A&A*, **343**, 571–584.

Haro, G. (1952). Herbig's nebulous objects near ngc 1999. *ApJ*, **115**, 572.

Herbig, G.H. (1950). The spectrum of the nebulosity surrounding t tauri. *ApJ*, **111**, 11.

Herbig, G.H. & Jones, B.F. (1981). Large proper motions of the herbig-haro objects hh 1 and hh 2. *Astronomical Journal*, **86**, 1232–1244.

Hollenbach, D. (1997). The physics of molecular shocks in yso outflows. In B.R..C. Bertout, ed., *Herbig-Haro Flows and the Birth of Stars*, vol. 182 of *IAU Symposium*, 181–198.

Hollenbach, D. & McKee, C.F. (1979). Molecule formation and infrared emission in fast interstellar shocks. i physical processes. *ApJS*, **41**, 555–592.

Hollenbach, D. & McKee, C.F. (1989). Molecule formation and infrared emission in fast interstellar shocks. iii - results for j shocks in molecular clouds. *ApJ*, **342**, 306–336.

Keegan, R. (2005). Long-duration simulations of the evolution of jet-driven molecular outflows. *Astronomy and Astrophysics*, **437**, 517.

Kirk, H., Johnstone, D. & Basu, S. (2009). The interplay of turbulence and magnetic fields in star-forming regions: Simulations and observations. *ApJ*, **699**, 1433–1453.

Kirk, J.M. (2007). The initial conditions of isolated star formation vii. spitzer mapping of pre-stellar cores. *Monthly Notices of the Royal Astronomical Society*, **375**, 843.

Lada, C.J. (1985). Cold outflows, energetic winds, and enigmatic jets around young stellar objects. *ARA&A*, **23**, 267–317.

Le Bourlot, J., Pineau des Forêts, G., Flower, D.R. & Cabrit, S. (2002). New determinations of the critical velocities of c-type shock waves in dense molecular clouds: application to the outflow source in orion. *MNRAS*, **332**, 985–993.

Lee, C.F., Mundy, L.G., Reipurth, B., Ostriker, E.C. & Stone, J.M. (2000). Co outflows from young stars: Confronting the jet and wind models. *ApJ*, **542**, 925–945.

Lee, C.F., Ho, P.T.P., Bourke, T.L., Hirano, N., Shang, H. & Zhang, Q. (2008). Sio shocks of the protostellar jet hh 212: A search for jet rotation. *ApJ*, **685**, 1026–1032.

Lery, T. (2007). Transit flows and jet asymptotics. In .E.W. J. Ferreira C. Dougados, ed., *Lecture Notes in Physics, Berlin Springer Verlag*, vol. 723 of *Lecture Notes in Physics, Berlin Springer Verlag*, 161.

Mac Low, M.M. & Klessen, R.S. (2004). Control of star formation by supersonic turbulence. *Reviews of Modern Physics*, **76**, 125–194.

Maret, S., Caux, E., Baluteau, J.P., Ceccarelli, C., Gry, C. & Vastel, C. (2001). The far infrared co line emission of orion bn/kl. In A.M.H.T.P..R.H. G. L. Pilbratt J. Cernicharo, ed., *The Promise of the Herschel Space Observatory*, vol. 460 of *ESA Special Publication*, 455.

Massaglia, S., Mignone, A. & Bodo, G. (2005). Time-dependent shocks and line emission in herbig-haro jets. *Memorie della Societa Astronomica Italiana*, **76**, 378.

McCaughrean, M.J., Rayner, J.T. & Zinnecker, H. (1994). Discovery of a molecular hydrogen jet near ic 348. *ApJL*, **436**, –189.

McKee, C.F., Storey, J.W.V., Watson, D.M. & Green, S. (1982). Far-infrared rotational emission by carbon monoxide. *ApJ*, **259**, 647–656.

Miettinen, O., Harju, J., Haikala, L.K., Kainulainen, J. & Johansson, L.E.B. (2009). Prestellar and protostellar cores in orion b9. *Astronomy and Astrophysics*, **500**, 845.

Mignone, A., Bodo, G., Massaglia, S., Matsakos, T., Tesileanu, O., Zanni, C. & Ferrari, A. (2007). Pluto: A numerical code for computational astrophysics. *ApJS*, **170**, 228–242.

Mundt, R. (1985). Mass outflows from t tauri stars and their interaction with the environment. In G. Serra, ed., *Nearby Molecular Clouds*, vol. 237 of *Lecture Notes in Physics, Berlin Springer Verlag*, 160–180.

Mundt, R. & Fried, J.W. (1983). Jets from young stars. *ApJL*, **274**, –83.

Neufeld, D.A. & Kaufman, M.J. (1993). Radiative cooling of warm molecular gas. *ApJ*, **418**, 263.

Norman, M.L., Winkler, K.H.A., Smarr, L. & Smith, M.D. (1982). Structure and dynamics of supersonic jets. *A&A*, **113**, 285–302.

O'Connell, B. (2005). The near-infrared excitation of the hh 211 protostellar outflow. *Astronomy and Astrophysics*, **431**, 223.

O'Connell, B.F. (2005). *The Impact of Protostellar Jets on their Environment*. Ph.D. thesis, AA(Armagh Observatory, College Hill, Armagh BT61 9DG, Northern Ireland).

Osterbrock, D.E. (1958). Two dense nebulae. *PASP*, **70**, 399.

Panoglou, D., Cabrit, S., Garcia, P.J.V. & Pineau Des Forêts, G. (2009a). *Survival of Molecules in MHD Disk Winds: Springer, 2009., pp.453-458*, 453–458.

Panoglou, D., Garcia, P.J.V., Cabrit, S. & Pineau Des Forêts, G. (2009b). *22 and CO in MHD Disk Winds of Class 0, Class I and Class II Stars: Springer, 2009., pp.593-594*, 593–594.

Quillen, A.C., Thorndike, S.L., Cunningham, A., Frank, A., Gutermuth, R.A., Blackman, E.G., Pipher, J.L. & Ridge, N. (2005). Turbulence driven by outflow-blown cavities in the molecular cloud of ngc 1333. *ApJ*, **632**, 941–955.

Reipurth, B. (2000). General catalogue of herbig-haro objects (reipurth+, 1999). *VizieR Online Data Catalog*, **5104**, 0.

Reipurth, B., Bally, J., Graham, J.A., Lane, A.P. & Zealey, W.J. (1986). The jet and energy source of hh 34. *A&A*, **164**, 51–66.

Rossi, P., Bodo, G., Massaglia, S. & Ferrari, A. (1997). Evolution of kelvin-helmholtz instabilities in radiative jets. ii. shock structure and entrainment properties. *A&A*, **321**, 672–684.

Schulz, N.S. (2005). *From Dust To Stars Studies of the Formation and Early Evolution of Stars*. Springer-Praxis books in astrophysics and astronomy.

Schwartz, R.D. (1975). T tauri nebulae and herbig-haro nebulae - evidence for excitation by a strong stellar wind. *ApJ*, **195**, 631–642.

Smith, M.D. & Rosen, A. (2003). The instability of fast shocks in molecular clouds. *MNRAS*, **339**, 133–147.

Smith, M.D. & Rosen, A. (2007). Hydrodynamic simulations of rotating molecular jets. *Monthly Notices of the Royal Astronomical Society*, **378**, 691.

Smith, M.D., Suttner, G. & Yorke, H.W. (1997). Numerical hydrodynamic simulations of jet-driven bipolar outflows. *A&A*, **323**, 223–230.

Smith, N., Bally, J., Churchwell, E., Whitney, B., Babler, B., Meade, M., Stassun, K., Brooks, K.J., Morse, J.A. & Walborn, N.R. (2005). Hst and spitzer surveys of the carina nebula: New irradiated herbig- haro jets. In *Protostars and Planets V*, 8240.

Snell, R.L., Loren, R.B. & Plambeck, R.L. (1980). Observations of co in l1551 - evidence for stellar wind driven shocks. *ApJL*, **239**, –17.

Spitzer, L. (1978). *Physical processes in the interstellar medium*.

Stone, J.M. & Norman, M.L. (1993). Numerical simulations of protostellar jets with nonequilibrium cooling. ii. models of pulsed jets. *ApJ*, **413**, 210.

Suttner, G., Smith, M.D., Yorke, H.W. & Zinnecker, H. (1997). Multi-dimensional numerical simulations of molecular jets. *A&A*, **318**, 595–607.

Tesileanu, O., Mignone, A. & Massaglia, S. (2008). Simulating radiative astrophysical flows with the pluto code: a non-equilibrium, multi-species cooling function. *A&A*, **488**, 429–440.

Velusamy, T., Langer, W.D. & Marsh, K.A. (2007). Highly collimated jets and wide-angle outflows in hh 46/47: New evidence from spitzer infrared images. *ApJL*, **668**, –159.

Völker, R., Smith, M.D., Suttner, G. & Yorke, H.W. (1999). Numerical hydrodynamic simulations of molecular outflows driven by hammer jets. *A&A*, **343**, 953–965.

Woitas, J., Bacciotti, F., Ray, T.P., Marconi, A., Coffey, D. & Eisl*ffel, J. (2005). Jet rotation: Launching region, angular momentum balance and magnetic properties in the bipolar outflow from rw aur. *Astronomy and Astrophysics*, **432**, 149.

Woodall, J., Agúndez, M., Markwick-Kemper, A.J. & Millar, T.J. (2007). The umist database for astrochemistry 2006. *A&A*, **466**, 1197–1204.

Yoshida, N., Omukai, K., Hernquist, L. & Abel, T. (2006). Formation of primordial stars in a Λcdm universe. *ApJ*, **652**, 6–25.

Zinnecker, H., McCaughrean, M. & Rayner, J. (1997). Hh212: a prototype molecular hydrogen jet from a deeply embedded protostar. In B. Reipurth & C. Bertout, eds., *Herbig-Haro Flows and the Birth of Stars*, vol. 182 of *IAU Symposium*, 198.

Acknowledgements

I would like to take the opportunity to thank the people who have supported me through my Ph.D. experience. There are several people I would like to thank, and without whom my work would not have been possible. First of all I am grateful to my supervisor Max Camenzind for giving me this perfect opportunity to return to science, and for his guidance, wisdom, and continuous support throughout the course of this project. Thanks to Robi Banerjee for kindly agreeing to referee this thesis and for useful suggestions to improve it, Reinhardt Mundt and Ulrich Platt for agreeing to act as examiners, and Immo Appenzeller for being available to stand in if necessary.

I am fortunate in that during this work I had the opportunity to work as part of a large community of researchers. This was made possible by the hard work of Tom Ray and all the board members, who through what must have been a lot of graft, forged the JETSET Research Training network. I consider myself priviledged to have been able to participate in such a community, with the best experience and expertise in the field distilled into a network that I had a lot of exposure to, it has been valuable both professionally and personally.

I would like to thank Prof. Silvano Massaglia for hosting me with his group in Torino on two occasions during the course of my study which proved to be both fruitful and enjoyable. I would also like to thank the Torino group members, Andrea, Petros, Ovidiu and Titos, for interesting discussions and advice on working with PLUTO.

Thanks also to Christian Fendt for helping me to integrate quickly in the IMPRS graduate school despite my late arrival, for managing a great graduate school and always giving a sense that there was someone "in your corner". To my friends and peers in the IMPRS school and number 39 people I know, thanks for being there. Coming to a place and immediately having a wide social circle is not to be taken for granted. Steve, Dusan, Giulia, Teo, Marie-Helene, Marik, Isabel, Martin, Pak Hin, Claudia, Giovanna, Bagmeet, Swapna, Ros, Christian, Olga, Eva, Vivi, Giovanni, Brian, Dan, it's been great hanging out, going out, and freaking out with all of you. I hope we can stay in touch (not on Facebook or Twitter though) Oh yeah, I know I probably forgot some people, and I know people remember when they haven't been mentioned, but I've been awake rather a long time now, sometimes sitting at the computer I even find myself forgetting which room I'm in, so don't be too pissed off.

I also thank my fellow Theory group members at the Nord Institut for their enthusiasm for discussion on topics both work and non-work related. Thanks to Teo for a good crash course in scaling and dimensionalisation in the early days, and for being such an agreeable officemate and friend throughout. Thanks to Steffen for LaTex help and translating my abstract, for being a friend and ambassador for German culture, and Bagmeet for those relaxing end-of-the-day chats on the bus downtown. Thanks also to our former resident guru Volker, for conferring upon me Godlike computer powers, for invaluable advice on everything related to linux, especially subversion and public key, which were indispensable during this (and probably all my future) work. Thanks to Dominik for advice and help getting the ball rolling in my work, Bernhard for being my astrophysics "sparring partner" in the weeks leading up to the PhD defense and the all the other current and former group members.

At this point, the end of my (formal) education after more than a quarter of a century, it's an opportune time to thank my teachers down through the years who

done real good (j/k), particularly St. Ailbe's school in Tipperary and NUI Galway, where over many years I received a valuable education and discovered the wonders of science.

Most of all I am indebted to my wonderful parents James and Nuala for providing me with everything I could possibly have needed on my way to this point in my life, for ensuring that I never lacked anything during my childhood and through all my educational endeavours. Thanks to Brendan for hosting me on several much-needed breaks from work in Chamonix, and helping me to keep in mind that there is life outside work and physics.